(12)

RADC-TR-85-171
In-House Report
August 1985

PHASED ARRAYS 1985 SYMPOSIUM – PROCEEDINGS

Dr. Hans Steyskal

Sponsored by
ELECTROMAGNETIC SCIENCES DIVISION
ROME AIR DEVELOPMENT CENTER
HANSCOM AFB, BEDFORD MASS. 01731

MITRE CORPORATION
BEDFORD MASS.

and

THE UNIVERSITY OF MASSACHUSETTS
AMHERST MASS.

DISTRIBUTION STATEMENT A
Approved for public release
Distribution Unlimited

ROME AIR DEVELOPMENT CENTER
Air Force Systems Command
Griffiss Air Force Base, NY 13441-5700

This report has been reviewed by the RADC Public Affairs Office (PA) and is releasable to the National Technical Information Service (NTIS). At NTIS it will be releasable to the general public, including foreign nations.

RADC-TR-85-171 has been reviewed and is approved for publication.

APPROVED: Paul H. Carr

PAUL H. CARR, Acting Chief
Antennas & RF Components Branch
Electromagnetic Sciences Division

APPROVED:

ALLAN C. SCHELL
Chief, Electromagnetic Sciences Division

FOR THE COMMANDER: John A. Ritz

JOHN A. RITZ
Plans Office

If your address has changed or if you wish to be removed from the RADC mailing list, or if the addressee is no longer employed by your organization, please notice RADC (EEAA), Hanscom AFB MA 01731. This will assist us in maintaining a current mailing list.

Do not return copies of this report unless contractual obligations or notices on a specific document requires that it be returned.

AD-A169 316

UNCLASSIFIED
SECURITY CLASSIFICATION OF THIS PAGE

REPORT DOCUMENTATION PAGE

1a REPORT SECURITY CLASSIFICATION: UNCLASSIFIED

1b RESTRICTIVE MARKINGS: N/A

2a SECURITY CLASSIFICATION AUTHORITY: N/A

2b DECLASSIFICATION/DOWNGRADING SCHEDULE: N/A

3 DISTRIBUTION/AVAILABILITY OF REPORT: Approved for public release; Distribution unlimited

4 PERFORMING ORGANIZATION REPORT NUMBER(S): RADC-TR-85-171

5 MONITORING ORGANIZATION REPORT NUMBER(S):

6a NAME OF PERFORMING ORGANIZATION: Rome Air Development Center

6b OFFICE SYMBOL (If applicable): EEA

7a NAME OF MONITORING ORGANIZATION: Rome Air Development Center

6c ADDRESS (City, State and ZIP Code)
Hanscom AFB
Massachusetts 01731

7b ADDRESS (City, State and ZIP Code)
Hanscom AFB
Massachusetts 01731

8a NAME OF FUNDING/SPONSORING ORGANIZATION: Rome Air Development Center

8b OFFICE SYMBOL (If applicable): EEA

9 PROCUREMENT INSTRUMENT IDENTIFICATION NUMBER: N/A

8c ADDRESS (City, State and ZIP Code)
Hanscom AFB
Massachusetts 01731

10 SOURCE OF FUNDING NOS.

PROGRAM ELEMENT NO.	PROJECT NO.	TASK NO.	WORK UNIT NO.
62702F	4600	14	01

11 TITLE (Include Security Classification): Phased Arrays 1985 Symposium - Proceedings

12 PERSONAL AUTHOR(S): Hnas P. Steyskal, Editor

13a TYPE OF REPORT: In-House

13b TIME COVERED: FROM ______ TO ______

14 DATE OF REPORT (Yr., Mo., Day): 1985 August

15 PAGE COUNT: 322

16 SUPPLEMENTARY NOTATION

17 COSATI CODES

FIELD	GROUP	SUB. GR.
09	03	
09	05	

18 SUBJECT TERMS (Continue on reverse if necessary and identify by block number)
Phased array antennas,
Phased array systems,
Digital Beamforming
Monolithic arrays,
Adaptive array antennas

19 ABSTRACT (Continue on reverse if necessary and identify by block number)

The Phased Arrays '85 Symposium, sponsored by the Rome Air Development Center, the MITRE Corporation, and the University of Massachusetts, was held at the MITRE Corporation 15-18 October and reviewed the state-of-the-art of phased array antenna systems and of the technology for next generation systems. This report contains the full papers which were presented with clearance for unlimited distribution.

20 DISTRIBUTION/AVAILABILITY OF ABSTRACT
UNCLASSIFIED/UNLIMITED ☒ SAME AS RPT. ☐ DTIC USERS ☐

21 ABSTRACT SECURITY CLASSIFICATION: UNCLASSIFIED

22a NAME OF RESPONSIBLE INDIVIDUAL: Hans P. Steyskal

22b TELEPHONE NUMBER (Include Area Code): (617) 861-2052

22c OFFICE SYMBOL: RADC/EEAA

DD FORM 1473, 83 APR EDITION OF 1 JAN 73 IS OBSOLETE

UNCLASSIFIED
SECURITY CLASSIFICATION OF THIS PAGE

Contents

TRENDS IN PHASED ARRAY DEVELOPMENT

ALLAN C. SCHELL

Electromagnetic Sciences Division
Rome Air Development Center
Hanscom Air Force Base, MA

In the past fifteen years several outstanding phased arrays have been brought into operation for defense applications. The Aegis, Firefinder, Patriot, and PAVE PAWS systems are illustrative of successful designs. Phased arrays offer near-instantaneous beam steering, real time pattern control, r.f. power conservation with beam agility, and reliability through redundancy and graceful degradation. Yet, the evolution of phased arrays has been a painfully slow process. The impact of phased array technology on radar and communications antennas has been minor in comparison to the impact of solid state technology on the other major subsystem, the signal processor.

The overriding reason for this slow introduction is cost. There is no commercial market to warrant the economies of scale. Hoped-for trends of price reduction of phase shifters have not occurred. And phased arrays have limited rather than expanded the potential for wideband or multiband operation.

The arrays discussed at the 1970 Phased Arrays Symposium were the forerunners of two categories of antennas. First are the large specialized arrays such as the SPADATS array at Eglin AFB, Florida, and the HAPDAR array at White Sands Missile Test Range. These one-of-a-kind antennas were constructed for unique missions, and the associated programs could not take advantage of mass production economies. The second category was typified by the TPN-19 and the SPS-48 arrays, which were put into production. Results in this area were mixed.

More recently there have been major successes in the fielding of phased arrays. The Firefinder series illustrates the potential of thick film circuitry and automated fabrication for cost reduction. The electronically agile radar (EAR) antenna and the Aegis array have met their performance goals. The FPS 117 radar with elevation plane electronic beam control and the PAVE PAWS phased arrays are examples of the success of conservative approaches with long design histories. Nonetheless, these are expensive systems.

It may be regarded as a myth that the cost of phased arrays can be lowered to the point that these antennas are widely used. Perhaps an analogy is that of the jet fighter aircraft. For years concern has been voiced over the escalating cost of fighters. The desired performance for each new model drove the price upward, although the curve has leveled somewhat. Yet, despite the imprecations, new planes are designed and assembled to meet the threat of potential adversaries with upgraded equipment.

The economics of phased arrays are apparent from a simple example. A conformal array operating at S-band and covering 8'x40' of an aircraft fuselage would have 10,000 elements. If the element module cost were $1000 each, the array face would total $10M - not a minor expense, but within the range of possibility. But the array is far from complete. The power distribution internal to the array face, the beam steering and calibration logic, and the radome are but three of several essential subsystems to be added. If, as has been recent experience, the cost per element were closer to $10,000, then the phased array is clearly not going to be the design choice.

The traditional path of per-element modular design has yielded some impressive results when viewed in context with fixed array and reflector alternatives. This approach is especially applicable to lower frequency operation (UHF to L-band), and some early attempts at application to X-band and higher frequency equipment were failures.

The per-element modular design appears to have several shortcomings. First and foremost, this approach is costly because it requires fabricating and installing elements individually. An analogy is the early days of transistor circuits, with the wiring of one transistor at a time into a circuit board. Integration at small and medium scales, with the attendant fabrication techniques, revolutionized the capabilities of circuitry and drastically reduced the per-gate cost of logic.

Second, the per-element modular approach inhibits the interconnection of elements for specialized applications or radiation patterns. Obvious examples are subarraying for limited scan or fixed elevation pattern shaping. It may be adequate in many applications to group and control several elements as a unit, thereby reducing the number of modules by a substantial factor.

Third, this approach, because it isolates the functional operation of an element from its neighbors, cannot accommodate variations among elements. Each element should appear identical to its neighbors, and corrections, calibrations, or compensations for errors must come from a complex centralized subsystem overlaid on the array. Consequently, designs tend towards rigid mechanical structures, near-perfect element patterns, and tightly controlled manufacturing tolerances of feed networks.

The per-element modular approach is one in which the signal and control paths are developed longitudinally, perpendicular to the array face. There is a minimum of intentional cross coupling among elements. A signal finds its way from the element to the output on a single path without diffusing throughout the network.

Yet it is the propagation of signals transverse to the face that may hold a key to improved solutions to phased array construction and operation. Rather than a collection of near-identical elements and paths with an external centralized control, an array can be envisioned that would have elements interconnected with its neighbors, and limited capability for control of its operation at the array face. Behind this level would be a layer with greater logical control, leading to the desired output level. All elements need not be functionally identical in the array; some might be selected for calibration, or used to generate spoofing signals while appearing as "thinned" elements in the main signal mode. This array is logically formed of transverse layers. At the array face, clusters of elements carry out simple functions of calibration and subarraying. Successive layers perform increasingly complex logical functions, leading to the combination not only of signals but of functional operations.

The techniques of photolithography are appropriate to the fabrication of a transversely-developed array. Today there is extensive use of lithography in the manufacture of shaped-beam subarrays of dipoles. The incorporation of active elements adds a dimension of complexity that is not uncommon today in advanced microwave circuit assembly.

For the lower microwave frequency bands, the scale of assemblies is such that specialized equipment will be required for precision construction of complex active r-f networks. Active elements and control devices would occupy a small percentage of the area of the face. New manufacturing techniques are needed to incorporate magnetic or electroacoustic control devices into the array. The introduction of versatile manufacturing capability will be a decided competitive advantage for future large scale production.

At the higher microwave frequency bands, photolithography may be the key to the construction of high performance arrays. Although the scale is not near that associated with large scale integration of logic circuits, the assembly of amplifiers, phase shifters, correlators and associated r-f components within the 0.5cm^2 area available for 44 GHz elements is a challenge. New methods for achieving isolation between components will be needed.

The issue of heat generation is a central topic in the incorporation of active elements. Considerable progress has been made in raising the efficiency of microwave amplifiers, and more can be expected. The improvement in active device performance that results from low temperature operation could lead to the use of cryogenic devices. Small millimeter wave arrays might come to resemble infrared sensors, but with the added advantage of coherent operations such as adaptive nulling.

Antennas of this type are integrated antennas. There is an integration of the radiators and r-f networks. There is an integration of the signal path and the logic circuitry through the incorporation of active and control devices. The lithographic manufacture of the entire assembly on a substrate is the means of realizing the antenna. The techniques of computer-aided design and manufacture are essential; no hand tailoring or assembly is the goal. These techniques have served the logic industry well, and appropriate versions can do the same for microwave and millimeter wave technology.

An aspect of phased arrays that will receive greater attention in the future is reliability, and in particular, element availability. In the early days of phased arrays, the ability of an array to continue to function with some inoperable elements was cited as the advantage of "graceful degradation." In the intervening years, the requirements associated with clutter reduction and ECCM have led to specifications for very low sidelobes. The loss of operating elements in an array leads to higher sidelobes, and in some instances there is no longer latitude within the performance envelope for the "graceful degradation" that can be expected from the loss of several elements during the typical maintenance cycle. This leads to design choices that minimize the effect of module failure. For example, an array of fixed subarrays in the azimuth plane and active modules in the elevation plane will be able to maintain low azimuth sidelobes in the event of module failures, versus the case of fixed elevation plane subarrays and active azimuth modules.

Simple geometrical choices will not address the problem of reliability for integrated antennas. Low yields for the active devices will lead to unacceptably high amounts of circuit repair and replacement during manufacture. Inhomogeneities and uneven depositions will cause unwanted variability in path gains and losses throughout the feed circuitry. Careful choices of materials and dimensions are essential to avoid the effects of migration and breakdown.

An option for the increase in reliability is the incorporation of built-in test and self-repair circuitry. Logic circuits imbedded in the array face can sense changes in operation, alter and calibrate the appropriate transmission paths, and adjust excitation weights for optimum performance, based on knowledge of the operating environment.

One of the limitations of phased arrays is the restriction imposed on the frequency ranges of operation by the array face geometry and the feed. Integrated antennas offer the potential for increased operating bandwidth. Amplifiers close to the radiating elements can minimize internal reflections, and transversal filters can be constructed in signal paths to compensate for varying amplitude and phase. Of greater interest is the use of specialized radiating structures which couple constructively to simulate larger elements at lower frequencies, decoupling at the higher bands to become a greater number of smaller radiators.

The development of integrated antennas is in its infancy. There are a host of problems needing creative solutions. Among the electromagnetic topics inhibiting effective operation are the propagation of surface waves across the substrate and the radiation and coupling of feed lines on the array face.

Integrated antennas can be constructed in versions that convert the r-f signals to digital form. There is a basic compatibility with the digital world that permits the introduction of processing close to the array face. This incorporation of digital beamforming can offer considerable flexibility in operation. In the future, integrated antenna technology will merge with computer technology in the areas of design, materials, and manufacture to produce a continuous and consistent signal path from free space to the output terminal or display. As in visual cortex, signals from input radiation will receive increasing amounts of processing as it moves through successive layers of the array. Intelligent subarrays will structure the electromagnetic functionality of the array face, and internal knowledge based logic will select signals for further combination based on their applicability to the desired function and the perceived environment. Outputs will no longer be based on the amount of power delivered to the terminal, but on the ability to carry out the intended system objective.

There is a long road between the present hardware and the hoped-for goals of integrated antennas. Many phased arrays of the current technology will enter the inventory before any photolithographic panacea appears on the scene. Yet the driving forces of this evolution are at work. The cost and the performance limitations of today's waveguide solutions are working to generate new ideas. The continuing revolutions of the logic industry and the microwave monolithic integrated circuit community are bringing relevant technology closer to the array face. It will be a shorter time than many would care to envision until the skills of an antenna designer are a transformation of the skills of a computer designer.

Comparison of Architectures for Monolithic Phased Array Antennas

David M. Pozar
Daniel H. Schaubert
Department of Electrical and Computer Engineering
University of Massachusetts
Amherst, MA 01003

ABSTRACT

This paper will consider a variety of potential configurations for monolithic phased array antennas, and discuss their relative advantages and disadvantages. Considerations such as bandwidth, maximum scan range, feeding methods, substrate real estate, and manufacturability will be addressed. Results of analyses for some particular configurations will be presented.

INTRODUCTION

The concept of a monolithic phased array, where active devices are integrated on the same substrate as the radiating elements, promises achievement of the long-awaited goal of a truly versatile and low-cost millimeter wave scanning antenna. Such an array, however, presents a number of challenging problems to the antenna designer, not least of which is the problem of how to best configure the radiating elements, active devices, and feed network. This paper will address this issue by considering a number of potential monolithic phased array architectures, and discussing their relative merits. Printed dipole, microstrip patch, broadside slot, and endfire slot elements will be considered in a number of different arrangements. The following list describes some of the criteria to be used in evaluating various architectures:

- Maximum scan range-this is dictated essentially by impedance matching and the possible existence of scan blindness.

- Bandwidth - printed dipoles and patches on grounded substrates have relatively narrow bandwidth. Bandwidth is increased by increasing the substrate thickness.

- Substrate real estate - there must be enough space on the substrate for the radiating antenna elements, the feed network, phase shifters, bias circuitry, etc., without deleterious cross-coupling.

- Feed radiation - spurious radiation from feed network discontinuities may degrade sidelobe levels, etc.

- Manufacturability - it is desired to reliably construct such an array in as "monolithic" a form as is possible.

- Heat removal - particularly at higher millimeter wave frequencies, heat removal from closely packed active devices is essential.

- Polarization - in some applications it is desired to have circular or dual polarization.

It should be noted that many of the above criteria (e.g., spurious radiation, heat removal), may not be significant at microwave frequencies, but often are quite important at millimeter wave frequencies. There are two reasons for this: first, the substrates required for MMIC work have relatively high dielectric constants, and second, at millimeter wave frequencies substrates are electrically thicker and active devices are physically closer together.

BROADSIDE SLOT ELEMENTS

Printed slot antennas and arrays can be made in the ground plan of a grounded dielectric slab [1], with microstrip feed lines or coplanar waveguide feeds. See Figure 1a. The main problem with this approach is that the radiation field from such a slot element is bidirectional. Thus, a 3dB loss in gain is incurred and, what may be worse, this undesired power can cause serious problems by interfering with other components or scattering to degrade sidelobe levels and polarization. Some suggested approaches to make the radiation unidirectional are discussed below.

One way is to use a ground plane reflector behind the array. This was done in [1], and has been suggested by others for phased array applications. This approach has been shown to be feasible for broadside arrays, but may not work for scanning arrays. As shown by Mailloux [2], a TEM waveguide mode can be excited in the parallel plate region, leading to scan blindnesses quite close to broadside. In the broadside case, the TEM mode is not excited because the uniform element phasing and spacing of near $\lambda/2$ tends to cancel such a mode.

Another approach to eliminate the bidirectional radiation is to use a cavity-backed slot element. See Figure 1b. This configuration takes the form of stripline, with the slot in one of the ground planes and fed by the center strip conductor. Plated-through holes surround the slot element and form a cavity, thus eliminating the parallel plate modes discussed above. A number of such antennas and arrays have been successfully tested at 20 GHz [3]. The main problem here is one of manufacturability. The large number of via-holes required for this approach cannot be produced reliably; in addition, stripline is not a preferred medium for active device integration.

ENDFIRE SLOT ELEMENTS

Endfire slot antennas can be made by etching tapered slot or "notch" antennas near the edge of a substrate, and feeding with microstrip or slotline, as shown in Figure 2a. A number of such substrates can be placed side by side to form a planar array. Circular or dual polarization requires some sort of "eggcrate" arrangement (Figure 2b), and may be difficult to fabricate in monolithic form. In addition, these types of endfire radiators have been known to exhibit scan blindnesses at microwave frequencies; the situation may be worse when high dielectric constant substrates are used.

PRINTED DIPOLES OR PATCHES ON A SINGLE SUBSTRATE

At present, it appears that printed dipole or microstrip patch elements may be the most promising element types for monolithic phased arrays. Probably the most direct approach is to print the dipoles or patches on a single grounded Gallium Arsenide substrate as shown in Figure 3, along with the active devices and feed network. A small broadside patch array on Gallium Arsenide was recently constructed in this manner [4]. It appears, however, that a number of problems may arise when using this approach for a monolithic phased array.

First, a single layer substrate probably does not have enough surface area to accommodate radiating elements, phase shifters, and feed networks. Antenna element spacings are required to be on the order of $\lambda_o/2$, and phase shifters generally require lines that are roughly $\lambda_g/4$ in length. The routing of a corporate feed network and bias lines further complicates the situation. Note that the C-band printed phased array reported by Cipolla [5] required a separate substrate for the phase shifters and power dividers, and was still quite dense.

Another issue with this geometry is the scan blindness/bandwidth tradeoff. Scan blindness in printed arrays [6], [7], [8], [9] is a condition whereby no real power leaves the face of the array, and is caused by a surface wave resonance at certain scan angles. This condition limits the maximum scan range of the array, thus it is desired to use configurations for which such blind angles are as far from broadside as possible. As discussed in [6], the blindness angle moves closer to broadside as the substrate becomes thicker. On the other hand, thick substrates are required for increased bandwidth. Thus, there exists a tradeoff between the maximum scan range of a printed phased array and its bandwidth. Figure 4 shows a plot of these two quantities versus substrate thickness, for a Gallium Arsenide substrate. The scan blindness angle is a function of element spacing, and gets closer to broadside as the element spacing gets larger [6]; data are shown for $\lambda_o/2$ spacing. It should also be noted that the bandwidth of Figure 4 is based on impedance mismatch; better bandwidth may be attainable if some type of impedance matching network is used. Closer element spacings will improve the blindness problems, but at the expense of increased complexity and cost.

The single layer configuration also suffers from the possibility of spurious feed radiation.

PRINTED DIPOLES AND PATCHES ON A TWO-LAYER SUBSTRATE

Figure 5 shows a possible two-layer design, where a grounded layer of Gallium Arsenide holds the active devices and feed network, and a superstrate or cover layer of a low dielectric constant material holds the radiating elements. Coupling from the feed to the antenna elements could be made by proximity coupling (as has already demonstrated with dipoles [10]), or via holes.

This configuration partially corrects the two major problems discussed above for the single layer substrate thickness. As can be seen from Figure 5, there now exists essentially twice the area for radiating elements, active devices, and feed networks. In addition, the radiating elements are now mounted on a composite substrate with an effective dielectric constant which is significantly lower than that of Gallium Arsenide. This is a desirable trend for both increased bandwidth and increased scan range.

There still are problems, however. First, spurious radiation from the active device/feed layer has not been eliminated, and actually may be more harmful here because of the possibility of strong coupling to the radiating elements directly above. Second, the gains in bandwidth and maximum scan range are not as great as one might hope. Figure 6 shows the blindness angle of an array on a two-layer substrate with $\lambda_o/2$ spacing, for various layer thicknesses. For 10% bandwidth and a Gallium Arsenide layer thickness of $0.02\lambda_o$, scan blindness occurs at about 68°, compared with 63° for a single layer GaAs geometry with 10% bandwidth. (Note: As a rule of thumb, the maximum scan range should be taken to be at least 10° less than the scan blindness angle, due to severe impedance mismatch near blindness.)

PRINTED DIPOLES OR PATCHES ON A TWO-SIDED SUBSTRATE

Figure 7 shows a two-sided geometry, where a Gallium Arsenide substrate is on one side of a ground plane, and contains the active devices and feed networks. A low dielectric constant substrate is bonded to the other side of the ground plane, and contains the radiating elements. Coupling can take place through apertures in the ground plane.

This type of design has the interesting advantage of using the best substrate for a given function: Gallium Arsenide for the phase shifters and active devices, and a low dielectric constant substrate for the antenna elements. For example, for an antenna substrate with ϵ_r=2.55, a thickness of about $0.05\lambda_o$ is required for 10% bandwidth, but the blindness angle occurs at about 80°. The situation would be even better for lower dielectric constant layers (e.g., hexcell). Another interesting feature of this design is that a ground plane separates the radiating aperture from the feed network, so the possibility of spurious radiation is greatly reduced. Also, the radiating elements will not be affected by gaps between individual

Gallium Arsenide wafers of the feed network, as would the single or two-layer designs discussed previously.

This design depends on adequate coupling through the ground plane to the radiating patches. One way to do this is to use via connections through holes in the ground plane, to microstrip feedlines on the bottom layer. It may be desirable, however, to avoid such long via holes, in which case an aperture coupling mechanism could be used.

Reference [11] describes a microstrip antenna coupled to a microstripline through an aperture in the ground plane. Figure 8 shows the geometry, and Figure 9 shows a Smith chart plot of the impedance locus of an X-band model. (Note that the double loop, by proper design, can be used to increase the impedance bandwidth of the patch antenna.) A rigorous theoretical analysis of the aperture coupled patch antenna is in progress.

Variations on the above approach, such as the use of slotlines in the ground plane for feed lines, as opposed to microstripline, are possible.

CONCLUSION

This paper has compared the relative advantages and disadvantages of a number of possible monolithic phased array architectures, in terms of scanning range, bandwidth, manufacturability, and other factors. It appears that printed dipole or microstrip patch antennas are the most likely candidate elements for such an array, but a basic problem is that the most desirable substrate parameters for the antenna elements conflict with the required use of a substrate like Gallium Arsenide for active device integration. The use of two-layer or two-sided configurations was discussed as way to alleviate this difficulty.

REFERENCES

[1] Y. Yashimura, "A Microstrip Slot Antenna", IEEE Trans. Microwave Theory and Techniques, Vol. MTT-20, pp. 760-762, Nov. 1972.

[2] R. Mailloux, personal communication.

[3] K. Arkind, personal communication.

[4] D. J. Martin, L. D. Sikes, and E. P. Valkenburg, "20 GHz GaAs Monolithic Array Design and Performance", presented at the 1984 IEEE Antenna and Propagation Symposium, Boston.

[5] F. W. Cipolla, "A 7.5 GHz Microstrip Phased Array for Aircraft-to-Satellite Communication", IEEE Trans. Antennas and Propagation, Vol. AP-29, pp. 166-171, Jan. 1981.

[6] D. M. Pozar and D. H. Schaubert, "Scan Blindness in Infinite Phased

Arrays of Printed Dipoles", IEEE Trans. Antennas and Propagation, Vol. AP-32, pp. 602-610, June 1984.

[7] D. M. Pozar and D. H. Schaubert, "Analysis of an Infinite Array of Rectangular Microstrip Patches with Idealized Probe Feeds", IEEE Trans. Antennas and Propagation, Vol. AP-32, pp. 1101-1107, October 1984.

[8] D. M. Pozar, "General Relations for a Phased Array of Printed Antennas Derived from Infinite Current Sheets", accepted for publication in the IEEE Trans. Antennas and Propagation.

[9] D. M. Pozar, "Analysis of Finite Phased Arrays of Printed Dipoles", submitted for publication in the IEEE Trans. Antennas and Propagation.

[10] W. G. Oltman and D. A. Huebner, "Electromagnetically Coupled Microstrip Dipoles", IEEE Trans. Antennas and Propagation, AP-29, pp. 151-157, Jan. 1981.

[11] D. M. Pozar, "A Microstrip Antenna Aperture Coupled to a Microstrip Line", Electronics Letters, Vol. 21, pp. 49-50, Jan. 17, 1985.

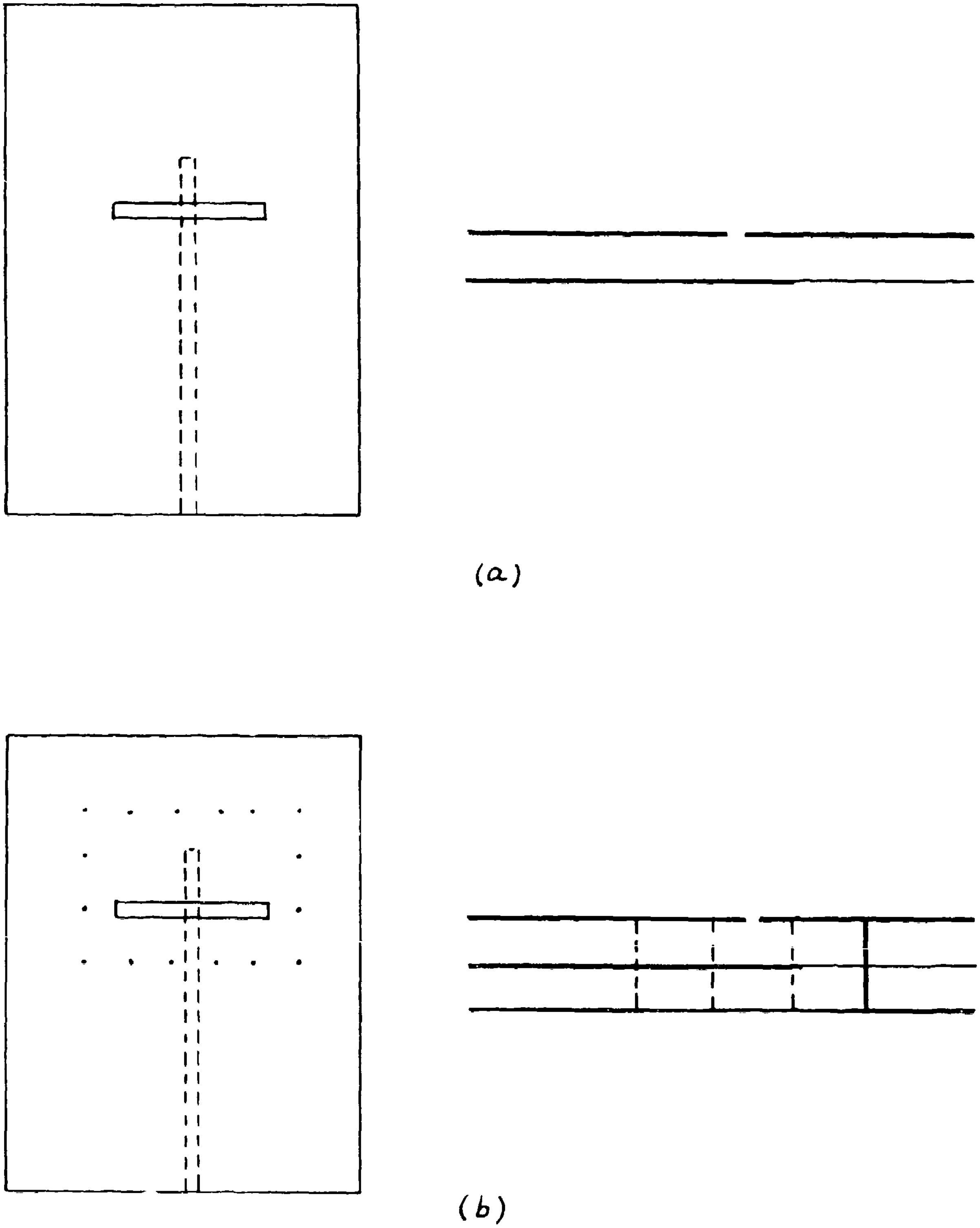

Figure 1. Slot elements for monolithic arrays. a) Bidirectional microstripline-fed slot. b) Unidirectional cavity-backed slot.

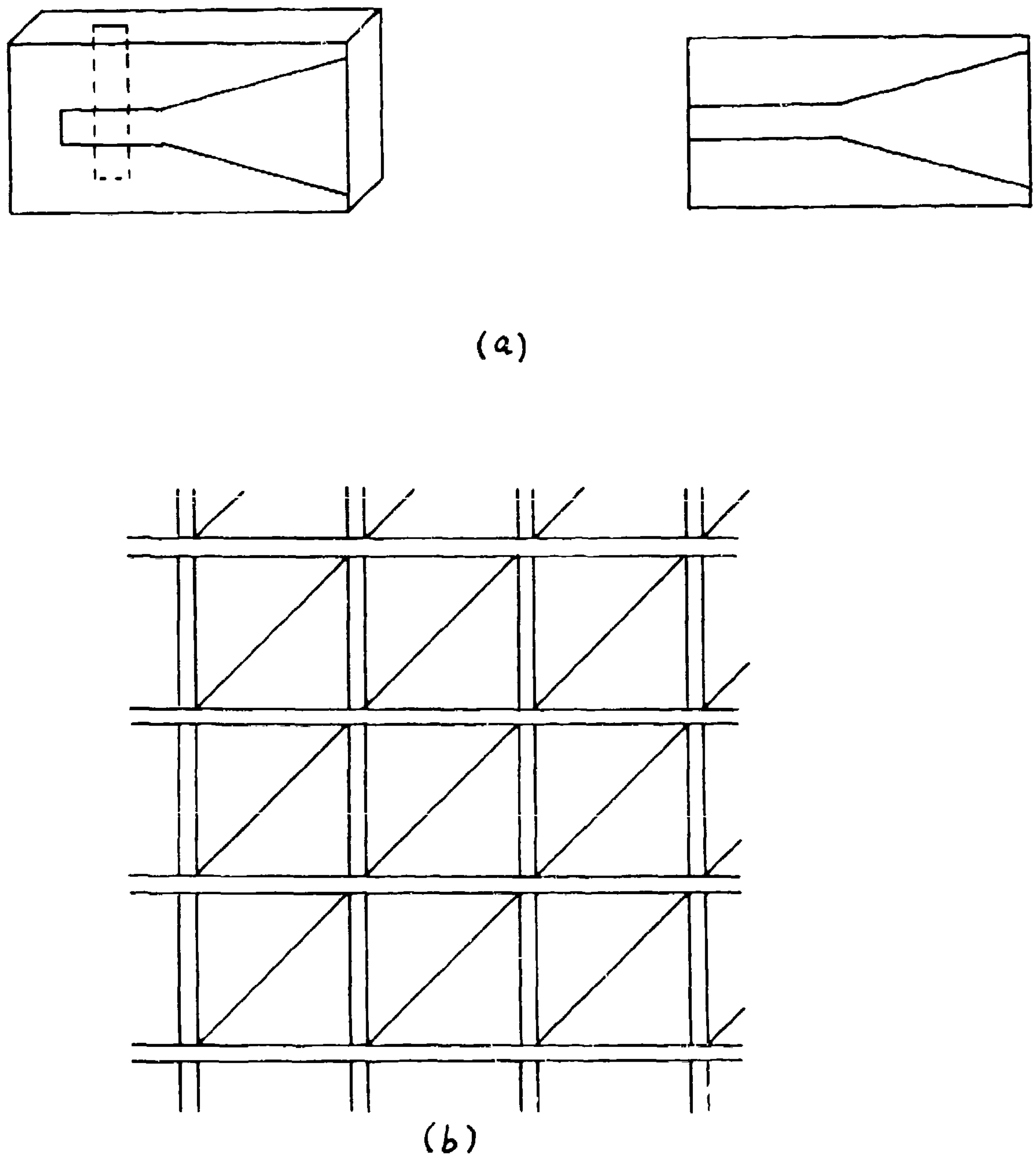

Figure 2. a) Endfire slot elements, and b) arrays for dual polarization.

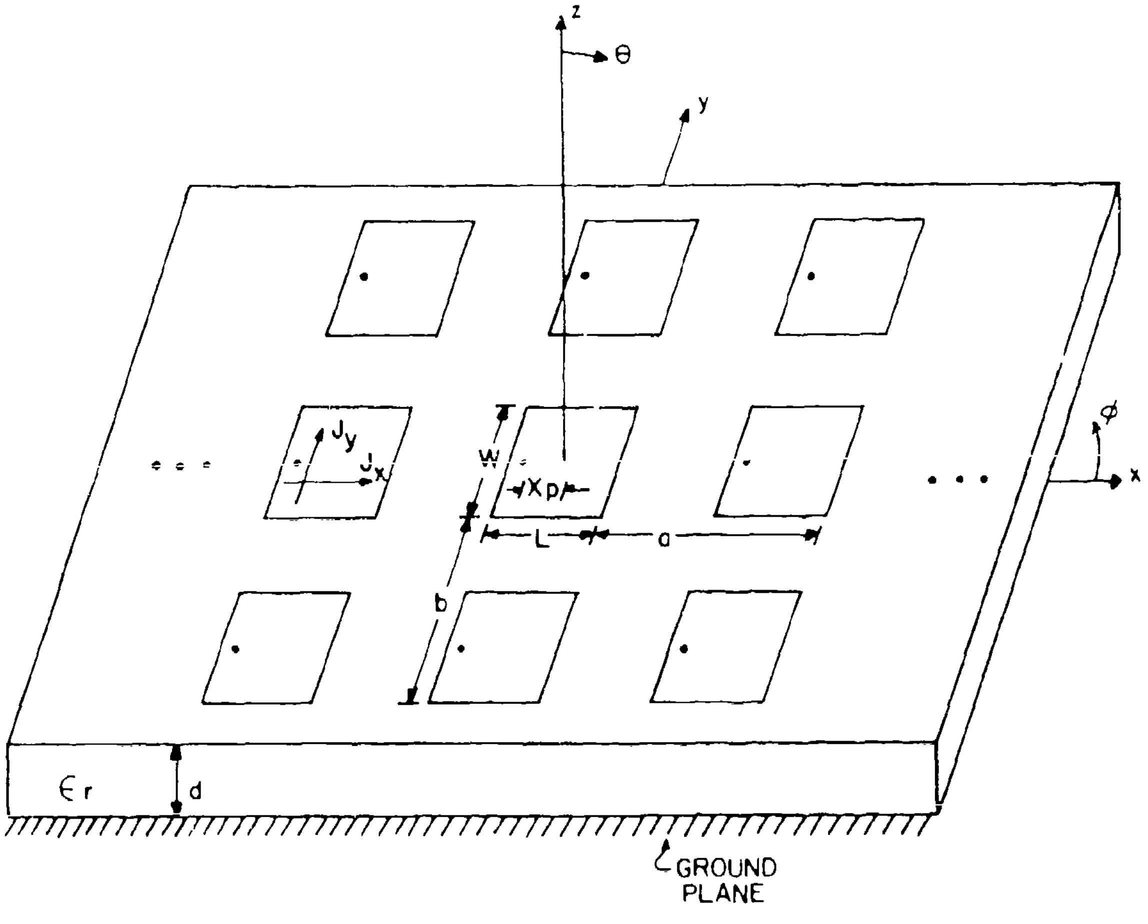

Figure 3. Geometry of an array of printed antennas on a single layer substrate.

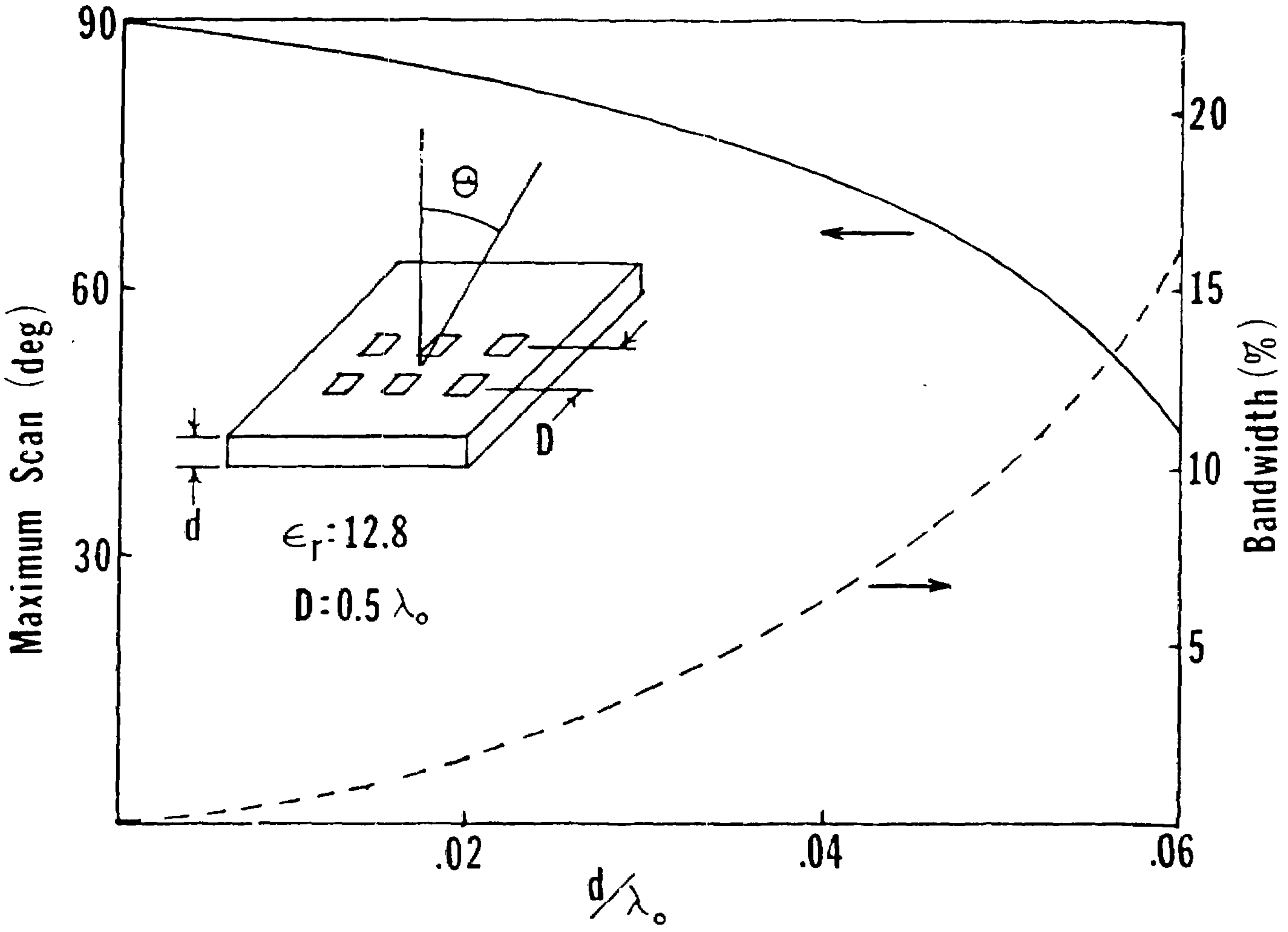

Figure 4. Maximum scan angle/Bandwidth tradeoff for a printed phased array on a single Gallium Arsenide substrate. Element spacing is $\lambda_o/2$.

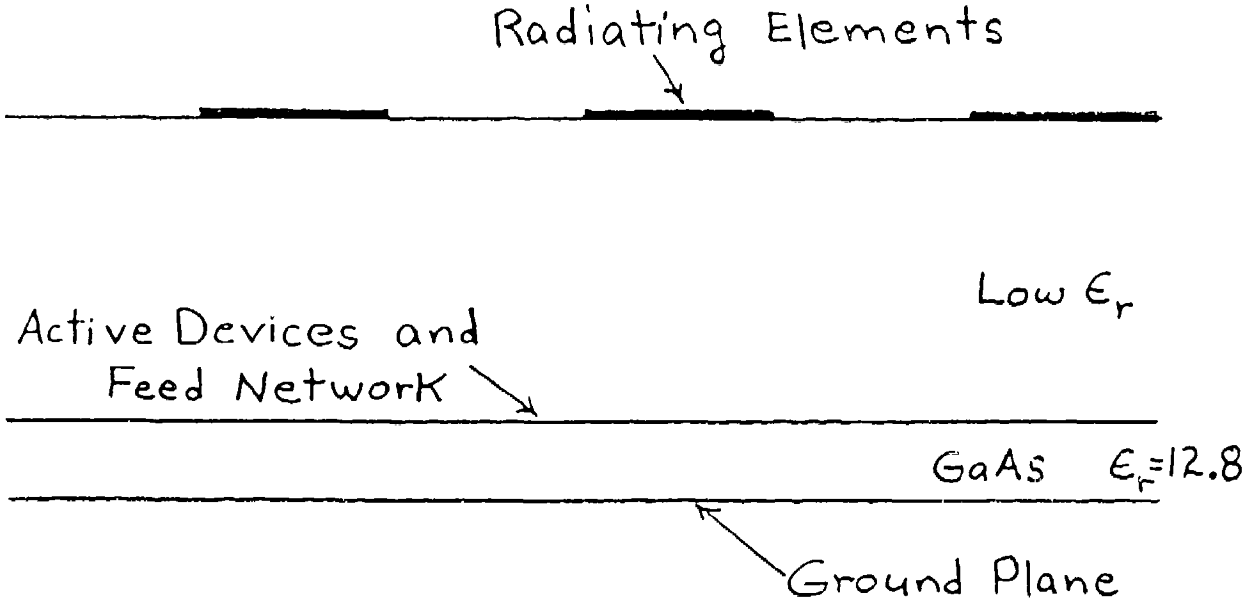

Figure 5. Cross-section geometry of a two-layer printed phased array design.

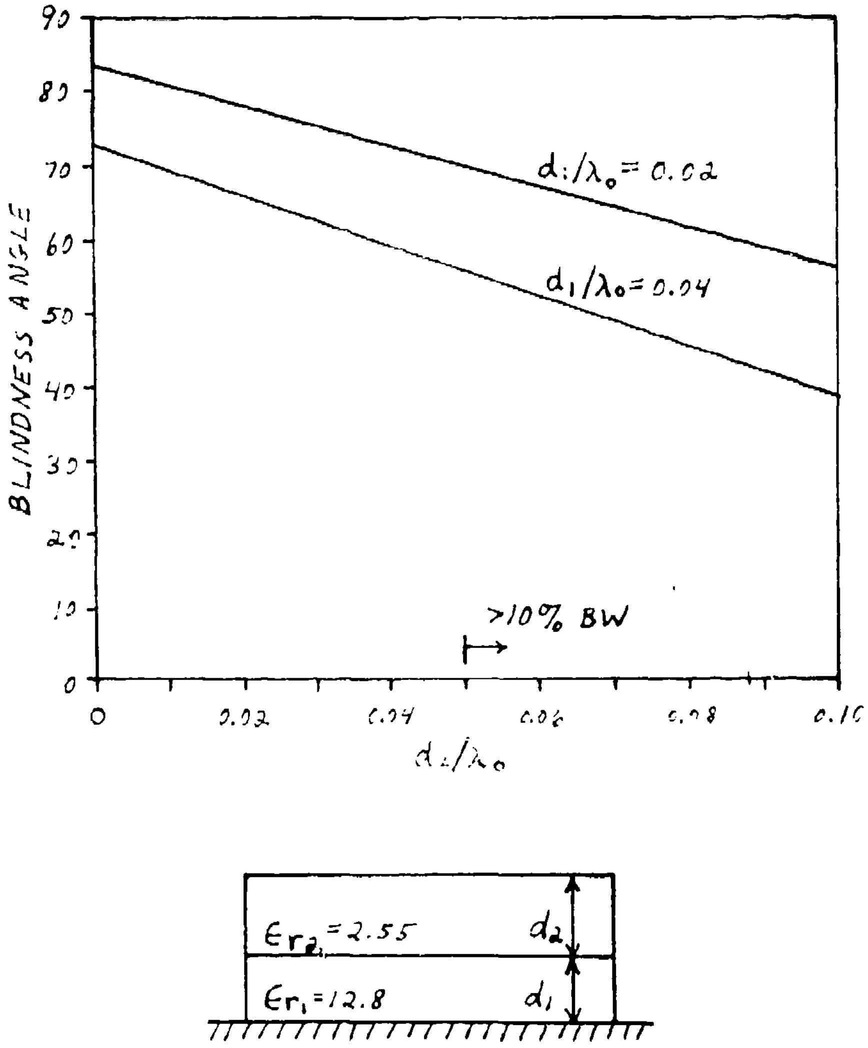

Figure 6. Scan blindness angle for a two-layer substrate geometry, versus layer thickness. Element spacing is assumed to be $\lambda_0/2$.

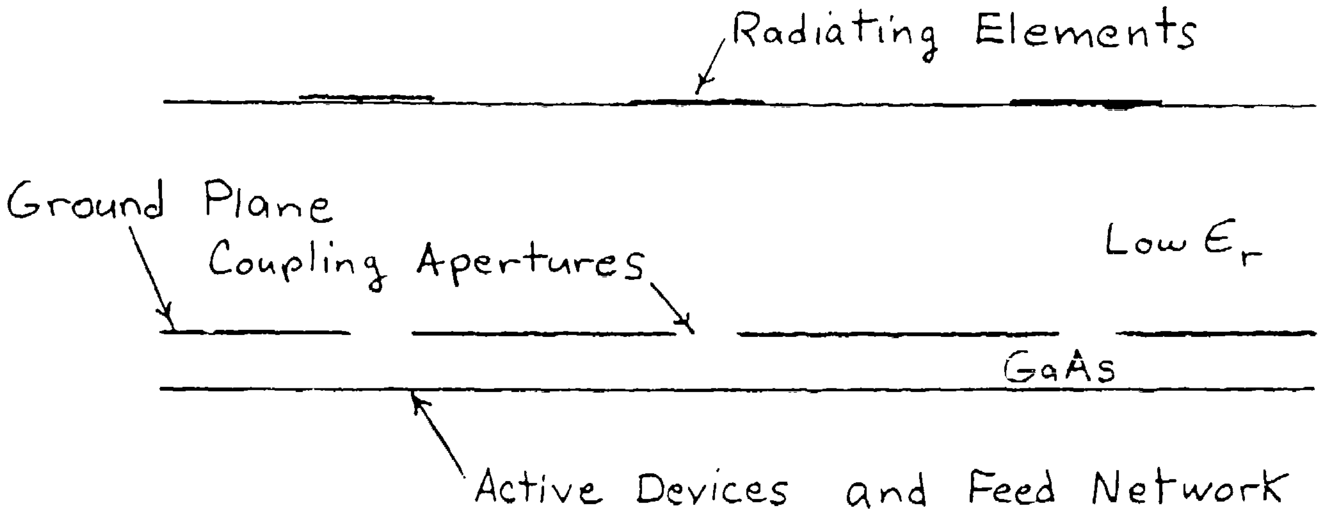

Figure 7. Cross-section geometry of a two-sided printed phased array design.

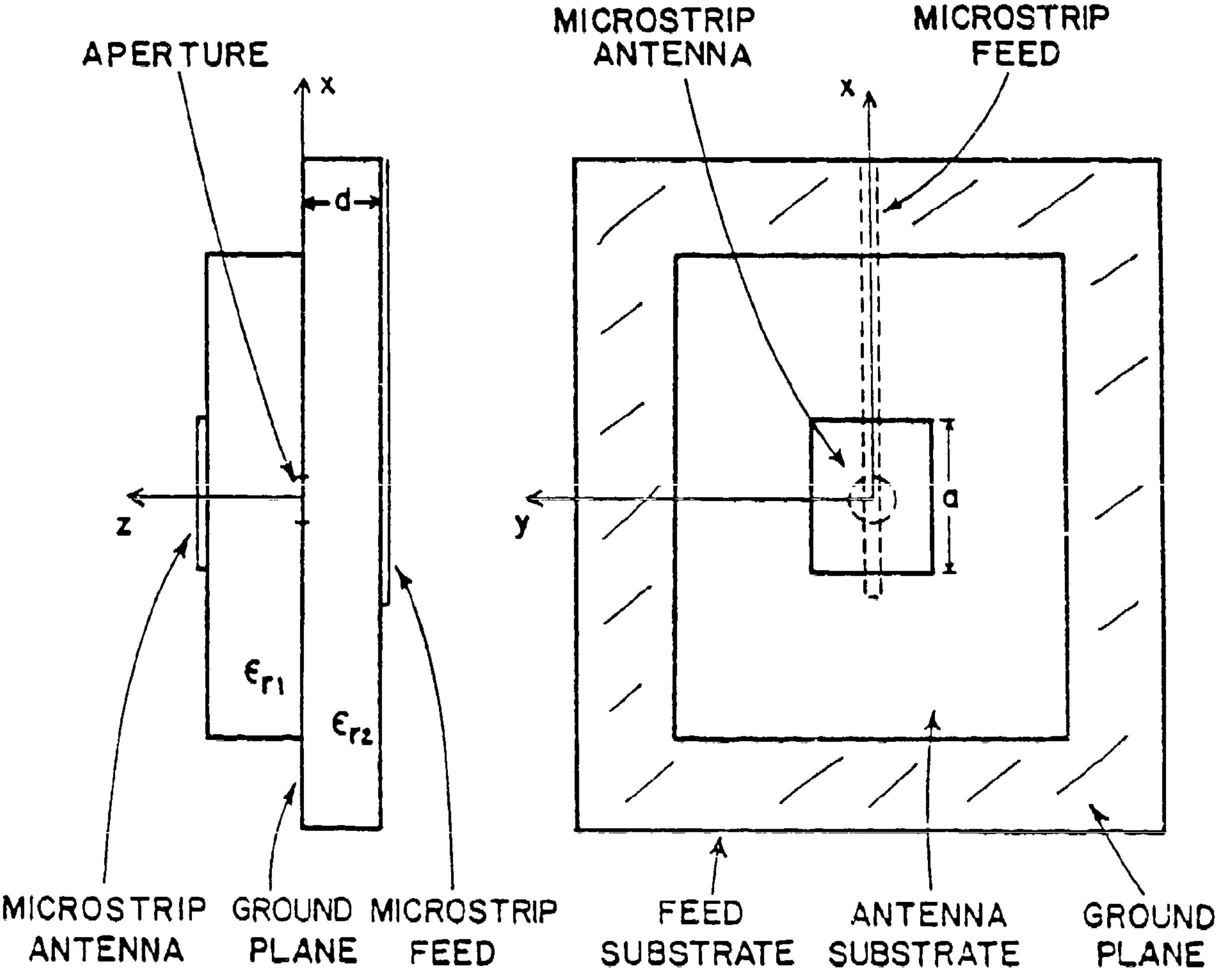

SIDE VIEW

TOP VIEW

Figure 8. Geometry of an aperture coupled microstrip antenna.

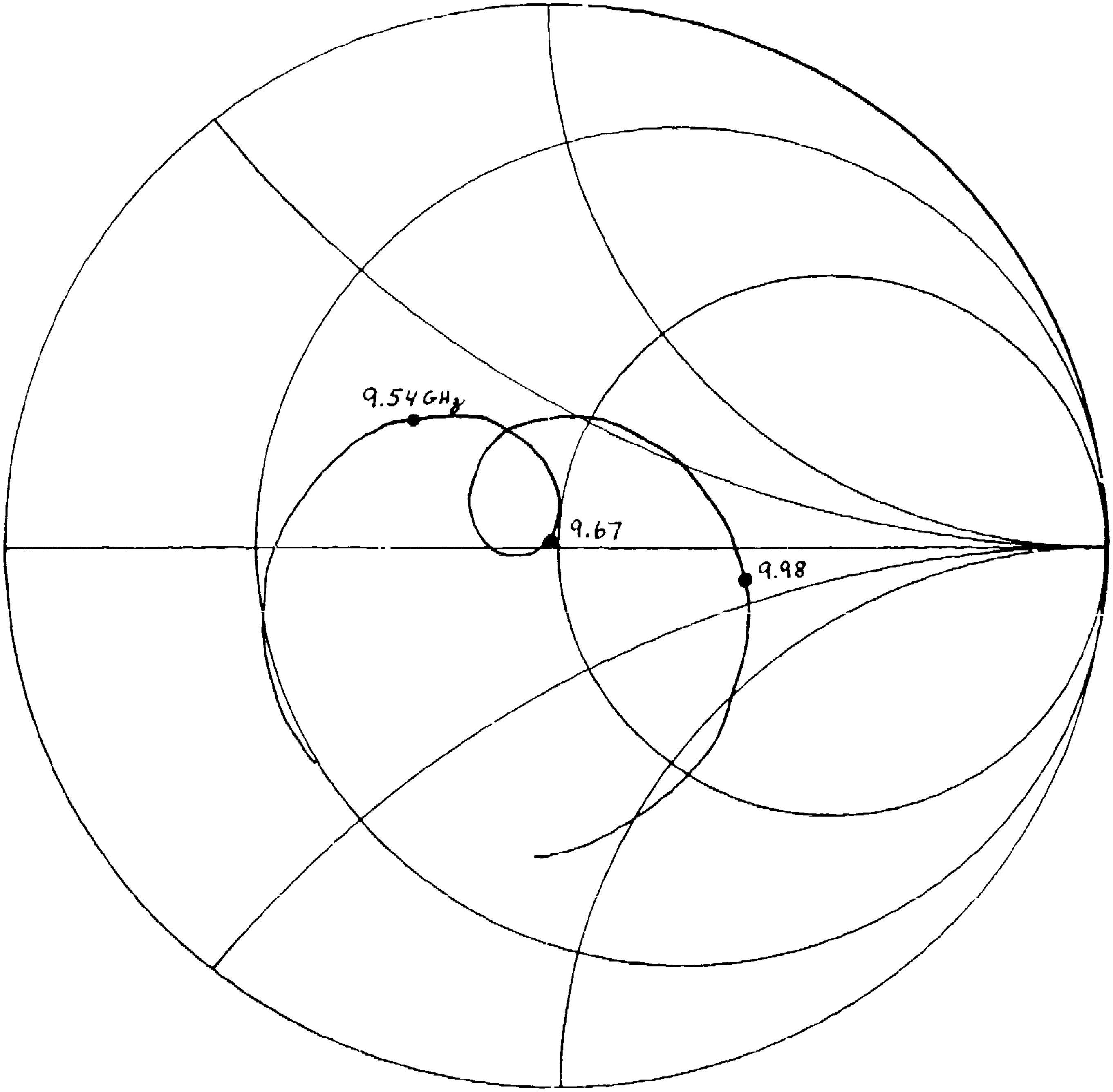

Figure 9. Measured impedance locus of an aperture coupled microstrip antenna at X-band. Feed substrate is 0.025" thick with a dielectric constant of 10.2; antenna substrate is 0.020" thick with a dielectric constant of 2.2. Patch size is 9.4mm by 12.8mm; coupling aperture is a rectangular slot 0.9mm by 3.5mm.

ELECTROMAGNETIC BACKSCATTER FROM MICROSTRIP ARRAYS: THEORY AND MEASUREMENT

Robert V. McGahan
Electromagnetic Sciences Division
Rome Air Development Center

B. Rama Rao
MITRE Corporation

SUMMARY

Electromagnetic backscattering from two dimensional microstrip arrays has been studied in this paper as a function of the frequency of the incident signal, array lattice spacing, angle of incidence, and antenna load mismatch conditions. Theoretical and experimental investigations have been conducted on two types of microstrip arrays: a) a 32 element triangular grid array consisting of coaxially fed circular disk microstrip elements and b) a 561 element square grid array of rectangular patch elements.

Significant antenna mode backscattering from the triangular grid array is observed when the incident frequency is the same as the resonant frequency of the fundamental TM_{11} mode of the circular microstrip disk element. Higher order mode backscattering from the array is also observed at large incidence angles when the incident frequency is the same as the resonant frequency of TM_{21} higher order mode of the microstrip element. Negligible backscatter from the array occurs when the incident frequency is well below the fundamental resonant frequency of the microstrip patch element. Theoretical results for the three frequency regimes are in good qualitative agreement with experimental measurements.

Electromagnetic Backscatter from Microstrip Arrays

1. Introduction: This paper describes the results of theoretical and experimental investigations into the electromagnetic backscatter from two dimensional microstrip arrays. Two types of microstrip arrays have been analyzed. The first is a 32 element triangular grid array consisting of coaxially fed, circular disc microstrip elements; the second is a 561 element square grid array consisting of rectangular patch elements. The scattering patterns of these arrays have been calculated for both in-band and out-of-band frequencies and examined as functions of array lattice spacing, element size, angle of incidence, and antenna load mismatch conditions. The computed results are in good qualitative agreement with measurements on the two types of arrays. Since the scattering response of an array is a strong function of frequency the problem has been examined in three different frequency regimes: 1) antenna mode scattering when $f_i = f_{res}$, 2) higher order mode scattering when $f_i > f_{res}$, and 3) low frequency structural mode scattering when $fi << f_{res}$. The frequency of the incident signal is f_i and f_{res} is the fundamental reasonant frequency of the microstrip element (lowest order TM_{11} mode).

2. Antenna Mode Scattering Theory: Antenna mode scattering occurs when the frequency of the incident energy is the same as the resonant frequency of the lowest order TM_{11} mode of the circular disc microstrip element. The RF energy absorbed by the antenna is partially re-radiated due to reflections at the feed terminals that occur when the antenna is not conjugate matched to the load. The direction of the peak sidelobe in the backscatter direction is a

function of the array lattice spacing.

The backscattering cross section σ_A of an array of MxN elements can be obtained by the addition of the scattered fields from the individual elements, taking into account the relative phase angle between the scatterers, [1,2]

$$\sigma_A = \left| \sum_{0}^{M} \sum_{0}^{N} (\sigma_{MN})^{1/2} \exp(j\phi_{MN}) \right|^2 \tag{1}$$

where σ_{MN} is the antenna mode cross section of the (m,n) element in the array, ϕ_{MN} is the relative phase angle associated with the (m,n) element in the array. The magnitude of the relative phase angle is determined by selecting a reference plane located at the (o,o) reference element in the array. If the scattering cross sections of the individual elements in the array are assumed to be equal, summation of the phase contributions from the elements in a triangular grid array results in

$$\sigma_A = \left|(\sigma_o)^{1/2} A_T A_x A_y\right|^2 \tag{2}$$

where σ_o is the scattering cross section of an array element and A_T, A_X, and A_Y are the array factors for the triangular grid array [3] as denoted below:

$$A_T = \left(1.0 + \exp(-jf_x)\ \exp(-jf_y)\right) \tag{3a}$$

where $f_x = kd_x \sin\theta \cos\phi$, (3b)

$$f_y = kd_y \sin\theta \cos\phi \ , \tag{3c}$$

(θ,ϕ) are the angular coordinates of the backscattered signal, λ_o is the wavelength, $k = 2\pi/\lambda_o$, and d_x and d_y are the inter-element spacings between the array elements along the x and y axes. Also,

$$A_x = \frac{\sin(kMd_x \sin\theta\cos\phi)}{\sin(kd_x \sin\theta\cos\phi)} \tag{4a}$$

and

$$A_y = \frac{\sin(kNd_y \sin\theta\cos\phi)}{\sin(kd_y \sin\theta\cos\phi)} \ . \tag{4b}$$

The backscattering cross section of the microstrip antenna element σ_o in equation 2 can be represented [4] as

$$\sigma_o = \frac{\lambda^2}{4\pi}\left|S(\theta,\phi) + |\Gamma_B| G_B(\theta,\phi) P_b\right|^2 \ . \tag{5}$$

The scattering cross section of the antenna element can be decomposed into two major components. The first term S in equation (5) is due to the "structural mode scattering" from the antenna array. It arises from the currents induced on the surface of the antenna element by the incident electromagnetic signal and is totally independent of the load connected to the antenna terminals. The structural scattering cross section of the array will be discussed later in this paper. The second term of the cross section attributable to has been called the "antenna mode" backscatter. The factor ΓG_b is the gain of the antenna element in the backscatter direction. Γ_b is the modified reflection coefficient defined in terms of the load impedance $Z_L = R_L + jX_L$ and the array element impedance $Z_a = R_a + jX_a$:

$$\Gamma_b = \frac{Z_L - Z_a^*}{Z_L + Z_a^*} \qquad (6)$$

where $Z^*_a = R_a - jX_a$ is the complex conjugate of the impedance of the array element. P_b is the polarization mismatch between the scattering array element and the incident electromagnetic signal.

The gain of a circular disc microstrip antenna element of radius a operated in its fundamental (lowest order) TM_{11} mode can be calculated from its radiated fields [5,6] and is given by

$$G_B(\theta,\phi) = 4G_N(\theta,\phi)/G_D \ , \qquad (7a)$$

where

$$G_N(\theta,\phi) = 4\{\cos^2\phi\ [J_2(k_o a \sin\theta\ ) - J_o(k_o a \sin\theta\ )]^2 + \cos^2\theta \sin^2\phi\ [J_2(k_o a \sin\theta\ ) + J_o(k_o a \sin\theta\ )]^2\} \quad (7b)$$

and

$$G_D = \int_0^{\pi/2} \{[J_2(k_o a \sin\theta\ ) - J_o(k_o a \sin\theta\ )]^2 + \cos^2\theta\ [J_2(k_o a \sin\theta\ ) + J_o(k_o a \sin\theta\ )]^2\} \sin\theta d\theta \quad (7c)$$

and a is the radius of the microstrip circular disc radiator. Similarly, the antenna impedance Z_a for a coaxially fed, circular disc microstrip element is given [5,7] by

$$Z_a = -\frac{j\omega\mu h}{2} \sum_{\ell=1}^{\infty} \{ J_\ell^2(k\rho_o)/A_n + J_n(k\rho_o)Y_n(k\rho_o)\} \quad (8a)$$

where

$$A_n = -\frac{pJ_n(ka) - jJ_n'(ka)}{pY_n(ka) - jY_n'(ka)} \quad (8b)$$

and

$$p = \eta_o(G_a + jB_a) \quad (8c)$$

In equation 8c,

$$G_A = 2P_T/h^2E_o^2J_n^2(ka) \quad , \tag{8d}$$

$$B_a = \frac{\varepsilon\omega\pi a^2}{h}\left[\left\{1 + \frac{2h}{\pi\varepsilon_r a}\left[\ln(\pi a/2h) + 1.7726\right]\right\}^{1/2} - 1\right] \quad . \tag{8e}$$

The total power lost by the microstrip radiator is P_t and is given by

$$P_T = P_r + P_c + P_d \tag{9a}$$

where

$$P_r = \frac{[hE_oJ_n(ka)k_oa]^2}{1920} G_D \quad , \tag{9b}$$

$$P_c = 1.68 \times 10^{-10}f^{-3/2}E_o^2 \quad , \tag{9c}$$

and

$$P_d = 0.805 \times 10^{-4}h\ \tan(\delta)E_o^2/f \quad . \tag{9d}$$

In the above equation,

h = thickness of the dielectric substrate (meters), a = radius of the microstrip radiator (meters), ε_r = relative dielectric constant of the substrate, E_o = E field amplitude of the exciting field (volts/meters),

$\tan \delta$ = loss tangent of the substrate, f = frequency (GHz), η_o = free space impedance, μ = permeability, and $k = k_o\sqrt{\varepsilon_r}$.

At the fundamental resonant frequency of the antenna, the contribution to total scattering cross section by the structural mode scattering is much smaller than the contribution from the antenna mode scattering. Mutual coupling effects between the array elements have been ignored in deriving equations 2 and 7. Equation 7 represents the gain of an isolated element in the array. The effect of mutual coupling effects in a large array can be accounted for [8] by multiplying the gain of an isolated element by $(\cos \theta)^{3/2}$.

3. Antenna Mode Scattering: Measurement and Comparison with Theory

A series of measurements were conducted at the RADC Ipswich Electromagnetic Measurements Facility to determine the scattering characteristics of microstrip arrays in the three frequency regimes. A two antenna, CW cancellation system was used. The antenna separation was six inches, with a measurement range of thirty five feet, making the bistatic angle 0.08^o for these measurements. The microstrip array chosen for the antenna mode scattering measurements consisted of circular disk microstrip radiators excited from the back by coaxial probes. The center pin of the coaxial connector was connected to the disk at a distance of one third the radius from the center of the disk. The center of the microstrip disk was shorted to the ground plane by a pin. Figure 1 shows a cross sectional sketch of the microstrip disk element. The characteristics of the array used in these measurements are center frequency = 7.25 GHz, number of elements = 32, 4 rows X 8 columns in a triangular grid lattice with element spacing = 2.768

cm x 5.537 cm. The diameter of microstrip disk element is 1.0 cm and the substrate thickness is 0.30 cm, dielectric constant = 4.4 ($\tan \delta = 0.0025$).

Since a low RCS antenna mounting structure was not available for this experiment, the scattering measurements on the array had to be carried out in two separate steps. Scattering cross section measurements were first made on a 2 ft. x 3 ft. metal plate. The microstrip array was then installed at the center of the metal plate and the measurements were repeated. The difference in the scattering patterns between the two measurements is an indication of the antenna-mode backscatter from the array. The difficulty with this technique is that the scattering from the edges of the metallic plate often interferes with and masks the backscattered signals from the array. At angles in the vicinity of broadside, the RCS of the plate is much greater than that of the array, hence scattered signals from the array are not identifiable in this angular region. The scattered signals from the array become more discernible at aspect angles sufficiently far from the broadside direction, where they are comparable to or higher than the edge scattering from the metal plate. To mitigate scattering from the plate at large aspect angles, some measurements were made with absorbing material placed on the edges of the metallic plate.

Scattering measurements on the flat plate and the array are shown in Figures 2 and 3. The data shown in these figures was taken with an open circuit ($Z_L = \infty$) across the coaxial input terminals of the microstrip antenna elements. The scattering cross section was measured with the E vector of the incident field parallel to the columns of the array. These figures show the measured cross section normalized with respect to the scattering cross section of the plate measured in the broadside direction ($\theta = 0°$). Figure 2 shows the scattered signals from the flat plate alone and of the flat plate with the array. No absorbing material was placed on the edges of the flat plate in the results shown in Figure 2. The data shown in Figure 3 was taken with absorbing material placed on the edges of the metal plate. An antenna mode scattering lobe from the array is clearly visible in Figure 3 at azimuth angles between 35^0 to 60^0. In Figure 2, multiple lobes are seen at these azimuth angles due to interference between the scattered signals from the array and the edges of the plate. The amplitude of the scattered return from the array is quite large considering that it has only 32 elements. The reason for this is that the peak of the lobe which appears at 45^0 is not significantly affected by mutual coupling effects within the array.

The theoretical scattering cross section of this array was calculated using equations 1-9 of Section 1. The scattering cross section of a metallic plate was also calculated using a physical optics approximation [9]. The combined scattering cross section of the array and metal plate was calculated as follows:

$$\sigma_T = \sigma_A + \sigma_P + 2(\sigma_A \sigma_P)^{1/2} \cos \tau \ , \qquad (10)$$

where

σ_A = backscattering cross section of microstrip array

σ_P = backscattering cross section of metal plate

τ = relative phase angle between the two scattered signals $\simeq$ kd $\cos \theta$, where d is the distance between the phase centers of the two scattering sources.

The computed backscattering cross sections for the microstrip array and the flat plate are shown in Figure 4. The theoretical results are in good qualitative agreement with the measured data shown in Figures 2 and 3. The theory predicts the presence of the backscattering lobe from the array that appears between 35^0 and 60^0. At these aspect angles, the scattering cross section of the array exceeds that of the metal plate. At aspect angles from 0^0 to 30^0 the metal plate has a much higher cross section than the array, hence scattered signals from the array are not visible in this angular region. The interference lobe pattern that appears between 35^0 and 60^0 is due to the interaction between scattered signals from the array and the metal plate.

Note that the theoretical results show many more sidelobes than the experimental data. This discrepancy is primarily due to the fact that the hybrid Magic-T phase bridge in the two antenna measuring system was not nulled for each aspect angle due to the vast amount of data that was collected. The bridge was initially balanced for the 0^0 aspect angle (array broadside direction); no further attempt was made to null the bridge for subsequent aspect angles, creating some degree of phase insensitivity.

4. Effect of Load Impedance on Antenna Mode Scattering

Experiments were also conducted to measure the effect of antenna load impedance on the scattering cross section of the array. Figure 5 shows the scattering cross section of the array measured under two different load conditions, namely $Z_L = \infty$ (open circuit) and $Z_L = 50 + j0$ ohms (50 ohm matched load). Both measurements were taken with absorber placed on the edges of the flat plate. Examination of the figure indicates that the antenna mode scattering lobe (occurring between 35-60 degrees) has greater peak amplitude at $Z_L = \infty$ than at $Z_L = 50$ ohms. The difference between the peak scattering amplitude for these load conditions is rather small. These results indicate that significant scattering can occur from the array even when the antenna input terminals are terminated by a 50 ohm resistive load; this is because the conjugate-match condition specified in equation(6) is not satisfied by this type of load. These results have also been corroborated by theoretical calculations.

5. Higher order mode scattering (TM_{21} mode)

When the frequency of the incident signal is above the fundamental (TM_{11} mode) frequency of the microstrip antenna higher order modes can be excited in the array elements, causing them to scatter once again in an antenna type mode. The radiation pattern of the elements for these higher order modes will be different from the fundamental TM_{11} mode; generally there will be a null at broadside and the peak lobes shift towards the endfire direction [13]. In this paper the scattering pattern of the array has been calculated at a frequency corresponding to the resonant frequency of the TM_{21} mode of the antenna element.

The resonant frequency f_{mn} of the TM_{mn} mode of a circular disc microstrip antenna of radius a is given by

$$f_{mn} = K_{mn}c \;/2\pi a_e\sqrt{\varepsilon_r} \tag{11}$$

where K_{mn} is the nth zero of the derivative of the Bessel function of order m, c is the velocity of light in free space, and ϵ_r is the relative dielectric constant of the substrate. The effective radius a_e of the antenna element is given by

$$a_e = a\left[1 + \frac{2h}{a\pi\sqrt{\epsilon_r}}\left\{\ln\left(\frac{\pi a}{2h}\right) + 1.7726\right\}\right]^{1/2} \tag{12}$$

where h is the thickness of the microstrip substrate and a is the radius of the microstrip antenna element. For the microstrip disk in the 32 element array, the resonant frequencies of the TM_{11}, TM_{21}, TM_{02} and TM_{31} modes occur at frequencies of 7.25 GHz, 12.44 GHz, 15.08 GHz and 16.54 GHz, respectively.

The gain of the TM_{21} mode in the backscatter direction can be calculated from its far field patterns and is given by

$$G_{21}(\theta,\phi) = 4G_{N21}(\theta,\phi)/G_{D21} \tag{13a}$$

where

$$G_{N21} = 4[\cos^2 2\phi \ \{J_3(k_o a \sin\theta) - J_1(k_o a \sin\theta)\}^2 + \cos^2\theta \sin^2 2\phi \ \{J_3(k_o a \sin\theta) - J_1(k_o a \sin\theta)\}^2] \tag{13b}$$

and

$$G_{D21} = \int_0^{\pi/2} [\{J_3(k_0 a \sin\theta) - J_1(k_0 a \sin\theta)\}^2 + \cos^2\theta \ \{J_3(k_0 a \sin\theta) + J_1(k_o a \sin\theta)\}^2] \sin\theta d\theta \ . \tag{13c}$$

The backscattering cross section of the array in the higher order TM_{21} mode can be calculated using the methods outlined in Section 2. Figure 6 shows the calculated backscattering cross section of the array at a frequency of 12.44 GHz, with the input terminals of the antenna open circuited. Experimental measurements have been conducted to verify the results.

6. Low Frequency Structural Mode Scattering: Theory and Measurement

When the frequency of the incident signal is well below the operating bandwidth of the array, the individual elements in the array cease to radiate and can no longer be considered as microstrip antenna elements. The array scattering now occurs in the structural mode, with energy being scattered in the specular direction due to the presence of the conducting ground plane a small distance behind the radiating face of the array. The energy scattered in the backscatter direction is negligible and is independent of the antenna load impedance since no RF power is absorbed by the antenna.

A survey of current unclassified literature has yielded very little work on the backscattering from microstrip arrays. Montgomery [10] has studied the specular reflection from infinite periodic microstrip arrays using Floquet model expansion and integral equation techniques. These techniques are not readily applicable to the evaluation of backscattering from a finite microstrip array. In this paper, the diffraction fields and the backscattering cross section has been calculated using the low frequency or Rayleigh approximation [2]. The presence of the metallic ground plane is accounted for by an image array [11] whose dipole moments are opposite to that of the array. The scattered field from the image array is added to that of the actual array through an appropriate phase factor, to account for the presence of the dielectric substrate. Munk et. al. [12] have considered the influence of dielectric medium on radiation from a periodic surface. A similar, but simplified technique has been employed in this paper, the details of which will be described at the symposium.

In order to investigate the low frequency scattering characteristics of the array, measurements were conducted at 7.25 GHz and at 10 GHz on an array of 561 elements whose design frequency was 20 GHz. The characteristics of this array are center frequency = 20 GHz, number of elements = 561, 27 rows X 27 columns square lattice delineated by a 7.85 inch diameter circle, element spacing = 0.295 inch X 0.295 inch, element type = 0.179 inch X 0.1069 inch rectangle, substrate = Rogers Duroid, substrate thickness = 0.0625 ins, dielectric constant = 2.23. Figure 7 and Figure 8 show the backscattering cross section of the 20 GHz array when measured at a frequency of 7.25 GHz and 10 GHz respectively. Both of these measurements were made with the antenna input terminals open circuited. These results show no perceptible differences between the cross section of the plate and that of the plate with the array, indicating that the scattering cross section of the array in the backscatter direction is negligible. These experimental results confirm the theoretical predictions.

7. Summary

Electromagnetic Backscattering from two dimensional microstrip arrays has been studied in this paper as a function of the frequency of the incident signal, array lattice spacing, angle of incidence and antenna load mismatch conditions. Theoretical and experiemental investigations have been conducted on two types of microstrip arrays: a) a 32 element triangular grid array consisting of coaxially fed circular disk microstrip elements and b) a 561 element square grid array of rectangular patch elements.

Significant antenna mode backscattering from the triangular grid array is observed when the incident frequency is the same as the resonant frequency of the fundamental TM_{11} mode of the circular microstrip disk element. Higher order mode backscattering from the array is also observed at large incidence angles when the incident frequency is the same as the resonant frequency of TM_{21} higher order mode of the microstrip element. Negligible backscatter from the array occurs when the incident frequency is well below the fundamental resonant frequency of the microstrip patch element. Theoretical results for the three frequency regimes are in good qualitative agreement with experimental measurements.

REFERENCES

1. J. W. Crispen, K. M. Siegel, "Methods of radar cross section analysis" Academic Press, 1968. pp.288

2. A. K. Bhattacharya, T. K. Sen "Electromagnetic scattering by a thin conducting flat plate with doubly periodic punched circular apertures" Proc. IEEE (London) Vol. 126, No. 22, Nov. 1979, pp. 1149-1154

3. E. D. Sharp, "A triangular arrangement of planar-array elements that reduces the number needed" IEEE Trans. Antennas & Prop. March 1960, pp. 126-129

4. R. B. Green "The general theory of antenna scattering" Ohio State University. Research Rept. 1223-17, 30 Nov. 1963 AD 429186

5. I. J. Bahl, P. Bhartia "Microstrip Antennas" Artech House 1980. pp. 86-109

6. J. R. James et al. "Microstrip Antenna - Theory and Design" Peter Peregrinus Ltd. 1981. pp. 82-86

7. S. Yano, A. Ishimaru "Input impedance of a circular microstrip disk antenna" IEEE International Symposium pp. 109-112

8. N. Amitay, V. Galindo, C. P. Wu "Theory and analysis of phased array antennas" Wiley-Interscience 1972, pp. 25-29

9. R. A. Ross "Radar cross section of rectangular flat plates as a function of aspect angle" IEEE Trans. Antennas & Prop. May 1965, pp. 329-335

10. J. P. Montgomery "Scattering by an infinite periodic array of microstrip elements" IEEE Trans. Antennas & Prop., Vol. AP-26, No. 6, Nov. 1978, pp. 850-854.

11. E. D. Nielsen "Square Van Atta reflector with conducting mounting plane" IEEE Trans. Antennas & Prop., Vol. AP-18, No. 1, January 1970

12. B. Munk et al. Private communication

13. G. Kumar, L. Shafai, et al. "Characteristics of higher order modes of circular microstrip antennas" IEEE International AP Symposium, Boston, MA June 25-29, 1984, pp. 573-576.

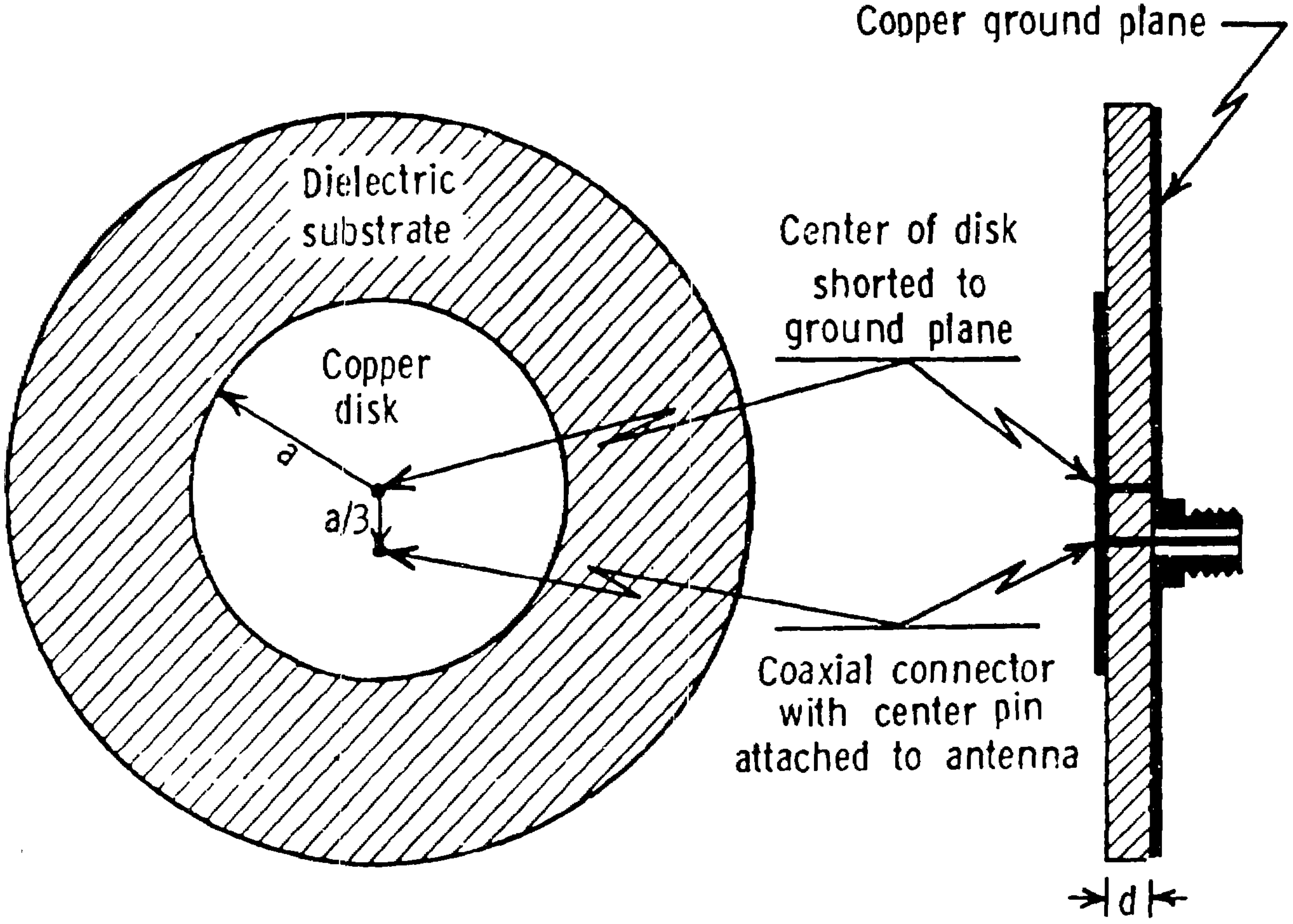

Figure 1.- Microstrip disk antenna fed from back.

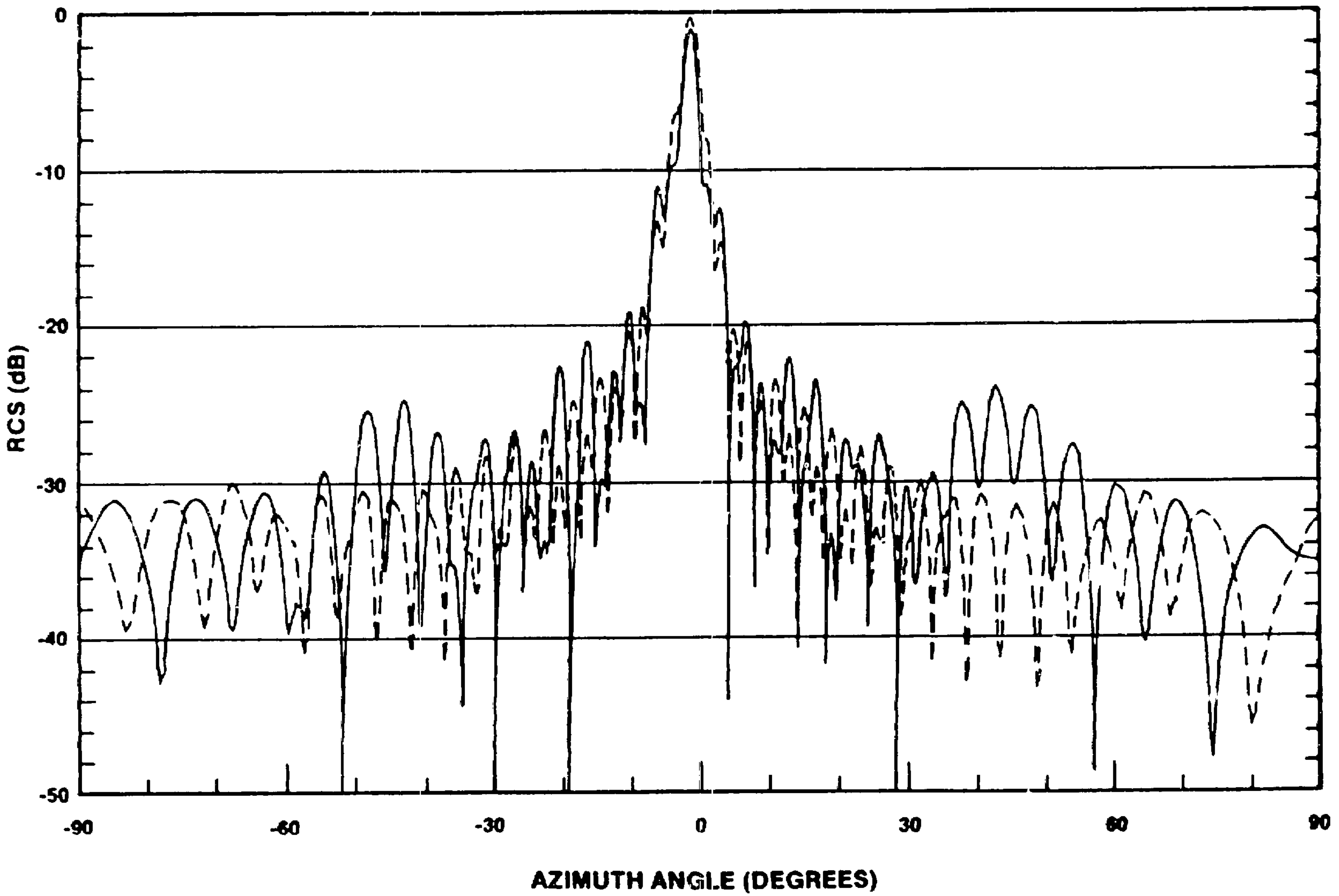

Figure 2. RCS of unterminated 32 element array plus flat plate compared to flat plate alone. Design frequency of array = 7.25 GHz, measurement frequency = 7.25 GHz. Plate plus array ——— , plate alone - - - , with no absorber at edges of flat plate.

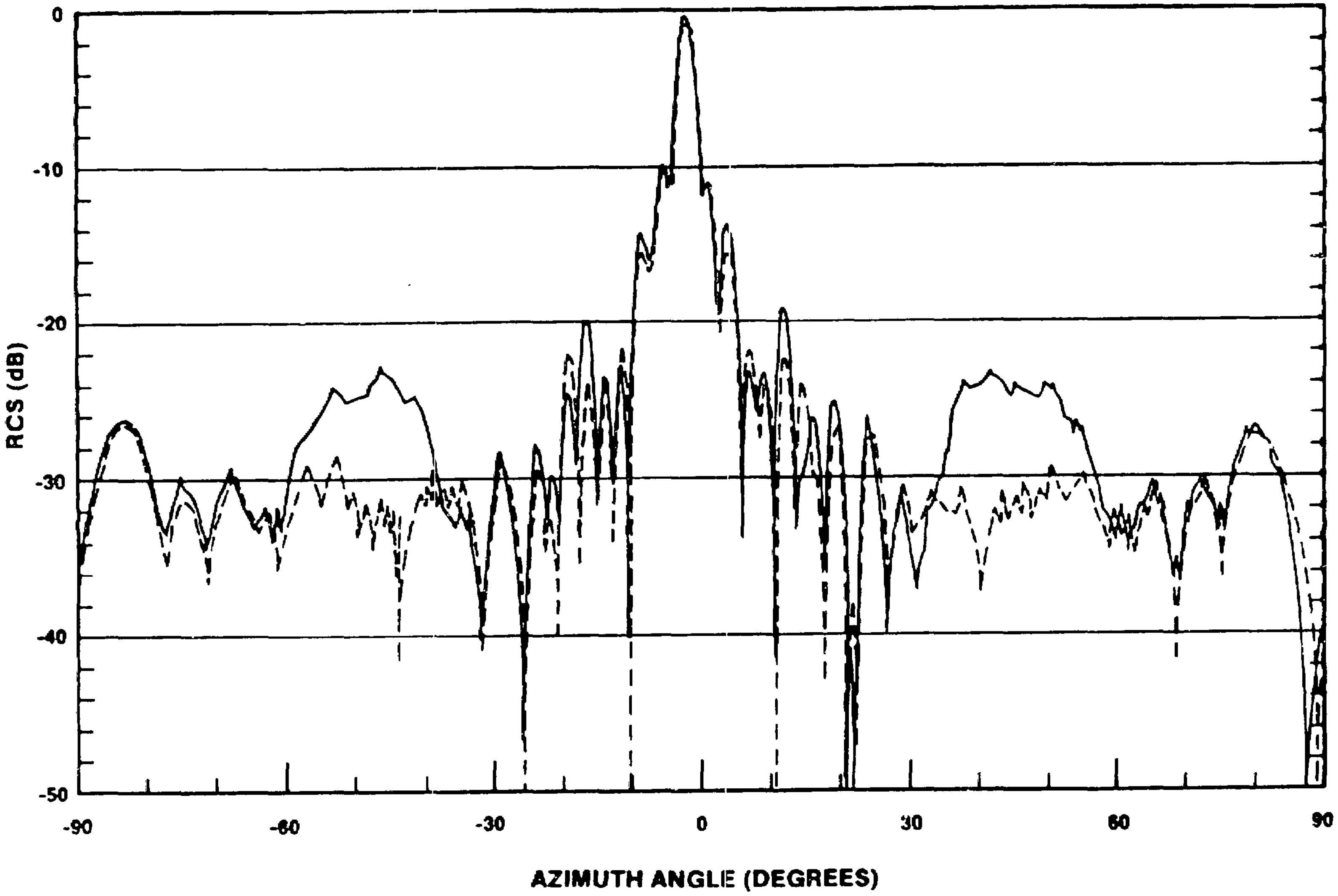

Figure 3. RCS of terminated 32 element array plus flat plate, compared to flat plate alone. Design frequency of array = 7.25 GHz, measurement frequency = 7.25 GHz. Plate plus array ——— , plate alone ---, with absorber at edges of flat plate.

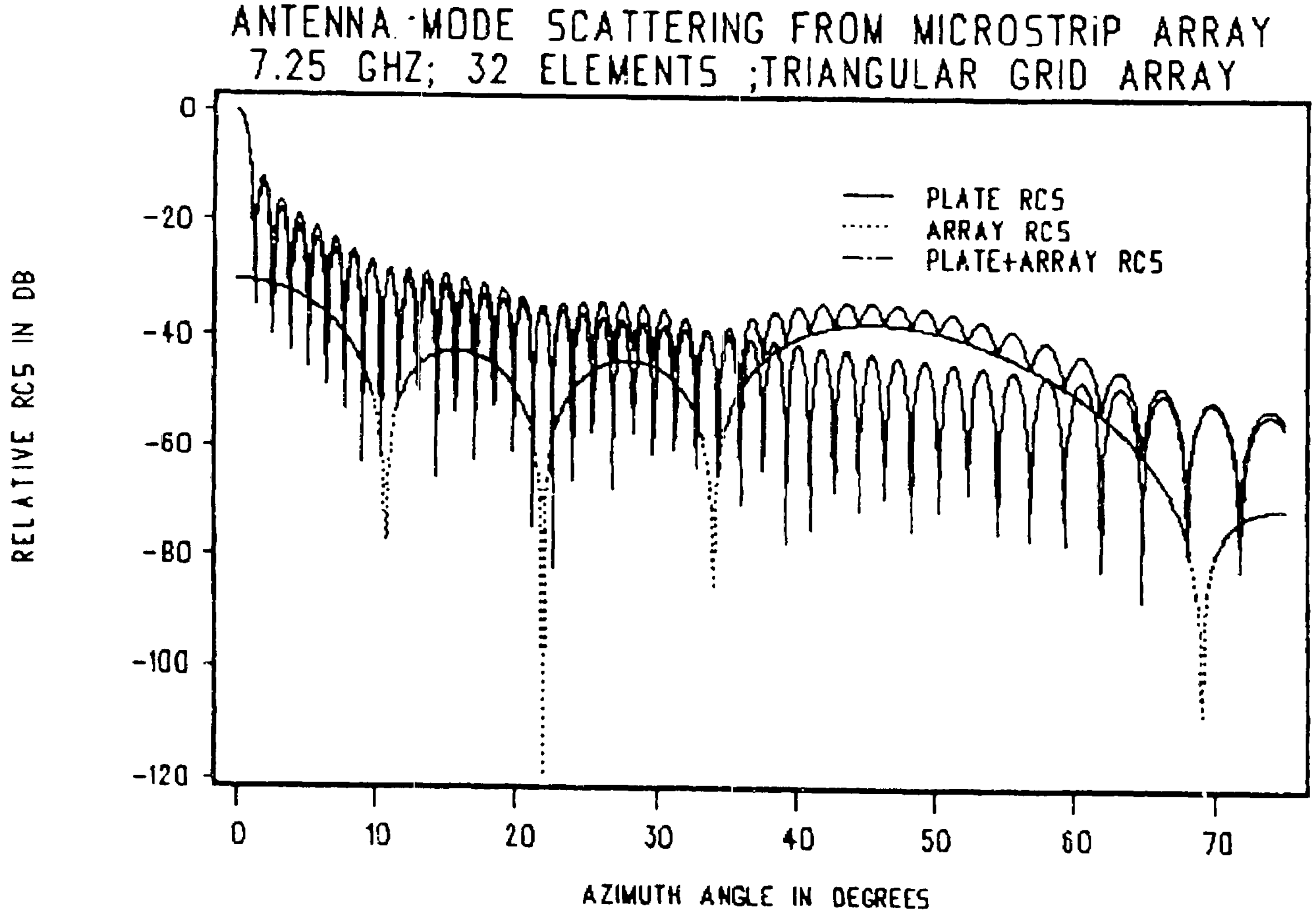

FIGURE 4.ANTENNA MODE SCATTERING FROM MICROSTRIP ARRAY : THEORY.

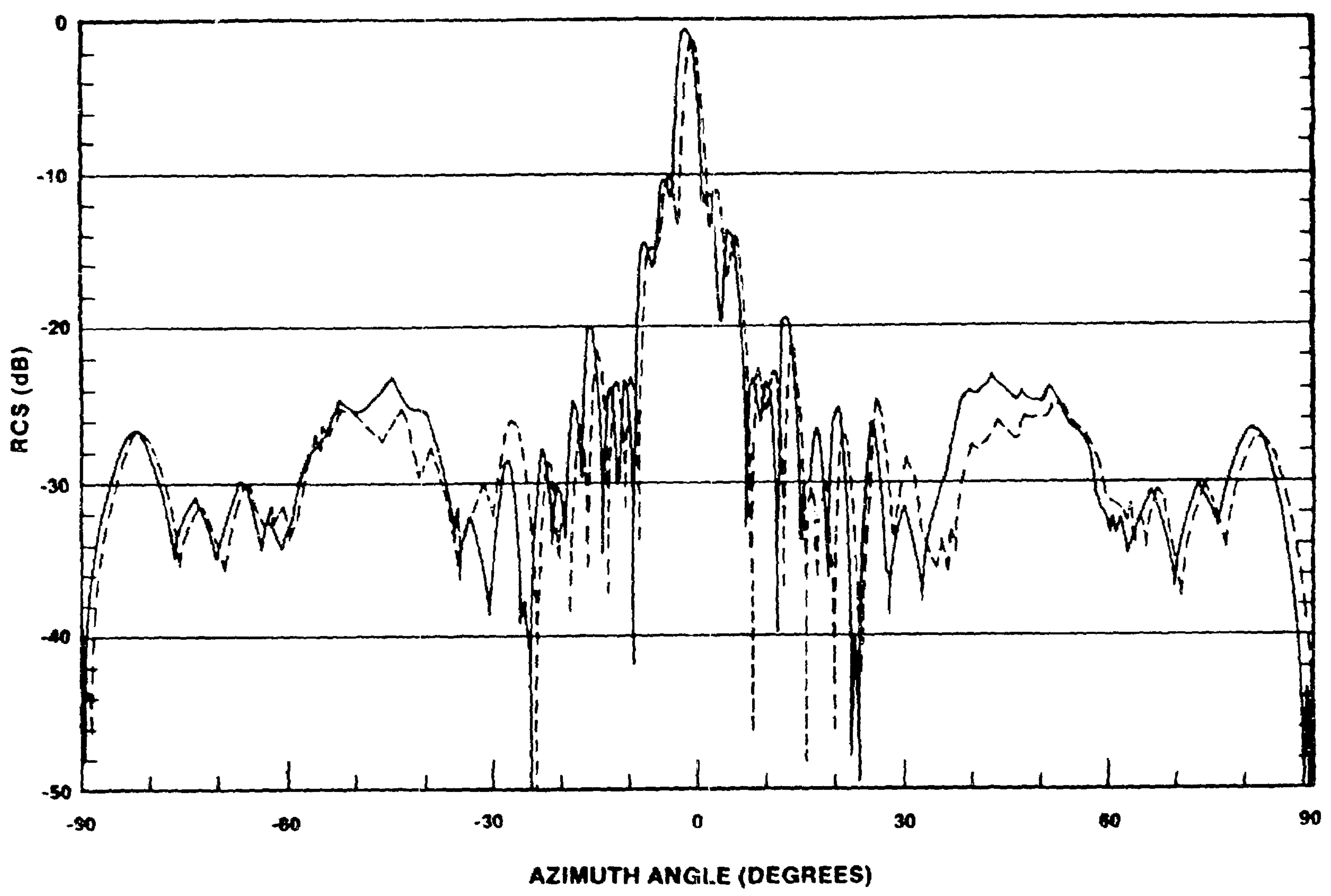

Figure 5. RCS of unterminated 32 element array plus flat plate compared to RCS of same with each element terminated with a 50 Ω load. Design frequency of array = 7.25 GHz, measurement frequency = 7.25 GHz. Unterminated ——— , terminated - - -. With absorber at edges of flat plate.

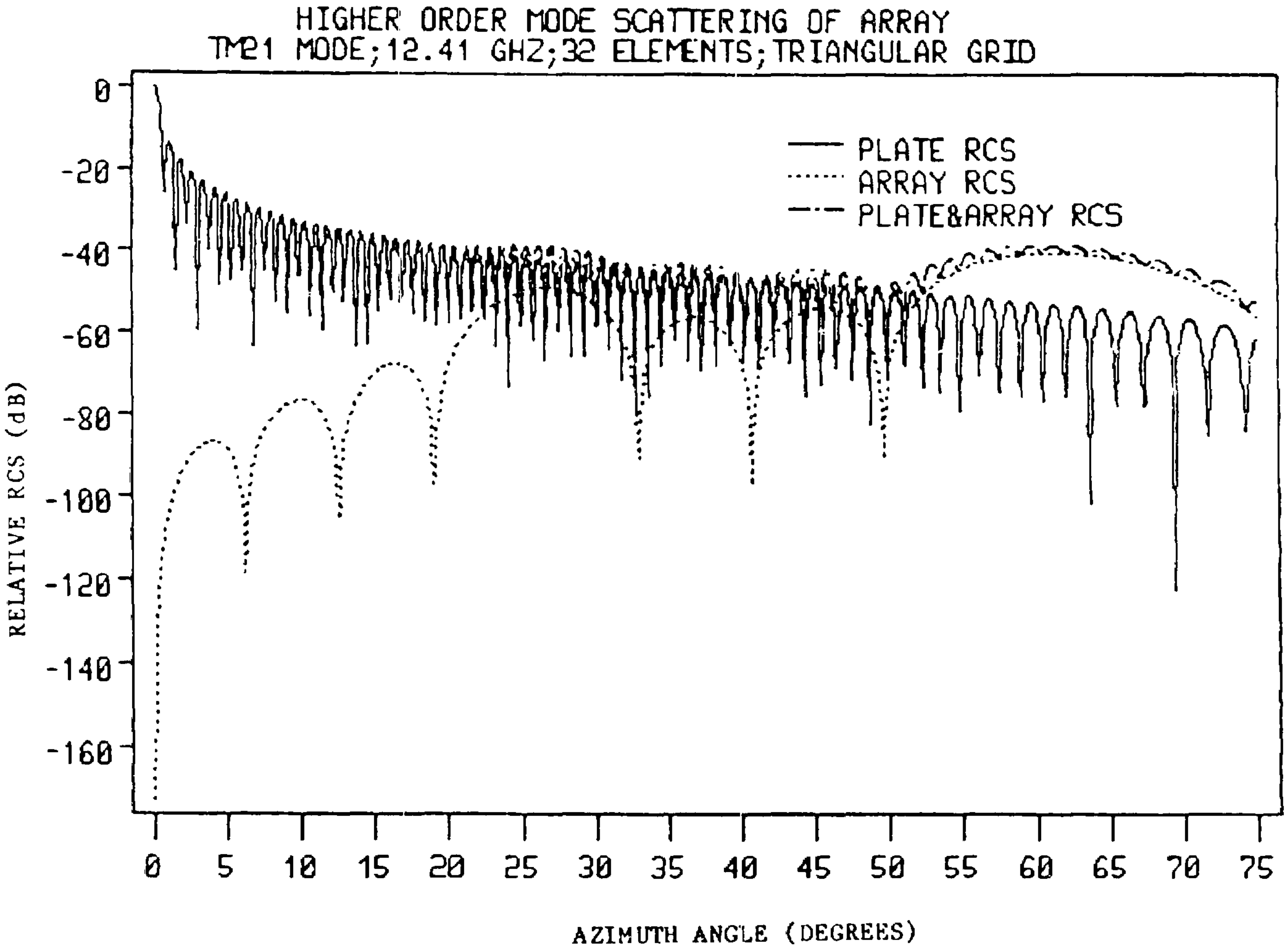

FIGURE 6. HIGHER ORDER MODE SCATTERING FROM ARRAY.
TM21 MODE; FREQUENCY = 12.41 GHz.

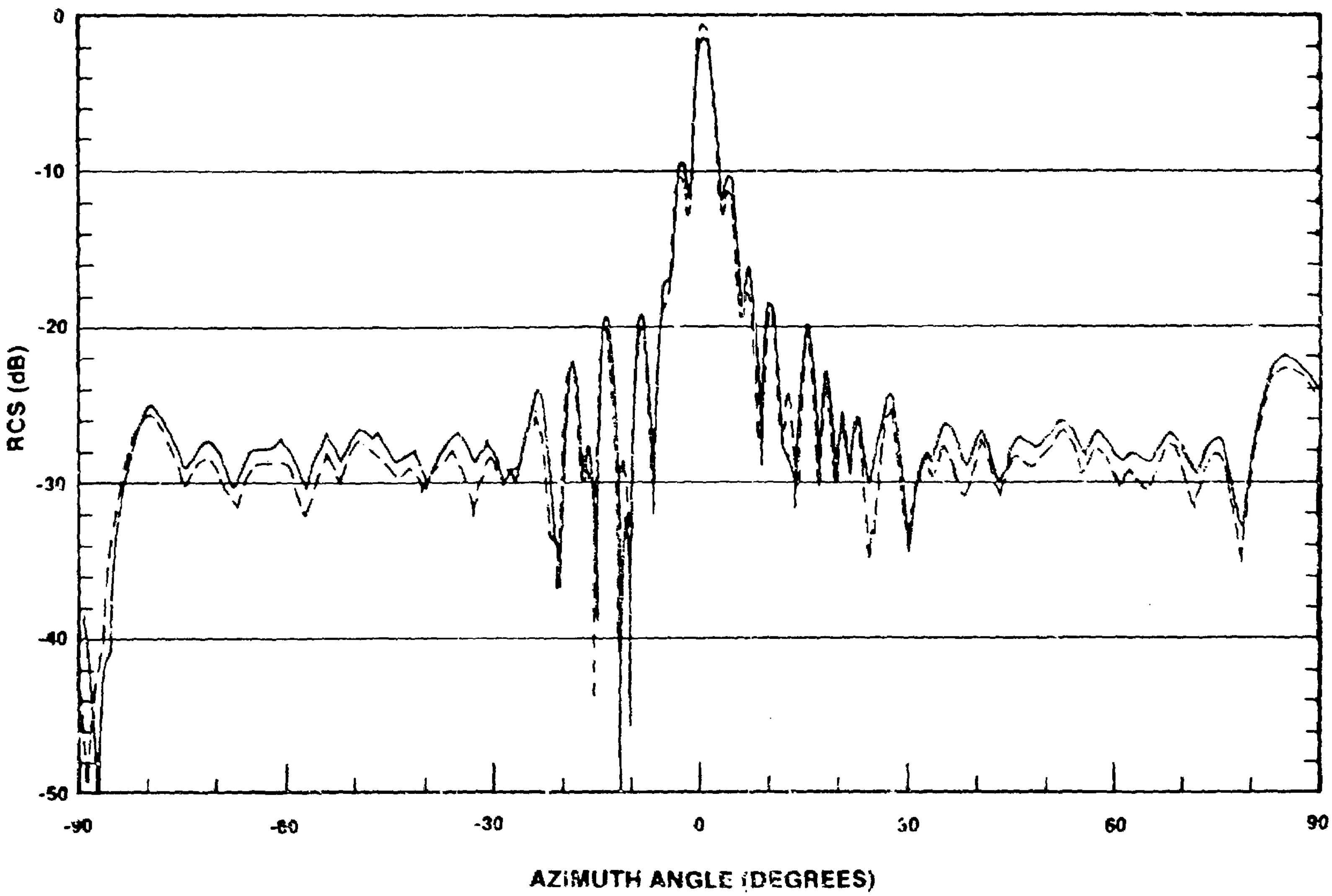

Figure 7. RCS of 561 element array plus flat plate compared to flat plate alone. Design frequency of array = 20 GHz, measurement frequency = 7.25 GHz. Plate plus array ——, plate alone - - -.

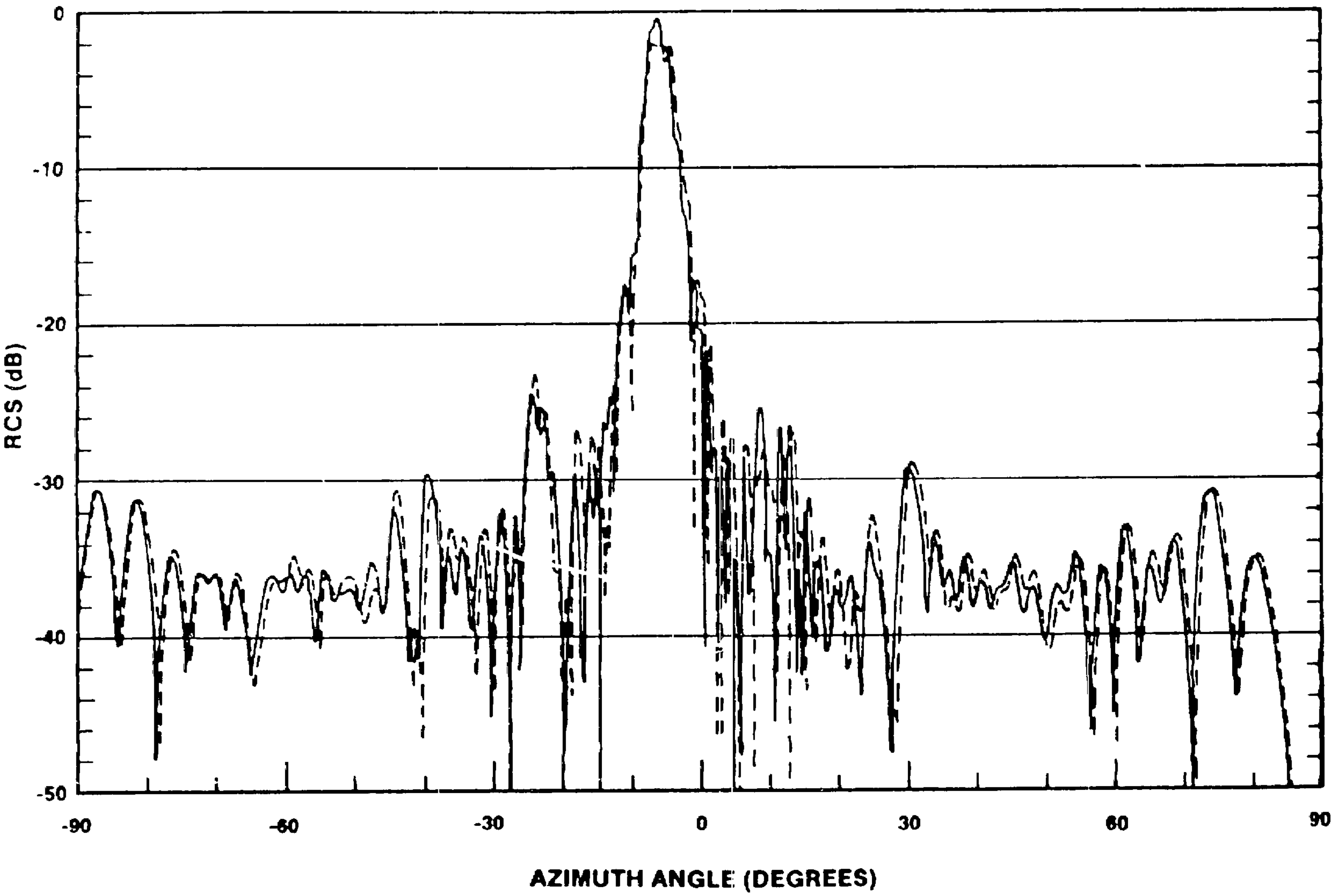

Figure 8. RCS of 561 element array plus flat plate compared to flat plate alone. Design frequency of array = 20 GHz, measurement frequency = 10 GHz. Plate plus array ——, plate alone ---.

PERFORMANCE BOUNDS ON MONOLITHIC PHASED ARRAY ANTENNAS

John K. Schindler
Electromagnetic Sciences Division
Rome Air Development Center
Hanscom Air Force Base, MA 01731

SUMMARY

Monolithic phased arrays represent a challenging combination of phased array and monolithic millimeter wave integrated circuit technologies. These arrays promise to have an immense impact on airborne and spaceborne communications terminals and radar systems in the millimeter wave frequency bands if substantial technological challenges can be met in future years.

Bounds on the performance of monolithic phased arrays are presented as they are limited by array, circuit and device performance estimates. Depending upon application, the performance of monolithic arrays is characterized by gain, effective isotropic radiated power or overall efficiency. Maximization of any or a combination of these performance criteria is limited by cost and array complexity, waste power dissipation, amplifier output power and junction temperature.

Results for maximum effective isotropic radiated power arrays are presented for final power amplifier designs which maximize amplifier gain, efficiency or saturated power output. Maximum achievable EIRP varies inversely with the square of frequency with junction temperature limiting EIRP at the lower frequencies and FET power density limiting EIRP at higher frequencies. Waste power is contributed primarily from the DC to RF inefficiencies of the FET power amplifiers and the waste power density necessary to be removed from the array remains approximately constant with frequency. This waste power density is significant, being approximately 100 times that which can be radiated by a black body at the corresponding junction temperature of 100 degrees Centigrade. Small signal active array gain is limited by semiconductor wafer size and achievable cost effective circuit realization at the lower frequencies and by microstrip circuit feed losses at higher frequencies. Even at the higher frequencies, the complexity of the maximum gain circuits greatly exceeds todays capabilities for monolithic circuit fabrication.

1. INTRODUCTION

Monolithic or integrated circuit phased arrays are active phased array antennas fabricated primarily on a semiconductor substrate. The array includes radiating, feed, control and amplifier components constructed on the substrate using monolithic microwave or millimeter wave integrated circuit fabrication techniques. The arrays can be either transmit or receive or possibly both transmit and receive if advanced levels of circuit integration and transmit-receive isolation are permitted by the fabrication technology.

Important adjuncts to monolithic array technology include mounting, supporting and cooling the array and feeding RF, DC and control signals to the complex monolithic array structure. The arrays are likely to be electrically and mechanically fragile and will require an external radome capable of protecting the array from the usual environmental factors as well as electrical interference from lightning or EMP.

A survey of hybrid and monolithic integrated circuit antenna technology has been published recently [1].

1.1. Potential of Monolithic Phased Arrays

Monolithic phased arrays may be an important technology for aircraft and space antennas in the lower millimeter wavelength bands from 20 to 60 GHz. It is anticipated that aircraft communications terminals and radars for modern high performance aircraft will require low profile or conformal antennas which occupy a minimum amount of space within the airframe. Conformality of the antenna permits a low radar cross section for the aircraft and reduces drag on a high performance airframe. Minimum airframe intrusion allows more efficient use of the valuable space within an aircraft but this requirement denies the use of space or lens fed antennas and forces the use of compact corporate feeds. These feeds are lossy, especially at millimeter wave frequencies, and will require the use of some form of active array. Within the aircraft and space environments, reliability and radiation hardening are important. GaAs technology appears to be radiation hard and the reduction in the number of wirebonds and discrete components employed in advanced systems will improve reliability.

The cost of precision millimeter wave arrays is a significant issue. Monolithic fabrication techniques offer the prospect of "mass producing" arrays in such a manner that unit costs are reduced. However, the monolithic fabrication process at millimeter wave frequencies is likely to be complex and require multistage, repeatable sub-micron lithography. A byproduct of the successful completion of this precision fabrication process is the control of electrical parasitics and the ability to produce wideband, high performance arrays from monolithic subarrays with nearly identical performance.

1.2 Problems with Monolithic Phased Arrays

There are significant design and fabrication problems associated with monolithic millimeter wave phased arrays. The use of sub-micron millimeter wave monolithic circuit techniques on reasonably large scale circuits and arrays presents a challenge to achieving adequate yields and realizing the cost potential of the arrays. Simplification of the production level monolithic circuit processing techniques employed in the advanced active devices used for low noise and power amplifiers and RF switches will be required. The design base for monolithic millimeter wave devices, circuits and radiators is emerging only now and will require significant advances before the efficient engineering design of this class of array can be conducted on a routine basis.

Conductor losses associated with transmission media such as microstrip operating on semi-insulating semiconductor at millimeter wave frequencies are significant. These losses limit achievable gain and introduce waste power which must be removed from the array. Increasing the thickness of the semiconductor substrate is desirable to permit reliable handling of the arrays during processing. However, thicker substrates make fabrication of via holes more difficult, increase the thermal resistance of circuitry and introduce the possibility of multimoding in the transmission lines used in the corporate feed. Thicker substrates can support surface waves and introduce blind spots and element mismatch upon scan of the monolithic array [2, 3, 4, 5, 6]. An evaluation of the practical significance of these and other design problems with monolithic arrays is being conducted under programs supported by the RADC Electromagnetic Sciences Division. In this paper we discuss comparative bounds on the performance of monolithic arrays operating in the 20-60 GHz bands as limited by fundamental design and technological constraints. The discussion of specific methods for designing and implementing monolithic arrays is presented elsewhere in this Symposium [8, 9]. Separate transmit, phase shift and receive modules are under development currently [9, 10].

2. OBJECTIVE OF PAPER

The objective of this paper is to establish performance bounds on monolithic phased arrays, principal technological limitations on these performance bounds and the sensitivity of these bounds to advances in device and fabrication technologies. The design of monolithic arrays for radar and communications systems are subject to differing design criteria depending on the application. Common design objectives are to maximize

- Active array gain
- Effective isotropic radiation power
- Active array efficiency

Achieving these maximum design measures is limited by constraints on the physical and cost realizability of the arrays. Principal constraints are

- Limitations on total or per area dissipated power
- Active FET amplifier junction temperature
- Active FET amplifier maximum power output
- Cost

In this section, these design objectives and contraints will be discussed in depth. They provide a rationale for selecting the important features to be included in the monolithic array model used in the analysis in this paper.

2.1 Design Criteria

Design criteria for monolithic arrays will be described in this section. Principal design criteria are the maximization of array gain, effective isotropic radiated power and efficiency. These design goals are not necessarily compatible and thus are appropriate under differing conditions. The conditions under which each design goal is appropriate will be described.

2.1.1 Maximum Achievable Array Gain

One important and commonly used active array characteristic is its directive gain. This property is a measure of the array's ability to direct RF power at its input terminals to a receiver or target located at a given angular direction from the array. In this paper, gain includes all losses in the array corporate feed, power dividers, phase shifters and radiating elements. It includes, as well, power gain associated with the active amplifiers included in the array. Directive gain, as used here, will be computed in the array broadside direction and will not include losses associated with scan or aperture taper for sidelobe control.

In the following analysis, gain will be computed assuming that the active amplifiers are operating in their linear region where output power is proportional to input power. Thus, active array gain as used here is associated with a linear system and it is implicitly assumed that the input drive power at the operating frequency of the array is limited. The important function for the array is is to efficiently direct this limited power to the communications receiver or scattering target, making the active array directive gain the important design criteria for limited input RF power systems.

2.1.2 Array Efficiency

Another important performance criteria for active monolithic arrays is overall efficiency - the capability of the array to efficiently convert input RF and DC power to output RF power at the receiving antenna or scattering target. This overall efficiency will be taken as the ratio of output RF power at a receiving aperture broadside to the array and in the far field of the array to the total DC and RF input power to the array.

Active array efficiency thus includes the effects of RF power dissipated in resistive portions of the corporate feed, phase shifters and radiating elements as well as the DC power dissipated in the active amplifiers. While mismatch losses may be important in reducing gain, efficiency and EIRP, these losses will be neglected; the assumption being that the active array is well-designed at all frequencies and scan angles and the effects of mismatch losses are negligible.

Array efficiency is an important design criterion when primary power limitations are placed on the array or when limits exist on the ability to remove waste power from the array or the overall system. The proportion of input power provided in the form of DC bias and RF drive may be important when the cost of generating RF drive power is significant at higher frequencies.

2.1.3 Maximum EIRP

Effective isotropic radiated power (EIRP) is a measure of the active array's ability to direct RF power to a given receiving system in the far field of the array - it represents an amount of input power which, if radiated isotropically with unit gain, would give the same far field power density as the actual active array. EIRP is commonly used in the design of communications systems as an effective measure of the transmitter-antenna subsystem performance.

The EIRP used in this paper will be associated with the maxium achievable radiated power from the array. Consideration will be given to the maximum power achievable from each active amplifier in the array as limited by the maximum junction temperature allowed or the gate breakdown voltage and channel carrier concentration. The active array will be assumed to have adequate input RF drive power such that the most restrictive limiting condition on each active amplifier is achieved. Thus while gain is an implicitly linear array characteristic, EIRP as used here gives implicit consideration to the non-linear power saturation or junction temperature limits of the active array.

As with the gain design criteria, EIRP will be calculated at a broadside direction with no scan or aperture taper loss included.

2.2 Design Constraints

The performance of monolithic arrays given by the design criteria in the previous section is limited by important and practical constraints on the permitted waste power dissipated in the array, allowable FET gate power and junction temperature and array costs. In this section, these constraints on monolithic array performance will be discussed.

2.2.1 Power Dissipation

Monolithic arrays may be relatively inefficient systems due to RF losses in the corporate feed, phase shifters, power dividers, and radiating elements as well as the relatively inefficient power amplifiers likely to be employed at millimeter wave frequencies. Thus a significant amount of waste power must be removed from the active array.

Two waste power dissipation constraints will be considered - the total waste power and the waste power area density. Total waste power limits are important when the ability of the total system to remove power is a factor. This can occur in the space environment where waste power is removed by large area thermal radiators. Waste power area density - waste power per unit area of array face - is important when some form of convective heat removal system is employed. In this case the ability of the limited flow rate convection system to remove waste power without significant increase in fluid temperature is important.

2.2.2 FET Junction Temperature

It is known that the allowable temperature of the FET junction is an important parameter in determining the reliability of FET amplifiers, although the exact relationship between temperature and lifetime for millimeter wave FETs is not established. The power dissipated in the FET amplifiers is known to be concentrated in the FET channel and the primary thermal path for dissipating this power and controlling junction temperture is through the semiconductor substrate.

In this paper, the FET amplifiers used in the active monolithic array will be assumed to have all waste power dissipated in their gates and thermally conducted to the ambient temperature substrate of the array. The junction temperature allowed from reliability considerations will place one limit on the power output from each active amplifier in the monolithic array.

2.2.3 Maximum FET Power Output

Microwave and millimeter wave FET amplifiers are known to have limits on the available output power they may deliver. This power is limited by the gate breakdown voltage, the maximum drain current as limited by the concentration of carriers in the channel and the width of the FET gate as limited by the ability to match the input impedance of FET device.

Either the maximum available output power or the allowable junction temperature will limit the amount of power which the monolithic array can deliver to space. These parameters thus limit the maximum EIRP available from the array and the resultant efficiency of the array.

2.2.4 Cost Limitations

A primary motivation for the use of monolithic arrays at millimeter wave frequencies is cost. Their cost effective application is assumed to come from the precision reproduction of the complex circuits on a large scale with the attendant amortization of large setup costs over a volume production. The item cost of each monolithic array will be small only if a large fraction of the complex circuits produced function properly. This fraction of functional arrays or yield is critically dependent on the quality and reproduceability of the materials and fabrication processes used in the manufacture of the monolithic arrays. Yield depends as well as on the complexity of the monolithic array expected to be produced.

The item cost and its relationship to yield and circuit complexity is very difficult to quantize. It is known that yield is dependent on the number of gates employed, gate dimensions and the functions required of the gates. For purposes of this analysis, the number of gates employed for active amplifiers and phase shifter switches will be used to determine the yield and the overall cost of the monolithic array.

2.3 Sensitivity Analysis

One objective of the analysis provided in this paper is to provide estimates on a common basis of the performance of monolithic arrays in the millimeter wave bands as a function of frequency and the type and scale of technology employed in the array fabrication.

A second and equally important objective is to determine the sensitivity of the performance bounds and constraints to technology advances. The analysis to be provided will include, as parameters, important performance characteristics of the devices, components and materials employed in the array fabrication. Marginal improvements in the array performance measures as a function of changes in these device, component or material characteristics will be evaluated to provide direction for future development efforts. As well, the sensitivity of array performance measures to uncertainty or lack of knowledge of device, component or material performance will be determined so that the most critical uncertainties in design knowledge can be resolved in advanced research programs.

2.4 Limits of Paper Analysis

The analysis provided here is limited in several ways. Current technology is challenged significantly by providing separate transmit and receive arrays even though research into difficulties with advanced transmit-receive arrays has been proposed. Thus, consideration is given to separate transmit and receive arrays. Only transmit arrays are discussed here; a similar comparative analysis of performance of receive only arrays will be conducted.

3. ANALYSIS

In this section the important properties of a monolithic array model are presented. A model is proposed from which performance characteristics of monolithic arrays can be computed as a function of design constraints and technology limitations. Quantitative expressions for these performance objectives and constraints are provided.

3.1 Important Model Properties

Any model proposed to evaluate the performance of monolithic arrays must include properties which adequately characterize important array losses which contribute to gain degradation and power dissipation as well as properties of the amplifiers which contribute to gain, DC power dissipation and output RF power limitations. These properties are described in this section as well as assumptions regarding factors which can be neglected in the model.

Resistive losses are important to the design of monolithic arrays at millimeter wave frequencies. Semiconductor and conductor losses can be significant contributors to losses in the corporate feed. These losses along the total path length of the corporate feed limit the maximum achievable gain from each array as well as contribute to the RF power dissipated in the array. Other important resistive losses come from the power dividers, phase shifters and the radiating element employed in each subarray. It is assumed that mismatch losses in the corporate feed and elements are negligible in reducing the array gain. Of course, this mismatch loss can be significant if thicker substrates which support surface waves are used in an array which is required to scan to the emergence of blind spots [2, 3, 4, 5, 6].

Active monolithic amplifiers employed in the array are a significant source of additional active array gain. However, FET amplifiers at millimeter wave frequencies are inefficient and result in a significant source of waste power which must be removed from the array. The power-added efficiency of each amplifier characterizes this feature. The amplifier is assumed to be biased such that all DC waste power is dissipated beneath the FET gate where the resultant heat is removed by thermal conduction to the ambient substrate of the array. Thus the gate dimensions and the thermal resistance of the semiconductor are important. A second important feature is the maximum achievable power produced by the FET. This is characterized by the product of RF power output per unit gate width and the maximum gate periphery for which the input impedance can be matched.

In this analysis, we neglect mismatch losses, radiation and coupling between transmission lines used in the feed system as well as losses associated with conversion of dominant mode energy in these lines. Losses associated with the array controller and phase shifter driver are not considered since power dissipated in these devices is assumed to be located away from the subarray. Finally, aperture taper and scan losses are neglected.

3.2 Monolithic Array Model

The model for the active array considered here consists of square, passive subarrays on a semi-insulating semiconductor. Each subarray is fed by a monolithic phase shifter and power amplifier. Each of these subarrays is, in turn, fed corporately with a transmission medium having different attenuation than the subarray. The complete structure is fed by a driver amplifier. The size of each passive subarray will be varied to include the case when <u>each</u> radiating element is driven by a monolithically integrated amplifier.

3.2.1 Subarray

The radiating subarray consists of a square array of microstrip or patch radiators located on half wavelength centers on semi-insulating semiconductor. There are $2^{2n}s$ elements and they are assumed to have an efficiency of η_e. The passive corporate feed for the radiating elements consists of some form of microstrip or stripline feed characterized by a resistive attenuation α_S. The subarray is assumed to be fed from the center with successive 2:1 power dividers distributing the RF energy to each radiating patch element. Each power divider is assumed to have an excess loss L_{DS} to each leg beyond the 3 dB power division expected.

While it is possible to hypothesize a corporate feed network using power dividers which are other than 2:1, the important loss mechanism which associates corporate feed losses with the size of the array is preserved in the model chosen here.

3.2.2 Amplifier/Phase Shifter Feed

Each of the subarrays (or possibly elements) is assumed to be driven by a phase shifter having insertion loss L_p and a monolithically integrated amplifier with gain G_S. Of course, the DC and RF power dissipated in these components is of importance. As noted, the waste power from the driver and controller associated with the phase shifter is neglected. These components are assumed to be located away from the monolithic subarray. However, the DC power dissipated in the amplifier is of importance. A convenient parameter which characterizes this DC power, P_{DC}, and its relationship with the RF power produced by the amplifier, P_o^{RF}, is the power added efficiency of the amplifier. This quantity is

$$\eta_{add} = \frac{P_o^{RF} - P_i^{RF}}{P_{DC}}, \tag{1}$$

and so the power into the amplifier is related to the input RF power P_i^{RF} as

$$P_{DC} = P_i^{RF} \frac{G_S(1 - 1/G_S)}{\eta_{add}}. \tag{2}$$

It is assumed the biasing of the amplifier FET is such that all of the DC power is dissipated beneath the gate of the FET.

The FET power amplifier is limited in output power either by device breakdown voltage and carrier concentration in the channel or the ability to maintain the junction temperature at a level consistent with reliable operation of the amplifier. To characterize these power limitations, each FET gate is characterized by its maximum achievable gate power density, P_d, expressed in Watts of RF power per unit of FET gate width. To characterize the power output, the maximum gate width W_g which can be adequately matched at each frequency will be assumed. To characterize power dissipation, the thermal conductivity and thickness of the semiconductor substrate will be specified as well as the gate length and width.

3.2 Subarray Corporate Feed and Preamplifier

Each active subarray is assumed to be fed by a passive corporate feed consisting of successive 2:1 power dividers coupled by stripline, microstrip or waveguide having attenuation per unit length of α_f . The power divider has excess loss L_{DF}. These parameters may be different than those which characterize the subarray permitting the use of fundamentally different transmission media.

The array is assumed to be fed by a pre-amplifier which exists to level the power throughout the array and control waste power dissipation.

3.3 Performance Criteria

In this section, expressions for the gain, efficiency and effective isotropic radiated power (EIRP) are developed for the monolithic array model proposed. Quantitative expressions for the significant design constraints are provided as a function of commonly defined characteristics of the device and amplifier technology expected to be applied in monolithic transmit arrays.

3.3.1 Gain

The active array gain is computed in a traditional manner by considering the power gain and loss of each stage in the array feed and amplifier sections to provide the effective power and field strength at each radiating element of the array in terms of the input RF power. The field strength from each array element is assumed to be coherently combined in the direction of the array broadside direction to provide the power output from the array. The result is the array directive gain which includes all array losses and active amplifier gain. Thus, the gain may be expressed as

$$G = \frac{G_e G_s(\alpha_s \ell_s) G_a G_f(\alpha_f \ell_f)}{L_p},$$

where

G_e = element gain,

$G_s(\alpha_s \ell_s)$ = subarray feed gain,

$G_a = G_s G_f$ = gain of subarray amplifier and preamplifier,

$G_f = (\alpha_f \ell_f)$ = subarray corporate feed gain,

and ℓ_s, ℓ_f = subarray and corporate feed path lengths.

The subarray and corporate feed gains are functions of the size of the subarray or feed and the attenuation of the transmission medium used. The monolithic array gain can be expressed as

$$G = \frac{4\pi A_a}{\lambda^2} G_a \eta_a = G_o \eta_a \ , \qquad (3)$$

where η_a expresses the traditional aperture efficiency of the array and G_o follows.

The subarray and corporate feed gain calculations require special consideration worth note. In the model for the subarray, input power is divided equally among the 2^{2n_s} elements with each 2:1 power divider having an excess loss of L_{DS}. One power divider section with its feed line of length ℓ to the next divider has a power loss of

$$\frac{e^{-\alpha_s \ell}}{2L_{DS}} .$$

From input to radiating element, the loss of the cascaded feed sections is

$$\left(\frac{1}{2L_{DS}}\right)^{2n_s} e^{-\alpha_s \ell_s} \ ,$$

where the total distance from input to radiating element for purposes of computing the feed attenuation is

$$\ell_s = \lambda_o[2^{n_s-1} - 1/2].$$

Including the element gain and coherently combining the field strengths in the far field main beam direction of the subarray gives

$$G_s(\alpha_s \ell_s) = G_e\left(\frac{2}{L_{DS}}\right)^{2n_s} e^{-\alpha_s \ell_s} .$$

Of course, a similar computation applies to the corporate feed structure where the subarray with its amplifier-phase shifter combination serve as an effective radiating element in the calculation.

3.3.2 EIRP

Traditionally, effective isotropic radiated power is the input RF power which, if radiated isotropically, would provide the same power density at the receiver or scattering target as the monolithic array. Of course, the monolithic array is an active system and may experience power saturation if driven too heavily. Since EIRP expresses at the system level the maximum deliverable power density from the array, we will use EIRP to express the radiated power density when some stage of amplification within the array is driven to maximum power output. This maximum power is limited either by the maximum permissible junction temperature or the maximum achievable output power from the array. We will compute these maximum amplifier output powers from which we can determine the necessary amplifier and array RF drive power to achieve the saturation condition. This maximum array input power when multiplied by the array gain provides our expression from maximum EIRP. Limits imposed on the output power from each amplifier will be discussed in the section on design constraints. It is assumed that each amplifier section maintains power gain at its maximum output power condition.

3.3.3 Efficiency

Overall DC to RF efficiency of the monolithic array is important when the cost of generating power is significant as in the space environment. Further, the total power dissipated in the array may be significant when the ability to carry waste power from the array is limited or when there are limitations on the total system ability to dissipate power. Finally, the proportions of dissipated power from DC and RF sources are important since it is likely that the cost of generating millimeter power is higher that the cost of generating regulated DC power.

An important design criterion is the overall DC to RF efficiency of the monolithic array. For the monolithic array illustrated in Figure 1, the efficiency η is expressed as

$$\eta = \frac{P_o}{P_I + P_{DC}} ,$$

where P_o = output power at receive aperture A_R at range R,

P_I = input RF power to the array,

and P_{DC} = DC power into the array.

Of course, the output power at the receiver can be expressed as

$$P_o = \frac{P_I G}{4\pi R^2} A_R$$

so that from (3)

$$\eta = \frac{G_o}{4\pi R^2} A_R \eta_a \frac{P_I}{P_I + P_{DC}} = \frac{G_o}{4\pi R^2} A_R \eta_a \frac{1}{1 + P_{DC}/P_I} .$$

Thus, the DC to RF efficiency is proportional to two efficiency factors, the traditional RF aperture efficiency η_a and a DC to RF efficiency associated with the active components in the array. The DC power efficiency can be expressed in terms of the amplifier power added efficiency (1) as

$$\frac{1}{1 + P_{DC}/P_I} = \frac{1}{1 + \frac{G_s(1 - 1/G_s)}{L\eta_{add}}} ,$$

where L is the loss to the subarray amplifier.

These efficiency factors will be computed for the array model given in the previous section. The proportions of total power dissipated from DC and RF sources will be noted as well.

3.4 Constraints

Practical constraints on achieving maximum performance arise from limits on the achievable power from the active amplifiers in the array, the DC waste power dissipated by these amplifiers and the RF power dissipated in the corporate feed, the size of the semiconductor wafers available and the cost of fabricating the monolithic array. In this section, quantitative expressions for these design constraints are provided.

3.4.1 Power Dissipated

Two sources of waste power exist in the array - DC bias power dissipated in the amplifiers and RF power dissipated in the lossy feed and array control components.

A convenient parameter to characterize the efficiency of RF amplifiers is the power added efficiency (1). Solving for the DC power into the amplifier in terms of its power gain gives (2). In this expression, the amplifier input RF power can be computed from consideration of the gains and losses in the array feed and the input RF power to the array.

RF power dissipation can be computed similarly if the losses which characterize the components are assumed to be resistive. For example, if the RF loss in the phase shifter is L_p, then the power dissipated in the phase shifter is

$$P_I^{rf} - P_O^{rf} = P_I^{rf}\left(1 - \frac{1}{L_p}\right).$$

Again, the RF power dissipated in the phase shifter or any other lossy component in the array can be computed in terms of its loss and the RF input power to the component.

3.4.2 Junction Temperature

The temperature of the FET junction is believed to be a critical parameter in determining the reliability of active microwave amplifiers and, in this case, the reliability of the monolithic arrays being designed [11]. Device transconductance and gain are decreased with increased junction temperature [12]. Typically, junction temperatures are constrained to be between 100 and 150 degrees Centigrade, with considerable stress placed on the lower of these bounds.

The source of the elevated gate temperature is primarily the power dissipated in the FET junction. In the analysis conducted here, this dissipated power is assumed to be due solely to the DC power into the amplifier - that is, no DC input power is dissipated in bias components for the amplifier on the monolithic subarray. It is further assumed that the primary mechanism for removing power from the FET gate is thermal conduction through the semiconductor substrate to the array ground plane which is assumed to be held at an ambient temperature of 20 degrees Centigrade by a waste power removal system. This thermal conduction process for gate heat removal is commonly considered in the design of power microwave and millimeter wave FETs using steady state Fourier heat flow analysis [12, 13]. This analysis gives the junction temperature T_j above the substrate ambient T_a as

$$\frac{T_j - T_a}{R_{TH}} = P_{DC},$$

where P_{DC} is the DC power dissipated in the junction and the thermal resistance of the junction to the ambient substrate is

$$R_{TH} = \frac{1}{\pi K_{TH} W_g} \ell n \left| \frac{16C}{\pi L_g} \right| \tag{4}$$

where K_{TH} = the thermal conductivity of the semiconductor substrate,

W_g, L_g = the gate width and length respectively,

C = the thickness of the semiconductor substrate.

In this expression, the DC power dissipated in the junction is computed from the power added efficiency of the amplifier (2).

For the designs given in this paper, equation (4) is used to determine the maximum input power to any amplifier permitted by limitations on the junction temperature. This limit on the amplifier input power bounds the input power to the array and provides a fundamental limit on the effective isotropic radiated power achieved by the array.

3.4.3 Maximum Power Output

The maximum achievable RF power from FET amplifiers is limited by the breakdown voltage of the FET and carrier concentration limitations on drain current. Typically, the maximum achievable output power density is limited to 0.5-1 Watt of RF power per millimeter of FET gate width for current technology GaAs MESFETs [14, 15, 16, 17, 18], with the lower limit occurring at higher frequencies. Recently, InP MISFET technology has demonstrated power densities in laboratory devices 3-5 times larger [19, 20, 21]. Specifically, Armand et al have demonstrated 3.5 W/mm at 9 GHz with 4 dB gain and 33% efficiency [19]. More conservatively operated devices have demonstrated 0.86 W/mm [20] and 1 W/mm [21].

The gate width assumed is given as follows:

Frequency (GHz)	Gate Width (microns)
20	2500
30	1100
45	490
60	280

These values were selected to provide a $1/f^2$ dependence on average power from the FET [14, 15, 16, 17, 18] scaled for 10 Watts at 10 GHz at the maximum power density.

3.4.4 Wafer Size

The monolithic arrays considered here are fabricated on the planar face of a GaAs or other semiconductor substrate. The radiating element is assumed to be a microstrip patch or other radiator fabricated on the semiconductor planar surface. Thus, the size of the semiconductor substrate is one factor in limiting the size of the monolithic array which can be fabricated.

Current defacto industry standards for the manufacture and handling of quality GaAs substrates limits wafer diameter to approximately 80-100 mm (3-4 inches) using liquid encapsulated Czochralski growth techniques [22]. Semi-insulating InP wafers are limited to approximately 80 mm (3 inches) in diameter and are of substantially greater cost at this time. Handling equipment for silicon wafers may be able to accommodate wafers with diameters up to 8 inches in the future but it is questionable now whether GaAs wafers of this same diameter can be handled because they are more fragile than silicon. Crystal pullers capable of producing GaAs boules greater than 4 inches are not common.

3.4.5 Cost and Circuit Complexity

An acceptable cost for monolithic arrays is critical to their successful application in military systems. The unit cost of a monolithic array is the sum of the production cost for each unit and the development cost amortized over the number of arrays anticipated in production. It is difficult to estimate these development and production costs with a technology which is as new as millimeter wave monolithics. However, certain qualitative trends are clearly important. For example, common application of a wide variety of subarrays or millimeter wave circuits in the subarray justifies extensive circuit characterization and production development to assure high yields during production. Yield, the fraction of production arrays which perform adequately during DC and RF test, is critical. As the complexity of the subarray increases, adequate circuit yields become increasingly difficult to achieve. Circuit complexity effects on yield are difficult to express quantitatively - the number of components and their complexity being primary considerations. For example, large biasing capacitors are sometimes shorted due to imperfect application of dielectrics while large periphery sub-micron gate FET's fail because of imperfections in gate fabrication with sub-micron lithography.

For purposes of this analysis, we will assume that the cost and hence yield of monolithic arrays is strongly dependent upon the number of sub-micron gate FET's employed in the amplifiers and phase shifters in the array. Thus, constraining the number of FETs limits yield and bounds the unit production costs of the array. The number of FETs can be limited by reducing the size of arrays employing amplifiers and phase shifters at the element level or by using these amplifiers and phase shifters to drive passive subarrays within larger monolithic arrays.

4. RESULTS

Results which compare the performance of monolithic active arrays fabricated entirely on GaAs or InP are presented here over the frequency range of 20 - 60 GHz.

In each case, the semi-insulating substrate is assumed to be 4 mils (4E-3 inches) thick for purposes of microstrip transmission line design and thermal resistance calculations. The microstrip loss was computed as a function of frequency for a 50 Ohm design using SUPERCOMPACT assuming chromium doped semi-insulating GaAs having a dielectric constant of 12.9 and loss tangent of 6E-4 [23]. Some samples of this material have loss tangents as high as 11E-4 at 60 GHz [24]. RMS surface roughness was taken to be 1 micron giving transmission loss predominated by microstrip conductor losses and ranging from 0.7 dB/cm at 20 GHz to 1.5 dB/cm at 60 GHz. These losses are likely to be optimistically small since higher order propagation modes at these millimeter wave frequencies are neglected. At the same time, surface roughness effects on microstrip losses become more important at higher frequencies. Without roughness, losses vary from 0.5 to 1.0 dB/cm over the 20 - 60 GHz band. Semi-insulating InP materials have a dielectric constant of 12.4 [25] and a loss tangent which is apparently unknown but assumed to be the same as GaAs (6E-4). In view of the fact that conductor losses dominate dielectric losses in GaAs, it appears reasonable to assume that InP will have the same microstrip attenuation as a function of frequency as calculated for GaAs.

The thermal conductivity of GaAs was selected to be 0.44 W/cm-degree Centigrade at 60 degrees Centigrade [13]. This value is optimistic since some measurements indicate that the conductivity can be as low as 0.25 - 0.3 W/cm-degree Centigrade [26]. InP has a somewhat higher thermal conductivity of 0.7 W/cm-degree Centigrade [25].

Drukier [27] has demonstrated the inconsistency of designing microwave or millimeter wave GaAs amplifiers to simultaneously maximize gain, output power and efficiency. His data demonstrate that only one of these parameters can be maximized in any design. In view of the varying design requirements of the monolithic arrays described here to achieve maximum gain, EIRP or efficiency, analysis was conducted assuming amplifiers designed for power, gain or power added efficiency. Nominal and optimistic values for each amplifier parameter were selected at each frequency of operation and array designs conducted with one parameter selected to assume its optimistic value and the others their nominal values. Optimistic values were chosen to meet or exceed current laboratory state of the art values so that the resulting benefits in array performance could be assessed.

Assumed values of amplifier power added efficiency are indicated in the following table and result from a model suggested by Weidler and Raghuraman [28].

GaAs MESFET
Power Added Efficiency

Frequency (GHz)	Nominal %	Optimistic %
20	20	41
30	17	34
45	14	28
60	11	22

Amplifier power gain was selected to vary between a nominal value of 4 dB and an optimistic value for a single stage amplifier of 9 dB.

In the results reported here, the average phase shifter insertion loss is assumed to be 4 dB, independent of operating frequency. This value is a challenge to todays monolithic phase shifter technology in view of the reported results of Ayasli et al [29] and Wilson et al [30] giving approximately 5dB insertion loss for monolithic, X band, four bit phase shifters and the results of Sokolov et al [31] and Bauhahn et al [32] showing an experimental 2.5 -3 dB per bit insertion loss at 30 GHz. 1.5 - 2 dB/bit appears possible at 30 GHz with advanced fabrication techniques. Power divider excess loss assumed was 0.1 dB for each leg of the 2:1 power divider.

Figures 2 - 5 show the performance of a monolithic array at 45 GHz. Results for array gain, efficiency, waste power density and EIRP are given as a function of array edge length in wavelengths. In all results given here, the amplifiers and phase shifters are assumed to be located at each array element. FET junction temperature of 100 degrees Centigrade limits some results.

Figure 2 gives results for the maximum subarray gain and percentage of the total power dissipated from DC and RF sources. Gain is maximized at a subarray size which approximates the 3 inch diameter wafer size available for GaAs monolithic circuit fabrication. A 3 dB increase in gain can be accomplished with the low loss microstrip feed on a very smooth substrate but this increase is accomplished with a larger size subarray. These maximum gain arrays can be achieved only through the use of large, complicated monolithic circuits. For example, the 8 wavelength edge subarray contains 256 radiating elements and a total of between 4000 and 6500 FETs for the amplifiers (assuming 1 FET/amplifier) and 4 bit phase shifters (assuming 4 - 6 FETs/bit). The subarrays are thus very complicated by todays standards of monolithic millimeter wave circuit fabrication and will likely be expensive because of poor yield.

Figure 2 also illustrates the proportions of dissipated power from DC and RF sources in the maximum gain array designs. The proportions change dramatically when maximum gain is achieved. For the smaller, more realizable arrays, the most significant source of dissipated power is from the DC biasing of the FET power amplifiers, emphasizing the importance of power efficient amplifier technology at this frequency.

Maximum efficiency array designs are illustrated in Figure 3. Here the sum of the decibel values of aperture and DC to RF efficiencies are plotted on the ordinate as a function of array edge length expressed in wavelengths. Two substrate losses are considered, corresponding to maximum and minimum substrate roughness. As might be expected, maximum array efficiency results from the use of amplifiers designed for maximum power added efficiency (E) - but only for small arrays where the predominant dissipated power results from DC power applied to the power amplifiers. For larger subarrays, maximum array efficiency results when maximum power gain (G) amplifiers are employed. These larger arrays have as their dominant loss mechanism the RF losses in the corporate feed for the subarray. High power gain amplifiers at the element level permit lower drive power in the lossy corporate feed and hence more efficient subarray designs.

Where arrays are fabricated on limited size subarrays to insure adequate yields, stress should be placed on the use of high efficiency power amplifiers when there is concern for maximizing the overall efficiency of the monolithic subarray designs.

Figure 4 illustrates the maximum EIRP and associated waste power as a function of array edge length at 45 GHz. Also shown are the corresponding densities, EIRP and waste power per unit area of array face. Of the amplifier designs which maximize output power, gain and efficiency, designs with maximum amplifier efficiency give the maximum EIRP. In the design, the maximum EIRP is limited by the 0.5 Watt/mm of GaAs gate power density rather than the 100 degree Centigrade gate temperature limit. It appears possible with InP MISFET technology to increase this gate power density. To evaluate this technological advantage, results for higher power density, higher thermal conductivity InP substrate arrays are provided for comparison. Power density was increased to 1.2 Watt/mm where the EIRP was simultaneously limited by gate junction temperature of 100 degrees Centigrade and gate power density. A significant increase of 3.7 dB EIRP results from this InP design.

Figure 4 also illustrates the waste power and power density for these same designs. The waste power density remains essentially constant for the smaller, more realizable arrays. This result is reasonable as we have observed previously that the losses in these arrays are dominated by amplifier inefficiencies. The improved performance InP designs result in a 3.7 dB increase in waste power density, reasonable since no improvement in the efficiency of the amplifier was assumed.

The waste power densities illustrated here are significant. For comparison, black body radiation from a 100 degree Centigrade object radiates only 0.1 Watt/square centimeter as compared to the approximate 10 Watt/square centimeter required to be removed from the array.

Figure 5 provides a comparison of these results as a function of frequency from 20 to 60 GHz for GaAs based arrays. The maximum achievable array gain varies between 26 and 28 dB with losses associated with the 1 micron RMS surface roughness microstrip conductor limiting the maximum gain. At 20 and 30 GHz the 3 inch GaAs wafer size limits the maximum achievable array gain. The maximum achievable EIRP for a 64 element monolithic array is shown also. The maximum EIRP varies approximately inversely with frequency squared over this band. At 20 GHz, the maximum EIRP results from a design employing maximum output power amplifiers and the EIRP is limited by the junction temperature of the amplifier gates. At 30 GHz and above, maximum EIRP results from designs employing maximum efficiency amplifiers and the EIRP is limited by the output power (gate power density) of the amplifier. The waste power and waste power density associated with the 64 element arrays are shown also. The waste power density is substantially constant with frequency since, for this size array, waste power is dominated by the DC power dissipated in the final power amplifiers in the array. The output power from the amplifier varies as wavelength squared which balances the increased number density of amplifiers giving the substantially constant power density. The logarithmic decrease in amplifier efficiency is not a strong factor in determining this waste power density in the monolithic arrays.

5. CONCLUSIONS

Monolithic phased arrays represent a challenging combination of phased array and monolithic millimeter wave integrated circuit technologies. These phased arrays promise to have an immense impact on airborne and spaceborne communications terminals and radar systems in the millimeter wave frequency bands if substantial technological challenges can be met in future years.

Bounds on the performance of monolithic phased arrays have been presented as they are limited by array, circuit and device performance estimates. Depending upon application, the performance of monolithic arrays is characterized by gain, effective isotropic radiated power or overall efficiency. Maximization of any or a combination of these performance criteria is limited by cost and array complexity, waste power dissipation, amplifier output power and junction temperature.

The monolithic arrays described here are assumed to be fabricated using primarily GaAs monolithic circuit techniques. The quality and quantity of GaAs substrate materials is rapidly improving as are domestic capabilities to provide the sub-micron device lithography necessary for millimeter wave power and low noise amplifiers. InP as a material base for millimeter monolithic arrays shows great promise. The material has higher thermal conductivity than GaAs. InP is capable of sustaining higher device voltages without breakdown and allows greater carrier saturation currents at these voltages than GaAs, thus permitting devices with greater output power.

Results presented here bound the performance of monolithic arrays due to limits on the performance of devices and monolithic components. These device and component performance limits are based on extrapolation from current state of the art laboratory results and physical limits on expected performance. Small signal active array gain is limited by semiconductor wafer size and achievable cost effective circuit realization at the lower frequencies and by microstrip circuit feed losses at higher frequencies. Even at the higher frequencies, the complexity of the maximum gain circuit greatly exceeds todays capabilities for monolithic circuit fabrication.

Results for maximum effective isotropic radiated power arrays are presented for final power amplifier designs which maximize amplifier gain, efficiency or saturated power output. Maximum achievable EIRP varies inversely with the square of frequency with junction temperature limiting EIRP at the lower frequencies and FET power density limiting EIRP at higher frequencies. Waste power is contributed primarily from the DC to RF inefficiencies of the FET power amplifiers and the waste power density necessary to be removed from the array remains approximately constant with frequency. This waste power density is significant, being approximately 100 times that which can be radiated by a black body at the corresponding junction temperature of 100 degrees Centigrade.

Significant technological challenges exist to make monolithic phased arrays in the frequency bands from 20 - 60 GHz realizable and cost effective in military applications. Stress must be placed on advancing the art of design and fabrication of monolithic arrays. Significant challenges to be addressed in the coming years involve improved power density millimeter wave FET devices such as might be achieved with the InP material base, improved efficiency amplifiers, improved, repeatable large scale fabrication techniques for millimeter circuits, improved design methodology to reduce the cost of monolithic array design and finally, monolithic techniques which can provide isolation between colocated transmit and receive arrays such as might be required in radar systems.

6. ACKNOWLEDGEMENTS

The helpful technical discussions with Scott Mitchell, Andrew Slobodnik, Richard Webster, Peter Franchi and John McIlvenna of the RADC Electromagnetic Sciences Division are gratefully acknowledged.

7. REFERENCES

1. Rutledge, D.B., et al, "Integrated Circuit Antennas", Infrared and Millimeter Waves, Vol. 10, Part II, (K.J. Button, editor), Academic Press, New York, 1983.

2. Alexopoulos, N.G., et al, "Substrate Optimization for Integrated Circuit Antennas", IEEE Transactions on Microwave Theory and Technique, Vol. MTT-31, no. 7, July 1983.

3. Pozar, D.M. and D.H. Schaubert, "Analysis of an Infinite Array of Rectangular Microstrip Patches with Idealized Probe Feeds", IEEE Transactions on Antennas and Propagation, Vol. AP-32, no. 10, October 1984.

4. Schaubert, D.H., et al, "Considerations for Millimeter Wave Monolithic Phased Arrays", Proceedings of 1984 Antenna Applications Symposium, RADC-TR-85 -14, Volume 1, January 1985. AD A153257

5. Mailloux, R.J., "Phased Array Architectures for Millimeter Wave Active Arrays", IEEE Antennas and Propagation Society Newsletter Feature Article, To Be Published.

6. Mailloux, R.J., "Printed Slot Arrays with Dielectric Substrates", 1985 IEEE AP-S International Symposium Digest, pp. 31-34, June 1985.

7. Pozar, D.M., "Surface Wave Effects in Phased Arrays of Printed Antennas", Phased Arrays 85 Symposium Record.

8. Pozar, D.M., and D.H. Schaubert, "Comparison of Architectures for Monolithic Phased Array Antennas", Phased Arrays 85 Symposium Record.

9. Anzic, G., and D.J. Connolly, "20 and 30 GHz MMIC Technology for Future Space Communications Antenna Systems", 1984 IEEE GaAs IC Symposium Digest, pp. 189-192, October 1984.

10. Gupta, A., et al, "A 20 GHz 5-Bit Phase Shift Transmit Module With 16 dB Gain", 1984 IEEE GaAs Symposium Digest, pp. 197-200, October 1984.

11. Irwin, J.C., "The Reliability of GaAs FETs", GaAs FET Principles and Technology, (J.V. DiLorenzo and D.D. Khandelwal, editors), Artech House, MA, 1982.

12. Wemple, S.H., and H. Huang, "Thermal Design of Power GaAs FETs", GaAs FET Principles and Technology, (J.V. DiLorenzo and D.D. Khandelwal, editors), Artech House, MA, 1982.

13. Cooke, H.F., "FETs and Bipolars Differ When the Going Gets Hot", Microwaves, February 1978.

14. DiLorenzo, J.V., and W.R. Wisseman, "GaAs Power MESFETs: Design, Fabrication and Performance", IEEE Transactions on Microwave Theory and Technique, Vol. MTT-27, pp. 367-378, 1979.

15. Johnson, E.O., "Physical Limitations on Frequency and Power Parameters of Transistors", RCA Review, Vol. XXVI, no. 2, pp. 163-177, June 1965.

16. J.V. DiLorenzo, "GaAs FET Development - Low Noise and High Power", Microwave Journal, Vol. 21, February 1978, pp. 39-42, 44.

17. Huang, H.C., "Fundamental Limits", Advanced III-V Semiconductor Materials Technology Assessment, (M. Nowogrodski, editor), Noyes Publications, New Jersey, 1984.

18. Vendelin, G.D., Design of Amplifiers and Oscillators by the S-Parameter Method, Wiley, New York, 1982.

19. Armand, M., et al, "High-Power InP MISFETs", Electronics Letters, Vol. 19, no. 12, June 1983.

20. Nagahama, K., et al, "InP High Power MISFET", 1984 IEEE IEDM Conference.

21. Itoh, T., and K. Ohata, "X-Band Self Aligned Gate Enhancement Mode InP MISFETs", IEEE Transactions on Electron Devices, Vol. ED-30, no. 7, pp. 811-815, 1983.

22. Narayan, S.Y., "Present Status of Technology", Advanced III-V Semiconductor Materials Technology Assessment, (M. Nowogrodski, editor), Noyes Publications, New Jersey, 1984.

23. Schlosser, W.O., and V. Sokolov, "Circuit Aspects of Power GaAs FETs", GaAs FET Principles and Technology, (J.V. DiLorenzo & D.D. Khandelwal, editors), Artech House, MA, 1984.

24. Afsar, M.N., and K.J. Button, "Millimeter-Wave Dielectric Measurement of Materials", Proceedings of the IEEE, Vol. 73, no. 1, pp. 131-153, January 1985.

25. Neuberger, M., III-V Semiconductor Compounds, IFI/Plenum, New York, 1971.

26. Holland, M.G., "Thermal Conductivity", Semiconductors and Semi-Metals, (R.K. Williamson, and A.C. Bier, editors), Academic Press, New York, 1966.

27. Drukier, I., "Power GaAs FETs", GaAs FET Principles and Technology, (J.V. DiLorenzo and D.D. Khandelwal, editors), Artech House, MA, 1982.

28. Weidler, D.E., and P. Raghuraman, Private Communication, January 1985.

29. Ayasli, Y., et al, "A Monolithic Single-Chip X-Band Four-Bit Phase Shifter", IEEE Transactions on Microwave Theory and Technique, Vol. MTT-30, no. 12, December 1982.

30. Wilson, K. et al, "A Novel MMIC, X-Band Phase Shifter", 1985 IEEE Monolithic Circuits Symposium Digest, pp. 10-14, June 1985.

31. Sokolov, V., et al, "A Ka-Band GaAs Monolithic Phase Shifter", IEEE Transactions on Microwave Theory and Technique, Vol. MTT-31, no. 12, December 1983.

32. Bauhahn, P., et al, "30 GHz Multi-Bit Monolithic Phase Shifters", 1985 IEEE Monolithic Circuits Symposium Digest, pp. 4-7, June 1985.

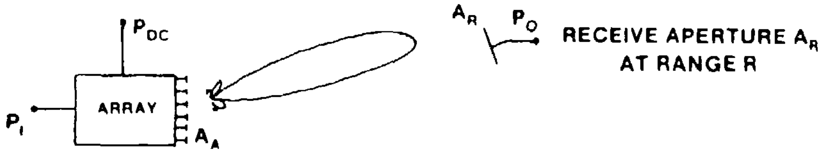

Figure 1. Monolithic Array Model for Calculation of Overall Efficiency.

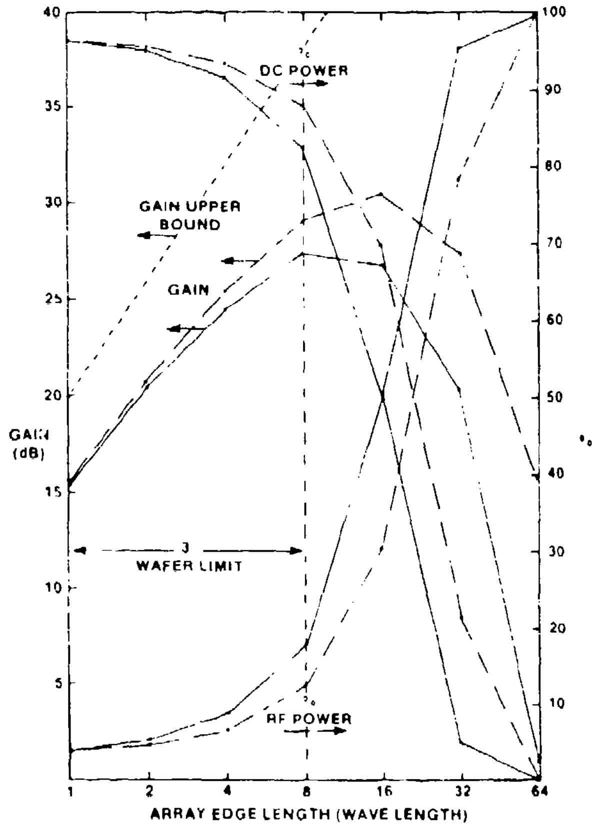

Figure 2. Maximum Amplifier Gain Microstrip Subarray Design at 45 Ghz. Array Gain, Gain Upper Bound and Percentage of DC and RF Waste Power versus Array Edge Length. Amplifier Power Gain = 9 dB.

Maximum Microstrip Loss = 1.2 dB/cm for 1 micron RMS surface roughness,

Minimum Microstrip Loss = 0.8 dB/cm for Smooth Substrate.

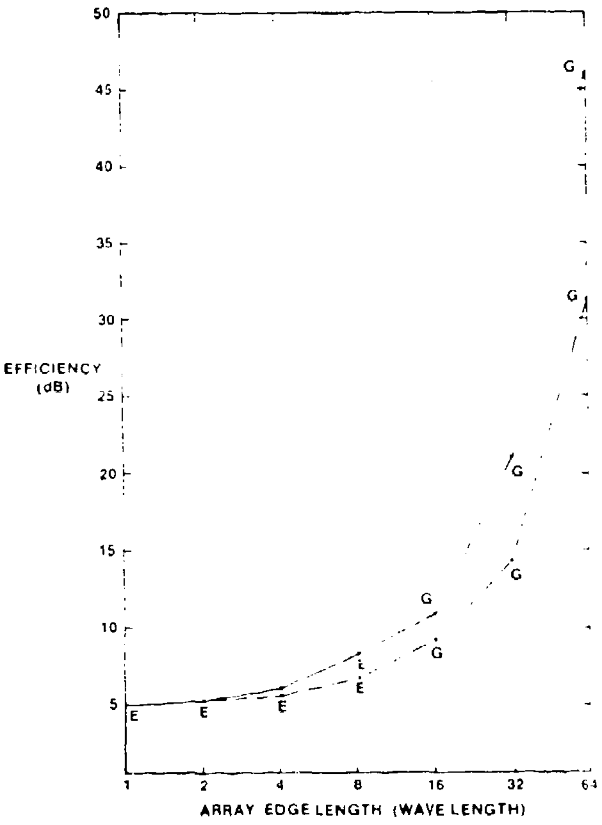

Figure 3

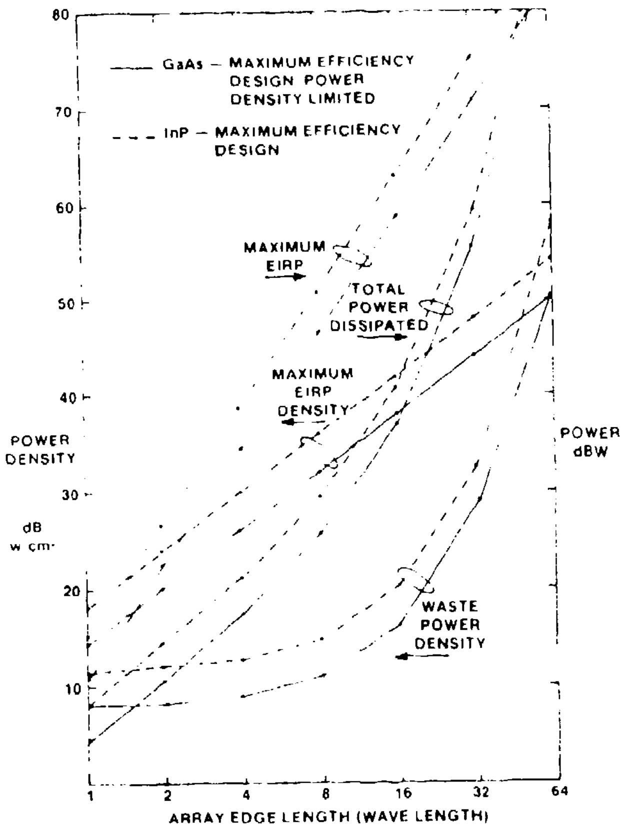

Figure 4

Figure 3. Maximum Efficiency Microstrip Subarray Designs at 45 GHz. Efficiency (Sum of Aperture and DC-RF conversion dB values) versus Array Edge Length. In this Figure, E denotes designs employing maximum power added efficiency amplifiers while G denotes designs employing maximum power gain amplifiers.

Maximum Microstrip Loss = 1.2 dB/cm for 1 micron RMS surface roughness,

Minimum Microstrip Loss = 0.8 dB/cm for Smooth Substrate.

Figure 4. Maximum EIRP, EIRP Density, Total Waste Power and Waste Power Density as a function of Array Edge Length. Maximum EIRP on GaAs Substrate Achieved with Maximum Efficiency Amplifier Design and Limited by FET Gate Power Density; InP Design with Maximum Efficiency Amplifier Design and increased Gate Power Density.

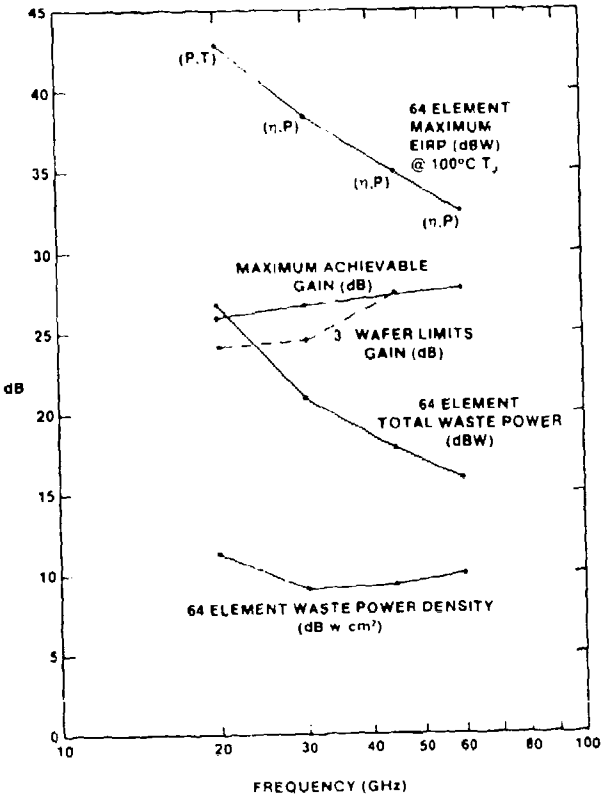

Figure 5. Comparative Monolithic Array Performance versus Frequency.

SURFACE WAVE EFFECTS IN PHASED ARRAYS OF PRINTED ANTENNAS

David M. Pozar
Dept. of Electrical and Computer Engineerng
University of Massachusetts
Amherst, MA 01003

ABSTRACT

The role of surface waves in printed antennas is addressed. Data is presented for the amount of surface wave power generated by single printed antenna elements, finite arrays, and infinite arrays. Printed dipole and microstrip patches are discussed, and the role of surface waves in the scan blindness phenomenon is presented.

INTRODUCTION

Printed antenna elements are currently of considerable interest because of their application to monolithic millimeter wave phased arrays, as well as other applications. In such a configuration, the substrate may have a relatively high dielectric constant (e.g., Gallium Arsenide, with ϵ_r=12.8), and be relatively thick, electrically. Such a situation is ripe for the excitation of surface waves.

Surface wave excitation generally has deleterious effects in the context of printed antennas. For single elements (dipole and patches) the amount of power lost to surface waves has been computed, and will be discussed below. Infinite arrays of such elements have also been studied, and it is known that surface waves, in general, cannot exist on such periodic structures. On the other hand, infinite arrays of printed antennas exhibit the scan blindness phenomenon, which turns out to be intimately connected to surface waves of the loaded structure.

A number of interesting questions thus arise. In a finite array of printed antennas, how much surface wave power is generated? Is it more or less than a single element would generate? How does this power vary with the scan angle of the array? How does the size of the array affect the amount of surface wave power? And how does the transition to an infinite array occur, where there is no surface wave power, except possibly at a blindness angle?

The above questions have been answered by analyzing a finite array of printed dipoles. Data is presented showing that the amount of power launched into surface waves by a printed array decreases as the size of the array increases, for all scan angles except a critical angle where the surface wave power increases with array size. This critical angle corresponds to the scan blindness angle of the infinite array.

SURFACE WAVE EXCITATION BY SINGLE ELEMENTS

The surface wave power generated by a single dipole or microstrip patch has been determined by a number of workers [1], [2], [3], [4], with general agreement between their results. Surface wave excitation is quantified by defining an efficiency, e, as

$$e = 1 - \frac{\text{Surface Wave Power}}{\text{Input Power}} \quad .$$

Figure 1 shows the efficiency of three types of printed antenna elements on a Gallium Arsenide substrate, versus substrate thickness. Observe that for very thin substrates, the efficiency is close to unity, meaning that little power is being converted to surface waves. The efficiency quickly drops off with increasing substrate thickness, and ceases to be monotonic as more surface waves begin to propagate. Clearly a low value of efficiency is undesirable, since not only do surface waves represent a loss of antenna gain, but surface wave power can diffract from substrate discontinuities (feed lines, edges, etc.) to degrade sidelobe levels, or couple to active devices on the substrate. Surface wave diffraction effects have been observed by a number of researchers.

For lower dielectric constants, the efficiency curves drop off more slowly with substrate thickness, and do not attain as low a value as the data in Figure 1 [1].

SCAN BLINDNESS IN INFINITE ARRAYS

At the other end of the size scale from single elements are infinite arrays of printed elements. The usual rationale for considering infinite arrays is that they can very accurately model the central elements in a large but finite array, and are substantially easier to treat analytically than finite arrays, since the infinite array can be handled as a periodic structure. Such solutions have been carried out for printed dipoles [5], and microstrip patches with idealized probe feeds [6], and general relations based on infinite current sheets have been derived in [7].

Figure 2 shows the reflection coefficient magnitude versus scan angle for an infinite array of printed dipoles, for E, H, and D (diagonal) scan planes. The array is matched at broadside, and becomes mismatched as the array is scanned. Of particular interest is the unity reflection coefficient at 46° in the E-plane. This is the scan blindness condition, where no real power is radiated from the face of the array [8]. The existence of such a "blind spot" generally limits the scan range of the array, as well as degrading the impedance match. It is thus desirable to have such blind spots as close to endfire as possible.

The blind spot position can be predicted from the equation,

$$\beta_{sw}^2 = \left(\frac{2m\pi}{a} + k_o \sin\theta \cos\phi\right)^2 + \left(\frac{2n\pi}{b} + k_o \sin\theta \sin\phi\right)^2$$

where β_{sw} is the surface wave propagation constant of the loaded (by the antenna elements) dielectric slab, a and b are the E-plane and H-plane element spacings, and m, n are positive or negative integers. The right-hand side of this equation represents the propagation constant of a Floquet mode of the array; when this constant equals the propagation constant of the source-free surface wave of the slab, a resonance can occur, leading to scan blindness.

Solutions to the above equation can be graphically illustrated using a "surface wave circle" diagram, as shown in Figure 3. This diagram is basically a grating lobe diagram, with the solid circles representing the propagating regions of the various Floquet modes. It is augmented with dashed circles, which represent surface wave modes. Scan blindness is possible whenever a dashed circle (radius β_{sw}/k_o) enters visible space (the o,o Floquet mode circle), unless the polarization is such that the wave is not excited (as in the H-plane of dipole arrays) [5].

The surface wave circle diagram shows that the blind spot will move closer to broadside as β_{sw}/k_o increases, which will occur as the substrate becomes thicker or the dielectric constant increases. Increasing the element spacing also moves the blind spot closer to broadside, since the grating lobe circles will move closer together. Figure 4 shows the effect of a thinner substrate, for a microstrip patch array.

Although the propagation constant β_{sw} in the above equation should be that of the substrate with the loading effect of the antenna elements accounted for, it has been found that negligible error in the blind spot position results from the use of the propagation constant of the unloaded substrate, for antenna elements near resonance.

Figure 5 shows the effect of a dielectric superstrate on an infinite array of printed dipoles. Such a superstrate has been proposed as a matching layer for printed phased arrays. The data of Figure 5, however, shows that such a matching layer may actually degrade performance, particularly in the E-plane, by moving the blindness angle closer to broadside. The position of this blind spot is easily predicted through the use of the surface wave circle diagram and the surface wave propagation constant of the two-layer substrate.

SURFACE WAVE EXCITATION FOR FINITE ARRAYS

The consideration of finite arrays of printed dipoles or patches requires the calculation of mutual coupling between each pair of elements in the array. This is the so-called "element-by-element" approach, and is a more formidable task from a computational point of view than either the single element case or the infinite array case. (As a matter of fact, the infinite array problem is easier to handle than the single element problem.) A few two-element dipole array examples were presented in [1], but only recently has the more general case of a finite planar array with an arbitrary number of printed dipoles been solved [9]. As well as being of practical interest in its own right, the analysis of a finite array provides the missing link in the comprehensive understanding of the role of surface waves in printed antennas and arrays.

Figure 6, showing the efficiency of a two-element dipole array on a quartz substrate, demonstrates some of the essential features of finite printed arrays. The efficiency is computed for two modes of excitation: even mode (both dipoles fed in-phase), and odd mode (dipoles fed 180° out of phase). The even mode corresponds to broadside radiation, while the odd mode corresponds to endfire radiation, so in effect we have a simple phased array, with the two modes corresponding to two different scan angles. Observe that a significant variation in efficiency occurs for the two modes, and that the broadside (even) excitation results in better efficiency than a single dipole, while the endfire (odd) excitation results in a lower efficiency. The above comments only apply for substrate thicknesses for which one surface wave mode is propagating; when two surface wave modes are propagating their different propagation constants preclude significant destructive or constructive interference.

Figure 7 shows the difference of various-sized square planar arrays of printed dipoles, for E-plane scan. The 1x1 array is a single element, and so its efficiency does not vary with scan angle. Notice that the efficiency improves steadily with increasing array size, at all scan angles except near 45° where it gets worse as the array size increases. In the limit as the array becomes infinitely large, the efficiency will approach unity (no surface wave power generated) at all scan angles except the critical angle at 45°, where the efficiency will become zero (all input power is converted to a surface wave). This critical angle corresponds to the scan blindness angle in the infinite array. In the H-plane scan of the array, the efficiency quickly approaches unity for all scan angles (since there is no blind spot in this plane), as the array size increases.

The effect of this surface wave power also shows up in the impedance properties of the array (as well as the active element pattern). Figure 8 shows the reflection coefficient magnitude versus scan angle for a 7x7 planar array, and an infinite array. The array and substrate geometries are the same as that of Figure 7. The reflection coefficient is taken at the center element for the finite array, and the arrays are matched at broadside.

Observe that the 7x7 array is already large enough to be reasonably approximated by the infinite array, and that the scan blindness phenomenon is showing up quite clearly in the E-plane of the 7x7 array result.

CONCLUSION

This paper has presented a comprehensive theory of the role of surface waves in printed antennas and arrays by showing how surface wave excitation is affected by substrate thickness and permittivity, array size, element spacing, and scan angle. The scan blindness phenomenon has been discussed, and the surface wave circle diagram used to graphically show the effects of element spacing and substrate parameters on the occurence of blind spots.

REFERENCES

[1] D. M. Pozar, "Considerations for Millimeter Wave Printed Antennas", IEEE Trans. Antennas and Propagat., Vol. AP-31, pp. 740-747, Sept. 1983.

[2] P. B. Katehi and N. G. Alexopoulos, "On the Effect of Substrate Thickness and Permittivity on Printed Circuit Antennas", IEEE Trans. Antennas and Propagat., Vol. AP-31, pp. 34-39, Jan. 1983.

[3] N. G. Alexopoulos and D. R. Jackson, "Fundamental Superstrate (Cover) Effects on Printed Circuit Antennas", IEEE Trans. Antennas and Propagat., Vol. AP-32, pp. 807-816, August 1984.

[4] P. Perlmutter, S. Shtrikman, and D. Treves, "Electric Surface Current Model for the Analysis of a Microstrip Rectangular Element", 1984 International IEEE Antennas and Propagation Symposium Digest, Boston, pp. 557-580.

[5] D. M. Pozar and D. H. Schaubert, "Scan Blindness in Infinite Phased Arrays of Printed Dipoles", IEEE Trans. Antennas and Propagat., Vol. AP-32, pp. 602-610, June 1984.

[6] D. M. Pozar and D. H. Schaubert, "Analysis of an Infinite Array of Rectangular Microstrip Patches with Idealized Probe Feeds", IEEE Trans. Antennas and Propagat., Vol. AP-32, pp. 1101-1107, Oct. 1984.

[7] D. M. Pozar, "General Relations for a Phased Array of Printed Antennas Derived from Infinite Currents Sheets", IEEE Trans. Antennas and Propagat., to appear.

[8] G. H. Knittel, A. Hessel, and A. A. Oliner, "Element Pattern Nulls in Phased Arrays and their Relation to Guided Waves", Proc. IEEE, Vol. 56, pp. 1822-1836, Nov. 1968.

[9] D. M. Pozar, "Analysis of Finite Phased Arrays of Printed Dipoles", IEEE Trans. Antennas and Propagat., submitted for publication.

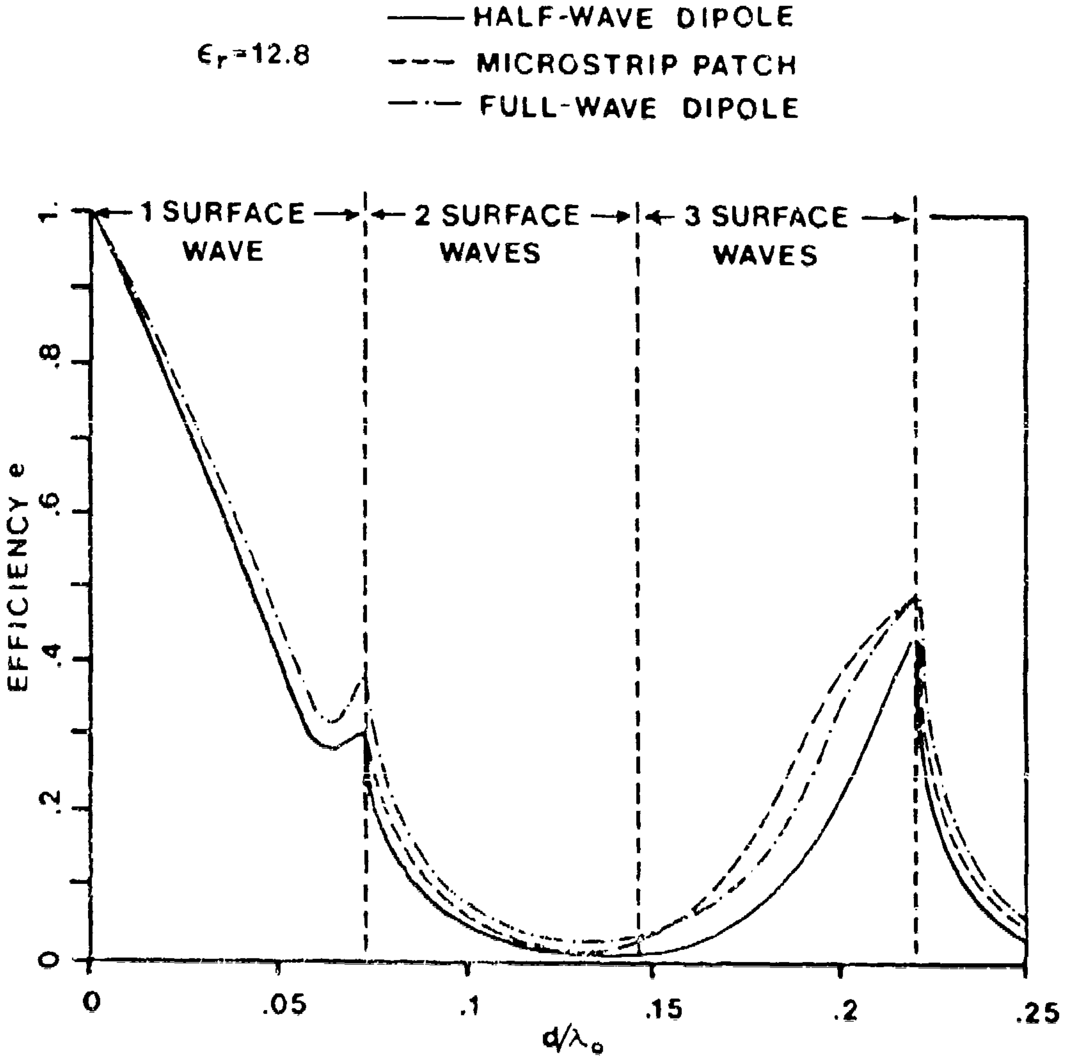

Figure 1. Single-element efficiency (based on power lost to surface waves) for three types of antennas printed on Gallium Arsenide substrates.

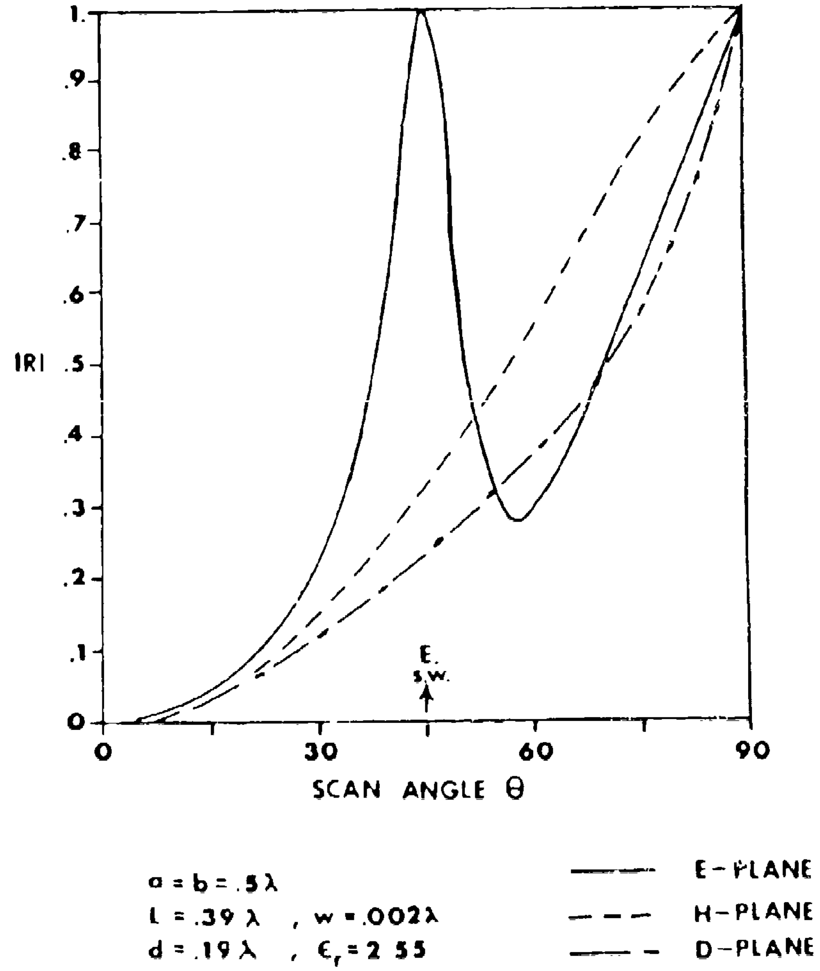

Figure 2. Reflection coefficient magnitude versus scan angle for an infinite array of printed dipoles. Element spacing in both planes is $\lambda_o/2$. Substrate thickness = $0.19\lambda_o$, dielectric constant = 2.55.

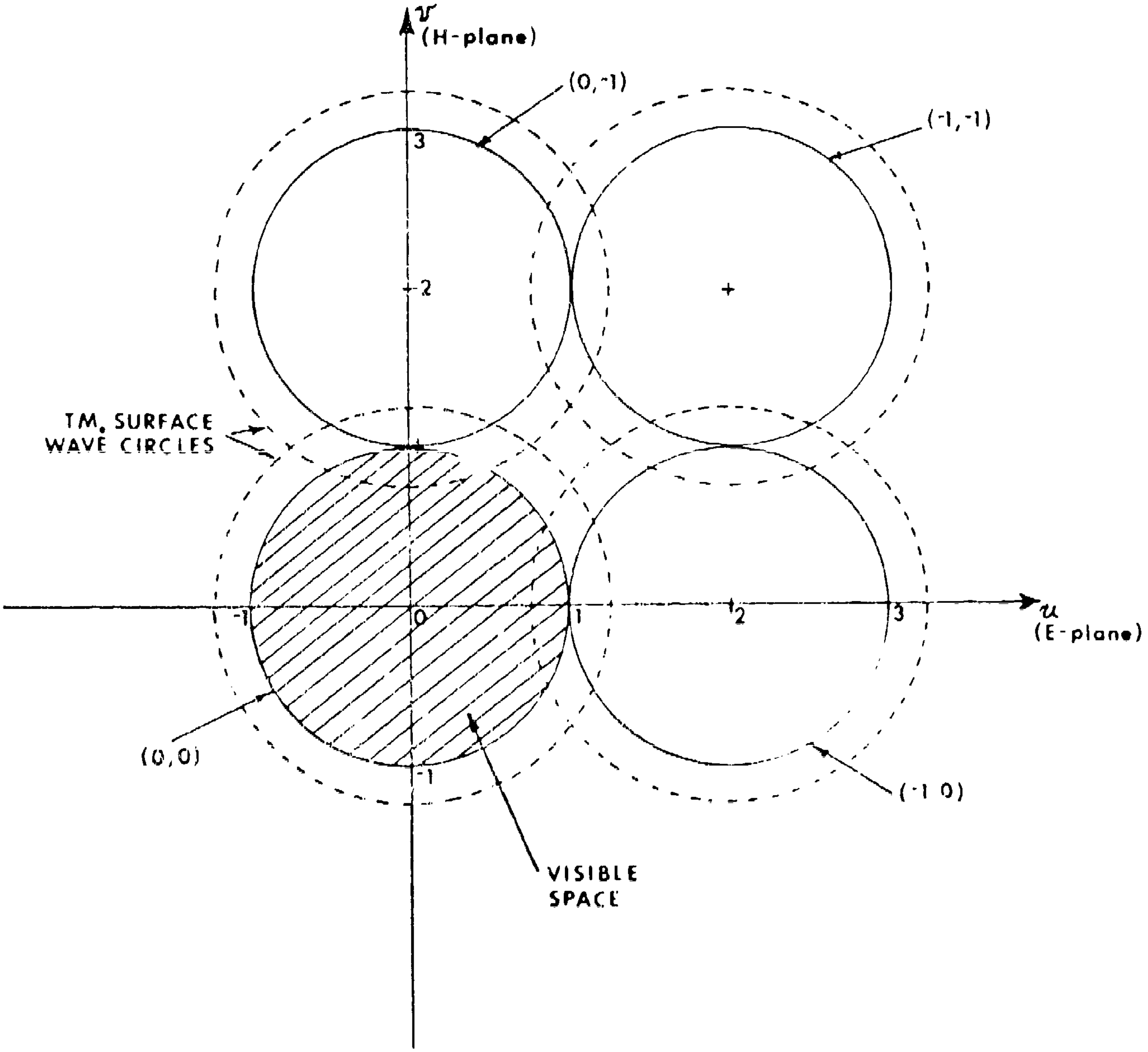

Figure 3. Surface wave circle diagram for the infinite array of Figure 2.

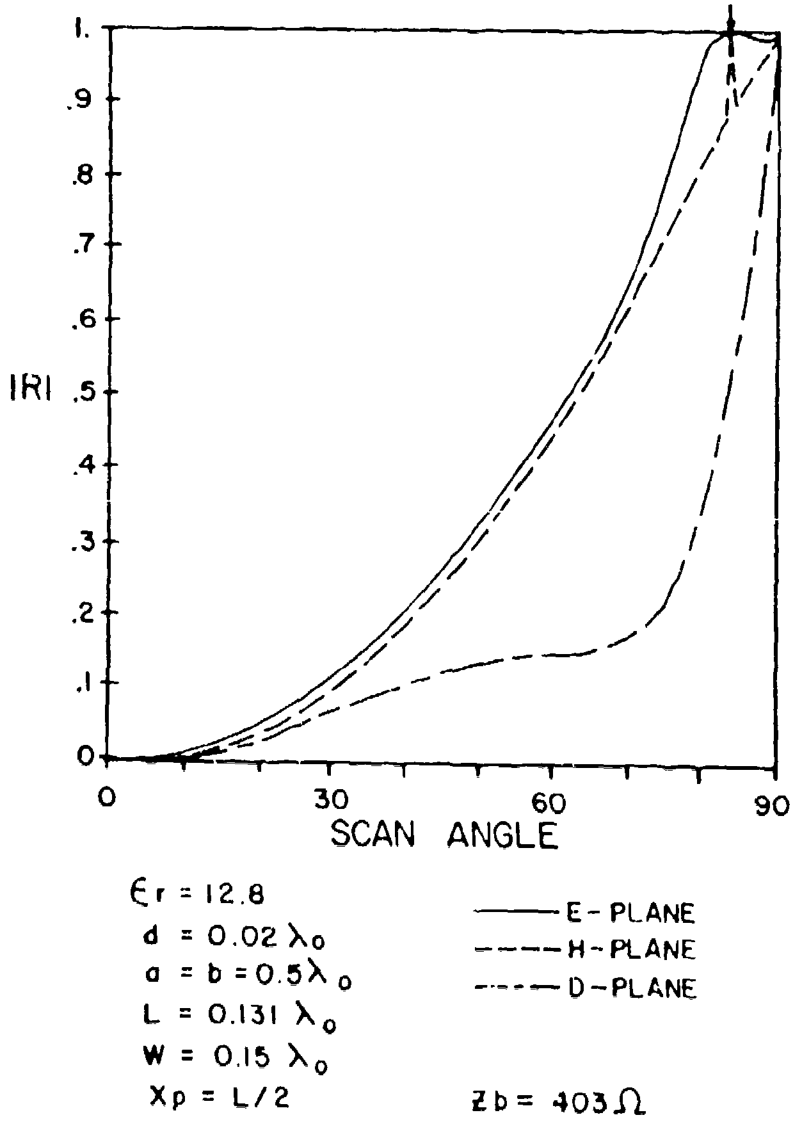

Figure 4. Reflection coefficient magnitude versus scan angle for an infinite array of microstrip patches. Element spacing in both planes is $\lambda_0/2$. Substrate thickness = $0.02\lambda_0$, dielectric constant = 12.8.

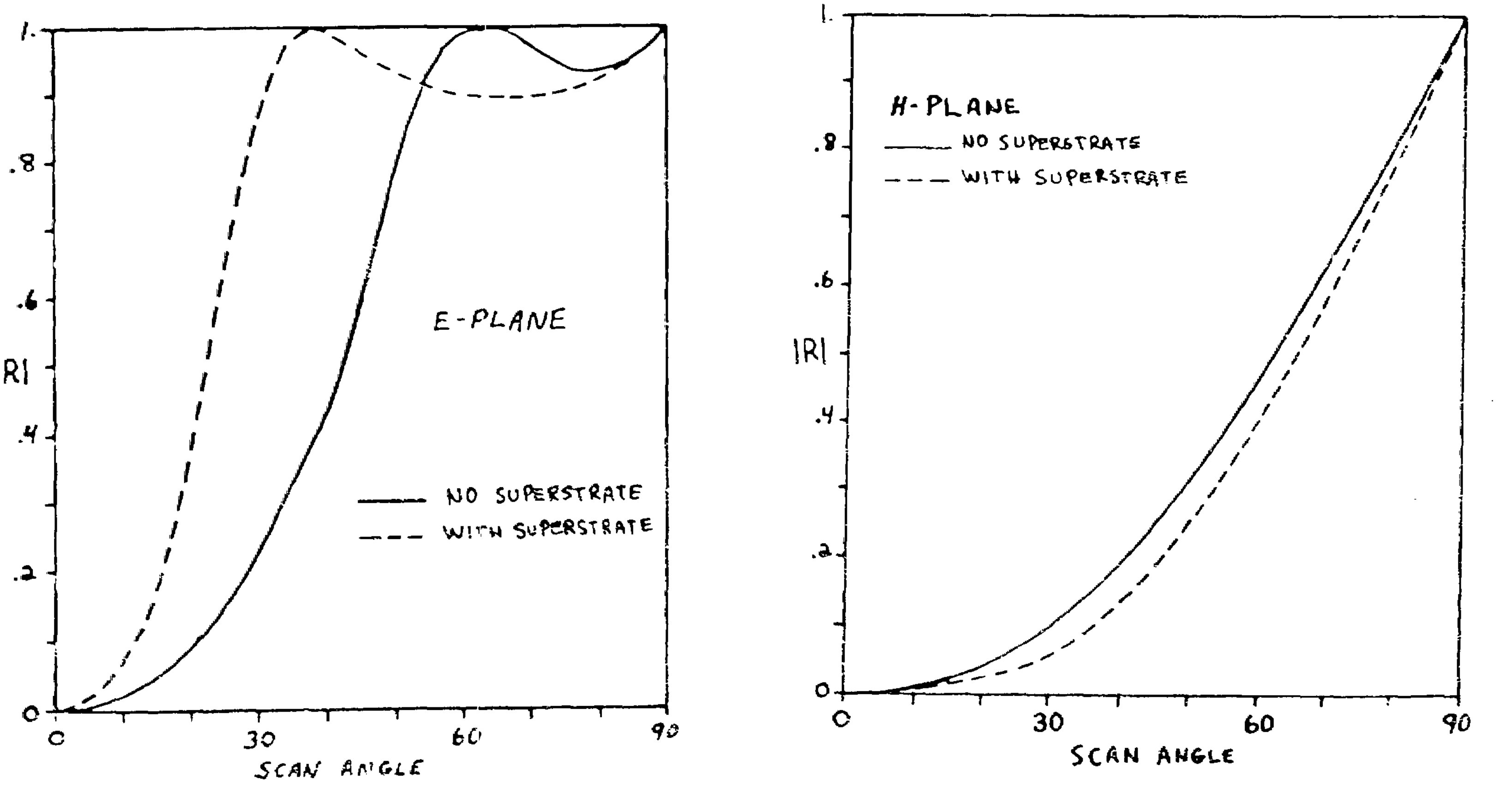

Figure 5. Reflection coefficient magnitude versus scan angle for an infinite array of printed dipoles, with a superstrate. Element spacing in both planes is $\lambda_o/2$. Substrate thickness = $0.05\lambda_o$, substrate dielectric constant = 12.8. Superstrate thickness = $0.05\lambda_o$, superstrate dielectric constant = 3.0.

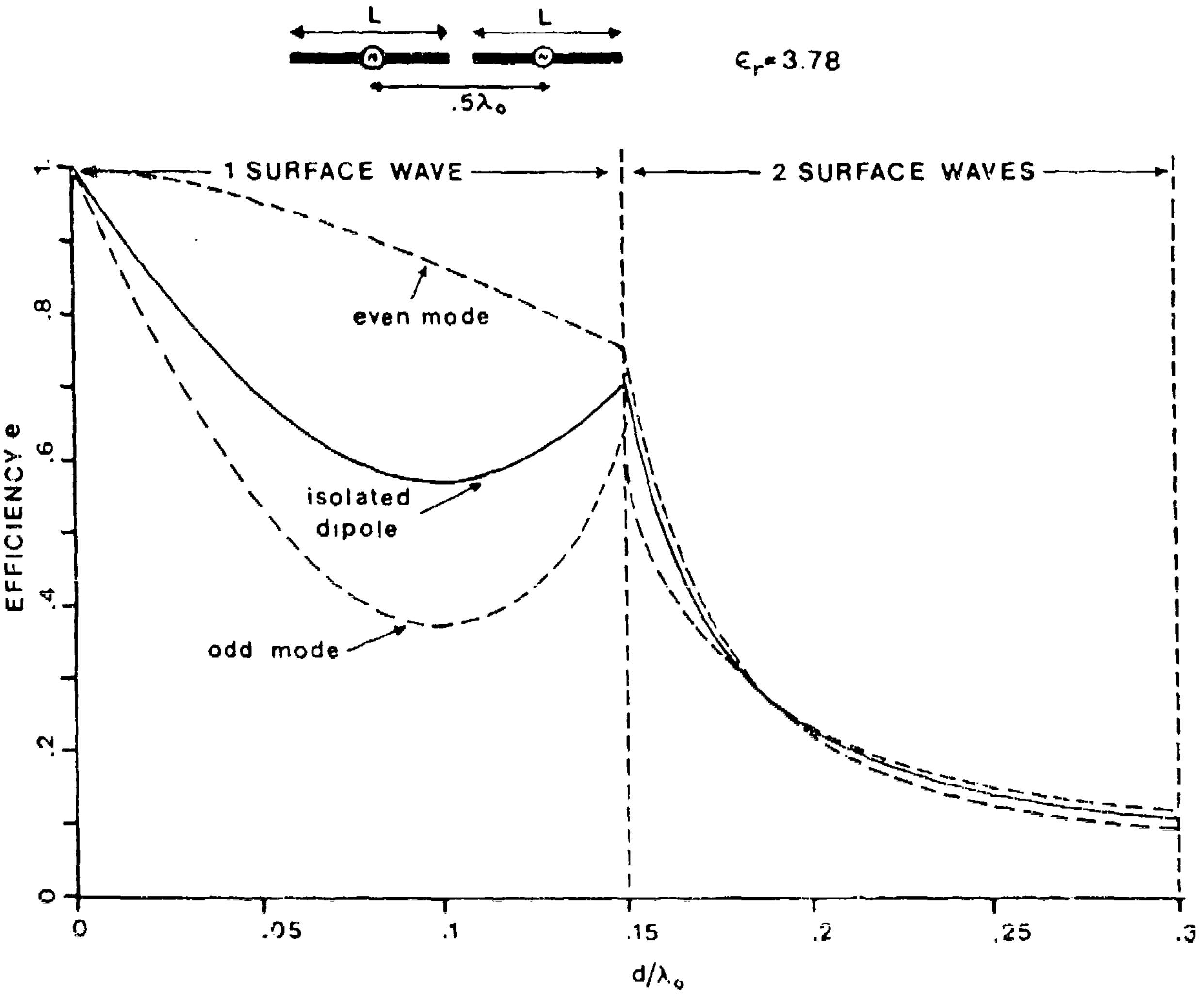

Figure 6. Efficiency (based on power lost to surface waves) of a two-element printed dipole array compared with the efficiency of a single dipole, versus substrate thickness.

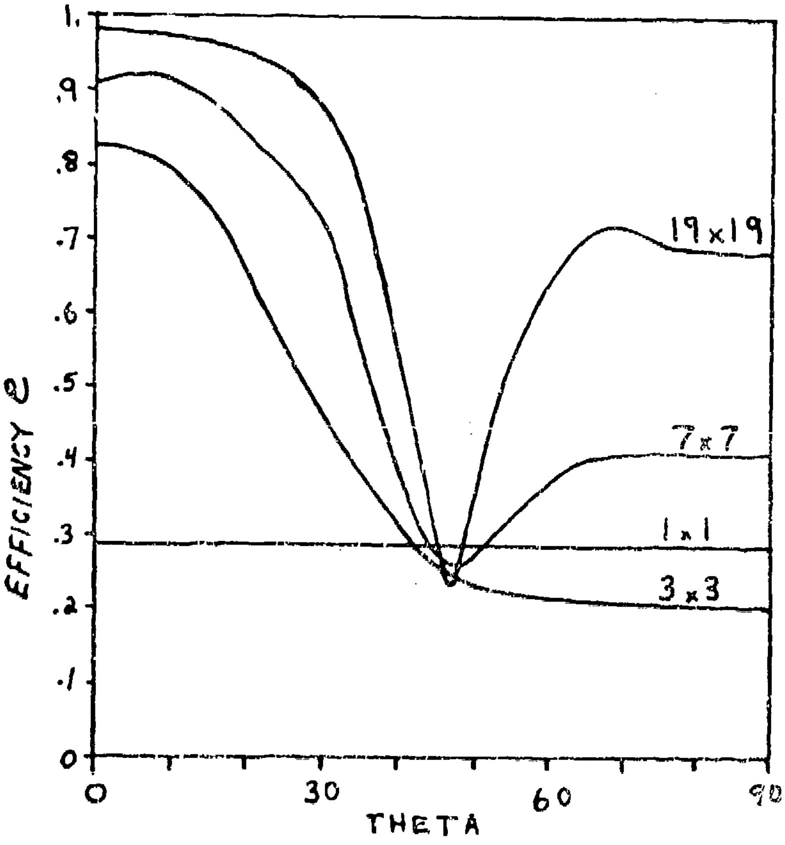

Figure 7. Efficiency (based on power lost to surface waves) of finite, square planar arrays of printed dipoles, versus E-plane scan angle. Element spacing in both planes is $\lambda_0/2$. Substrate thickness = $0.06\lambda_0$, dielectric constant = 12.8.

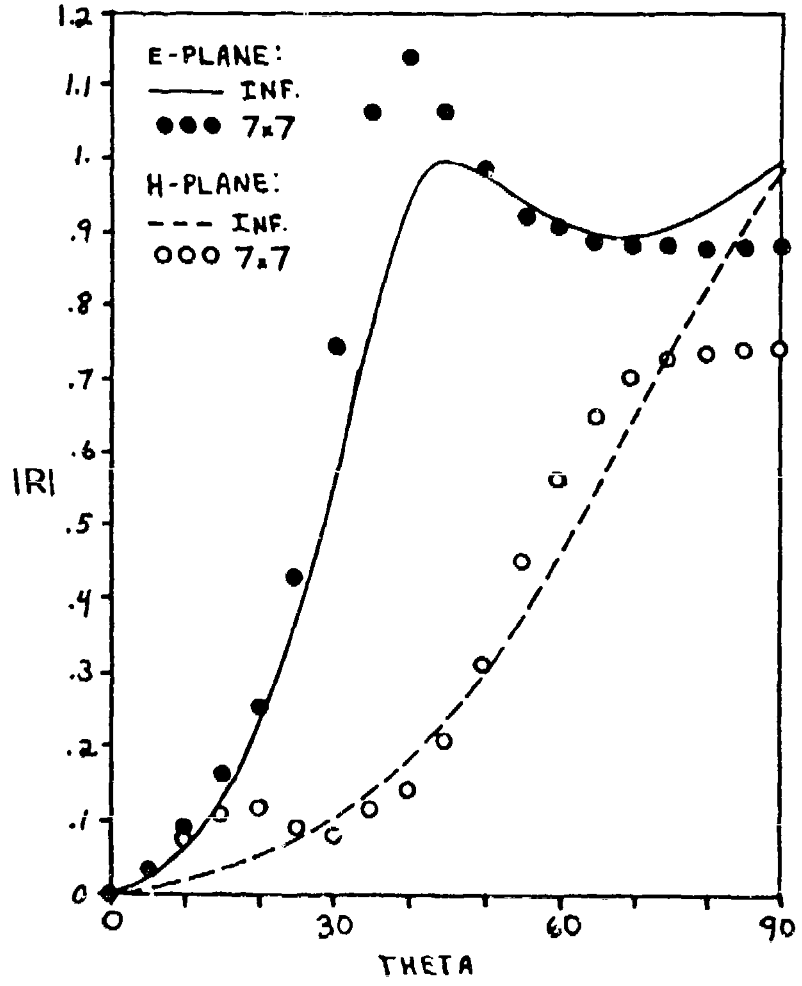

Figure 8. Reflection coefficient magnitude of a 7x7 printed dipole array (same geometry as Fig. 7) versus scan angle. Results are compared with an infinite array of the same geometry.

AN ACTIVE MICROSTRIP PHASED ARRAY
FOR SHF SATCOM APPLICATIONS

Brian C. Considine
RAYTHEON COMPANY Equipment Division, Wayland, MA

ABSTRACT

This paper describes an electronically steerable, left hand circularly polarized (LHCP), active, microstrip radiating aperture that operates over the 7250 MHz to 7750 MHz frequency band. It utilizes flush mounted construction techniques in which the various elements of the array are microwave printed circuits. The patch radiators are printed on teflon fiberglass and the circular feed/hybrid layer and the combiner layer are printed on duroid. In addition, row and column steering commands and bias signals are included in the bonded structure. The grid configuration and element spacing impact the microstrip combining network and vice-versa, hence, the design of the various layers of the antenna is interdependent.

The major features incorporated into this microstrip radiating aperture include the following:

a) increased radiator bandwidth;

b) minimization of radiation loss from the microstrip combiner circuit;

c) active matching of the radiator for the array environment over a 60° scan cone;

d) development of fabrication procedures for low-cost flush mounted array applications including modularization approaches to large array fabrication;

e) development of active receive modules employing monolithic microwave integrated circuits (MMIC); and

f) fabrication of an active array by incorporating the MMIC modules into the combiner layer.

Performance goals of -12 dB sidelobes at boresight (equal illumination), 20 dB gain, and 60° scan capability were demonstrated.

Array Description

A cross-sectional view of the array is shown in Figure 1. The array consists of a bonded multi-layer sandwich of five microwave and d.c. printed circuit boards. The entire assembly is bonded without the receive modules which are assembled after the layered structure is complete. Figure 2 shows the complete array.

The radiating element is comprised of two microstrip layers, a patch radiator layer, and a circularly polarized (CP) feed layer. One R.F. feed-thru per element connects the feed point to the corporate combiner. Plated thru-holes are used for the R.F. and d.c. interconnections. In all there are over 1100 plated thru-holes in the assembly, each passing through one or two ground planes.

Receive modules are set into the 1/16" thick spacer provided below the combiner layer to accommodate the module package. Ultimately modules will be fabricated co-planar with the combiner eliminating the spacer and decreasing the array thickness.

To make the design appropriate for general use, the element spacing was calculated such that the array can scan up to 60° from broadside. A triangular grid was used to minimize the number of elements for an array whose scan volume is a cone. The row spacing "d" to keep the grating lobe at the edge of real space is given by:

$$d = \lambda/(1 + \sin \theta_s) \qquad (1)$$

The element spacing calculated from the row spacing, and adjusted slightly to keep the grating lobe entirely out of real space, is 0.91 inch.

Antenna Element

The antenna element chosen for this application is the printed circuit or patch antenna. The element differs from the usual element in that there is a layer of dielectric covering the ground plane and part of the feed (the quadrature hybrid) is printed on the radiating side of the ground plane to maximize the space available for phase shifters on other layers of the antenna. The antenna element has an operational bandwidth of 500 MHz centered at 7.5 GHz. Because of tolerances on the dielectric constant of commercial dielectrics, the design bandwidth is about 600 MHz.

The bandwidth of a microstrip element is directly proportional to the substrate thickness. However, increasing the substrate thickness is undesirable as it enhances the coupling to the surface wave mode and increases the radiation of the feed structure adjacent to the patch. The mutual coupling to nearby antenna elements is directly proportional to the energy in e surface wave which may cause the element pattern notch, usually associated with the grating lobe, to occur at angles for which the grating lobe is far from real space. Uncontrolled feed structure radiation will degrade performance at some angles. For these reasons, it is desirable to minimize substrate thickness.

By adding a series tuned resonant circuit to the patch it is possible to increase the bandwidth, while at the same time significantly reducing feed radiation. The feed configuration shown in Figure 3 was determined empirically. A rigorous mathematical treatment of the element was not attempted but the empirical results were modeled.

Circular polarization is obtained by feeding the two linear ports of the antenna element with a quadrature hybrid packaged with the tuned circuit on the feed layer.

Element Measurements

Element impedance was measured for the isolated element, and in a waveguide simulator. Also, the active reflection coefficient was calculated from mutual coupling measurements in a 30 element array. In all cases, the impedance measurements were made at the input to the antenna feed without the quadrature feed that is normally located at that point. The maximum VSWR is about 1.6:1 over a 600 MHz band. Patterns measured on the isolated element in a large ground plane are shown in Figure 4. It is seen that the patterns are reasonable with the "E" plane pattern broader than the "H" plane pattern. These patterns are not significantly different than the isolated patterns of a waveguide type radiator so that similar performance in an array environment is probable.

Impedance data was also taken in a waveguide simulator. Data for the element in free space and in the simulator for two different scan angles are similar and fall within a 2:1 VSWR circle. These results are of interest because it appears that the good isolated element match leads to acceptable results when the element is tested in a simulator indicating that the element match in an actual array will also be acceptable.

Measurements in a Small Array

The measurements on the isolated patch and the patch in the simulator showed no unexpected results. However, sometimes, in the array environment, unusual effects occur. It was felt that some form of verification in a small array was necessary. A 30 element array was built and used to make pattern and mutual coupling measurements. The array was constructed at 'S'-band because of the availability of an element design and the non-critical nature of the assembly procedure.

Pattern Measurements

Patterns of a near central element were measured at 2.4, 2.5, and 2.6 GHz. The 2.5 GHz data is shown in Figure 5. The transmitting antenna radiated vertical polarization and a pattern was measured using the appropriate port on the patch. Then, the transmit antenna polarization was rotated 90° and the pattern measured using the other port on the patch. The ripples on the pattern appear to be due to the finite size of the ground plane. The gain difference is believed to be due to the ripples in the other plane. Measurements were also made for other rotations of the receive array and for other elements in the array. It was noted that, as expected, beamwidth varied inversely with increasing frequency. Also, no notches indicating array resonance were observed, and cross polarization was about 16 dB down.

The details of the pattern, such as the exact beamwidth and ripples, should be ignored since these could be changed significantly by varying the conditions at the ground plane edges. In summary, pattern measurements in the small array did not indicate any problems in the use of this element.

Mutual Coupling Measurements

Mutual coupling measurements were made on the 30 element array of Figure 5 and the active driving point impedance in the 'E' and 'H' planes was computed using the co-polarized coupling data. The results of this computation at an arbitrary reference plane is shown in Figure 6. Note that S_{11} has been set equal to zero. The reason for this is that previous data indicated that a good isolated element match is a reasonable choice for a good match in the array. By setting $S_{11} = 0$ and plotting the active impedance, the magnitude of the error in this assumption is easily seen. From cross polarization coupling measurements, it was noted that S_{11} should be about 0.2 at midband to optimize the impedance at 45°. Hence, the isolated element match is a good starting point in the design procedure.

To estimate the magnitude of the coupling from the cross-polarized elements, the mutual coupling between all horizontally polarized inputs to one vertically polarized input was measured making no assumptions of symmetry (for co-polarized coupling there is symmetry between the first and third quadrants and also between the second and fourth quadrants). The magnitude of the voltage coupled to the vertically polarizer port as a function of scan angle in sine space was measured and plotted.In the principal planes, the maximum coupling is 0.11 volts and is less than 0.1 volts over most of the scan volume of interest. Hence, a reasonable estimate of the driving point impedance can be obtained by measuring only co-polarized coupling.

In estimating the performance of a phased array, it is desirable to know, among other things, the power reflected back into the terminals. Even though the cross-polarized component is not a major contributor, a complete set of measurements was taken at midband so that the total reflection from the two feed points of the element could be determined assuming that the horizontally polarized arms were driven in phase quadrature with the vertically polarized arms. The results of these measurements and computations indicate that the reflected power is 11% of the incident power at θ = 0° and typically below 13% over the 60° scan volume.

R.F. Power Combiner Network

The R.F. power distribution network combines all of the array module outputs into a single port. The combiner requirements are that equal path lengths to all elements be maintained and the circuit loss and area be minimized. Calculations of copper loss, dielectric loss, and radiation losses were made for various substrate materials and thicknesses. Choice of the transmission line was based on minimization of loss.

A reactive power combiner was designed because it requires less area than an isolated power combiner. It is also considerably less expensive and allows the system noise temperature to be slightly less than with an isolated combiner. However, in the event of a failure of one of the modules such that it looked like a high mismatch, a reactive power combiner is affected much more than the isolated type.

The array feed network is actually two 1:64 combiners as shown in Figure 7. The basic building block is a 1:16 combiner that is replicated 8 times. Measured performance of the 1:16 combiner is given in Table I.

TABLE I. 1:16 Combiner Performance

Amplitude error:	-	0.45 dB rms
Phase error:	-	3° rms
VSWR:	-	1.22:1 max.
Insertion Loss:	-	0.45 dB ave.

Receive Module

The module is shown schematically in Figure 8 and described in Reference 7. The limiter and biasing circuitry utilize conventional components on an Epsilam-10 substrate. The phase shifter and LNA are MMIC circuits grown on 4 mil thick gallium arsenide. The module package is Kovar with glass/Kovar bias feeds and 50 ohm R.F. input and output feed lines. GaAs interconnections are made with 1 mil gold wire thermocompression bonded, while the Epsilam-10 substrate and conventional devices are soldered with solders of various melting points in a specified assembly order. Figure 9 is a photograph of a typical module.

The phase shifter for the SHF receive module is a three-bit monolithic design grown on 4 mil gallium arsenide. The circuit uses a loaded line design for the 45° bit and a hybrid coupled design for the 90° and 180° bits, with all R.F. lines in microstrip. Power FET's are used as switching devices in all three bits as shown in the schematic. Frequency range of operations is 7.25 to 7.75 GHz. The chip size of all bits is .030" x .185", giving the phase shifter a size of .240" x .185".

Test of the individual bits from breadboard wafers yielded the following results. Phase shift accuracies of + 5° per bit over an 800 MHz band were measured with VSWR < 1.5:1 for each bit. Insertion loss of the individual bits was in the order of 1 to 2 dB.

A single stage monolithic GaAs FET amplifier was designed and fabricated using 1 micron gate FET's monolithically grown on 4 mil GaAs. Performance is in good agreement with the design goals of 7.0 dB gain and 3.5 dB noise figure over the SHF frequency band. The amplifier uses a Raytheon type 832 low noise FET having a 1 μm gate length and a 0.5 mm periphery. Distributed element R.F. matching circuits were grown on the GaAs chip with the FET. The design was optimized for maximum gain using CAD techniques.

Although selected modules demonstrated 10° phase shift accuracies with 0 dB insertion loss, in order to fully populate the 128 element array with these state-of-the-art MMIC devices, much larger errors were tolerated. Typical modules average 2 dB of insertion loss at midband with up to 15° phase errors per bit.

Beam Steering Unit

The beam steering unit (BSU) uses a TRS-80 model III personal computer. Steering commands for the array are computed in the TRS-80 and data is output via the line printer to an interface network that buffers, multiplexes, and converts the pulse train from TTL to CMOS logic required by the phase shifter drivers. Steering the antenna is accomplished by inputting the frequency and the two beam pointing angles (azimuth and elevation) desired. The TRS-80 then computes Δx and Δy, the incremental row and column phase differences given by the equations:

$$\Delta x = 2\pi/\lambda \ dx \sin \theta_0 \cos \emptyset_0$$

$$\Delta y = 2\pi/\lambda \ dy \sin \theta_0 \sin \emptyset_0$$

where dx and dy are the element spacings in the rows and columns, and $\emptyset_0$ and θ_0 are the azimuth angle and angle from the zenith. The SHF array is actually two 64 element arrays, each having 8 rows and 16 columns because of the triangular array grid. Thus, there are 48 row and column angles computed from the phase differences (Δx and Δy) which are then quantized into 22.5° increments.

The phase shifter drivers utilize CMOS logic because -10 volts d.c. is required to pinch off the FET's used in the phase shifters in one bias state, the second (ungated-on) bias state being 0V d.c. The TRS-80 produces a TTL, 0 to +5V d.c., output pulse train. The interface board consists of a parallel input 4-bit down counter, 1 to 48 multiplexer, and 48 TTL-to-CMOS converters to provide the proper pulse train for the drivers.

The drivers consist of a counter to count the row and column pulse train and a buffer so that a new beam position can be loaded while the antenna is being used. The TRS-80 limits the rate at which beam positions can be changed to about 250 millihertz (one every 4 seconds). The CMOS drivers can run at a clock rate of up to 4 MHz, limiting the beam switching rate to one every 500 µsec (2 KHz rate). The buffer output sets the R.F. downtime to 100 microseconds per beam position change.

Antenna Tests

Two 128 element arrays were fabricated during the program. Both arrays were identical except that one was completed with 50 ohm lines in place of the receive modules in the combiner layer. This assembly is referred to as the "breadboard" array. The second array was completed with modules, drivers, and the BSU and is the deliverable ADM receive-only array.

Antenna tests were conducted on both 128 element arrays. The breadboard array, being non-steerable, was used to confirm the array design at boresight while the receive modules were being assembled in the ADM array. Linear and CP radiation patterns were recorded for 64 element and 128 element arrays over the SHF band. In addition, gain and input VSWR were measured.

Gain

Aperture gain, calculated as the gain of the individual patch multiplied by the number of patches, is 23.7 dB for the full array. Array losses including all combining, VSWR, and feed line losses totalled 2.45 dB for the breadboard array. The measured gain to either linear polarization of the breadboard array was 21.45 dB compared to the calculated gain of 21.25 dB (23.7 - 2.45 dB). In the ADM array the gain measurement is complicated by the receive modules, whose gain and phase errors cause significant combining losses. At 7.25 GHz the measured gain is within 0.45 dB of the calculated gain, which includes the insertion loss and combining losses due to phase and amplitude errors in the modules.

Radiation Patterns

Radiation patterns were recorded for linear vertical, linear horizontal, and circular polarization for the 128 element array as well for each 64 element subarray for both the breadboard and ADM configurations. Patterns were recorded at 7.0, 7.2, 7.25, 7.5, and 7.75 GHz. In addition, beam steering was demonstrated and patterns recorded for random steering angles with the ADM array.

Figure 10 shows the one way radiation patterns of the two 64 element breadboard subarrays for horizontal linear polarization at 7.25 GHz. Peak sidelobe levels are -12 dB, as epxected given the uniform illumination function, and the 3 dB beamwidth of 12.5° is correct. Note the 2° offset between beams 1 and 2. This is due to the fact that the centers of the small arrays are separated by a finite distance and the patterns were recorded in a short (16')anechoic chamber. Figure 11 is the one way rotating linear (CP) radiation pattern of the combined 128 element breadboard array. The two 64 element arrays are combined via an equal phase 2:1 combiner. Beamwidth is 6.3°, peak sidelobes are -12 dB, and the axial ratio is 0.1 dB. Similar measurements over the frequency range show that the array exhibits the desired 500 MHz bandwidth with 1 dB axial ratio at the band edges.

Figure 12 is the one way radiation pattern of the full ADM array at boresight measured at 7.5 GHz with a horizontally polarized source. Both azimuth and elevation cuts are recorded. The peak sidelobe level is -9.5 dB and beamwidth is 6° for an azimuth cut. Note that the beamwidth nearly doubles in the elevation pattern as the projected aperture of the full array is decreased by almost a 2:1 ratio as it is viewed at 90°. The one way azimuth and elevation radiation patterns taken along the lattice axis of the rray, 60° to the linear polarization source, are shown in Figure 13. Peak sidelobe levels for this case are -13 dB or lower and the beamwidths are as expected, between 6° and 12°, a function of the projected aperture.

Beam steering was demonstrated with the full array as well as the 64 element arrays. Figure 14 is a one way radiation pattern at 7.5 GHz with the full ADM array scanned to 49.9° in azimuth and -11.5° in elevation. Peak sidelobe levels are -10 dB and the beamwidth is 12°. Figure 15 is a composite of beam steering experiments on subarray No. 1. Note that as the beam is successively steered in 10° increments, in azimuth, there is a gain loss on the peak of the beam. [For clarity sidelobes have been omitted from this figure. As expected the sidelobe levels continue to degrade the farther the beam is scanned.] Calculations were made using the exact module phase and amplitude errors in array No. 1 and the predicted beams are similar to the actual beams of Figure 15. Gain loss with scan from 3 to 8 dB was calculated while values of 4 to 10 dB were measured. Similarly the predicted sidelobe levels agreed reasonably well with measured values.

Acknowledgement

The author wishes to thank Messrs. C. Dahl, L. Parad, and D. Wandrei for their contributions to the array design and also to W. Hall and J. McStay for developing the necessary array fabrication and assembly techniques. This work was supported by Rome Air Development Center under Contract F30602-80-C-0066.

References

[1] Pucel, R. A., Masse, D. J., and Hartwig, C. P.,(1968) "Losses in Microstrip", IEEE Trans., Vol. MTT-16, pp. 342-350.

[2] Considine, B. C. and Wandrei, D. L.,(1982) "SHF SATCOM Microstrip Phased Array Antenna", Proceedings of the 1982 Antenna Applications Symposium, Sept. 22-24, 1982, Monticello, Illinois.

[3] Pucel, R. A., (1981) "Design Considerations for Monolithic Microwave Circuits", IEEE Trans., Vol. MTT-29, No. 6, June 1981, pp. 513-534.

[4] Cullen, A. L., (1954) "The Excitation of Plane Surface Waves", Proc. IEEE, Vol. 101, Part IV, pp. 225-234.

[5] Wood, C., (1981) "Analysis of Microstrip Circular Patch Antenna", Proc. IEEE, Vol. 128, Pt. 4, No. 2, pp. 69-75.

[6] Lewin, L., (1960) "Radiation from Discontinuities in Stripline", Proc. IEEE, Part C, Vol. 107, pp. 163-170.

[7] Considine, B. C. and Wandrei, D., (1983) "X-Band Receive Module Using Monolithic GaAs MMIC's", GaAs International Symposium. Oct. 1983.

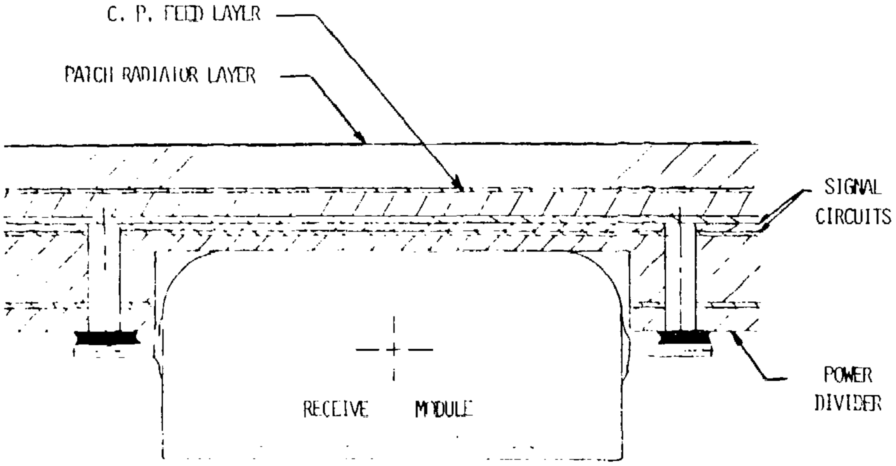

FIGURE 1. Array Cross Section

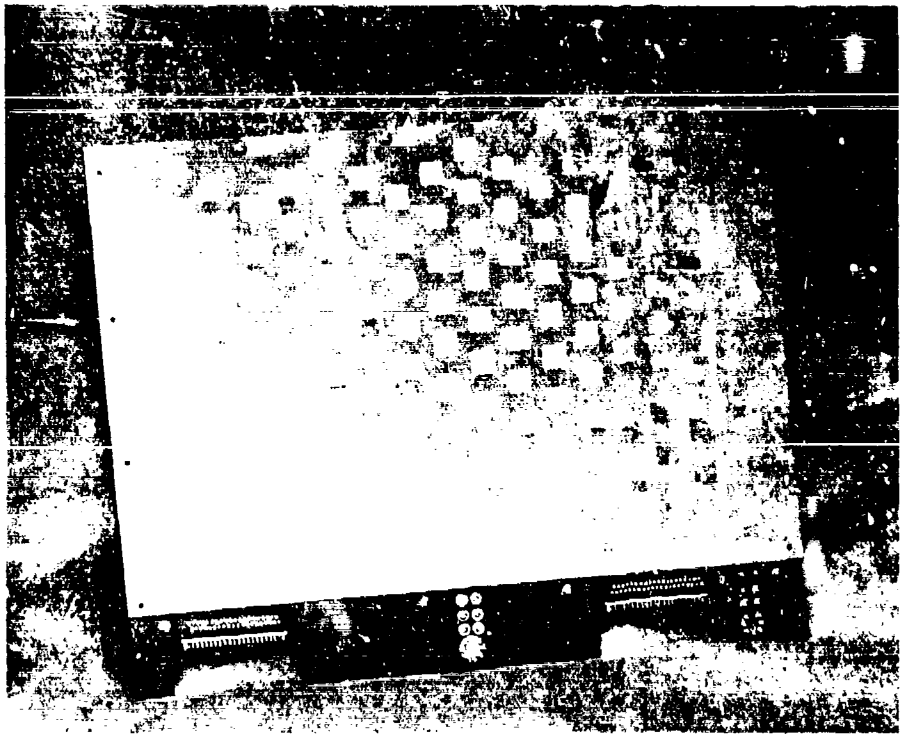

FIGURE 2. 128 Element Receive Array

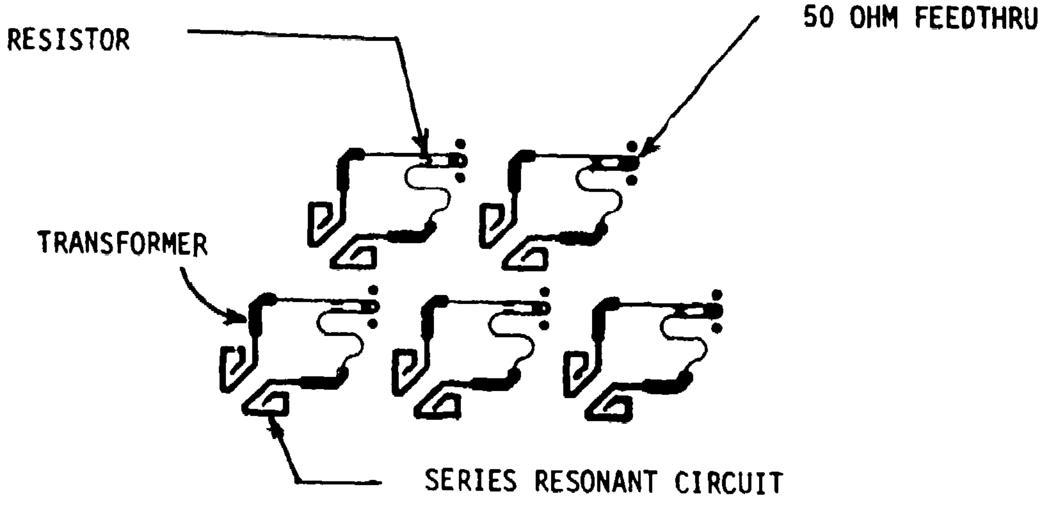

FIGURE 3. Quadrature Feed for Five Elements

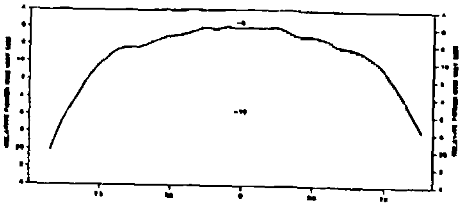

A.) ISOLATED E-PLANE ELEMENT

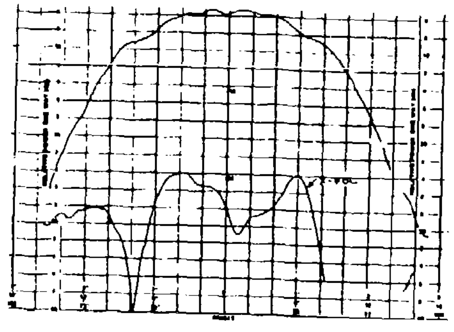

B.) ISOLATED H-PLANE ELEMENT

FIGURE 4. Patterns of 7.5 GHz Patch Radiator

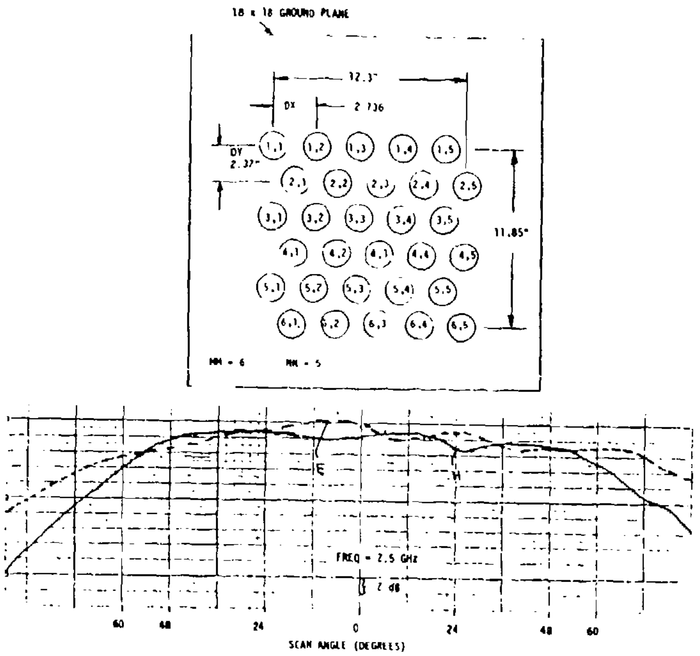

FIGURE 5. Pattern Measurement in Small Array

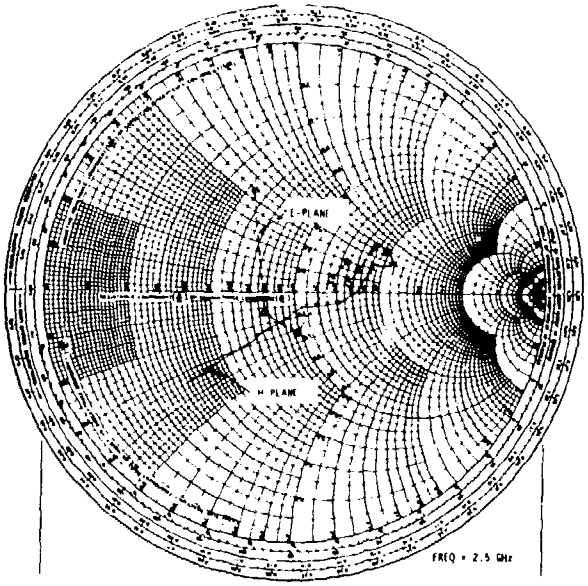

$S_{11} \equiv 0$ for Computations (Actually $|S_{11}| = 0.16$)

FIGURE 6. Active Principle Plane Impedance for Vertical Polarization

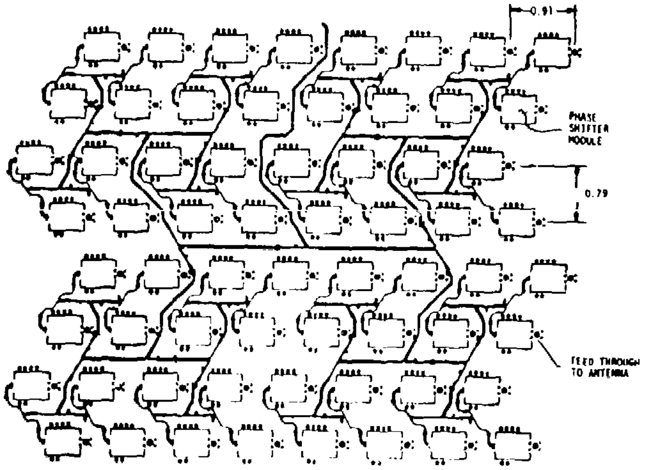

FIGURE 7. 64:1 Combiner Layer

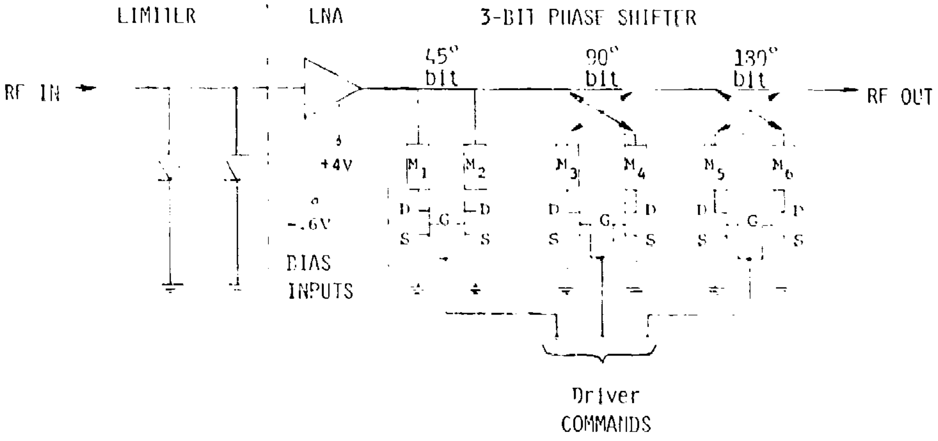

FIGURE 8. ADM Receive Module Schematic

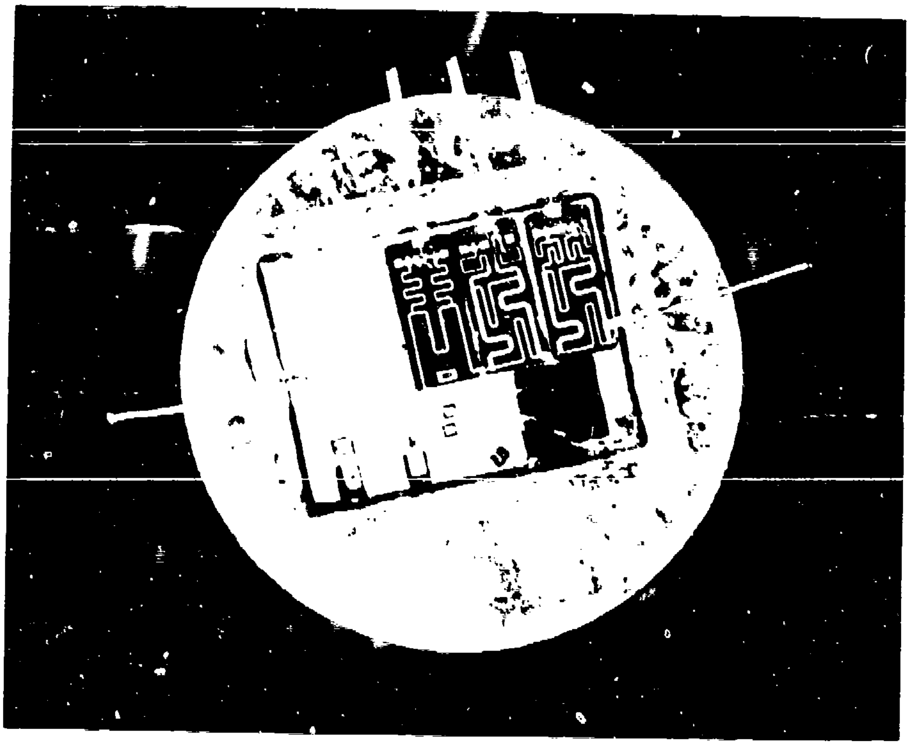

FIGURE 9. Receive Module

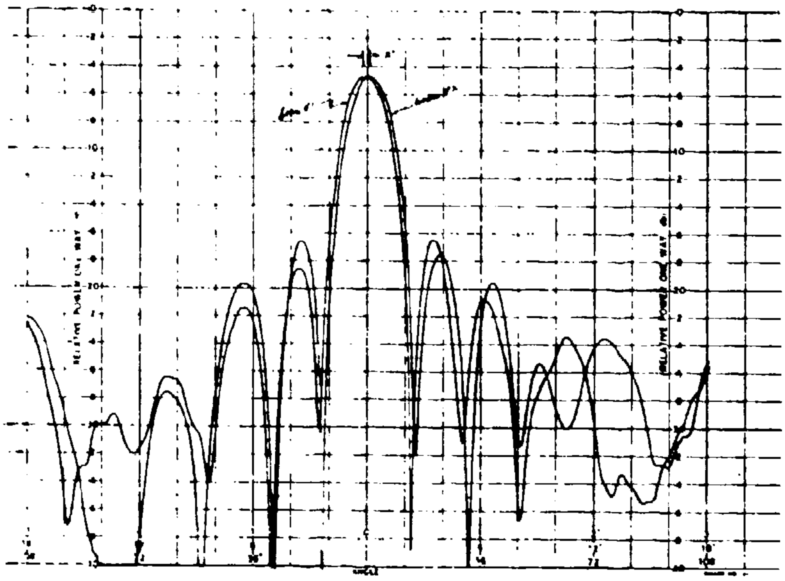

FIGURE 10. Horizontal Linear Radiation Pattern: Breadboard 64 Element Arrays

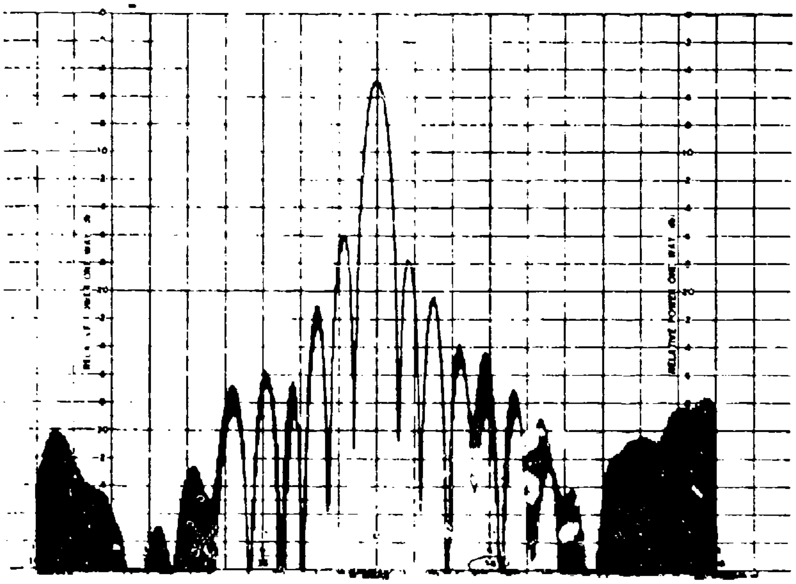

FIGURE 11. Rotating Linear (CP) Radiation Pattern Breadboard 128 Element Array

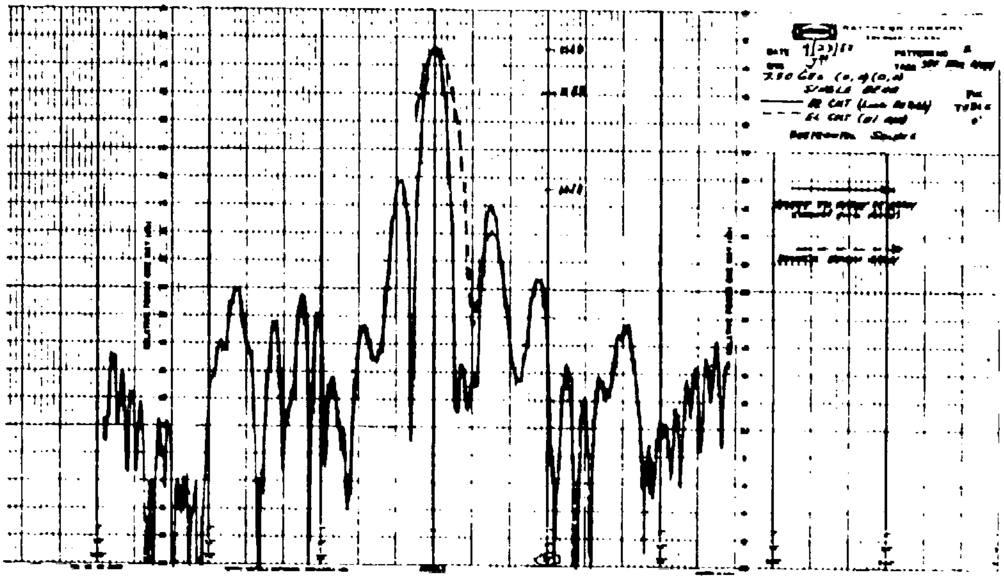

FIGURE 12. Horizontal Linear Radiation Patterns, Azimuth and Elevation. Full ADM Array

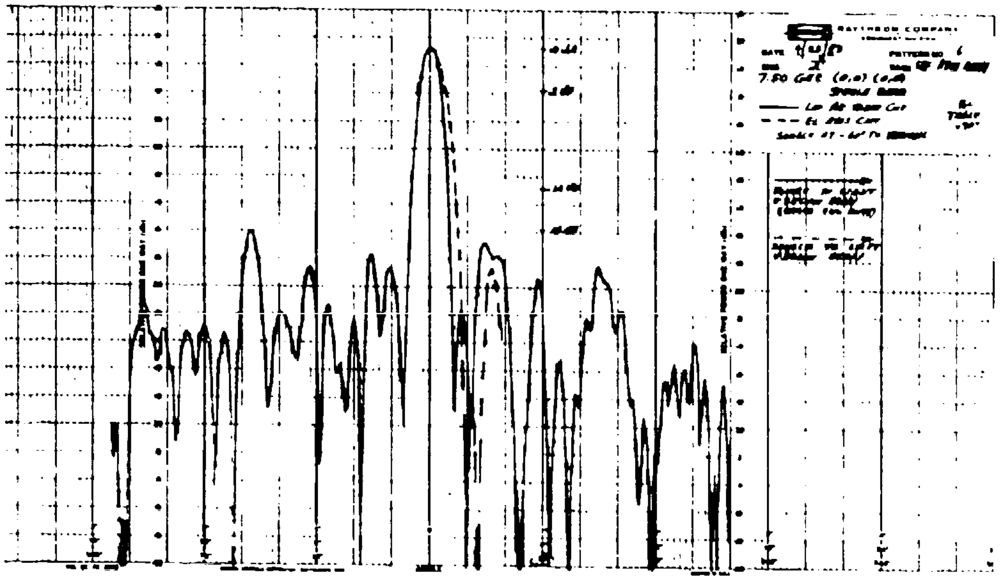

FIGURE 13. Linear Radiation Patterns, Source at 60° to Vertical. Full ADM Array

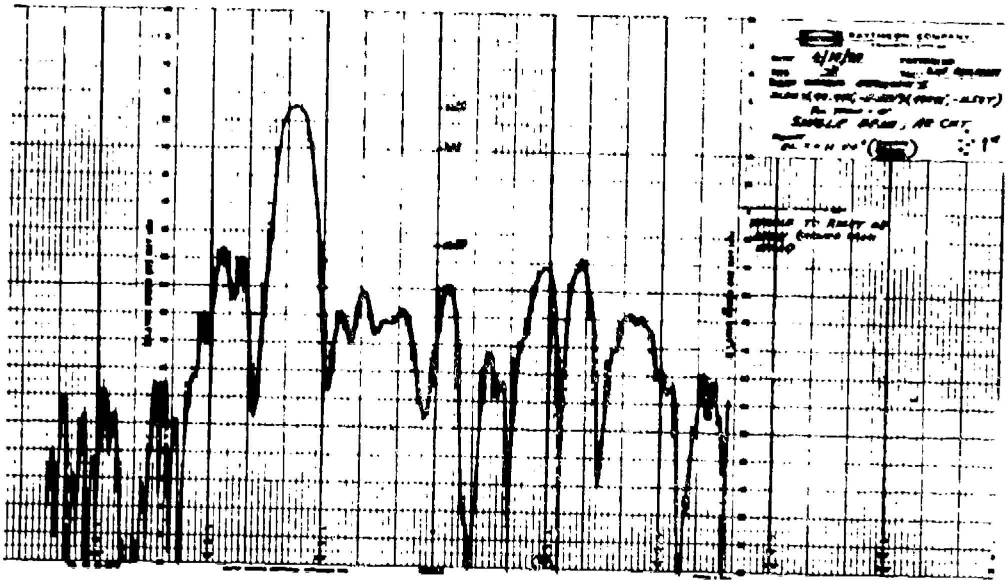

FIGURE 14. Linear Polarization: Beam Steered to 49.9° Azimuth, -11.5° Elevation. Full ADM Array

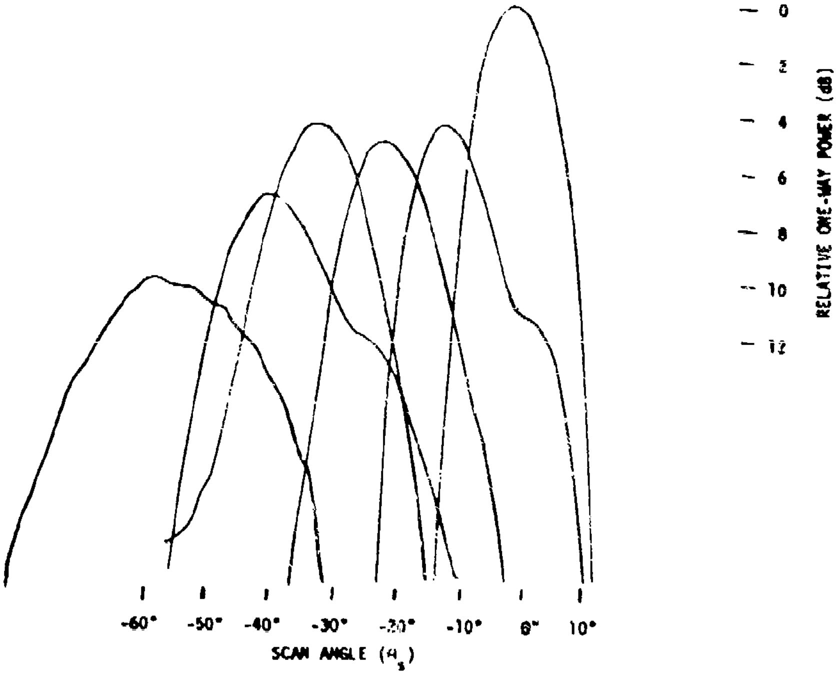

FIGURE 15. 64 Element ADM Array Scanned 0° to 60° in Azimuth

USING SPECTRAL ESTIMATION TECHNIQUES IN ADAPTIVE ARRAY SYSTEMS

William F. Gabriel

Naval Research Laboratory, Washington, DC

ABSTRACT

Improved spectral estimation techniques hold promise for becoming a valuable asset in adaptive processing array antenna systems. Their value lies in the considerable amount of additional useful information which they can provide about the interference environment, utilizing a relatively small number of degrees-of-freedom (DOF). The "superresolution" capabilities, estimation of coherence, and relative power level determination serve to complement and refine the data from faster conventional estimation techniques.

This paper discusses two conceptual application area examples for using such techniques; partially-adaptive low-sidelobe arrays, and fully-adaptive tracking arrays. For the partially-adaptive area the information is utilized for efficient assignment of a limited number of DOF in a beamspace constrained adaptive system in order to obtain a stable mainbeam, retention of low sidelobes, considerably faster response, and reduction in overall cost. These benefits are demonstrated via simulation examples computed for a 16-element linear array. For the fully-adaptive tracking array area the information is utilized in an all-digital processing system concept to permit stable nulling of coherent interference sources in the mainbeam region, efficient assignment/control of the available DOF, and greater flexibility in time-domain adaptive filtering strategy.

1.0 INTRODUCTION

Improved spectral estimation techniques are an emerging technology which derives largely from modern spectral estimation theory of the past decade and adaptive array processing techniques [1,2,3]. Coupled with the phenomenal advances in digital processing, these techniques are becoming a valuable asset for adaptive array antenna systems. Their value lies in the considerable amount of additional useful information which they can provide about the environment, utilizing only a relatively small number of degrees-of-freedom (DOF). For example, current spectral estimation algorithms can provide asympototically unbiased estimates of the number of interference sources, source directions, source strengths, and any cross-correlations (coherence) between sources [4,5]. Such information can then be used to track and "catalogue" interference sources, hence assign adaptive DOF.

These newer techniques are not viewed as a "superresolution" replacement for more conventional estimation methods such as mainbeam search, analogue beamformers, or spatial discrete Fourier transforms (DFT). Rather, the new technology is considered complementary to the other methods and best used in tandem. For example, "superresolution" techniques cannot compete with the speed of a DFT. Some comparisons of the various methods may be found described in the literature [3,5,6].

The purpose of this paper is to present two conceptual application areas for using spectral estimation techniques; partially-adaptive low-sidelobe antennas, and fully-adaptive tracking arrays. A partially adaptive array is one in which only a part of the DOF (array elements or beams) are individually controlled adaptively [7,8,9]. Obviously, the fully adaptive configuration is preferred since it offers the most control over the response of the antenna system. But when the number of elements or beams becomes moderately large (hundreds), the fully adaptive processor implementation can become prohibitive in cost, size, and weight.

The paper is divided into three principal parts. Section 2.0 discusses partially-adaptive, low-sidelobe antennas with the focus upon a constrained beamspace system; Section 3.0 considers source estimation and beam assignment from "superresolution" techniques; and Section 4.0 discusses an all-digital, fully-adaptive tracking array concept.

2.0 PARTIALLY-ADAPTIVE LOW-SIDELOBE ANTENNAS

The antenna system addressed in this section is assumed to be a moderately large aperture array of low-sidelobe design wherein the investment is already considerable and one simply could not afford to make it fully adaptive. The assumption of low-sidelobes (30 dB or better) is intended to give us good initial protection against modest interference sources and to reduce the problems from strong sources, i.e., in regard to the number of adaptive DOF required and the adaptive dynamic range of the processor. Thus, retention of the low sidelobes is considered a major goal in our adaptive system. In the discussion to follow, it is shown that using improved spectral estimation techniques in such a system can result in the following benefits over a fully adaptive array system:

a. Reduction in overall cost because relatively few adaptive DOF are implemented.

b. Simple adaptive weight constraints permit minimal degradation of both the mainbeam and sidelobe levels.

c. Reduction in computation burden.

d. Considerably faster adaptive response.

e. Compatible with a larger number of adaptive algorithms, including even analogue versions.

f. Greater flexibility in achieving a "tailored" response due to greater information available.

On the negative side, a partially-adaptive system can never be guaranteed a cancellation performance equal to that of a fully adaptive array and, in addition, will deteriorate abruptly in performance when the interference situation exceeds its adaptive DOF. These risks are an inherent part of the package and must be carefully weighed for any specific system application.

2.1 A Low-Sidelobe Eigenvector Constraint. We begin this section by reviewing that unconstrained adaptive arrays can experience very "noisy" sidelobe fluctuations and mainbeam perturbations when the data observation/integration time is not long enough, even though the quiescent mainbeam weights are chosen for low sidelobes. Consider the simple schematic shown in Fig. 1, and let us compute the complex adaptive element weights W_k from the well-known Sample Matrix Inverse (SMI) algorithm [9,10]. Expressed in convenient matrix notation,

$$\underline{W} = \mu \underline{\hat{R}}^{-1} \underline{S}^{*} \qquad (1)$$

where $\underline{W}$ is the adaptive weights vector,

$\underline{\hat{R}}$ is the sample covariance matrix,
$\underline{S}^*$ is the quiescent mainbeam weights vector, and μ is a constant.
$*$ denotes the conjugate of a complex vector or matrix.

Furthermore, compute the sample covariance matrix via the simple "block" average taken over N snapshots,

$$\underline{\hat{R}} = \frac{1}{N} \sum_{n=1}^{N} [\underline{E}(n)\underline{E}(n)^{*t}] , \qquad (2)$$

where $\underline{E}(n)$ is the element signal data vector received at the nth time sampling. The data observation/ integration time in (2) is the parameter, N. If $\underline{\hat{R}}$ is estimated over a lengthy observation time, like thousands of snapshots, then the sidelobe fluctuations from $\underline{W}$ updates will be relatively small. However, practical system usage often demands short observation times on the order of hundreds of snapshots or even less.

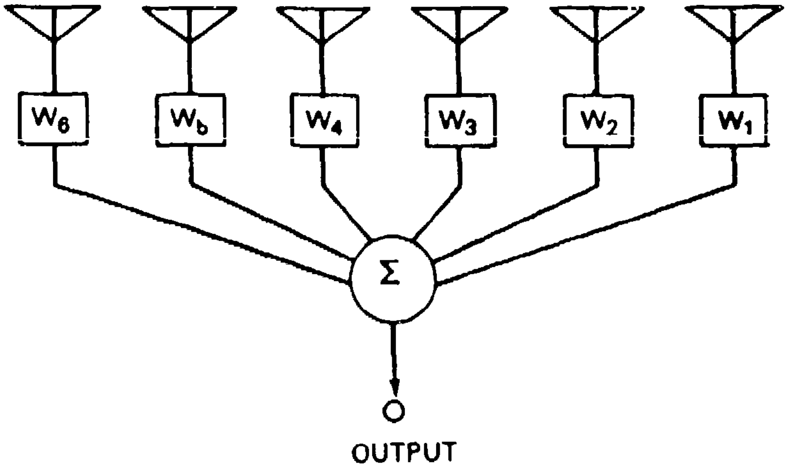

FIGURE 1 - Schematic of Adaptive Array

Figure 2 illustrates typical adapted pattern behavior for independent estimates of $\underline{R}$ using N=256 snapshots per update for the case of three 30 dB non-coherent sources located at 14, 18, and 22 degrees. The antenna aperture chosen for this example is a 16-element linear array with half-wavelength element spacing and a 30 dB Taylor illumination incorporated in $\underline{S}$*. Note that the adaptive algorithm maintains the mainbeam region and successfully nulls out the interference sources, but that it also raises the sidelobe levels elsewhere. The adaptive patterns are in continual fluctuation in the sidelobe regions and may exceed the quiescent sidelobe level by a considerable margin. Also, the mainbeam suffers a significant modulation which would degrade tracking performance. These effects worsen as the value of N decreases.

To understand the reason for this undulating pattern behavior, it is helpful to analyze the optimum weights in terms of eigenvalue/eigenvector decomposition. Reference [11] contains a derivation of such a decomposition for Eq. (1), and we reproduce here Eq. (34) from that report,

$$\underline{W} = \mu' \left[\underline{S}^* - \sum_{i=1}^{K} \left(\frac{\beta_i^2 - \beta_o^2}{\beta_i^2} \right) \alpha_i \, \underline{e}_i \right] \qquad (3)$$

where $\alpha_i = \underline{e}_i^{*t} S^*$ and $\mu' = \mu/\beta_o^2$

t denotes the transpose of a vector or matrix. The β_i^2 and $\underline{e}_i$ are the eigenvalues and eigenvectors, respectively, of the sample covariance matrix, and β_o^2 is equal to receiver channel noise power level. Equation (3) shows that $\underline{W}$ consists of two parts: the first part is the quiescent mainbeam weight $\underline{S}^*$; the second part, which is subtracted from $\underline{S}^*$, is a summation of weighted, orthogonal eigenvectors. This is a clear expression of the fundamental principle of pattern subtraction which applies in adaptive array analysis [9,12].

We introduce the term "principal eigenvectors" (PE) to mean those eigenvectors which correspond to unique eigenvalues generated by the spatial source distribution; and the term "noise eigenvectors" to mean those eigenvectors which correspond to the small noise eigenvalues generated by the receiver channel noise contained in the finite $\underline{R}$ estimates. The PE are generally rather robust and tend to remain relatively stable from one data trial to the next, whereas the noise eigenvectors tend to fluctuate considerably because of the inherent random behavior of noise. This difference in behavior is illustrated in Fig. 3 for the three source case described above, wherein there are three PE and thirteen noise eigenvectors associated with each $\hat{\underline{R}}$ estimate. Figure 3a shows the stability of the three PE for nine trials, and Fig. 3b shows the random behavior of typical noise eigenvectors for the exact same trials. Thus, we would expect that the sidelobe undulations in Fig. 2b are associated primarily with the noise eigenvectors. This thesis is verified in Fig. 4, which illustrates the adapted patterns resulting from Eq. (3) when only the PE are subtracted.

The above adaptive array pattern behavior leads to the following observations for source distributions which do not encroach upon the mainbeam and involve a small number of the available degrees-of-freedom:

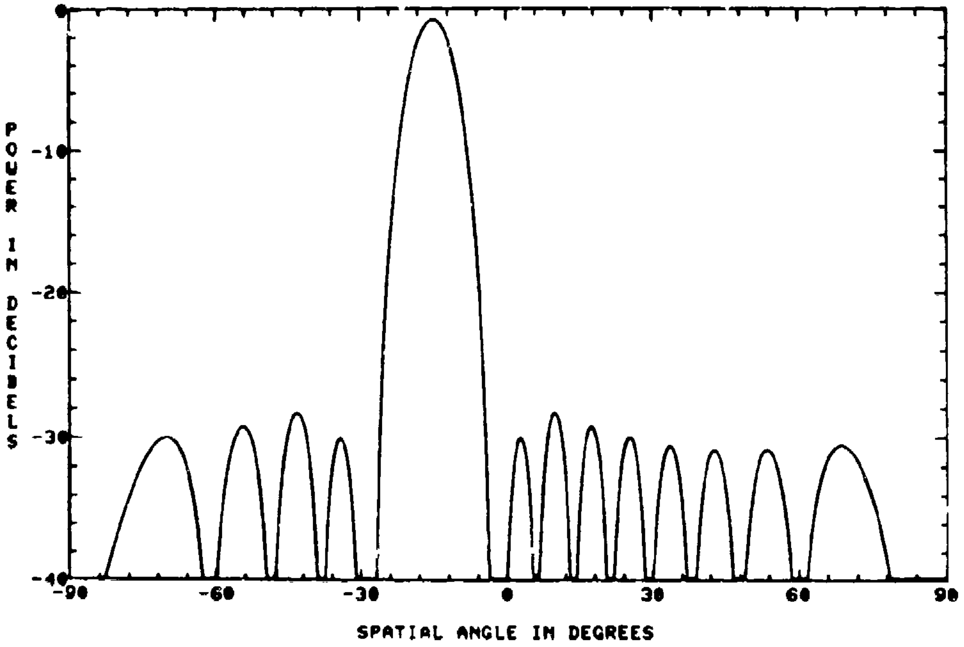

(a) Quiescent Mainbeam pattern, 30 dB Taylor weighting.

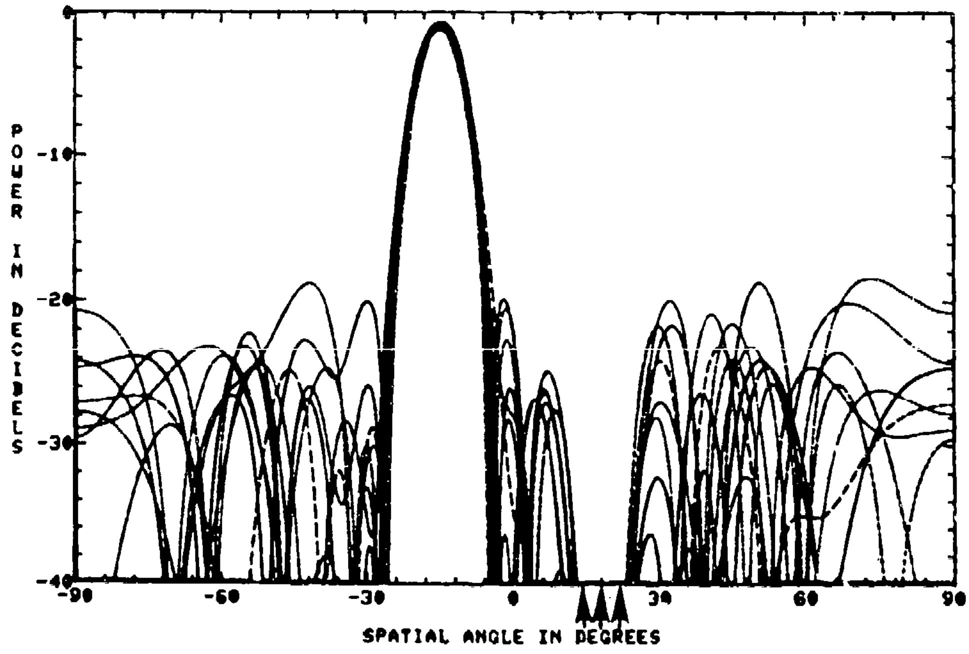

(b) Typical adapted patterns, nine update trials plotted.

FIGURE 2 - Fully adaptive 16-element linear array, SMI algorithm with $\hat{\underline{R}}$ estimated from 256 snapshots per update, three 30 dB non-coherent sources located at 14, 18, and 22 degrees.

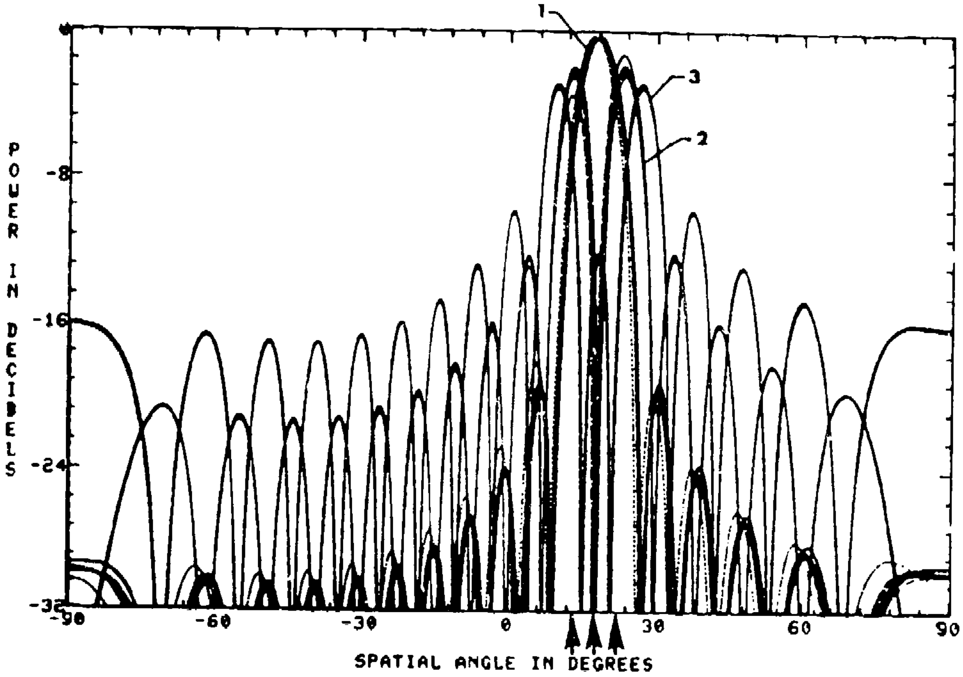

(a) Principal eigenvectors (PE) Nos. 1, 2, and 3.

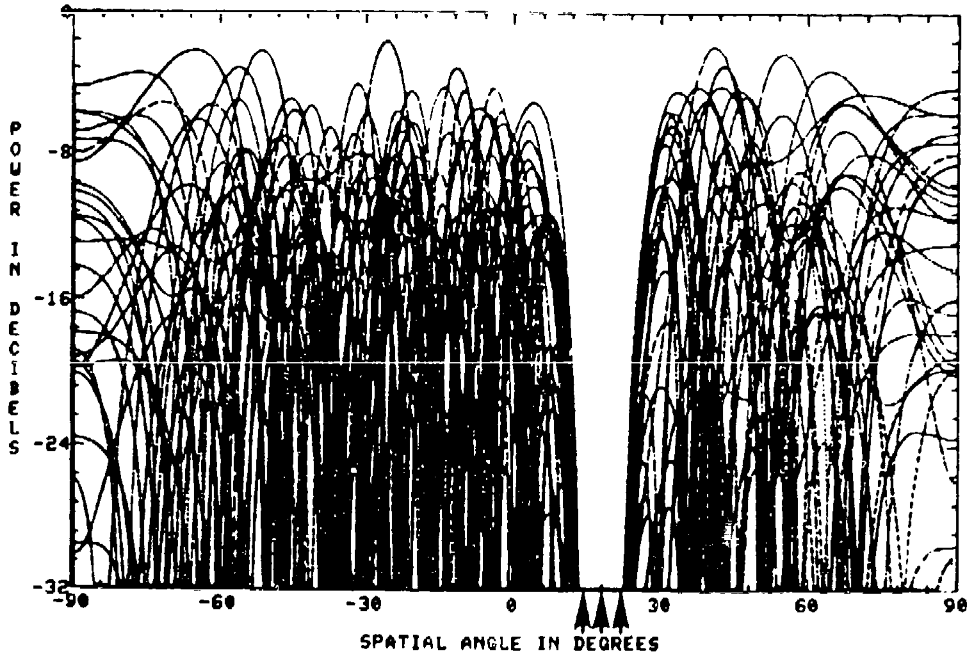

(b) Typical noise eigenvectors Nos. 4, 10, and 16.

FIGURE 3 - Plots of principal eigenvectors (PE) and noise eigenvectors computed from $\underline{\hat{R}}$ estimates associated with the three-source case of Fig. 2, nine update trials.

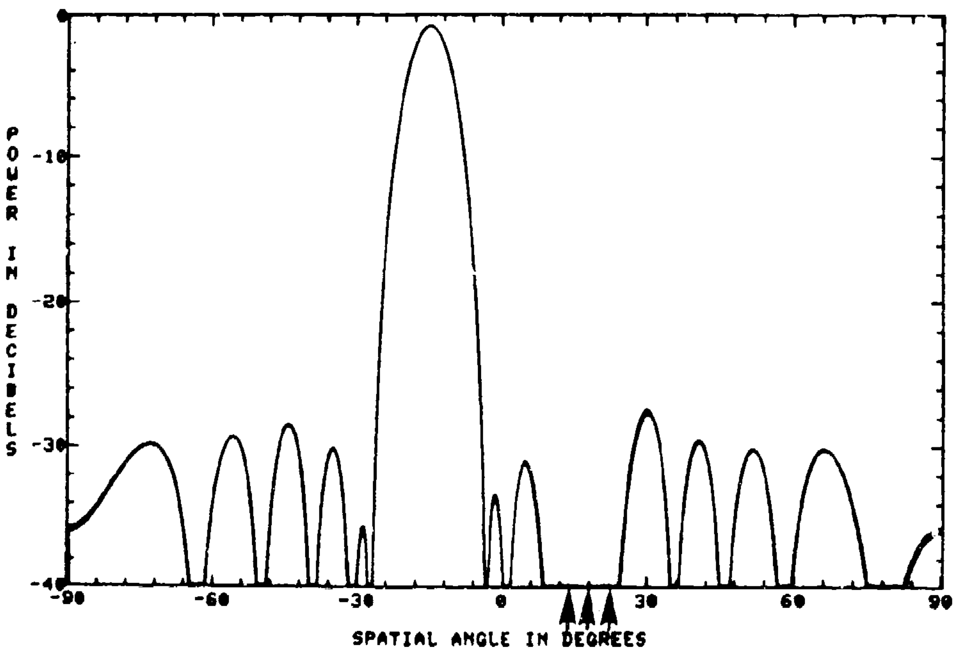

FIGURE 4 - Typical adapted patterns resulting from the constraint of utilizing only the PE, three-source case of Fig. 2.

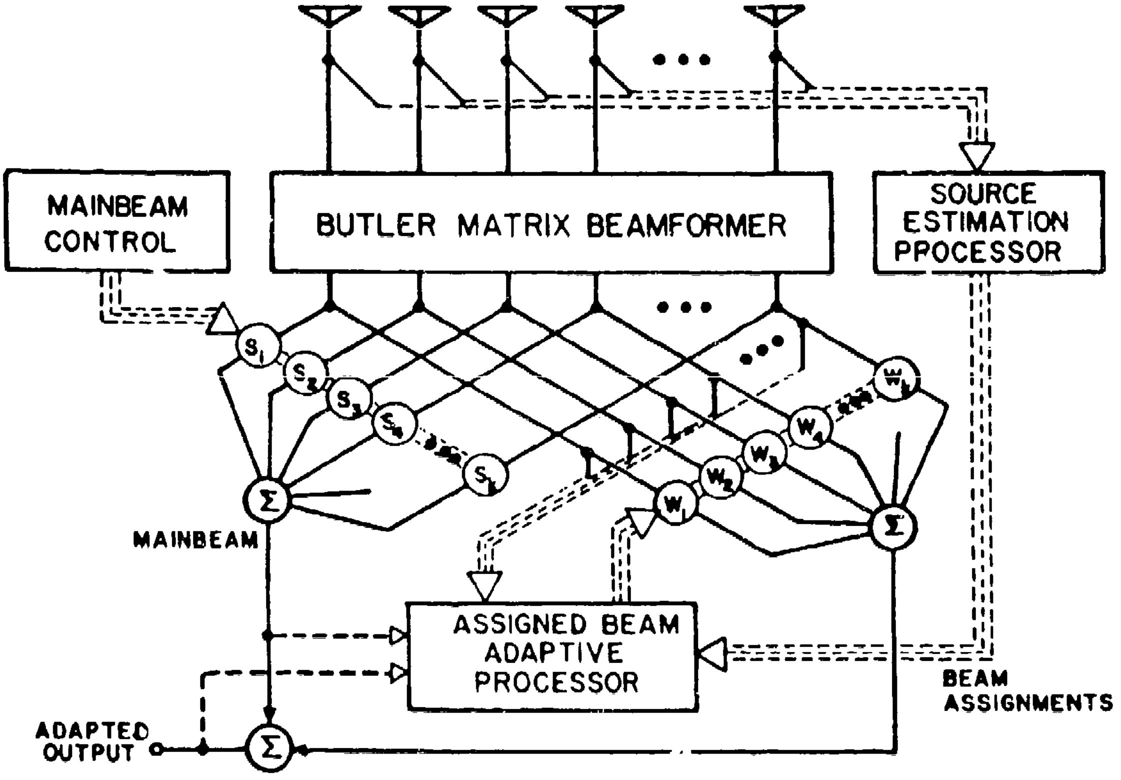

FIGURE 5 - Beamspace Adaptive Array with a separately weighted mainbeam.

1. It is possible to retain low sidelobes in the adapted patterns, even with short observation times, by constraining our algorithm (3) to utilize only the PE. The weight solution is unique and therefore stable.

2. Utilizing only the PE is tantamount to operating our adaptive system in beamspace (as opposed to element space) with a set of weighted orthogonal canceller beams.

3. The fully adaptive array automatically forms and "assigns" its PE canceller beams to cover the interference source distribution, with one beam per each DOF needed.

Therefore, we have set forth a low-sidelobe eigenvector constraint algorithm for this type of restricted interference situation.

2.2 Low-Sidelobe Constraints for a General Beamformer. Consider next a more interesting configuration shown by the schematic diagram of Fig. 5, where we represent an adaptive array system operating in beamspace so as to have available some pre-adaption spatial filtering. Applebaum and Chapman [8,9,13] first described beamspace systems of this type, utilizing a Butler matrix beamformer wherein the vector of beamformer outputs, $\underline{E}$, may be expressed,

$$\underline{\dot{E}} = \underline{B}^t \, \underline{E} \qquad (4)$$

where $\underline{B}$ is a KxK matrix containing the beamformer element weights. Other descriptions of beamspace systems are also available in the literature [9,14,15,16], of which Adams et al [15] is particularly germane to our discussion. Chapman [8] pointed out that when utilized in a partially adaptive configuration, such beamspace systems are susceptible to aperture element errors and cannot arbitrarily compensate the random error component of their sidelobe structure. This makes it necessary to control element errors in accordance with the quiescent mainbeam sidelobe level desired, and fits into our initial assumption of low-sidelobe design mentioned earlier. A separate weighted mainbeam summing is indicated which may be obtained either by coupling into the beamformer outputs as shown, or by coupling off from the elements and providing suitable phase shifters for steering plus a corporate feed network. Our purpose here is to examine the sidelobe performance of such a partially-adaptive beamspace system in which element errors are kept low and beamformer beams are subjected to simple constraints.

Spatial estimation data on the interference source distribution shall determine which beamformer beams are to be adaptively controlled. Such beams are defined herein as "assigned" beams, and the idea is to assign only enough beams to accommodate the DOF required by the source distribution. Whenever the two are equal, the adaptive weight solution is unique and we avoid adding any extra "noisy" weight perturbations. The reader will recognize that we are attempting to replace the PE beams of the previous section (2.1) with assigned beams from our general beamformer. Thus, we are defining a partially-adaptive array which will utilize only a relatively small number of its available DOF. In addition to this assigned beam constraint, we seek to limit the adaptive weights of assigned beams to a maximum level, γ, chosen to exceed the mainbeam sidelobe level by only a few dB. This prevents an excessive rise in adaptive sidelobe level, including the condition where the number of assigned beams exceeds the DOF required. Υ actually represents the product of assigned beam gain and adaptive weight magnitude, such that we have the option of working with beamformer beams which are considerably decoupled/attenuated.

An equation formulation may be expressed in terms of the same pattern subtraction principle as utilized in Eq. (3) for K beams,

$$\underline{W}_o = \underline{S}^* - \sum_{k=1}^{K} W_k \, \underline{b}_k \qquad (5)$$

where $|W_k| \leq \Upsilon$ for J assigned beams and $W_k = 0$ for all other beams. $\underline{b}_k$ is the kth Butler matrix beam element-weight vector. When $W_k = 0$, that beam port is essentially disconnected from the output summation and it is much to our advantage to reduce the DOF of the adaptive weight processor accordingly, i.e., this processor reduction relates directly to the computational burden, response time, sidelobe degradation, and overall cost mentioned earlier. For example, utilizing the SMI technique described in equations (1) and (2), we would now have the advantage that our sample covariance matrix of signal inputs, $\underline{\hat{R}}$, involves only the J assigned beams and its dimensions reduce from KxK down to JxJ, thereby greatly easing the computation burden involved in obtaining its inverse [9]. The equivalent "steering vector", $\underline{\Lambda}$, per Applebaum [7] is also reduced to dimension J and consists of the cross-correlation between the mainbeam signal V and the J assigned beam outputs, $\underline{Y}$,

$$\underline{\Lambda} = \frac{1}{N} \sum_{n=1}^{N} V(n) \underline{Y}^*(n). \qquad (6)$$

The jth assigned beam output for the nth snapshot signal sample is simply

$$Y_j(n) = \underline{E}^t(n) \underline{b}_k \ , \ k \text{ set by } j \qquad (7)$$

where the particular value of k must be selected for the jth assigned beam. Our J dimension adaptive weight solution thus becomes,

$$\underline{W} = \underline{\hat{R}}^{-1} \underline{\Lambda} \qquad (8)$$

Equation (8) gives us the J assigned beam weights required in Eq. (5). The proposed constraint $|W_k| \leq \Upsilon$ can be applied directly to the solution from (8), but recognize that this is a "hard" constraint and the results will not be optimal when the limit is exceeded.

A softer, more flexible constraint for our purposes is one suggested by Brennan* based upon Owsley [17], where one selects weights which simultaneously

---

* Private communication, L.E. Brennan, Adaptive Sensors, Inc.

minimize both the output and the sum of the weight amplitudes squared, i.e.,

$$\text{minimize} \quad \{ \overline{|V - \underline{W}^t\underline{Y}|}^2 + \alpha \, \underline{W}^t \underline{W}^* \} .$$

where the overbar denotes averaging over N snaps. The solution is a simple modification to Eq. (8) wherein

$$\underline{W} = \left[\underline{R} + \alpha \underline{I} \right]^{-1} \underline{\Lambda} \tag{9}$$

where $\alpha = \frac{\gamma^2}{J}$ Trace $[\underline{R}]$.

Note that Eq. (9) adds a small percentage of the average assigned beam power to the diagonal terms of $\underline{R}$. Recall that γ was selected to be close to the mainbeam sidelobe level. Although α is a small percentage of the Trace $[\underline{R}]$, it is generally much larger than the receiver noise level, $\beta_o{}^2$, and this domination over receiver noise by a constant will tend to severely dampen weight fluctuations due to noise. Of course, Eq. (9) deviates from the optimum Weiner weights and will result in a slightly larger output residue, but the cost is negligible compared to the remarkably stable results achieved from this rather simple constraint. It essentially permits the number of assigned beams to exceed the DOF required, and yet retain low sidelobe levels. Equations (5) thru (9) were utilized in computing the adaptive pattern examples which follow. The reader should recognize that the J dimension adaptive weight solution may be arrived at via any of the current adaptive processing algorithms such as Howells-Applebaum [7], Gram-Schmidt [9], Sample Matrix Inverse Update [18], etc.

Applying these constraints to our three-source case of Fig. 2, we would assign beamformer beams Nos. 10, 11, and 12 to cover the sources, as illustrated in Fig. 6a. These assigned beams are then given a maximum gain level about 5 dB above the -30 dB mainbeam sidelobes. Thus, the assigned beam weights are constrained to $|W_k| \leq 0.055$. All other W_k are set to zero. Typical resultant adapted patterns are shown in Fig. 6b, where nine trials of 160 snapshots each are plotted. The pattern stability is near-perfect for a unique solution like this, and note that the three sources have been nulled with very little perturbation of the mainbeam sidelobes except in the immediate vicinity of the sources. Since we are inverting a matrix of only 3x3 dimension in Eq. (8) for this case, it follows that the number of snapshots processed per trial could be reduced by an order of magnitude [10] and still have excellent results. The adaptive weights will become "noisy" if we include even one extra DOF beyond the unique solution. However, if we use the "soft" constraint of Eq. (9) in solving for the weights, stable performance is again restored despite the extra DOF.

Although not shown here, another example of interest was the case of using a two-beam cluster (Nos. 11 and 12) to cancel a single 40 dB broadband source located at 22 degrees. It was found that the source could be adequately cancelled at bandwidths up to 15 percent.

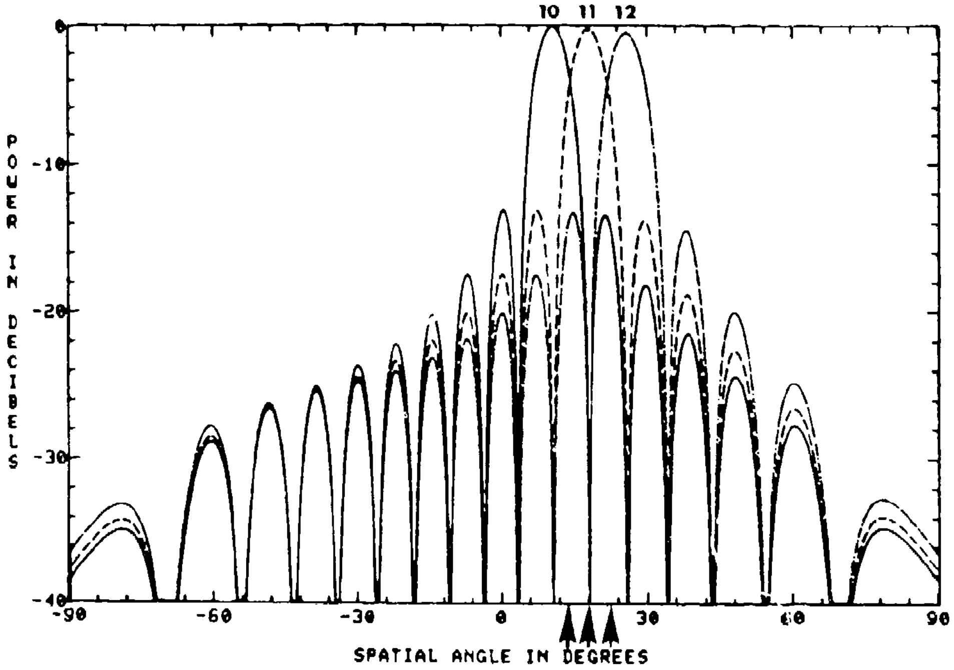

(a) Beamformer beams Nos. 10, 11, and 12.

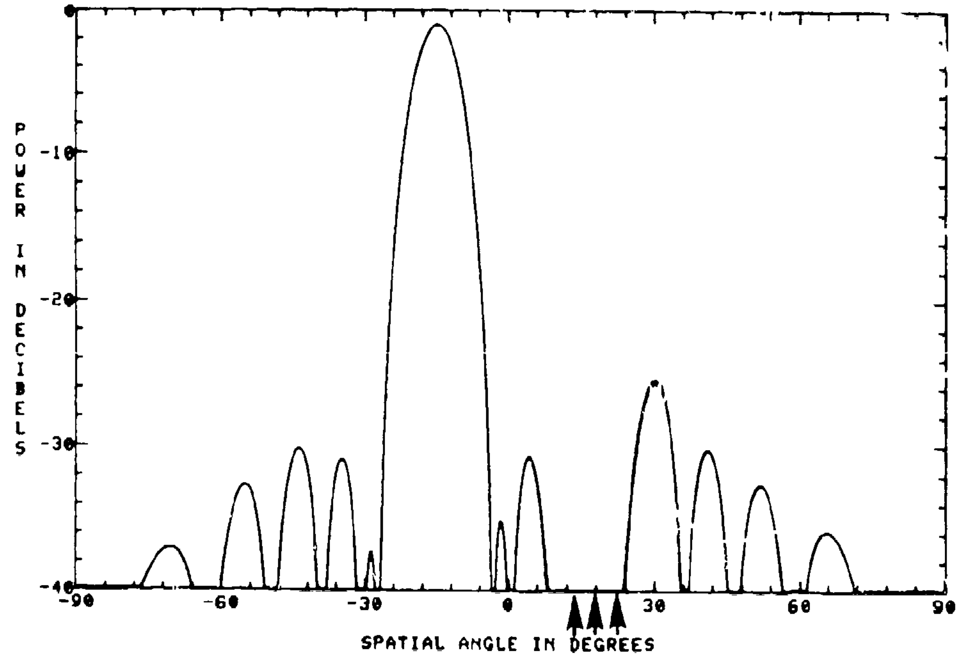

(b) Typical adapted patterns, nine trials of 160 snapshots.

FIGURE 6 - Partially-adaptive linear array of 16 elements, using three assigned beams for the three-source case of Fig. 2.

Many other combinations of source distributions and assigned beams were tested to further verify the technique, and the partially-adaptive performance was satisfactory provided that the assigned beams were sufficient to cover the DOF demanded by the source distribution.

2.3 Interference Sources in the Mainbeam Region.

Extension of the foregoing partially-adaptive array technique for mainbeam interference is straightforward, provided we relax the constraint upon the value of γ in Eq. (5). Obviously, the low-sidelobe strategem becomes secondary to the greater menace of an interference source coming in thru our high-gain mainbeam. Low sidelobes could still be retained, if necessary, by implementing a beamformer which is capable of producing a family of low-sidelobe assigned beams [15].

3.0 SOURCE ESTIMATION AND BEAM ASSIGNMENT

Modern spectral estimation techniques are a welcome addition to the conventional methods for tracking and cataloging interference sources. They do not interfere with any functions of the mainbeam, and they are capable of providing superior source resolution from fewer elements. The latter advantage is gained in part because we assumed low sidelobes for the mainbeam, i.e., the only sources that require estimation are those few which are of sufficiently high SNR to get thru the mainbeam sidelobes. Resolution performance is always directly related to SNR, of course [2,5,6].

The principle of achieving source estimation from a small fraction of the aperture DOF has been demonstrated via many techniques, both conventional and optimal [1,3,19]. It is not within the scope of this paper to attempt a comprehensive comparison of such techniques, but, the point is important to our concept so that an example of a half-aperture linear array estimator is given in this section. The type of application envisioned is illustrated in Fig. 7, where we represent a KxK element aperture system in which the adaptive beam DOF are to be assigned on the basis of estimates derived from two orthogonal linear arrays of K/2 elements each. An extension of the 2D (two-dimension) beamspace adaptive array system of Fig. 5 to the 3D sytem suggested by Fig. 7 permits several beamformer options, including:

a. Two orthogonal 2D beamformers of which one is coupled into a row and the other coupled into a column of elements.

b. A complete 3D beamformer [20] coupled into the aperture elements, perhaps on a thinned basis.

The separate mainbeam must be summed from all K^2 elements in order to attain the desired low sidelobes.

Although they involve relatively few elements from the aperture, the linear array estimators represent a significant increase in system expense because they are all-digital processing subsystems. Processing of the digital signals to estimate the sources may be carried out in accordance with a number of spectral estimation algorithms available in the literature [1 thru 6]. Reference [11] discusses several algorithms that were utilized in the simulations conducted for this paper. For example, Fig. 8 illustrates a comparison plot of our mainbeam search scan vs. half-aperture eigenanalysis processing results for the 16-element linear array case of Fig. 2.

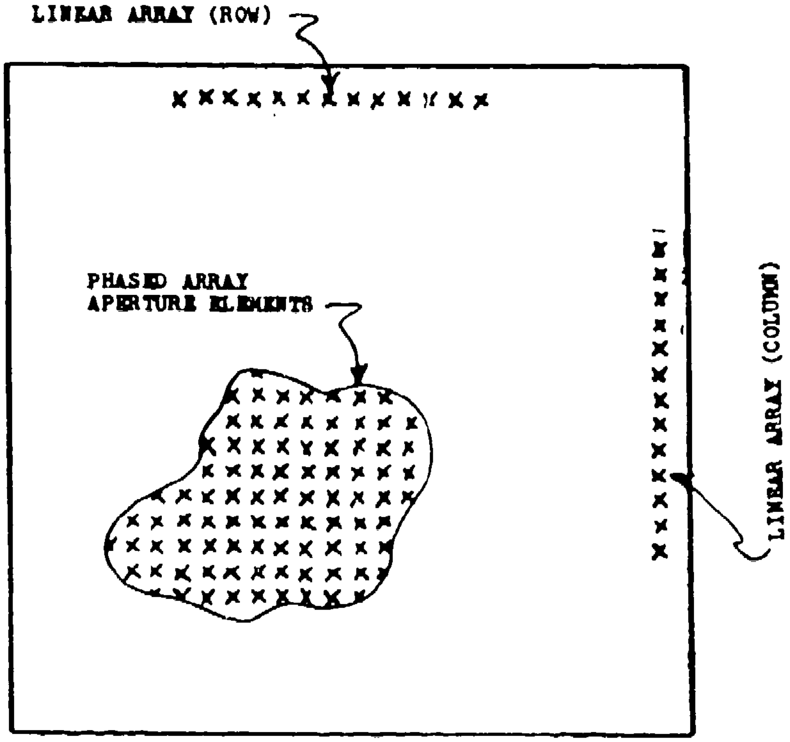

FIGURE 7 - (K x K) Element aperture within which row/column linear arrays couple into source estimation processors.

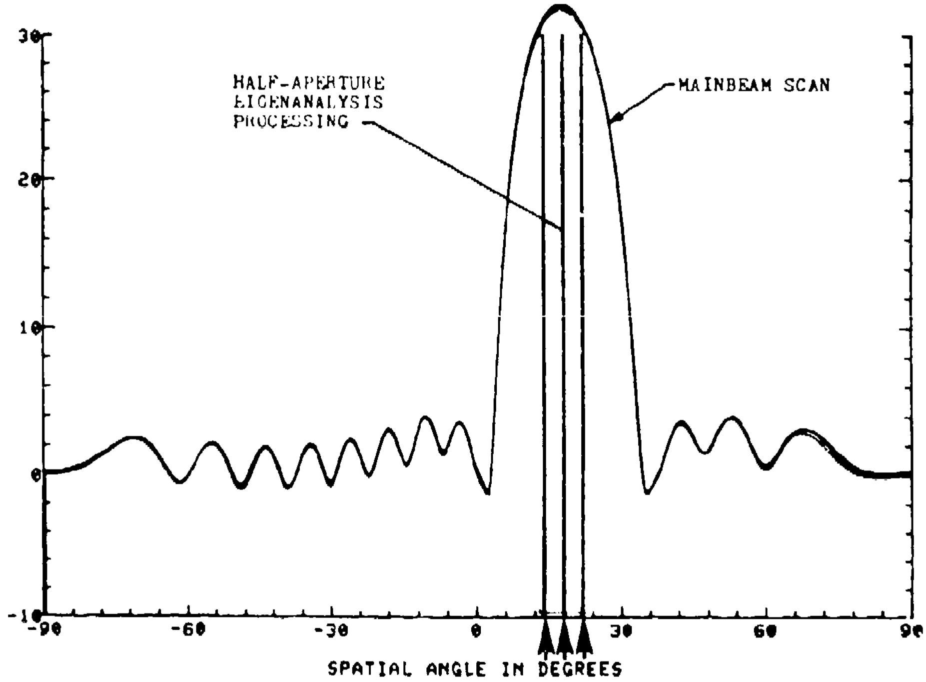

FIGURE 8 - Comparison of mainbeam scan vs. half-aperture eigenanalysis source estimation for three-source case of Fig. 2

Once the source estimation information is available, then we can assign beamformer beams via a computer logic program. For the simulations reported in this paper, a Fortran IV computer code named "BEAMASSIGN" was developed which accepts source information updates, compares the new data against a source directory kept in memory, computes track updates for sources already in memory, determines priority ranking, and assigns beams to cover the sources of highest priority. An important point to note is that beam assignment does not require great accuracy, i.e., a half-beamwidth is usually close enough. Also, clusters of two or three adjacent beams may be assigned for doubtful cases.

A demonstration of beam assignment was conducted with a moving source simulation involving the 16-element linear array of Fig. 2. Four sources of unequal strength were set up in the farfield, traveling in criss-crossing patterns. Two of the sources are of 30 dB strength with start angles of 3.0 and 39.0 degrees, and two are of 43 dB strength with start-angles of 5.0 and 70.0 degrees. The estimation of the scanned mainbeam for this example is shown in Fig. 9(a). Each time-unit plot cut is computed from $\underline{R}$ averaged over 160 snapshots,

$$P_o = \underline{S}^t \underline{R} \, \underline{S}^* \qquad (10)$$

where $\underline{S}^*$ is the mainbeam steering vector used to generate the display plot. As expected, this simple Fourier output is dominated by the two stronger sources. In contrast, Fig. 9(b) shows the source estimation derived from eigenanalysis processing using only half of the aperture (8 elements). Note that the "super-resolution" characteristics of this type of optimal estimation produces excellent source tracking, even in the vicinity of cross-over of three of the sources.

The results of using the source information data contained in Fig. 9(b) to continuously update beam assignments is illustrated in the adapted pattern cuts shown in Fig. 10(a). Note that the mainbeam remains steady and the sidelobes seldom exceed their quiescent 30 dB peak level, despite the drastic shifting of the nulls as the moving sources criss-cross in the sidelobe region. In contrast, Fig. 10(b) illustrates the adapted pattern cuts obtained when we utilize the SMI algorithm weights with the array fully adaptive. Although the source cancellation is excellent, the mainbeam suffers significant modulation and the peak sidelobe levels rise considerably.

4.0 AN ADAPTIVE ARRAY TRACKING APPLICATION

A second area where spectral estimation techniques can provide valuable assistance is that of adaptive array tracking systems. Here we are dealing with the problem of attempting to track targets under the condition of having interference sources present in the mainbeam region. Some early proposed solutions in this area evolved from the growing adaptive array technology of the 1970's. For example, a paper by White [21] discusses the radar problem of tracking targets in the low-angle regime where conventional tracking radars encounter much difficulty because of the presence of a strong surface-reflected ray.

The first extension of fully adaptive arrays to angle estimation in external noise fields is the contribution of Davis et al. [22], who developed an algorithm

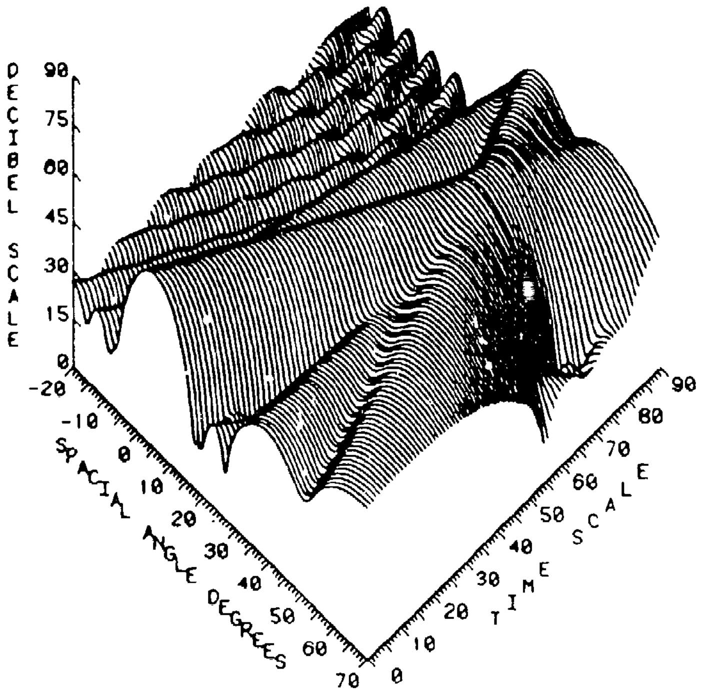

(a) Conventional mainbeam scanning, 16 elements

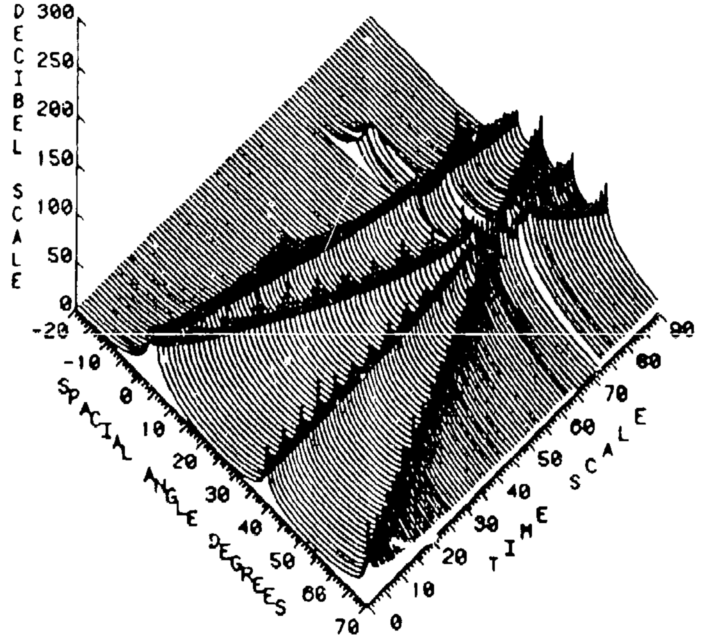

(b) Half-aperture eigenanalysis source estimation.

FIGURE 9 - Estimation of four moving sources via mainbeam scan and half-aperture eigenanalysis algorithm, 160 snapshots averaged per plot cut.

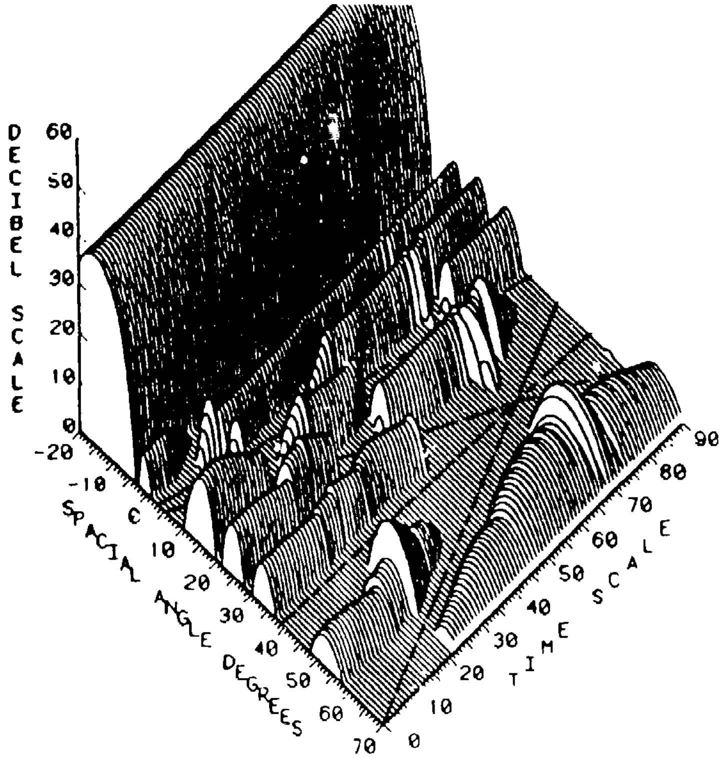

(a) Partially-adaptive, constrained, assigned beams.

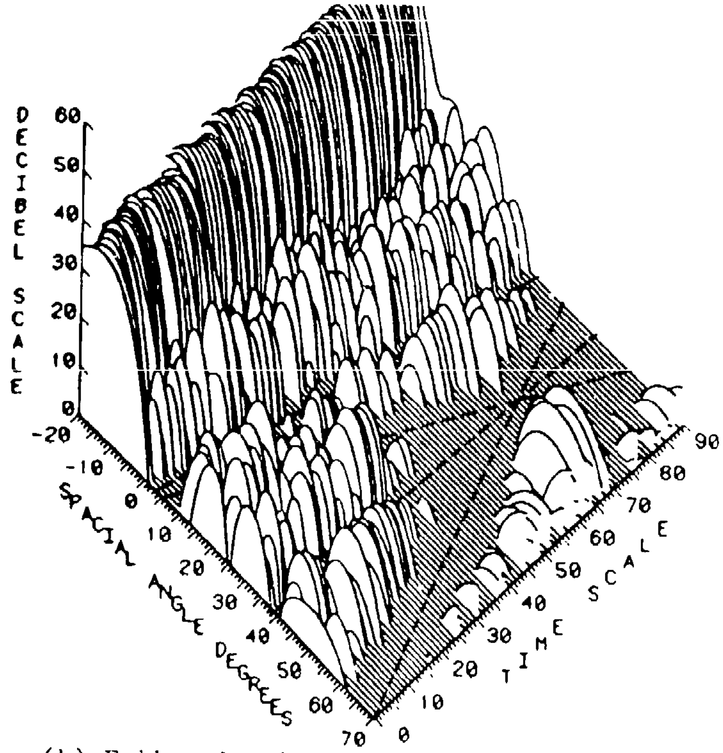

(b) Fully adaptive array, no constraints.

FIGURE 10 - Adaptive patterns for 16-element linear array, SMI algorithm, four moving sources case of Fig. 9.

based on the outputs of adaptively distorted sum and difference beams. The adaptive beams filter (null) the external noise sources, and distortion correction is then applied in the resultant monopulse output angle estimate. Their work is particularly appropriate as a starting point for this section, where we discuss the advantages of using spectral estimation techniques in an all-digital, fully adaptive, array tracking system. Reference [15] is also pertinent.

4.1 Coherent Spatial Interference Sources. The existence of significant coherence between spatial sources as, for example, in multipath situations involving a specular reflection, continues to represent a serious problem area even for a fully adaptive tracking array. Reasons include,

a. Coherent signals are not stationary in space [2,5,23].

b. Adaptive systems may perform cancellation via weight phasing rather than null steering [5, 23, 24, 25,26].

c. Adaptive tracking beam distortion is highly sensitive to coherent signal phasing.

d. Signal fading under anti-phase conditions.

To demonstrate these reasons, adaptive characteristics were computed for a 16-element linear array for an interference case in which there are two 13 dB coherent sources in the mainbeam region at -7.6 and -4.0 degrees. There is also a third source, non-coherent, in the nearby sidelobe region at -21 degrees to act as a stable null comparison point.

In Fig. 11(a), we illustrate the severe changes in our mainbeam caused by variation of the phase shift between the two coherent sources. The quiescent mainbeam has the same Taylor weighting as in Fig. 2(a). Figure 11(b) illustrates the spatial insertion loss associated with the three adaptive weightings involved. Note that for phasing of 0° and 180°, the adaptive weights are not achieving cancellation by steering nulls onto the coherent sources but, rather, by the weight phasing itself. The array output was driven down to receiver noise level for all three phases. The plots for 90° phase are very similar to what one would obtain if all three sources were non-coherent, i.e., cancellation is achieved by adaptive null steering in this instance.

Such severe sensitivity to coherent source phasing in the mainbeam region produces different distortions in tracking estimates from adaptive Σ (sum) and Δ (difference) patterns, as shown in Fig. 12. Reference [11] contains the equation development for this type of plot, but the main point here is to show the considerable changes in track angle estimates just due to phase variation. Once again, if all three sources were non-coherent, the distortion plot would be stable and very similar to the one shown for 90° phase.

4.2 All-Digital Tracking System Concept. The separate estimation of interference source data (total number, power levels, location angles, coherence) and its utilization to improve the output SNR of desired signal detections is a mode of system operation that has been addressed in the literature a number of times for various applications [5,6,15,16]. In this section, we briefly review such a system wherein the estimated data is used to drive a fully adaptive tracking processor [11]. The concept is illustrated in Fig. 13. Starting on the left-hand side, the system continuously computes/updates a sample covariance matrix $\underline{R}$.

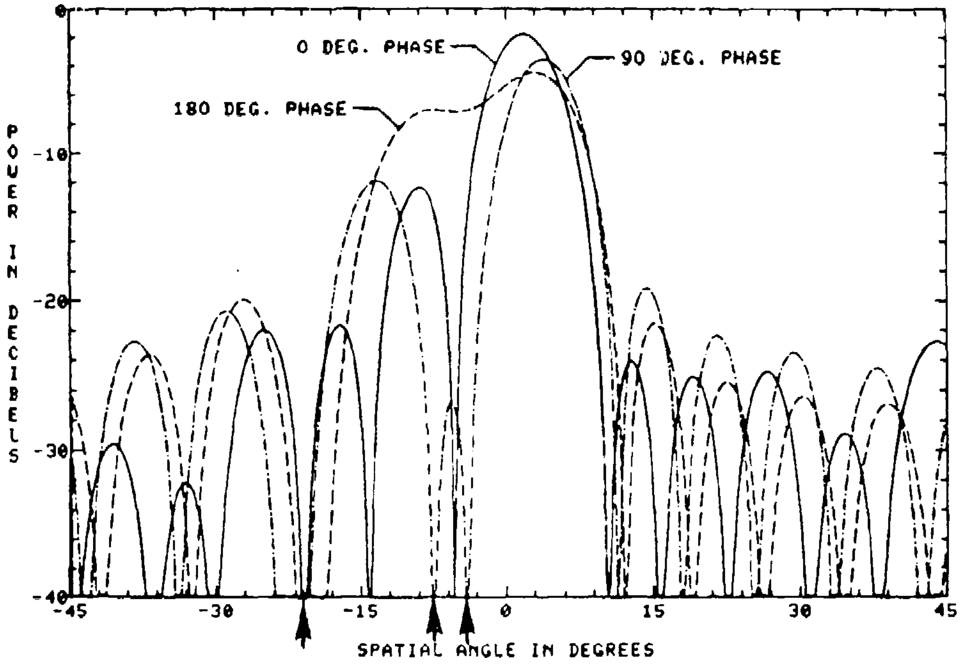

(a) Typical adaptive patterns for three coherent phases.

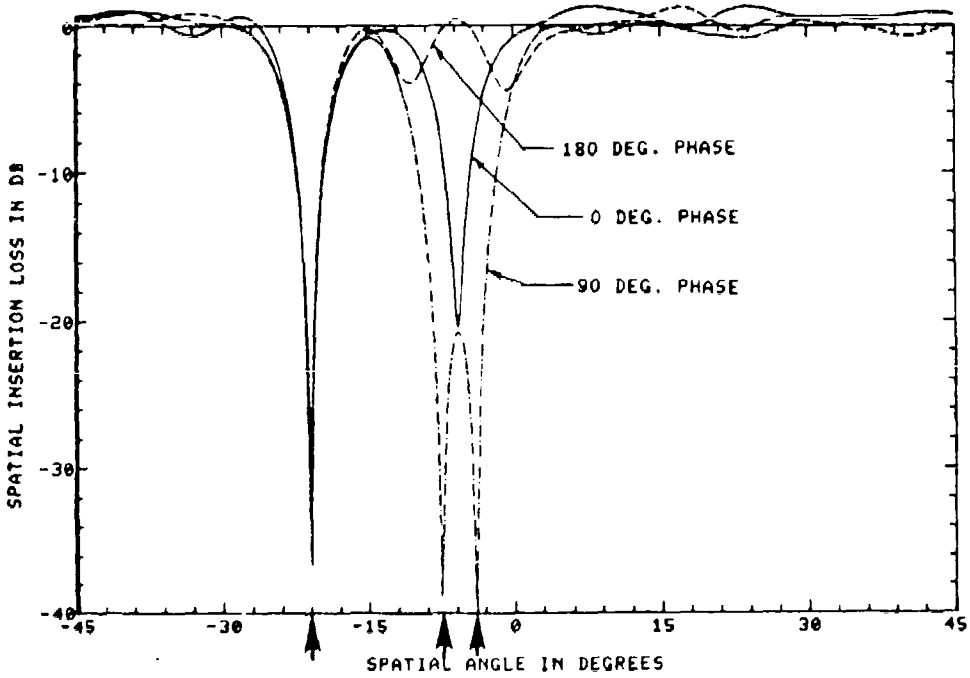

(b) Insertion loss associated with adaptive weighting.

FIGURE 11 - Mainbeam interference adaptive characteristics for 16-element linear array, SMI algorithm, 256 snapshots.

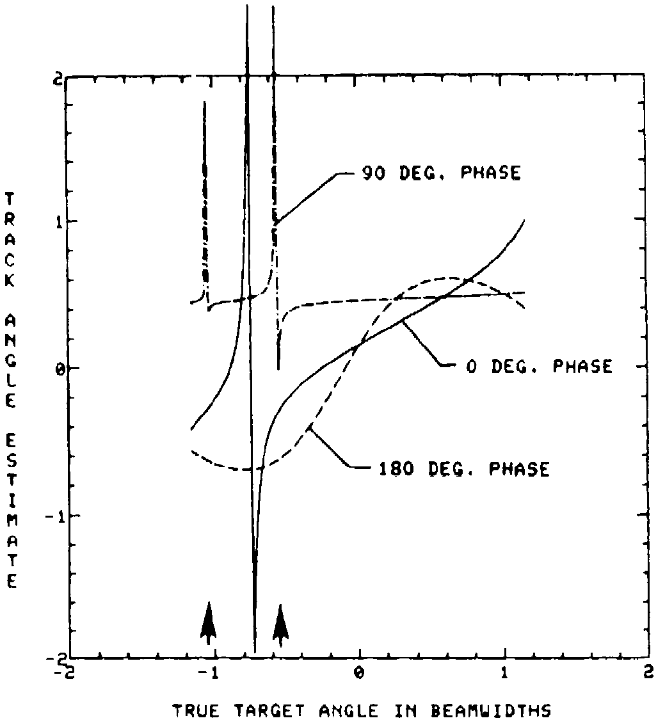

FIGURE 12 - Track estimate distortion resulting from adaptive Σ and Δ tracking b eams for coherent interference.

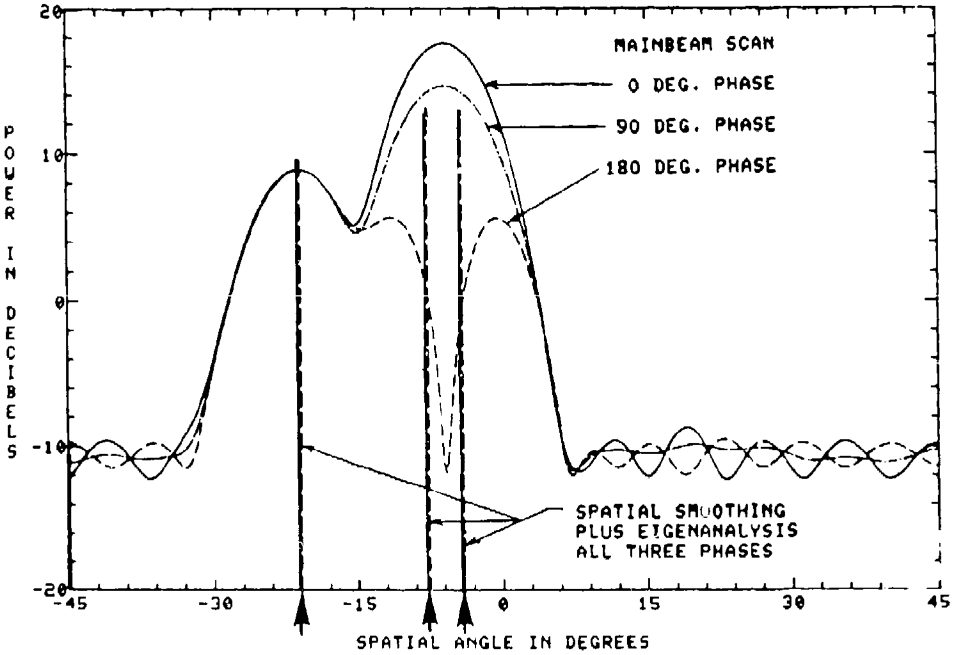

FIGURE 14 - Comparison of mainbeam scan vs. spatial smoothing processing for coherent source case of Fig. 11, PEGS eigenanalysis, 256 snapshots per trial.

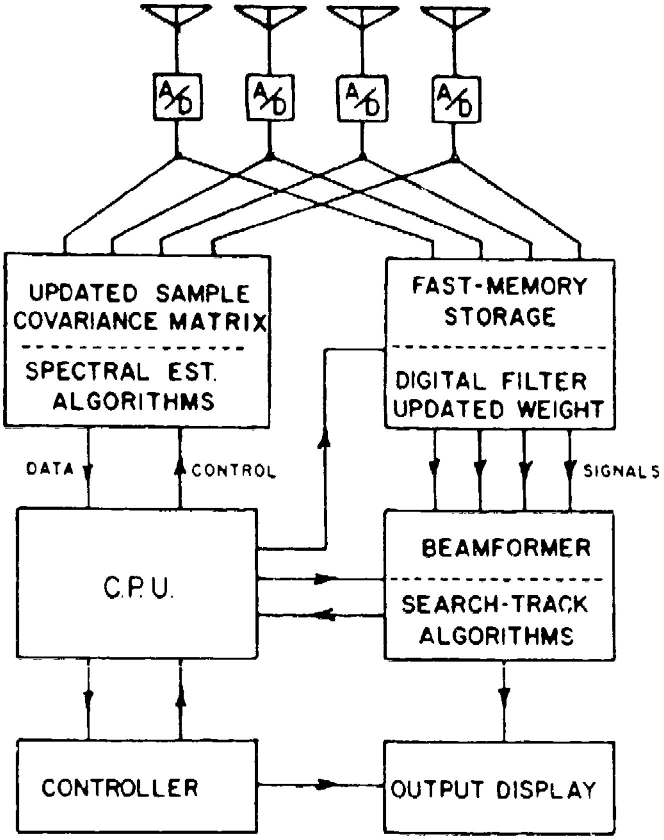

FIGURE 13 - All-Digital Adaptive Array Tracking System Concept

Of particular significance is the fact that $\underline{R}$ may be dimensioned either equal to or less than the total number of array elements, i.e., the model order of the estimate is selectable per subaperture averaging option choice. Off-line processing on $\underline{R}$ is then conducted at periodic intervals to estimate the locations and relative power levels of interference sources via the most appropriate spectral estimation algorithms. The central processor unit (CPU) then applies these data to the computation of optimized adaptive spatial filter weights for the right-hand side of Fig. 13. Separation of source estimation from adaptive filter weight computation can be done accurately only in an all-digital processing system, but it permits the following benefits,

a. Estimation of coherent interference source locations for deliberate adaptive null filter placement.

b. Remembering slowly changing or time-gated sources, and "colored-noise" distributions.

c. Anticipating sources from apriori data inputs.

d. Flexibility in time-domain control of the filtering to counter interference time strategies.

e. Tracking/cataloging/ranking sources.

f. Efficient assignment of available DOF.

g. Compatible with fast-response adaptive algorithms, i.e., parallel algorithm processing.

The right-hand side of Fig. 13 indicates a fast-memory storage capability which is intended to permit selected time delays of the snapshots for feeding into the filter weights. The idea is to synchronize selected snapshots with their filter weight updates if possible.

Finally, the filtered signal output residue is fed into a beamformer which is weighted to produce the desired search and monopulse track beams for target detection and tracking. The algorithms of Davis et al. [22] may be applied for estimating the target signal angle of arrival, based upon the outputs of adaptively distorted sum and difference beams.

As an example, let us apply this concept to the coherent source case utilized for Figs. 11 and 12 wherein we would utilize a 16-element linear array feeding into our all-digital processor. An appropriate estimation algorithm is that of forward-backward subaperture spatial smoothing [5,27,28] combined with eigenanalysis, and the results are plotted in Fig. 14 in comparison with a scanned mainbeam output. From this source estimation data, we can construct an equivalent covariance matrix dimensioned for the full aperture, and compute its inverse for obtaining the adaptive filtering. If we define the constructed covariance matrix as $\underline{M}$, then its inverse may be viewed as a matrix set of adaptive "beamformer" filter weights to give us the filtered output nth snapshot vector $\underline{E}_f(n)$,

$$\underline{E}_f^t(n) = \underline{E}^t(n)\,\underline{M}^{-1} \quad . \tag{11}$$

Conventional beam weighting $\underline{S}^*$ can then be applied to the filtered output residue to obtain the final output for the nth snapshot,

$$Y_o(n) = \underline{E}_f^t(n)\underline{S}^* = \underline{E}^t(n)\underline{M}^{-1}\underline{S}^* \tag{12}$$

or

$$Y_o(n) = \underline{E}^t(n)\underline{W}_o$$

where $\underline{W}_o$ is the familiar optimum Wiener filter weight.

Note that the constructed covariance matrix, $\underline{M}$, permits options such as adding synthetic sources or changing power levels. Furthermore, since it is always Toeplitz, solutions may be simplified somewhat.

For the current example, the computed adaptive characteristics would be very similar to those plotted in Figs. 11 and 12 for the 90 degrees phase angle. Other examples, together with a more detailed discussion of the processing, may be found in [11].

REFERENCES

1. D.G. Childers, ed., MODERN SPECTRUM ANALYSIS, IEEE Press, New York, 1978.

2. W.F. Gabriel, "Spectral Analysis and Adaptive Array Superresolution Techniques," Proc. IEEE Vol. 68, Jun 1980, pp. 654-666.

3. Special Issue on Spectral Estimation, Proc. IEEE Vol. 70, Sep 1982.

4. R. Schmidt, "Multiple Emitter Location and Signal Parameter Estimation," Proc. of the RADC Spectrum Estimation Workshop, RADC-TR-79-63, Rome Air Development Center, Rome, NY, Oct 1979, p. 243. AD A081736

5. J.E. Evans, J.R. Johnson, and D.F. Sun, "Application of Advanced Signal Processing Techniques to Angle of Arrival Estimation in ATC Navigation and Surveillance Systems," MIT Lincoln Laboratory Tech. Report 582, (FAA-RD-82-42), Jun 1982.

6. A.J. Barabell et al, "Performance Comparison of Superresolution Array Processing Algorithms," MIT Lincoln Laboratory Report TST-72, May 1984.

7. S.P. Applebaum, "Adaptive Arrays," IEEE Trans. Antennas Propagat., Vol. AP-24, pp. 585-598, Sep 1976.

8. D.J. Chapman, "Partial Adaptivity for the Large Array," IEEE Trans. Antenna Propag., AP-24, pp. 685-696, Sep 1976.

9. R.A. Mozingo and T.W. Miller, "Introduction to Adaptive Arrays," John Wiley and Sons, New York, 1980.

10. I.S. Reed, J.D. Mallett, and L.E. Brennan, "Rapid Covergence Rate in Adaptive Arrays," IEEE Trans. Aerosp. Electron, Syst., Vol. AES-10, pp. 853-863, Nov 1974.

11. W.F. Gabriel, "A High-Resolution Target-Tracking Concept Using Spectral Estimation Techniques," Naval Research Laboratory Report No. 8797, May 1984.

12. W.F. Gabriel, "Adaptive Arrays - An Introduction," Proc. IEEE, Vol. 64, pp. 239-272, Feb 1976.

13. S.P. Applebaum and D.J. Chapman, "Adaptive Arrays with Mainbeam Constraints," IEEE Trans. Antennas Propagat. Vol. AP-24, pp. 650-662, Sep 1976.

14. J.T. Mayhan, "Adaptive Nulling with Multiple-Beam Antennas," IEEE Trans. Antennas Propag., AP-26, pp. 267-273, Mar 1978.

15. R.N. Adams, L.L. Horowitz. K.D. Senne, "Adaptive Main-Beam Nulling for Narrow-Beam Antenna Arrays," IEEE Trans. Aerosp. Electron. Syst., Val. AES-16, pp. 509-516, Jul 1980.

16. E.C. DuFort, "An Adaptive Low-Angle Tracking System," IEEE Trans. Antennas Propag., AP-29, pp. 766-772, Sep 1981.

17. N.L. Owsley, "Constrained Adaption," Array Processing Applications to Radar, Academic Press, 1980.

18. E. Brennan, J.D. Mallett, and I.S. Reed, "Adaptive Arrays in Airborne MTI Radar," IEEE Trans. Antennas and Propagation, Vol. AP-24, pp. 607-615, Sep 1976.

19. B.M. Leiner, "An Analysis and Comparison of Energy Direction Finding Systems," IEEE Trans. AES, AES-15, pp. 861-873, Nov 1979.

20. J.P. Shelton, "Focusing Characteristics of Symmetrically Configured Bootlace Lenses," IEEE Trans. Antennas and Propagation, Vol. AP-26, Jul 1978, pp. 513-518.

21. W.D. White, "Low-Angle Radar Tracking in the Presence of Multipath," IEEE Trans. AES, AES-10, pp. 835-853, Nov 1974.

22. R.C. Davis, L.E. Brennan and L.S. Reed, "Angle Estimation with Adaptive Arrays in External Noise Fields," IEEE Trans, AES, AES-12, pp. 179-186, Mar 1976.

23. W.D. White, "Angular Spectra in Radar Applications, IEEE Trans. Aerosp, Electron, Syst. AES-15, pp. 895-899, Nov 1979.

24. A. Cantoni and L. Godara, "Resolving the Directions of Sources in a Correlated Field Incident on an Array," J. Acoust. Soc. Am., Vol 64, pp. 1247-1255, 1980.

25. B. Widrow, et al, "Signal Cancellation Phenomena in Adaptive Antennas: Causes and Cures," IEEE Trans. Antennas and Prop., Vol. AP-30, pp. 469-478, May 1982.

26. T.J. Shan and T. Kailath, "Adaptive Beamforming for Coherent Signals and Interference ," to be published in IEEE Trans. Acoust., Speech, Signal Processing.

27. A.H. Nuttall, "Spectral Analysis of a Univariate Process with Bad Data Points, via Maximum Entropy and Linear Predictive Techniques," NUSC-TR-5303, Naval Underwater Systems Center, New London, CT, Mar 1976.

28. L. Marple, "A New Autoregressive Spectrum Analysis Algorithm," IEEE Trans. Acoust., Speech, Signal Process. ASSP-28, pp. 441-454, Aug 1980.

ADAPTIVE - ADAPTIVE ARRAY PROCESSING

Dr. Eli Brookner and James M. Howell
Copyright © 1985 By
Raytheon Company, Wayland, MA 01778

ABSTRACT

A technique is described which provides the jammer cancellation advantages of a fully adaptive array without its many disadvantages such as an excessively large number of computations, poor sidelobes in the directions other than the jammer locations and poor transient response. This is done at the expense of the hardware complexity. The technique involves transforming a large array of N elements into an equivalent small array of J+1 elements, where J is the number of jammers present. The technique involves estimating the number and locations of the jammers by a discrete Fourier transform of the array element outputs or by the use of standard maximum entropy methods (MEM) or by other super-resolution techniques. Once the number and locations of the jammers have been determined, beams are formed in the direction of the jammers using the whole array. The outputs of these jammer beams together with the output of the main signal beam from the transformed array now consist of J+1 ports instead of N ports. The standard sample matrix inversion (SMI) or the Applebaum algorithm can be applied to the J+1 ports of the equivalent adaptive-adaptive array. Whereas N may be very large, like 10,000 for large arrays, J+1 for the equivalent array could be very small. For example, if there are only 10 jammers then J+1 becomes 11. The total number of multiplies needed to do the adaptive array processing reduces from something of the order of $2N^3 = 2(10,000^3) = 2 \times 10^{12}$ to about 10^5 a reduction in the computation complexity by seven orders of magnitude. In addition, the settling time for the adaptive-adaptive array is much faster. For the above example the settling time for the full array is about 20,000 samples, whereas for the adaptive-adaptive array it is only 22 time samples, for an improvement of three orders of magnitude.

SUMMARY

A technique is described for adaptive array processing which eliminates the complex computation problem (see Table 1) of a large fully adaptive array while at the same time provides essentially the same optimum performance as obtained for the fully adaptive array in Ref. 1. The technique also has the advantage of not significantly degrading the antenna sidelobe levels at angles where the jammers are not present; see Figure 1. This feature is important in the presence of intermittent short pulse interference coming through the radar sidelobes and for ground radars which have clutter in the sidelobes and the mainlobe. The adaptive-adaptive array also has the advantage of a much faster settling time; see Table 1.

The technique uses a two-step process. First the number of interfering jammers and their locations are estimated by such techniques as a spatial discrete Fourier transform of the array outputs (digitally or by use of a Butler matrix or Rotman lens), by maximum entropy method spectral estimation techniques [2,3] or just by a search in angle with an auxiliary beam. Once the

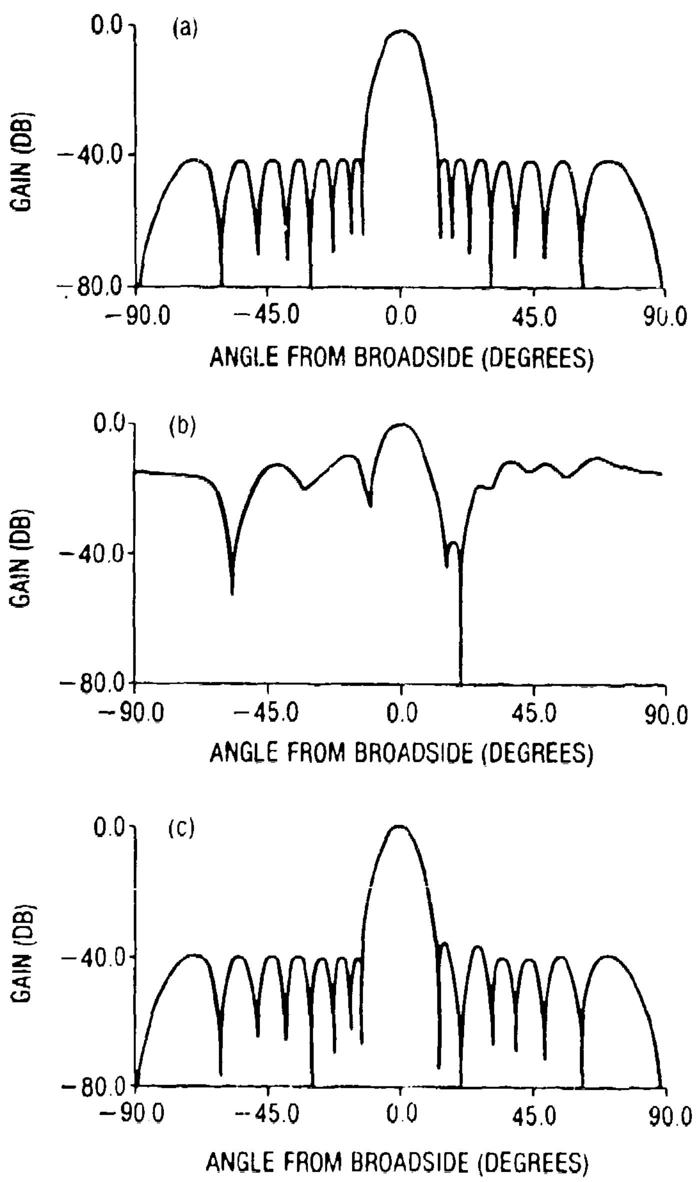

Figure 1. 16 element array having 40 dB antenna sidelobes (Chebyshev weighting). Jammer at 20° (peak of second sidelobe).

Figure 1a. Unadapted antenna pattern.

Figure 1b. Antenna pattern for fully adaptive array (SMI algorithm). M=2N=32.* For the fully adaptive array, not only is there a degradation of the antenna sidelobes, there is also a degradation in the antenna main lobe peak gain. The peak gain degradation was found to be as much as 5 dB in the simulations carried out.

Figure 1c. Antenna pattern for adaptive-adaptive array processing. M=2(J+1)=4.

*M equals the number of time samples used to estimate the adaptive antenna weights.

Table 1. Comparison of Computations Required

Assumption: J = Number of Jammers = 10;

Type Array Antenna	Jammer Cancellation Technique	Number of Complex Multiples To Calculate Weights	Complex Multiplies To Form Array Output per Signal Time Sample #	Transient Time (Units of Signal Time Samples)
1-Dimensional (N Elements = 100)	Fully Adaptive	$2N^3 = 2 \times 10^5$	$N = 10^2$	$2N = 200$
	Adaptive-Adaptive	$2(J+1)^3 + 7NJ^*$ $\doteq 10^4$	$J+1 = 11$ $\doteq 10$	$2(J+1) = 22$
	(Improvement)	200	10	~ 10
Square 2-Dimensional (N Elements = 10^4)	Fully Adaptive	$2N^3 = 2 \times 10^{12}$	$N = 104$	$2N = 2 \times 10^4$
	Adaptive-Adaptive	$2(J+1)^3 + N\log_2 \sqrt{N}^{**}$ $\doteq 7 \times 10^4 \doteq 10^5$	$J+1 = 11$ $\doteq 10$	$2(J+1) = 22$
	(Improvement)	$\sim 2 \times 10^7$	10^3	$\sim 10^3$

Does not include computations of column three.

* Second term assumes MEM algorithm used to locate jammer. This term drops out if jammers located using search beam. For this case number of multiplies = $2(J+1)^3 = 2 \times 10^3$ and improvement becomes $\sim 10^3$.

** Second term assumes Fast Fourier Transform (FFT) Algorithm used to locate jammer. Terms drops out if jamme located using search beam (or beams). In this case number of multiplies = $2(J+1)^3 \doteq 2 \times 10^3$ and improvement becomes $\sim 10^9$.

number of jammers and their locations have been determined, auxiliary beams are formed pointing at these jammers, with one beam being pointed at each jammer; see Figure 2. These beams are formed using the whole array. They are formed using beamforming networks parallel to the main signal beam network. The number of beams formed is equal to the number of jammers. These beams could be formed using amplitude weighting to achieve low sidelobe levels if desirable. The outputs of the auxiliary jammer beam ports together with the main signal beam port form the adaptive-adaptive transformed array. The number of degrees of freedom in this transform array is reduced from N, the number of elements in the original array, to one plus the number of jammers J. Thus for the adaptive-adaptive array a (J + 1) (J + 1) matrix has to be inverted instead of a N x N matrix. Furthermore, the conversion time for the adaptive-adaptive array is much faster than for the full array. For the SMI algorithm the number of time samples needed to form the weights is equal to two times the number of degrees of freedom in order to obtain cancellation within 3 dB of the optimum[4]. Thus for the adaptive-adaptive array 2(J + 1) time samples are needed instead of the 2N required for the full array; see Table 1.

ONE-DIMENSIONAL ARRAY; NARROW BANDWIDTH JAMMER

Assume a one-dimensional array consisting of N elements. Let the interference received by the ith element at time s be given $X_{is} = J_{is} + N_{is}$, where i = 0, 1, ..., N-1, J_{is} is the jammer signal at the ith element at time s and N_{is} is the thermal noise at the ith element at time s. An estimate of the spatial correlation function of the array interference is given by

$$\hat{R}(i - 1) = \frac{1}{M} \sum_{s=1}^{M} X_{1s} X_{is}^{*} \tag{1}$$

where the carat over the R indicates estimate. $\hat{R}(i-1)$ represents an estimate of the first row of the array covariance matrix used in the sample matrix inversion (SMI) algorithm[4]. An estimate of the jammer locations can be obtained by taking a spatial discrete Fourier transform (DFT) of (1), that is,

$$\hat{U}(k) = \frac{1}{N} \sum_{n=1}^{N} \hat{R}(i - 1) \exp(-j \frac{2\pi}{N} nk) \tag{2}$$

$\hat{U}(k)$ represents an estimate of the spectrum of the jammers in angle space, actually in u-space where $u = (2 \pi d/\lambda) \sin \Theta$, Θ is the angle off mechanical boresight, d is the separation between array elements, and λ is the signal wavelength. A suitable threshold could be set above the noise level of the discrete Fourier transform to detect the jammers. The locations of the jammers would be determined by the peaks of the spatial spectrum.

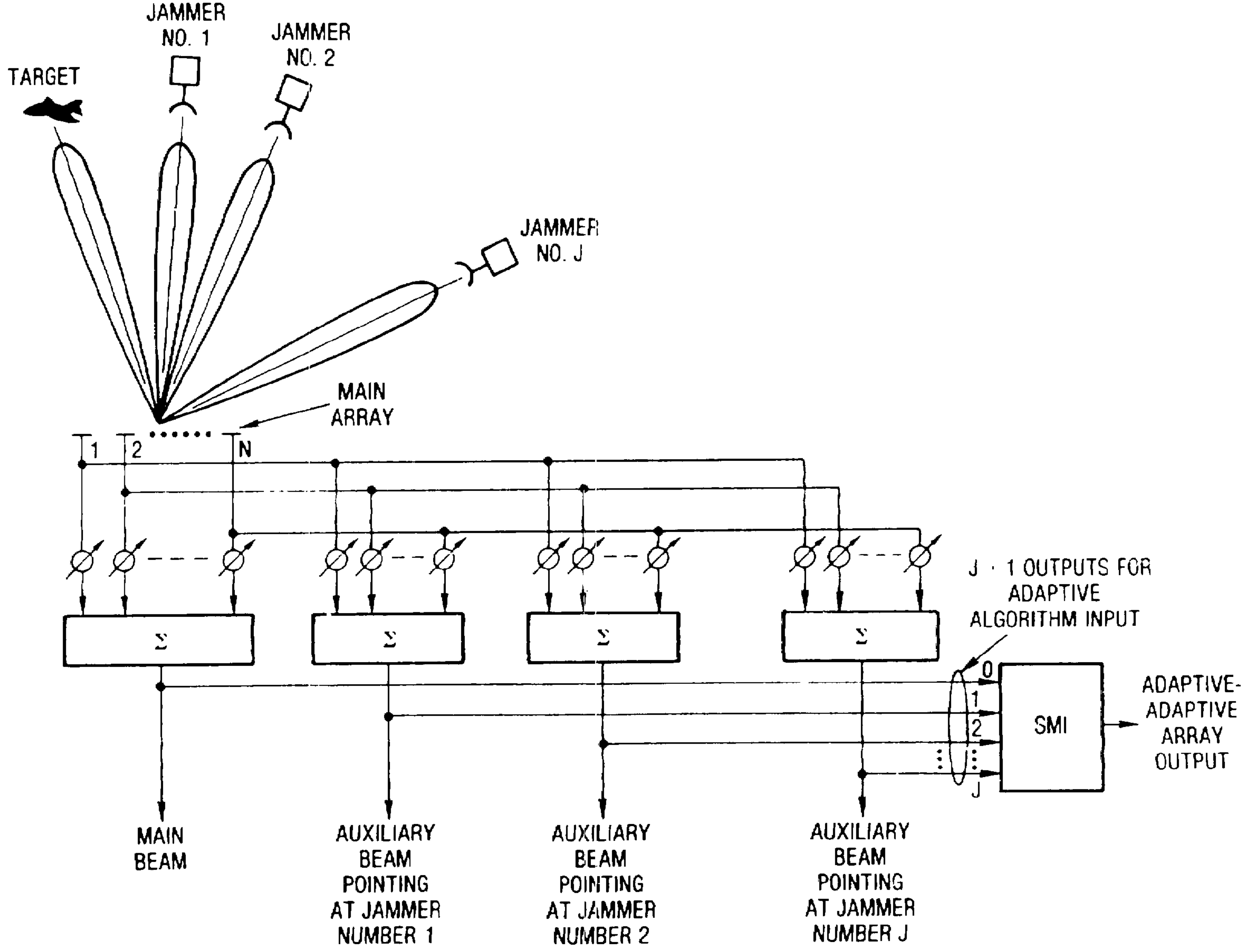

Figure 2. Adaptive-adaptive array configuration. N element array is reduced to J+1 element array where J is equal to the number of jammers.

An alternate method for locating the jammers involves taking a spatial discrete Fourier transform directly of the element voltages X_{is}, i = 0, 1, ..., n - 1 as follows

$$S(k)_s = \frac{1}{N} \sum_{n=1}^{N} X_{is} \exp(-j \frac{2\pi}{N} nk) \qquad (3)$$

Physically this represents a digital beamformer with N beams being formed across the angle space from -90° to +90°. In u-space these beams are equally spaced. The estimate U(k) is obtained from (3) by

$$U(k) = \frac{1}{M} \sum_{s=1}^{M} |S(k)_s| \qquad (4)$$

When the jammers are strong enough, the case of interest, the estimate of the spatial spectrum U(k) can be obtained using M = 1, that is, with only one time sample. This will be the case when Np_{Ji}/p_N is large (≥ 10) where p_{Ji} the ith jammer noise power at each element of the array and p_N is the thermal noise power at each element of the array. The accuracy to which the ith jammer can be located using (4) is approximately given by[5]

$$\sigma_{\theta_i} = \frac{\Theta_3}{\sqrt{2M(J/N)_i}} \qquad (5)$$

where Θ_3 is the antenna one-way 3 dB width, specifically, $\Theta_3 \doteq \lambda/[(N + 1)d]$ in radians; $(J/N)_i$ equals the jammer-to-noise level for the ith jammer after the spatial discrete Fourier transform, specifically, $(J/N)_i = Np_{Ji}/p_N$.

For the case where the array voltages obtained with one time sample are used to locate the jammer by the discrete Fourier transform method, only about $(N/2) \log_2 N$ complex multiplies are required to locate the jammers.

If closely spaced jammers are to be handled, then the maximum entropy method (MEM) or one of the other super-resolution techniques should be used.[2,3] With these algorithms, again only the voltage samples obtained at one time need be used to located the jammers. If the MEM algorithm is used then only 7NJ complex multiplies are required to locate the jammers.

Once the jammers have been located, auxiliary beams can be generated which point in the directions of the jammers as shown in Figure 2. If J jammers are located then J auxiliary beams are formed. The standard sample matrix inversion algorithm or Applebaum algorithm can now be applied to the J auxiliary beam outputs together with the main signal beam output. Thus the original array of N elements has been transformed into an equivalent array of J+1 elements to which the adaptive algorithms are to be applied. The SMI algorithm can be applied to the outputs of the J+1 ports as shown in Figure 2. Let M_T be the estimate of the correlation matrix of the transformed array. The optimum weights for the adaptive-adaptive array are then given by[1]

$$W_o = \hat{M}_T^{-1} T \tag{6}$$

where T is a 1 x (J+1) array given by $T^t = [1, 0, 0, \ldots, 0]^t$, where t stands for transpose.

It is simple to show using an analysis paralleling that in Section 4 of Reference 1 by Applebaum that the adaptive-adaptive array has essentially the same jammer cancellation performance as the fully adaptive array when the jammers are approximately orthogonal to each other and to the main channel signal. Specifically the jammer cancellation for the adaptive-adaptive array is given approximately by

$$\Gamma \doteq \frac{1}{1 + (Np_{Ji}/p_N)} \tag{7}$$

which for $Np_{Ji}/p_N >> 1$ becomes

$$\Gamma \doteq \frac{p_N}{Np_{Ji}} \tag{7a}$$

It is speculated that the performance of the adaptive-adaptive array is essentially the same as that of the fully adaptive array for arbitrary jammer locations, specifically for closely spaced jammers as long as all the jammers have been located, or equivalently, as long as the number of auxiliary beams equals or exceeds the number of jammers.

Because the SMI is applied in the adaptive-adaptive array to J+1 array outputs instead of the original N array outputs, the number of computations is significantly reduced. Instead of inverting an N x N matrix a (J+1) x (J+1) matrix has to be inverted. To invert an N x N matrix, N^3 complex multiplies are required. For the adaptive-adaptive array only $(J+1)^3$ complex multiplies are required to invert the matrix.

The number of computations required to estimate the array covariance matrix is also much less for the adaptive-adaptive array than for the full array. Assume that the SMI algorithm is used. Then the number of time samples required to estimate the N x N covariance matrix for the fully adaptive array is 2N in order to achieve a cancellation performance within 3 dB of the optimum.[4] Correspondingly, for the adaptive-adaptive array 2(J+1) time samples are required. For the N x N covariance matrix of the fully adaptive array the number of distinct matrix terms is equal to $[N^2 - (N^2 - N)/2] = N(N+1)/2$. Thus the number of complex multiplies required to estimate the weights for the fully adaptive array becomes $N_{FA} = N^3 + (2N)N(N+1)/2 = 2N^3$ for large N. An additional N multiplies is needed per signal time sample to form the fully adaptive array output.

Accordingly, for the adaptive-adaptive array about $2(J+1)^3$ complex multiplies are required to form the equivalent array weights. An additional 7NJ complex multiplies are required to estimate the number of jammers and their locations if the MEM algorithm is used [2,3]. (If the jammers are located using the array main beam to search them out, then the number of multiplies needed to locate the jammers becomes zero. The penalty is that it takes longer to locate the jammers by this procedure, about N times longer. If the signal bandwidth is 1 MHz, then it might take 100 µs instead of 1 µs if N = 100.) Thus a total of $N_{EA} = 2(J+1)^3 + 7NJ$ complex multiplies are required to form the weights for the adaptive-adaptive array. An additional J+1 multiplies are needed to form the array output per signal time sample. Also, to form the J+1 beams, (J+1)N phase shifts are required for the implementation of Figure 2 (however, by using the time multiplexing of one beam former only 2N shifters would be needed).

By way of an example, assume a linear array consisting of N=100 elements, and that J=10 jammers are present. For the fully adaptive array $N_{FA} = 2 \times 10^6$ complex multiplies are needed to form the array weights. For the adaptive-adaptive array, $N_{EA} = 10^4$ are needed, over two orders of magnitude lower than for the fully adaptive array. An additional 100 complex multiplies are required per time sample to form the fully adaptive array output. For the adaptive-adaptive array an additional 11 complex multiplies are needed per time sample to form the array output. Thus for a 1 MHz signal bandwidth an additional 10^8 complex multiplies per second (CM/sec) are required to form the fully adaptive array output as compared to 1.1 x 10^7 CM/sec for adaptive-adaptive array. (This rate is given in column four of Table 1 in units of multiplies per time sample.) These computations are in addition to those required to form the array weights. An additional 10 x 100=1000 phase shifts are needed per time sample to form the J+1 beam outputs. Finally, the fully adaptive array requires 2N=200 time samples to settle whereas the adaptive-adaptive array requires only 2(J+1)=22 time samples, an order of magnitude faster.

There is an additional important advantage of the adaptive-adaptive array. Specifically, cancelling the jammer does not degrade the sidelobe levels of the antenna at angles away from the jammer as does happen for the fully adaptive array. This is illustrated for a 16-element linear array in Figure 1. The figure shows the unadapted array pattern in the absence of the jammer. A Chebychev antenna pattern with 40 dB down sidelobes is assumed. Also shown are the antenna patterns obtained for the fully adaptive array and the adaptive-adaptive array when a jammer is present at a 20° off-boresite angle. The jammer-to-noise ratio was assumed to be 30 dB at the output of the unadapted array. For both the fully adaptive and adaptive-adaptive array the jammer-to-noise ratio is about the -40 dB predicted using (7). For the fully adaptive array 32 time samples were used whereas for the adaptive-adaptive array only 4 time samples were used. The figure shows that the sidelobe levels for the fully adaptive array are completely destroyed for angles away from where the jammer is located, whereas for the adaptive-adaptive array they are nearly unchanged. The degradation of the fully adaptive array sidelobes presents a serious problem when intermittent pulse interference is present and when there is sidelobe clutter present as well as mainlobe clutter for a ground radar. It is difficult, if not impossible, to handle spurious intermittent pulsed interference with the fully adaptive array. The duration of the intermittent interference is too short for the fully adaptive array loops to respond to. For a stationary ground-based radar, the fully adaptive array would not be able to suppress the sidelobe clutter without destroying the mainlobe if there is ground clutter in the mainlobe as well as in the sidelobes. For the fully adaptive array, not only is there a degradation of the antenna sidelobes, there is also a degradation in the antenna mainlobe peak gain. The peak gain degradation was found to be as much as 5 dB in the simulations carried out.

It is useful to physically understand why the adaptive-adaptive array does not degrade the antenna sidelobes. The adaptive-adaptive array subtracts one auxiliary beam pointed at the jammer and containing the jammer signal from the main signal channel beam as illustrated in Figure 3. The gain of the auxiliary beam in the direction of the jammer is made to equal the gain of the main channel beam sidelobe in the direction of the jammer. As a result the subtraction produces a null at the angle of the jammer in the main channel sidelobe. It is apparent from Figure 3 that the auxiliary antenna pattern subtraction does not significantly degrade the main antenna beam sidelobe levels. For the fully

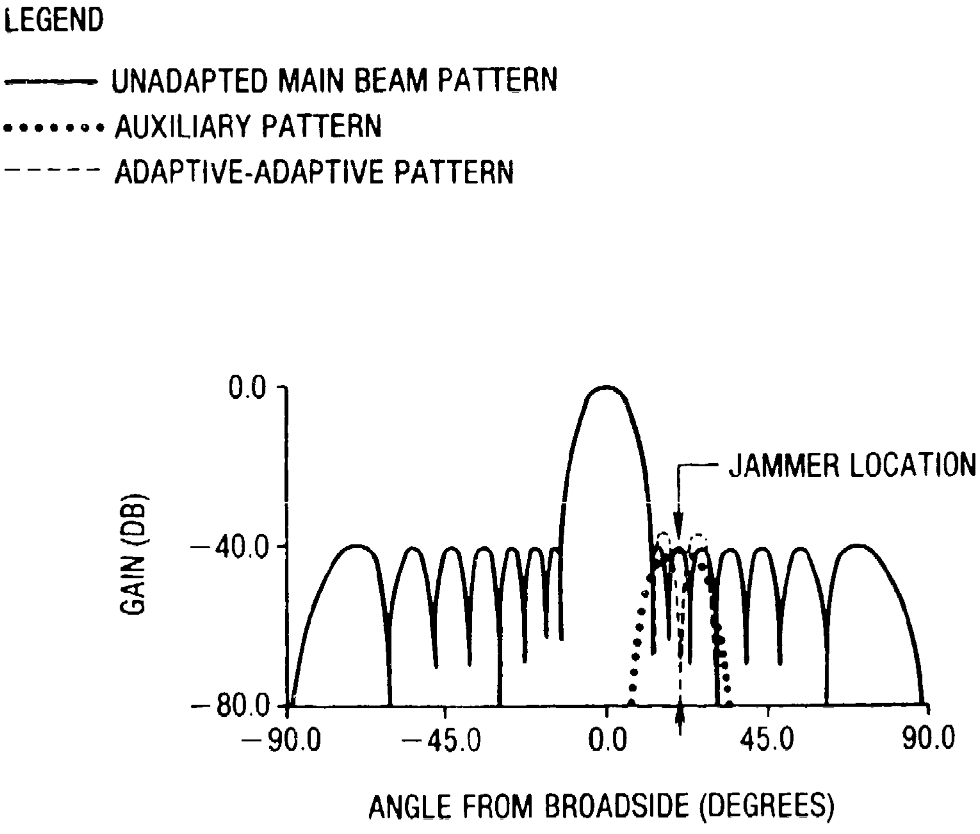

Figure 3. Main unadapted array pattern, the auxiliary jammer beam pointed at the jammer that is subtracted from the main beam at the jammer location and the resultant adaptive-adaptive pattern.

adaptive array N retrodirective beams are formed based on the eigenvalues and eigenvectors of the full array covariance matrix[6]. Because of the presence of thermal noise in the array elements, the estimates of the covariance matrix of the fully adaptive array and in turn the retrodirective beams are poor for M = 2N. Instead of forming only one retrodirective beam as desired when one jammer is present, N retrodirective beams are formed for the fully adaptive array. The N-1 retrodirective beams for which there are no jammers are the ones which degrade the antenna sidelobe levels at the angles where no jammers exist. It is found that even if 3,000 time samples are used, the sidelobe levels are still severely degraded for the fully adaptive array system although considerably improved; see Figure 4. The adaptive-adaptive array technique first locates the jammers that will degrade the system performance. Once the locations of these jammers are determined the array adapts to the situation by placing retrodirective beams only at these angles. Consequently the beams at other angles where there are no jammers are not formed and do not as a result degrade the antenna sidelobes at these angles.

A number of variations are possible on the above adaptive-adaptive array system. First the MOSAR method of Reference 7 can be used to locate the jammer position based on a single time sample. Second it is not necessary to use the whole array to locate the jammers. Instead part of the array could be used and in turn this same part used to form the auxiliary retrodirective beams pointing at the jammers. This method will not perform as well as the method using the full array. This is because the retrodirective auxiliary beam of Figure 3 becomes wide and will degrade the sidelobes in a region equal to the retrodirective beamwidth. Third, if the jammers can be located so as to come through the backlobes, then an auxiliary array (or arrays) is needed which covers the backlobes or whatever angles are not covered by the main array. Fourth, it is possible to use only one parallel beam forming network instead of J with this beam forming network being time multiplexed so as to produce the J beams pointed at the J jammers and in this way reduce the hardware complexity of the adaptive-adaptive array processor. Finally, if the jammers are essentially orthogonal to each other at the outputs of the auxiliary beams then the (J+1) x (J+1) matrix inversion degenerates to J trivial 2x2 matrix inversions, each auxiliary jammer output beam being independently correlated with the main signal channel and separately subtracted from the main channel with an appropriately determined weight.

The physical explanation given above together with Figure 3 helps in understanding the performance of the adaptive-adaptive algorithm for non-perfect conditions and leads to the following insights. Even if the jammer location is in error by plus and minus a half beamwidth, jammer cancellation results similar to those in Figure 1c will still be obtained. There will only be a degradation of the sidelobe to the right or left of the null by the 3 dB. Furthermore, if the cancellor weights calculated using the SMI (or some other adaptive algorithm) are inexact, the null depth will be degraded but it is apparent from Figure 3 that the sidelobe level will be unaffected except for a small amount for the sidelobes just to the right and left of the null. Increasing M for the SMI computation will increase the null depth. If a jammer is not detected than it will not be cancelled out. This, however, will tend to occur only if the jammer is weak, a case not of as much concern because the jammer will then only cause

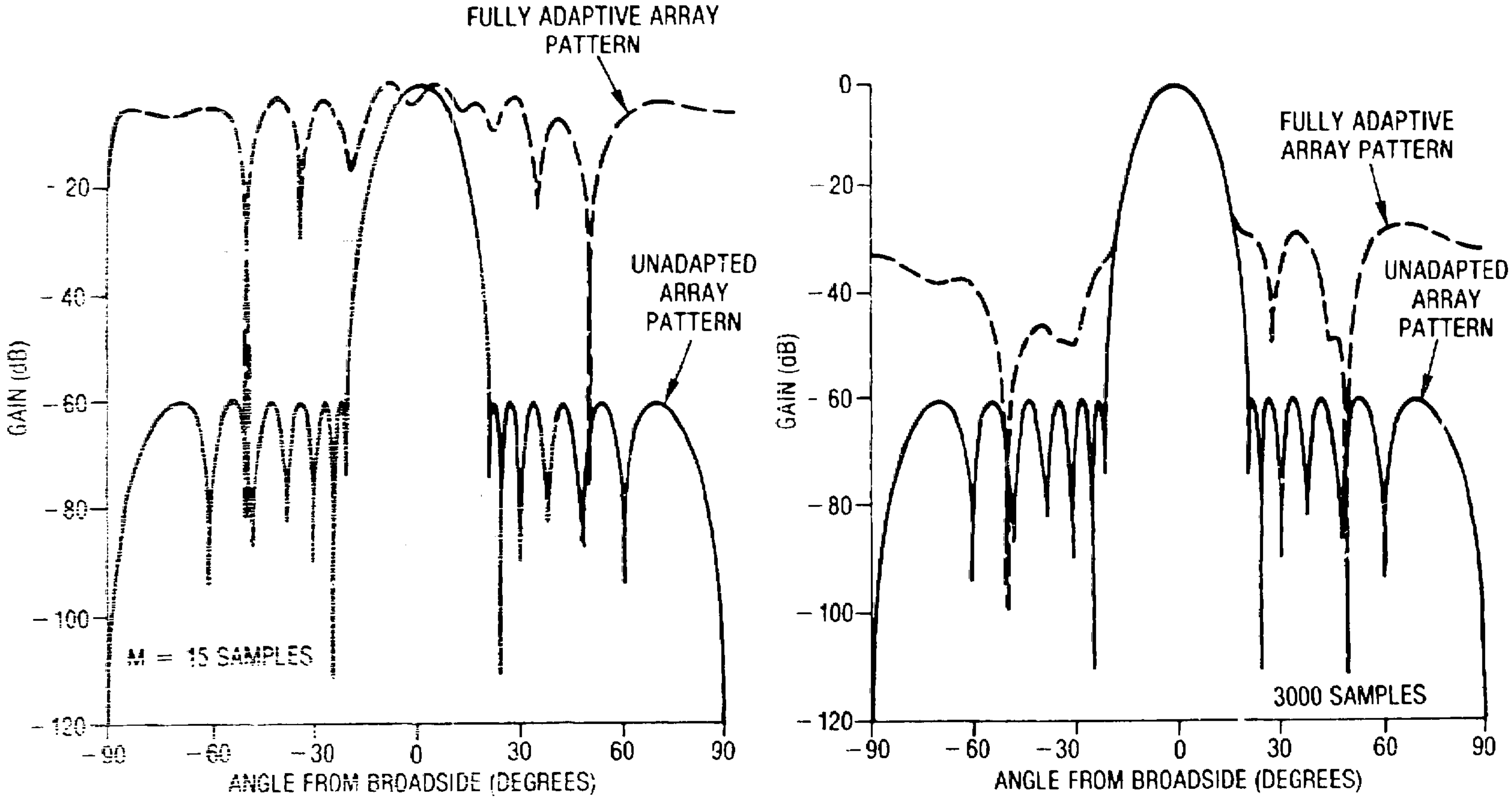

(a)

(b)

Figure 4. Fully adaptive array sidelobe level as a function of the number of time samples M used to estimate the covariance. SMI algorithm used 14 element array. 60 dB sidelobes (Chebyshev) for quiescent pattern. Two jammers located at ±50°. (a) M=15, (b) M=3000.

a small degradation in signal-to-interference ratio. If a jammer is estimated to be present when in fact it is not, the system will incur very little degradation in signal-to-interference ratio and in antenna sidelobe level because the SMI weights for the channel pointing in the direction where no jammer actually exists will be very low, the weight being established by the correlation between the noise in the main channel and the noise in the auxiliary channel pointing at no jammer with these noises being independent so that the correlation on the average is zero. If there are a large number of jammers then there can be antenna sidelobe level degradation if the auxiliary jammer beams have sidelobe levels that are not low enough. If J jammers are present then in order to avoid sidelobe level degradation in the main channel the auxiliary channel antenna sidelobe levels should be greater than $10 (\log_{10} J)$ dB down, a condition that can generally be met.

ONE DIMENSIONAL ARRAY: WIDEBAND JAMMER

To handle wideband jammer interference signals, the array of N elements would be subarrayed into M_S smaller contiguous arrays of equal size. These subarrays would be made small enough so that the jammer signal can be considered to effectively have narrow bandwidth, that is, the time dispersion across the subarray in the direction of the jammer is small compared to one over the bandwidth of the jammer. For simplicity assume that only one jammer is present. In this case each subarray would have its beam pointing toward the jammer. The outputs of these ports from the subarray would then be combined using time delay steering so as to form a narrow beam using the whole array pointing at the jammer. The number of subarrays M_S required will be dependent on the size of the antenna, the bandwidth of the jammer and the location of the jammer relative to the antenna boresite. All these parameters will be known so that M_S can be determined. Specifically, the jammer bandwidth can be taken to be equal to the signal bandwidth because jammer cancellation is only required over the signal bandwidth, the jammer noise outside the signal bandwidth being filtered out. The further the jammer is off mechanical boresite the larger the number of subarrays that would be required. Hence the number of subarrays required could be varied as a function of jammer location. If there is more than one jammer then J such time delay steered beams pointing at the J jammers would be formed. The number of subarrays for each of these jammers could be different depending on the jammer location, however, in practice M_S would probably be made the same for all the jammers, the largest M_S ever needed being selected for all jammers. When dealing with wideband jammers the adaptive-adaptive array has the additional advantage that the number of degrees of freedom does not increase as the bandwidth increases, a problem that exists with the conventional fully adaptive array. For the conventional fully adaptive array the number of degrees of freedom has to increase from N to something greater than M_SN when a wideband jammer has to be dealt with. These extra degrees of freedom are obtained by using adaptive tapped delay line filters at the output of every array element, with each tapped delay line filter having M_S taps. As a result an M_SNxM_SN matrix has to be inverted. In contrast for adaptive-adaptive array still only a $(J+1)x(J+1)$ matrix has to be inverted with thus no increase in the computation complexity.

TWO DIMENSIONAL ARRAY

The extension to a two-dimensional array is straightforward. For example, to locate the jammers a two-dimensional spatial discrete Fourier transform of the two-dimensional array outputs could be used. Then J jammer beams would be formed using the full two-dimensional array with these beams pointing at the J jammers. The SMI algorithm would then be applied to the outputs of the J auxiliary jammer beams together with the main signal beam. Thus for the two-dimensional adaptive-adaptive array there would still be only J+1 degrees of freedom after the transformation. The simplification in the number of complex multiplies for the two-dimensional array case can be even more dramatic than for the one-dimensional array case because of the much larger number of array elements that is usually involved in a two-dimensional array. By way of an example, assume that $N = 10,000$ and that the number of jammers J equals 10. Then with the fully adaptive array algorithm the number of complex multiplies required to form the adaptive array weights is $N_{FA} = 2 \times 10^{12}$. For the adaptive-adaptive array using the spatial two-dimensional discrete Fourier transform to locate the jammers, the number of complex multiplies required to form the adaptive array weights is

$$N_{EA} = 2(J+1)^3 + N \log_2 \sqrt{N} = 7\times10^4 = 10^5$$

over seven orders of magnitude less than for the fully adaptive array. (If the jammers are located by using the main beam to search for it then N_{EA} equals only about 3×10^3 and the improvement is about nine orders of magnitude. For $B = 1$ MHz, it would take of the order of $N/B = 10,000$ μs to locate the jammer.)

For the 1 MHz signal bandwidth, the adaptive weights multiplications have to be done at a rate of 10^{10} CM/sec for the fully adaptive array versus 1.1×10^7 CM/sec for the adaptive-adaptive array -- a saving of 3 orders of magnitude in throughput rate; see column four of Table 1. If hard wired multipliers are used, one for each weight, to do this weighting, then the number of multipliers could be reduced from 10,000 to 11 a reduction of 3 orders of magnitude. Furthermore, the settling time for the adaptive-adaptive array is much less than for the fully adaptive array. For the fully adaptive array the settling time is $2N = 2 \times 10^4$ time samples, whereas for the adaptive-adaptive array it would be $2(J+1) = 22$ time samples, three orders of magnitude factor.

ACKNOWLEDGEMENT

The idea of pointing high gain auxiliary antenna beams in the direction of the jammers appears to have first been suggested by Paul W. Howells, the inventor of the IF sidelobe cancellor.[8] He did not, however, form multiple auxiliary high gain beams in an array to achieve jammer nulling performance essentially that of a fully adaptive array while avoiding the associated sidelobe degradation problem as done in this paper. W.F. Gabriel of NRL has independently done this. Figure 1 was obtained using a simulation written by Carl D. Brommer (Raytheon).

REFERENCES

1. Applebaum, S.P., "Adaptive Arrays", IEEE Trans. on Antennas & Propagation, Vol. AP-24, No. 5, September 1976, pp. 585-598.

2. Key, S.M. and S.L. Marple, Jr., "Spectrum Analysis - A Modern Perspective", Proc. of the IEEE, Vol. 69, No. 11, November 1981, pp. 1380-1418.

3. Burg, J.P., "Maximum Entropy Spectral Analysis", Ph.D. Dissertation, Dept. of Geophysics, Stanford U., Stanford CA, May 1975.

4. Reed, I.S., J.D. Mallett and L.E. Brennan, "Rapid Convergence Rate in Adaptive Arrays," IEEE Trans. Aerosp. Electron. Syst., Vol. AES-10, No. 6 pp. 853-863, November 1974.

5. Barton, D.K., "Detection and Measurement", Chapter 2 in Brookner, E. (Ed.), Radar Technology, Artech House, 1977.

6. Gabriel, W.F., "Adaptive-Arrays--An Introduction", Proc. of IEEE, Vol. 64, No. 2, pp. 239-272.

7. Johnson, M.A., "Phased-Array Beam Steering by Multiplex Sampling", Proc. IEEE, Vol. 56, pp. 1801-1811, November, 1968.

8. Howells, P.W., "Explorations in Fixed and Adaptive Resolution at GE and SURC", IEEE Trans. on Antennas and Propagation, Vol. AP-24, No. 5, Sept. 1976, pp. 575-584.

PHASE-ONLY OPTIMIZATION OF PHASED ARRAY EXCITATION BY BI-QUADRATIC PROGRAMMING

Kazuhiro Hirasawa
Institute of Applied Physics
University of Tsukuba
Sakura, Ibaraki 305, Japan

ABSTRACT

An iterative method called bi-quadratic programming is introduced for phase-only optimization of phased array excitation. One excitation phase is changed at a time and an optimizing function has one maximum and one minimum value with respect to one excitation phase. These extremum points and the corresponding phase changes are analytically calculated at each iteration, and does not have to be small. The example shows the rapid convergence property of this method.

INTRODUCTION

Excitation phase adjustments and constant excitation amplitudes of antenna array feeding are very useful to high speed electronic scanning. A perturbation method and a general nonlinear optimization method have been applied to the phase-only optimization of antenna array excitation [1] ∿ [5].

In this paper, an iterative method called bi-quadratic programming is introduced. At each iteration one excitation phase is changed and an optimizing function becomes a bi-quadratic form. It has one maximum and one minimum value with respect to one excitation phase. These extremum values and the corresponding phases are obtained exactly in a closed form expression. Thus the best phase change at each iteration is calculated at once and does not have to be small.

The application of this iterative method to pattern shaping and optimization of gain is described. Numerical results for gain optimization of linear, planar and circular arrays are obtained and the convergence characteristics are shown.

OPTIMIZING FUNCTION

For pattern shaping an optimizing function G is defined as

$$G = \sum_{i=1}^{M} w_i |E_i - E_{0i}|^2 \qquad (1)$$

where E_i and E_{0i} are the normalized radiation field value and the desired value for the ith direction, respectively. M is the number of the specified directions and w_i (≥ 0) is the weighting function.

In (1) the normalized field is given by

$$E_i(\theta_i,\phi_i) = \frac{E_i'(\theta_i,\phi_i)}{E_0'(\theta_0,\phi_0)} \quad . \qquad (2)$$

The field $E'(\theta,\phi)$ is calculated by the method of moments with N' subsectional current expansion functions on the antenna and is obtained in a matrix form as [6]

$$E'(\theta,\phi) = [\Phi][Y][V'] \qquad (3)$$

where [Y] is the N'× N' generalized admittance matrix and each element is the admittance between expansion functions.

The vector [V'] is the N'× 1 generalized voltage matrix and the only nonzero elements are the ones corresponidng to the feed voltages. The vector [Φ] is the 1 × N' phase matrix and each element has phase difference information between an expantion function and a far field point. The constants such as the distance from an antenna to a far field point are included in the vector [Φ].

In (3) the columns of [Y] corresponding to the zeros of [V'] are deleted and $E'(\theta,\phi)$ are expressed by feed voltages as

$$E'(\theta,\phi) = [B][V] \qquad (4)$$

where [B] is the 1 × N matrix and its elements are obtained from [Φ][Y]. The vector [V] is the N × 1 feed voltage matrix and N is the number of the feeds. By using (4), (2) becomes

$$E_i(\theta_i,\phi_i) = \frac{[B_i][V]}{[B_0][V]} . \tag{5}$$

Equation (1) is rewritten by using (5) as

$$G = \frac{[\tilde{V}^*][A][V]}{[\tilde{V}^*][D][V]} . \tag{6}$$

where [A] and [D] are N × N Hermitian matrices, and are positive semi-definite. The symbols ∿ and * denote transpose and complex conjugate, respectively. In (6) G is the ratio of quadratic forms with respect to [V].

The inverse of a power gain can also be expressed in the form of (6) [6]. In this case the matrix [A] is positive definite, and minimization of G is usually desired.

Thus the optimizing functions for pattern shaping and gain optimization become ratics of quadratic forms, and bi-quadratic programming can be applied for these cases. The optimization procedure for G is described in the next two sections.

ONE-DIMENSIONAL MINIMIZATION

Let the ith feed voltage be

$$V_i = V_{i0}e^{j\alpha} \tag{7}$$

where V_{i0} is the initial complex voltage and α is the phase variable. The optimizing function G in (6) is minimized with respect to α. The rest of the feed voltages are assumed constant with respect to α.

By inserting (7) into (6) and with the Hermitian property of [A] and [D] the function G is given by

$$G = \frac{ae^{j\alpha} + a^*e^{-j\alpha} + c}{be^{j\alpha} + b^*e^{-j\alpha} + d} \tag{8}$$

where a and b are complex constants, and c and d are real constants.

The function G is the ratio of quadratic forms with respect to $e^{j\alpha}$, and may be called bi-quadratic forms. Antenna systems can often be characterized by performance indexes which are bi-quadratic forms. Examples are input resistance and reactance, coupling coefficient, gain and so on [7].

Differentiating G in (8) with respect to α and setting $\partial G/\partial\alpha = 0$, one has

$$(ad - bc)e^{2j\alpha} + 2(ab^* - a^*b)e^{j\alpha} - (a^*d - b^*c) = 0. \qquad (9)$$

Equation (9) has the solution

$$e^{j\alpha} = \frac{2j\mathrm{Im}(ab^*) \pm \sqrt{|ad - bc|^2 - 4[\mathrm{Im}(ab^*)]^2}}{ad - bc} \qquad (10)$$

where Im is its imaginary part. It can be easily shown that the magnitude of the right-hand side of (10) is 1. Then α becomes always real.

The function G has one maximum and one minimum value when α satisfies (10). Fig. 1 shows the characteristics of G with respect to α. The phase α for the extremum G can be easily calculated from (10), and by using this α the extremum G is obtained from (8).

BI-QUADRATIC PROGRAMMING

The characteristics of G with respect to α described in the previous section is used to find a local minimum G by more than one excitation phase adjustment.

The procedure is as follows: Choose all the initial excitation phase $\alpha_1 = \alpha_2 = \cdots = \alpha_N = 0$ where the initial G is G_0. Then, for the excitation phase of the first feed, obtain the phase change $\Delta\alpha_1 = \alpha_1^0$ for the minimum G $(= G_1^0)$ under the conditions $\alpha_2 = \alpha_3 = \cdots = \alpha_N = 0$. The minimum G_1^0 obtained is always smaller than or equal to G_0. For the excitation phase of the second feed, obtain the phase change $\Delta\alpha_2 = \alpha_2^0$ for the minimum $G(= G_2^0)$ under the conditions $\alpha_1 = \alpha_1^0$, $\alpha_3 = \alpha_4 = \cdots = \alpha_N = 0$ where $G_1^0 \geq G_2^0$. After the phase change $\Delta\alpha_N = \alpha_N^0$ and the minimum G_N^0 are obtained, repeat the procedure for the new initial conditions $\alpha_1 = \alpha_1^0$, $\alpha_2 = \alpha_2^0, \cdots, \alpha_N = \alpha_N^0$.

Each minimization starts at the previous minimization and each phase change is analytically obtained. The excitation phase and G are obtained as

$$
\begin{aligned}
\alpha_1 &= \alpha_1^0 + \alpha_1^1 + \cdots \\
\alpha_2 &= \alpha_2^0 + \alpha_2^1 + \cdots \\
&\vdots \qquad \vdots \\
\alpha_N &= \alpha_N^0 + \alpha_N^1 + \cdots \\
G_0 &\geq G_1^0 \geq G_2^0 \geq \cdots \geq G_N^0 \geq G_1^1 \geq G_2^1 \geq \cdots .
\end{aligned}
\tag{11}
$$

The iteration can be repeated until it becomes evident that further improvement of G can not be expected.

NUMERICAL RESULTS

Optimum power gains of a 24 element linear array, a 5 × 5 element planar array and a 24 element circular array are calculated by using bi-quadratic programming.

As an array element a center-fed half-wave dipole antenna with the radius 0.005λ is chosen. All the excitation amplitudes are set equal to unity. The interelement spacing between parallel elements is 0.5λ and the one between colinear elements is 0.1λ.

To obtain elements of [A] and [D] in (6), the array is analysed by the method of moments with piecewise sinusoidal expansion and weighting functions. Mutual coupling between antenna elements are all taken into account.

The inverse of the power gain in the direction $\theta = 90°$ and $\phi = 70°$ is optimized by varying all the excitation phases. The iterative procedure is started from zero excitation phases.

The convergence characteristics of 1/G are shown in Fig. 2. The optimum gains are 46.1 after about 50 iterations (i.e. 50 excitation phase evaluations) for the linear array, 41.0 after about 55 iterations for the planar array, and 30.8 after about 90 iterations for the circular array.

As a second example the same planar array as before is considered and the inverse of the power gain in the direction $\theta = 70°$ and $\phi = 70°$ is optimized. All the initial excitation phases are zero where 1/G = 0.012, and after about 50 iterations an optimum 1/G (= 38.1) is obtained. The vertical pattern for $\phi = 70°$ and the pattern for $\theta = 70°$ are shown in Figs. 3 and 4, respectively.

CONCLUSIONS

Bi-quadratic programming was introduced to optimize the excitation phase of phased arrays. Each step of iterations required only one excitation phase change, and the necessary phase change was obtained analytically at once from the bi-quadratic form of the optimizing function.

The example for linear, planar and circular array gain optimization showed the rapid convergence property of the method. Mutual coupling between antenna elements was taken into account in the calculation. This method may be applied to optimize excitation phases of any antenna system which can be accurately analysed.

REFERENCES

[1] Cheng, D.K.: "Optimization techniques for antenna arrays", Significant phased array papers, ed. R.C. Hansen (Artech House, Inc., Massachusetts, 1973), pp.23-33, or Proc. IEEE, 59, pp.1664-1674, Dec. 1971.

[2] Steyskal, H.: "Simple method for pattern nulling by phase perturbation", IEEE Trans. Antennas & Propagat., AP-31, pp.163-166, Jan. 1983.

[3] Goto, N. and Tsunoda, Y.: "Sidelobe reduction of circular array with a constant excitation amplitude", IEEE Trans. Antennas & Propagat., AP-25, pp.896-898, Nov. 1977.

[4] Giusto, R and Vincenti, P.D.: "Phase-only optimization for the generation of wide deterministic nulls in the radiation pattern of phased arrays", IEEE Trans. Antennas & Propagat., AP-31, pp.814-817, Sept. 1983.

[5] Shore, R.A.: "Nulling at symmetric pattern location with phase-only weight control" IEEE Trans. Antennas & Propagat., AP-32, pp.530-533, May 1984.

[6] Harrington, R.F.: "Field computation by moment methods" Macmillan Co., New York, 1968.

[7] Hirasawa, K.: "Bounds of uncertain interference between closely located antennas", IEEE Trans. Electromagn. Comp., EMC-26, pp.129-133, Aug. 1984.

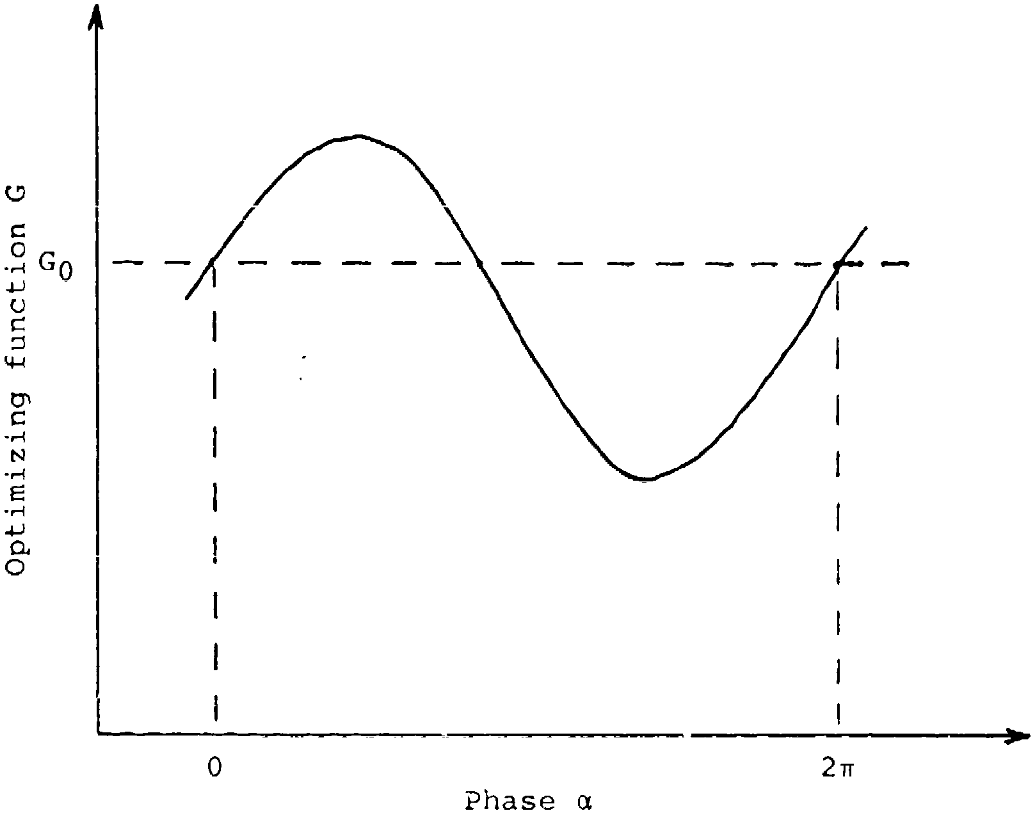

Fig. 1 An optimizing function with respect to a phase α.

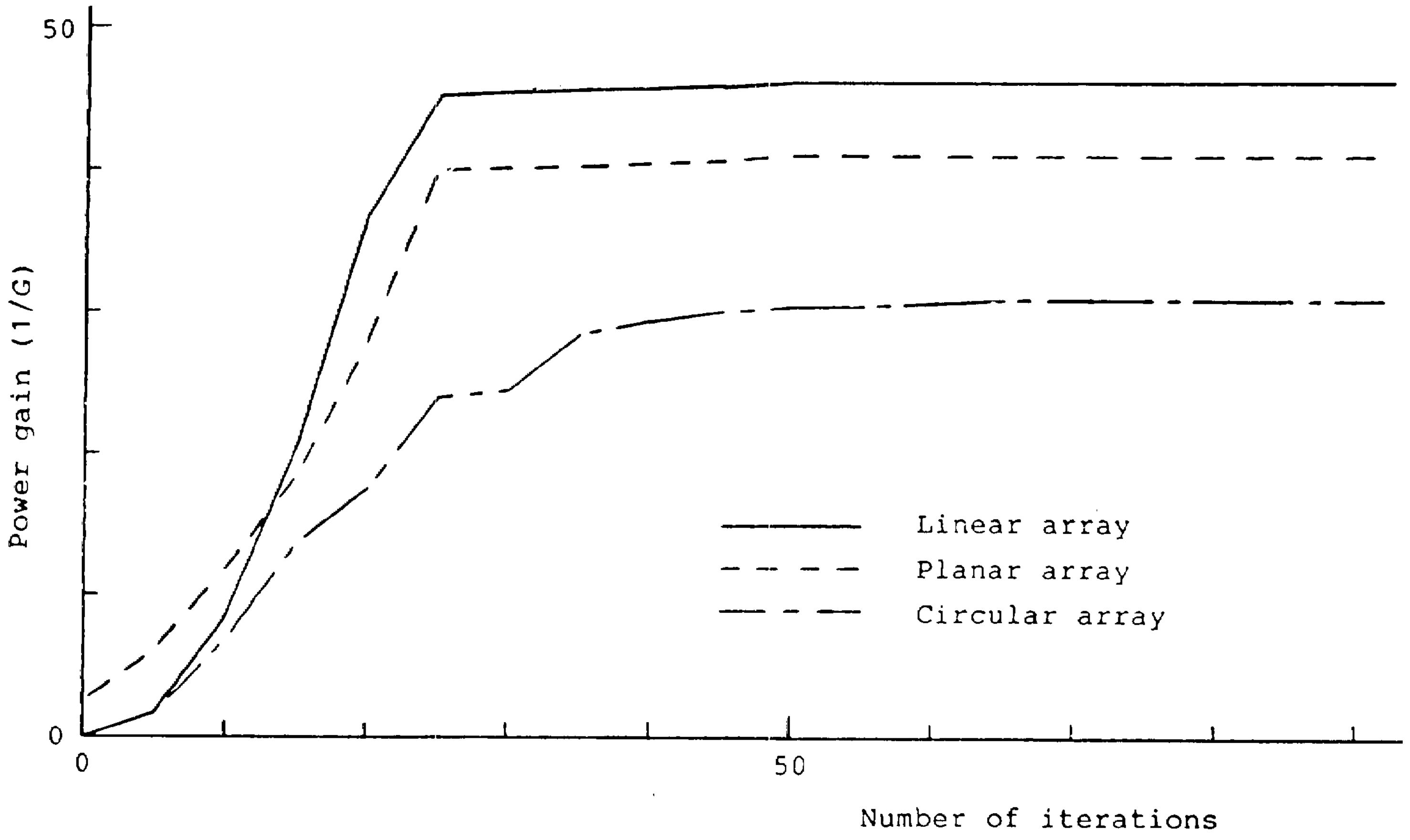

Fig. 2 Convergence characteristics.

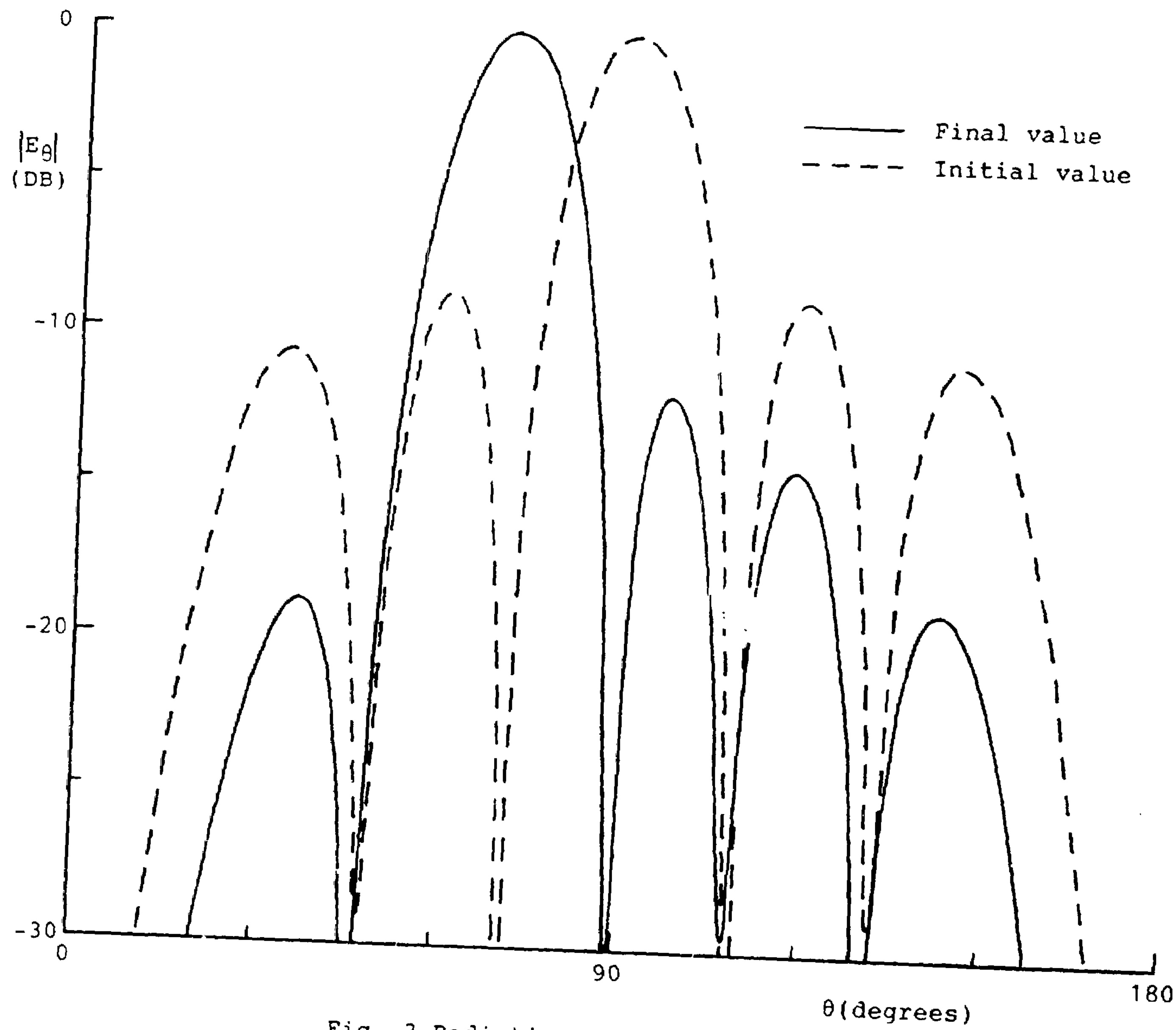

Fig. 3 Radiation pattern (ϕ = 70°).

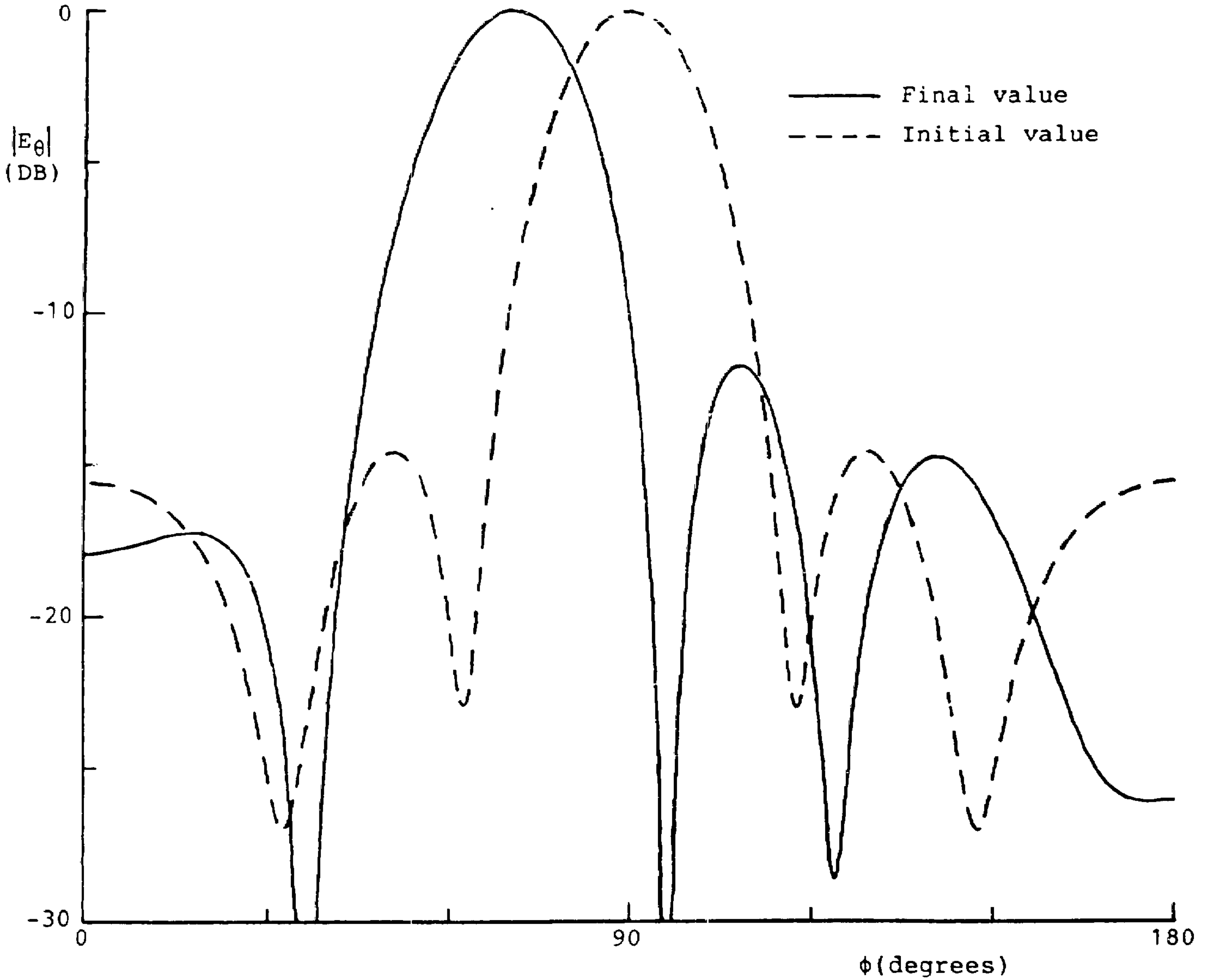

Fig. 4 Radiation pattern (θ = 70°).

A NEARLY FREQUENCY-INDEPENDENT SIDELOBE SUPPRESSION TECHNIQUE FOR PHASED ARRAYS

By: George Monser
Raytheon Company
P.O. Box 1542
Goleta, CA 93117

ABSTRACT

Described herein is a practical technique for achieving low sidelobes over wide bandwidths and wide angles in receive phased-array applications. Using phase-matched broadband attenuators with each array element, the signal outputs were modified to approximate the prescribed low sidelobe illumination. Several illumination functions were then modeled to show sidelobe and beam efficiency trade-offs. Test results for two short, lens-fed, linear arrays (N<20) are included and compared against predicted values. Sidelobes compared favorably with predicted values (within 1 to 3 dB). Measured efficiencies agreed within 1 to 2 dB to the computed values.

INTRODUCTION

This paper describes a nearly frequency-independent technique for achieving low sidelobes by using illumination-shaping attenuators to approximate the prescribed low-sidelobe aperture distribution, recognizing that a fixed aperture distribution provides low sidelobes which are frequency independent (except for small apertures). Initially, -25 dB (or lower) sidelobes were deemed necessary for our application. Later, trade studies indicated -18 dB would be acceptable. Results given herein pertain to lens-fed linear arrays of N=20 or fewer elements. However, the design method is not restricted.

MODELING

Figure 1 shows the basic design model, consisting of a short linear array of typically N=20 or fewer elements and signal paths to the lens occurring through coaxial cables, each differing in electrical length. Combined with a lens, the cables provide various phase gradients yielding beam coverage over a wide sector, as illustrated in Figure 2.

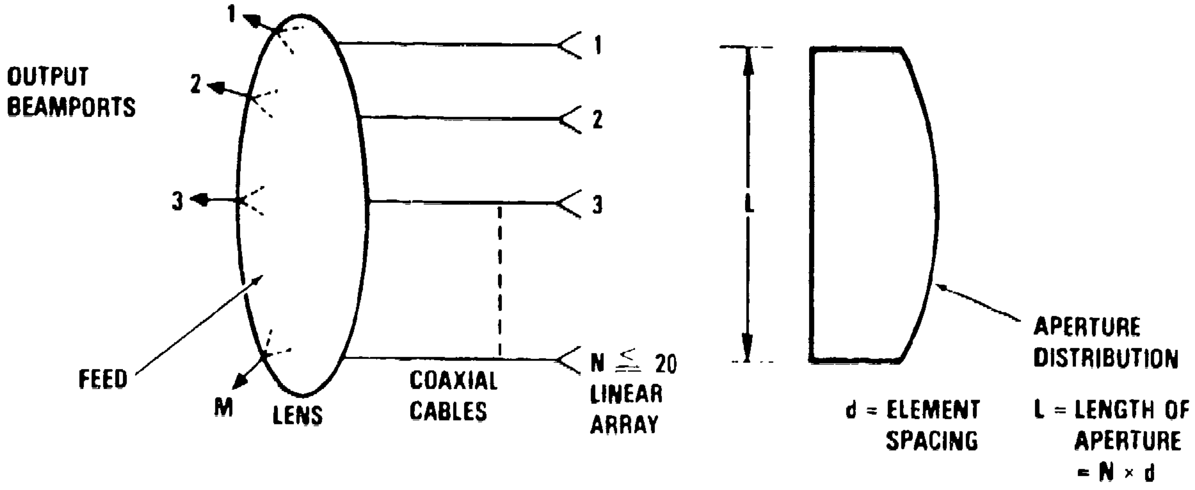

FIGURE 1. BASIC GEOMETRY

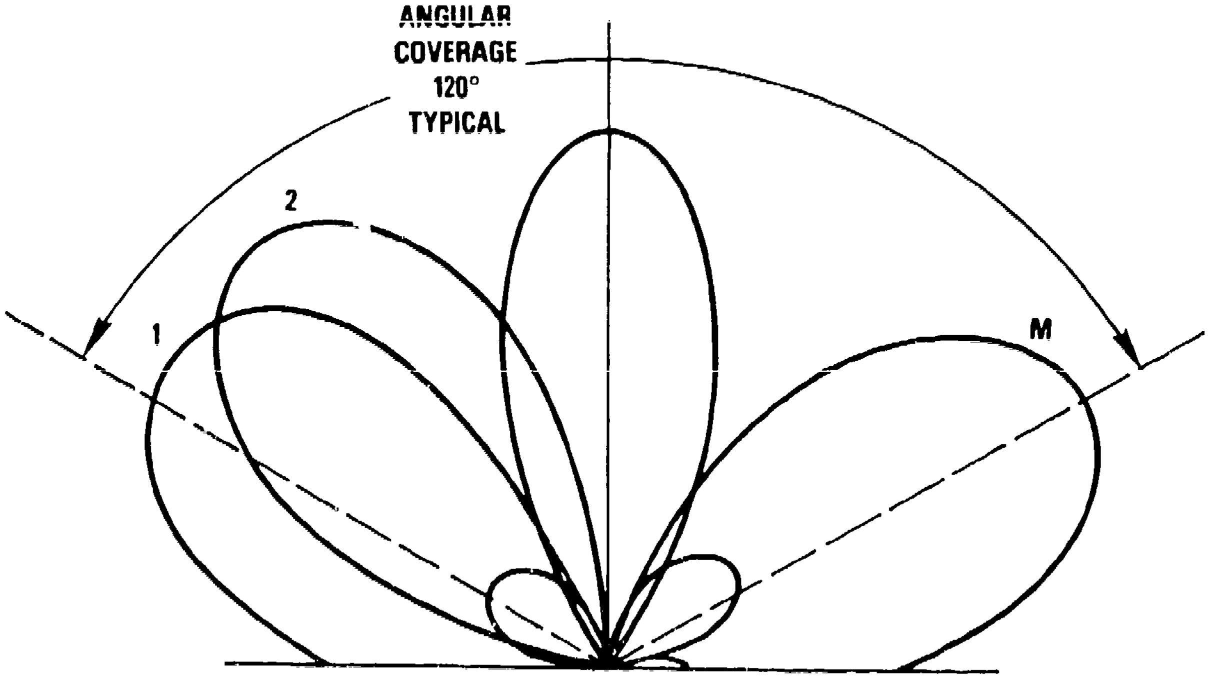

M = NUMBER OF BEAMS DISTRIBUTED OVER ANGULAR SECTOR

FIGURE 2. ANGULAR COVERAGE (IDEALIZED)

For the simple model shown in Figure 1, the illumination function or linear aperture distribution determining sidelobe levels is established by the lens and beamport feed geometries. Reasonably low sidelobes are attainable by appropriate lens design and/or multiple beamport feeds. However, the behavior tends to be frequency dependent.

Figure 3 shows an alternative, nearly frequency-independent design. For this case attenuators are added between the lens and the array, each differing in attenuation value. All are phase matched.

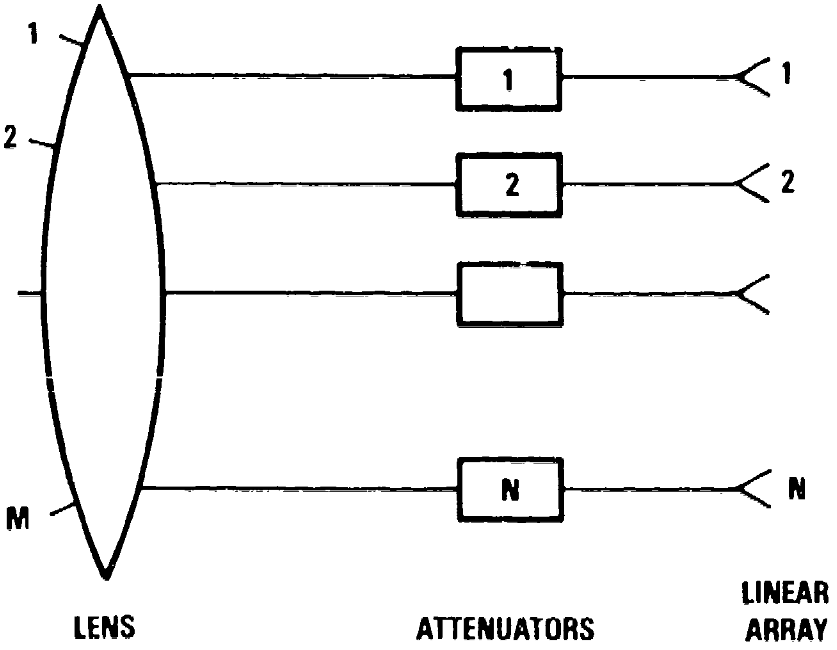

FIGURE 3. BASIC DESIGN WITH ATTENUATORS

Figure 4 illustrates the function of the attenuators in approximating the distribution. Typical calculated beam patterns for several distributions (N=12) are shown in Figure 5. Both the Dolph-Tschebyscheff and cosine-square models yielded low sidelobes. However, the monotonic roll-off of the cosine-squared distribution seemed preferable compared with the flat sidelobe distribution resulting from the Dolph-Tschebyscheff design. As expected, comparison of cosine versus the cosine-squared models showed the latter yielding much lower sidelobes. However, further modeling, using typical random amplitude and phase errors, showed that the cosine-squared design degraded 9 dB compared with 4 dB for the cosine design for RSS errors of 1 dB and 5 degrees. These results, taken with greater efficiency and less beam broadening, lead to the selection of a cosine distribution for the hard models. A small pedestal was added to the cosine distribution, slightly improving efficiency, but also slightly degrading sidelobe levels (-22 dB).

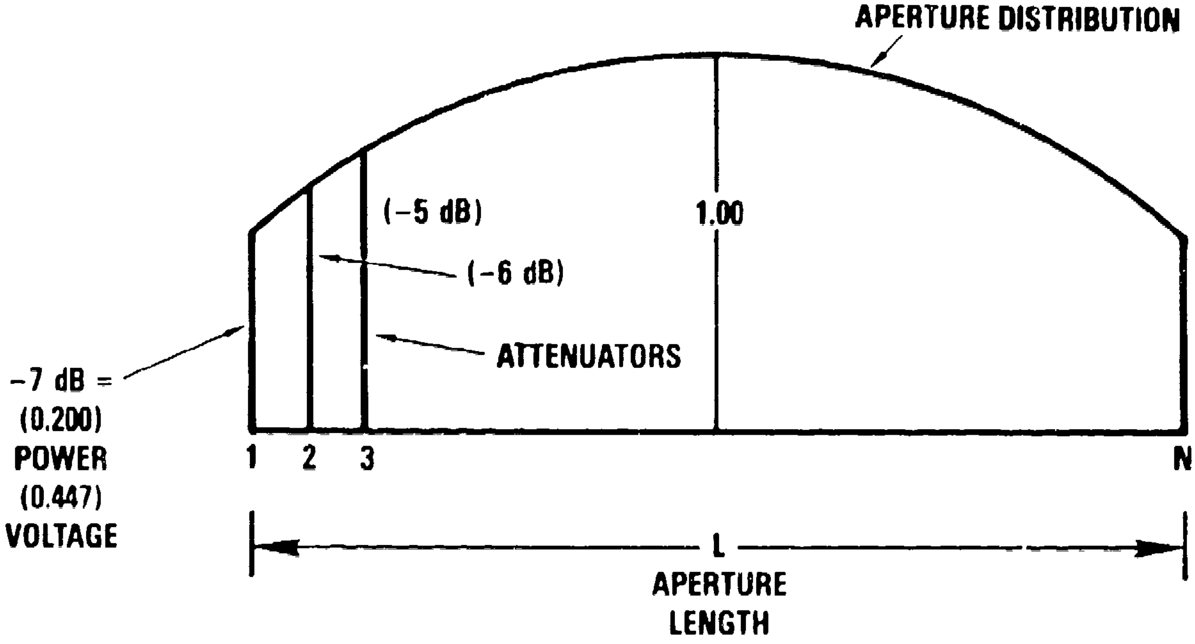

FIGURE 4. ILLUMINATION-SHAPING ATTENUATORS

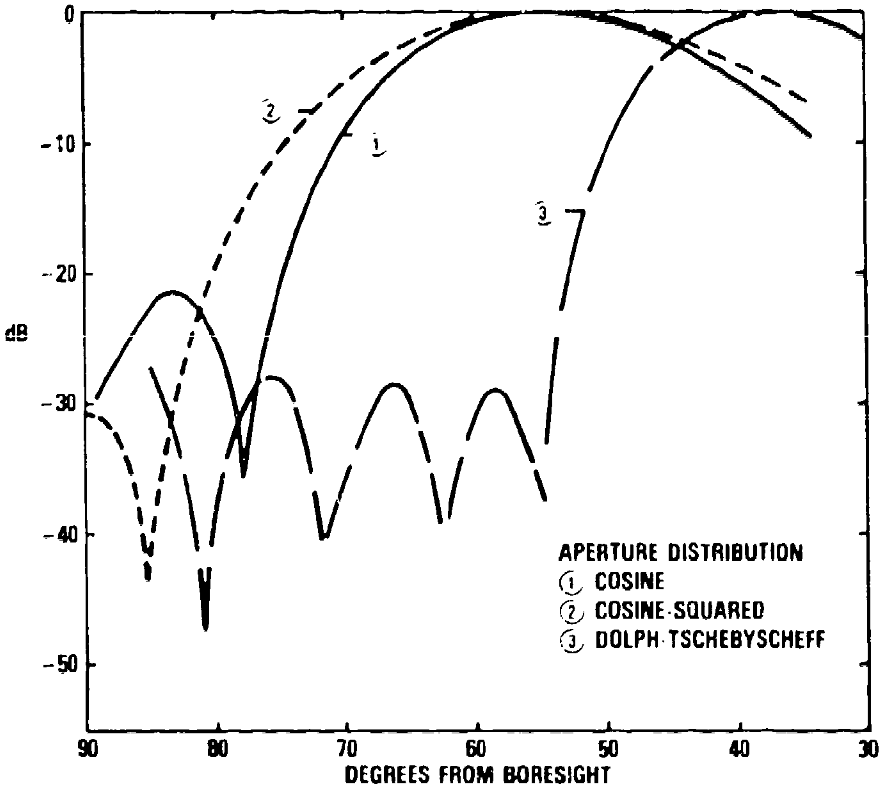

FIGURE 5. BEAM SHAPES FOR VARIOUS APERTURE ILLUMINATION FUNCTIONS (COMPUTER GENERATED)

SELECTION OF ATTENUATORS

As indicated earlier, the attenuators should be phase matched, independent of attenuation value over the full frequency band. A typical set of specifications follow:

Phase Tracking: ± 5° (max)

Temperature Sensitivity: 0.0001 dB/(dB x°C) (max)

Amplitude Tracking: ± 0.3 dB up to 10 dB;
± 0.5 dB up to 20 dB

TEST RESULTS

Two designs, as shown in Figure 6, were evaluated; an N=12 design, from 11 to 18 GHz and an N=18 design, from 3 to 5 GHz. Since the arrays were dual-polarized, couplers were used to combine each element output. In addition, circulators were used to reduce interaction effects. All components, including attenuators, were checked for amplitude and phase tracking before installation into the models. A typical 3-GHz field-of-view multibeam pattern for the N=18 model is shown in Figure 7. Worst-case sidelobes of about -18 dB can be observed.

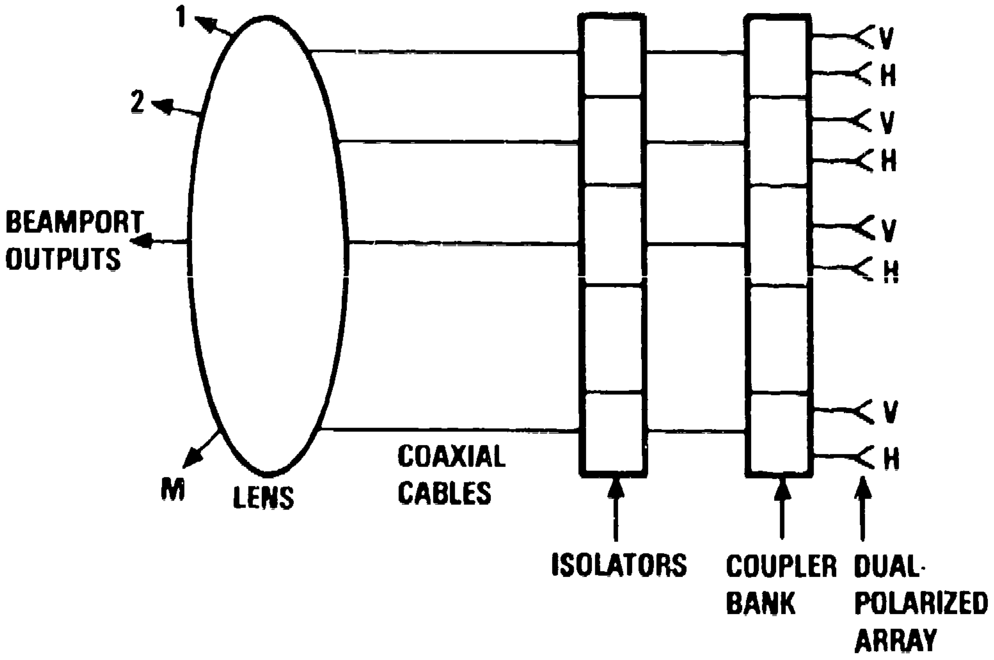

FIGURE 6. HARD MODEL(S) SCHEMATICS

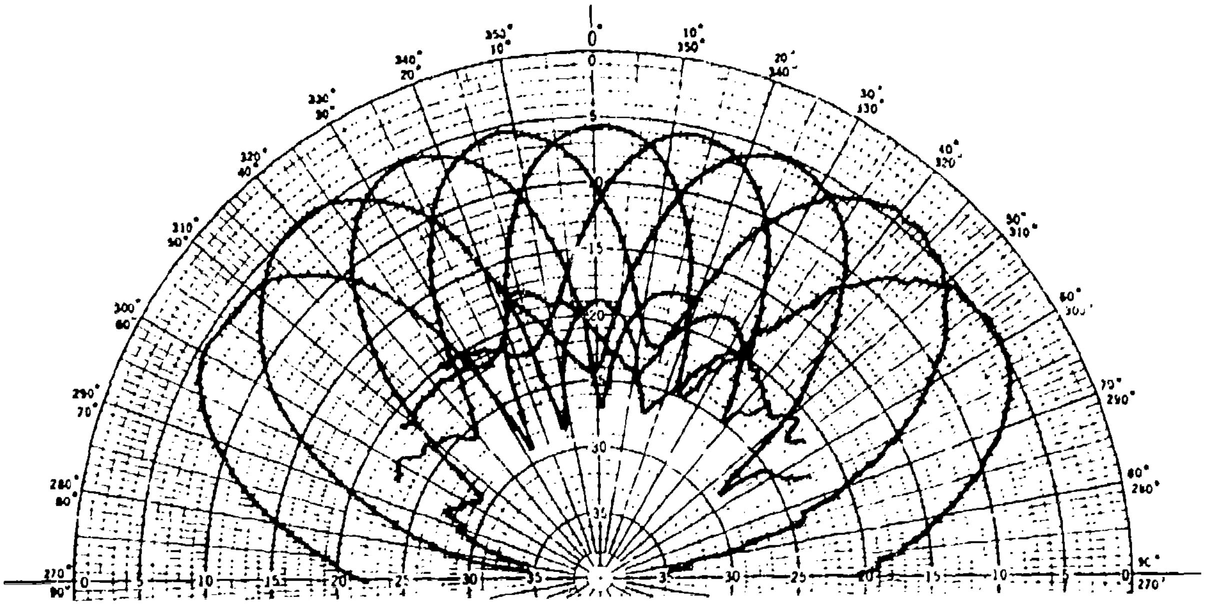

FIGURE 7. N=18, VERTICAL POLARIZATION, F=3 GHz

Figure 8 shows a 15-GHz multibeam pattern for the N=12 model with worst-case sidelobes of about -12 dB. Figures 9 and 10 show sidelobe behavior for all beams at 3 and 5 GHz for the N=18 model.

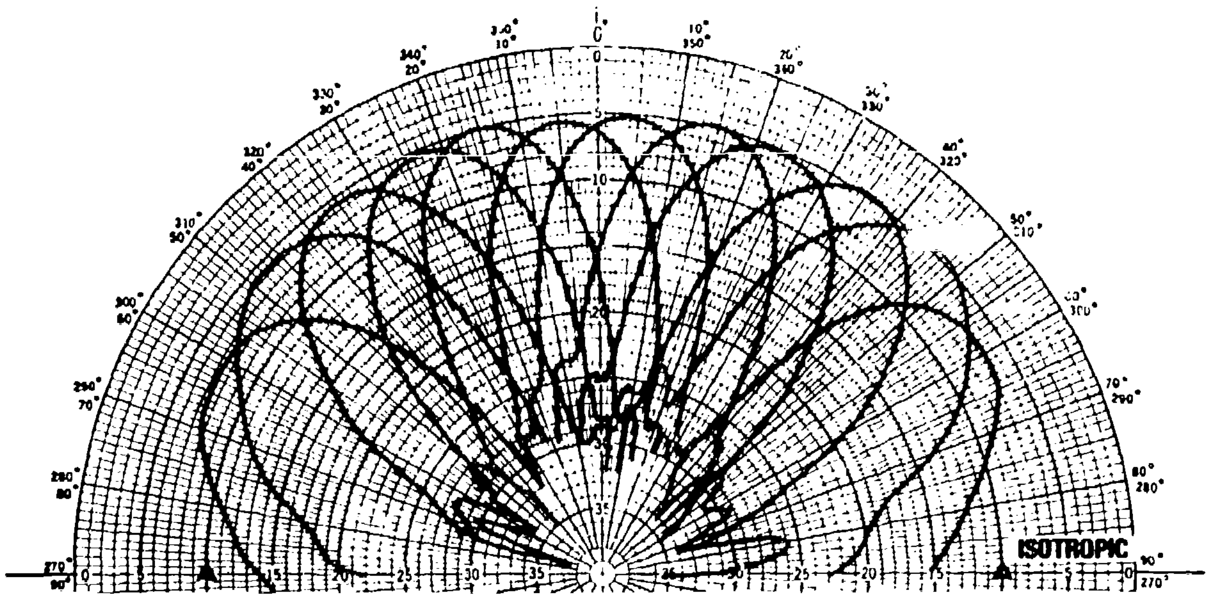

FIGURE 8. N=12, VERTICAL POLARIZATION, F=15 GHz

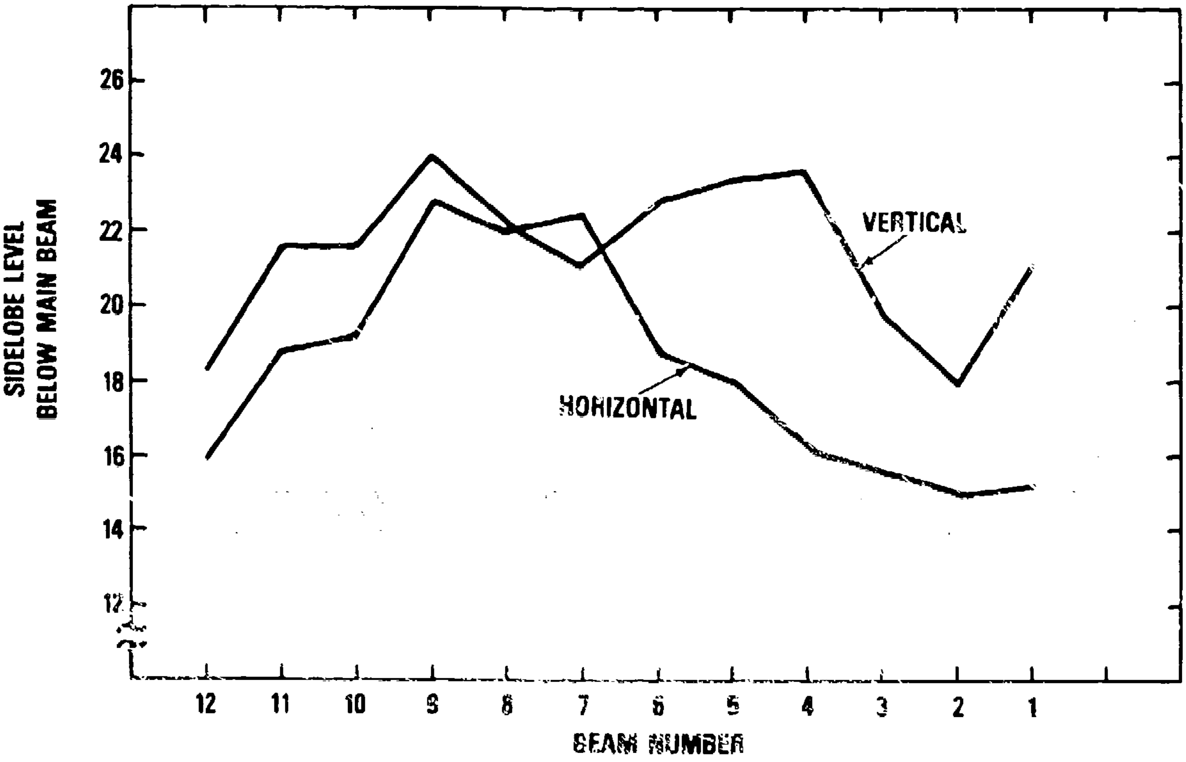

FIGURE 9. N=18, SIDELOBE LEVEL, ALL BEAMS, F=3 GHz (TWO POLARIZATIONS)

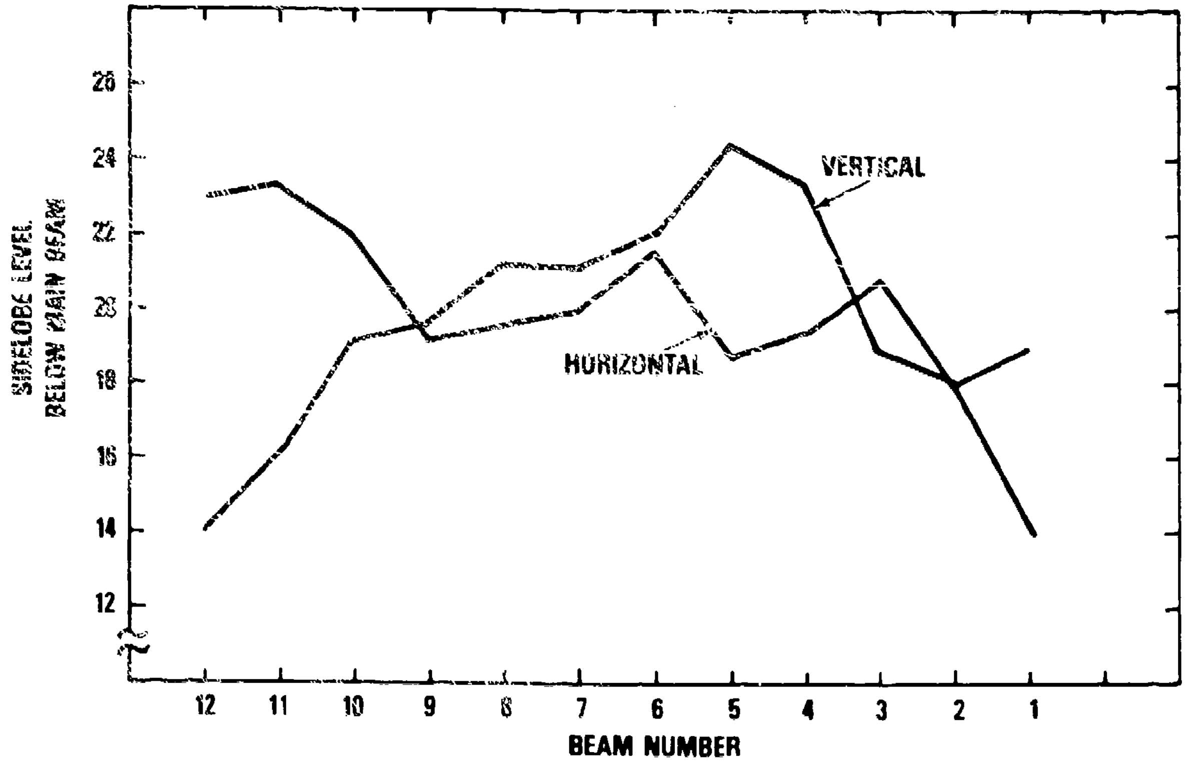

FIGURE 10. N=18, SIDELOBE LEVEL, ALL BEAMS, F=5 GHz (TWO POLARIZATIONS)

Table 1 shows both the measured lens-plus-attenuator loss and the cosine-computed loss for each model. The excess loss, beyond the 3.5 dB*, is attributed to the cables and lens.

TABLE 1. LOSS ASSESSMENT

NUMBER OF ARRAY ELEMENTS	COMPUTED COSINE ON PEDESTAL LOSS (dB)	MEASURED LOSS, ATTENUATORS, CABLES, AND LENS (dB)
18	3.52	7.9
12	3.49	6.5

DISCUSSION

The results given earlier showed that the combined loss (lens and attenuators) was about equal for two models. This was expected since both lenses were of similar designs causing comparable spill-over losses. However, the lenses differed in that diverse dielectrics were used so that the dissipative and reflective losses varied.

As stated, -22 dB or lower sidelobes was a design objective for both models. The beam patterns and analysis of behavior for the lower frequency model (N=18) approached the objective. However, the N=12 model exhibited higher sidelobes. RSS amplitude and phase errors for the higher frequency model (N=12) were more significant because component errors tend to increase with frequency. Also, amplitude variations in both the lens and the array were higher due to the fewer elements and edge or end effects.

Finally, each of the tested models consisted of more than an array, lens, and attenuators. In addition, couplers and circulators were installed in each line. Thus, the combined RSS errors of the tandem components was much higher than for the attenuators alone. Consequently, the sidelobes increased above the design objective.

CONCLUDING REMARKS

A practical method for achieving low sidelobes over wide bandwidths has been demonstrated. Using phase-matched attenuators in tandem with the array, illumination tapers consistent with low sidelobes can be approximated. However, careful attention and minimization of other sources of error must be achieved in order to maintain these results.

Current trade literature indicates that it may be practical to use these design concepts up to 40 GHz.

ACKNOWLEDGEMENTS

The author wishes to express his appreciation to George S. Hardie and Juan M. Duarte for the computer-generated beam patterns and the RSS assessments of sidelobe behavior.

---

* See Appendix A for method of calculation.

APPENDIX A: LOSS COMPUTATION

Loss of the network, shown in Figure 3, is readily found by considering the unit in a transmit mode.

For example, for a central lens beamport, outputs are delivered to each lens array output and subsequently to each array element. The far-field voltage is a summation of 'N' voltages. Placing attenuators in each line (as shown) reduces the power according to the attenuation value and the voltages proportional to the square root of the powers. Comparison of the voltage summation with and without attenuators yields the effective loss.

As an example, select a condition where the lens is offering equal excitation to all 'N' elements of the array. Without attenuators in place, for N=12 the resultant voltage = 12.00. Now with attenuators:

ELEMENTS	ATTENUATOR VALUE (dB)	POWER RATIO	VOLTAGE RATIO
1 and 12	12.0	0.063	0.251
2 and 11	7.0	0.199	0.447
3 and 10	4.0	0.398	0.631
4 and 9	2.0	0.631	0.794
5 and 7	1.0	0.794	0.891
6 and 7	0.0	1.000	1.000

Total Voltage = 8.028

$$\text{Loss} = 20 \log_{10} \frac{8.028}{12.000} = 3.49 \text{ dB}$$

It should be noted that this computed loss includes both the normal attenuation loss and the aperture distribution loss.

A similar computation was performed for N=18 yielding 3.52 dB. Finally, using an N=6 array with outer elements loaded on each end, relative gains without the attenuators in place were measured over band for the following attenuator distribution.

Y	Y	Y	Y	Y	Y
2 dB	1 dB	0 dB	0 dB	1 dB	2 dB

Frequency (GHz)	Levels with Respect to Gain Standard (dB) W/O Attn's	With Attn's	|Δ|
8.0	-18.0	-19.0	1.0
10.0	-13.6	-14.8	1.2
12.0	-15.8	-15.8	0.0
14.0	-13.5	-14.4	0.9
16.0	-14.6	-15.9	1.3
18.0	-17.7	-19.0	1.8

Yielding an average loss over the band of 1.03 dB versus a computed loss of 0.96 dB.

OPTIMIZATION OF ANTENNA SURFACES FOR CONFORMAL ARRAYS

by: G. D. Arndt and J. H. Suddath - NASA/JSC, Houston, Texas
J. R. Carl - Lockheed, Houston, Texas

ABSTRACT

Two conformal array programs are presented: (1) an initial shaping of the antenna surface, together with a minimization of the number of antenna elements, to achieve a given coverage profile, and (2) a design program, with inputs from the initial optimization program, provides antenna pattern characteristics and allows refinements in the surface shaping and element sizing. Two antenna applications of these programs are discussed.

INTRODUCTION

Conformal arrays are normally fitted on the contours of a vehicle, e.g. aircraft and missiles, where the surface shape is dictated to the antenna designer. A conformal array is usually better suited than a planar array for applications requiring moderate gain and wide angular coverage. This condition might well exist in serving widely dispersed simultaneous users. In these latter systems, shaping of the array surface may be available to the designer. The purpose of this paper is to present optimization and design programs for shaping an antenna's radiating surface to achieve a given spatial coverage/gain characteristic. The number of radiating antenna elements is minimized, thereby lowering the hardware costs, particularly in distributed antennas, by reducing the number of phase shifters, low-noise amplifiers, power amplifiers, etc.

The computer program which determines the antenna configuration solves the problem of arranging and sizing array elements to provide a specified far field pattern and an initial estimate of the antenna element configuration. The far field is specified as given values of gain at selected values of angle-off-of-bore-sight. The initial configuration is specified by the number of elements, their in-plane dimensions, gain, and tilt angle relative to bore sight.

Using the results of the initial optimization program as inputs to a conformal array simulation, the detailed design and antenna performance characteristics (main beam, grating lobes, Step 4) Let x be a 3N-vector whose elements are the variables that can be adjusted, i.e.,

$$x = \text{col.}\,[A_1, A_2, \cdots A_N, \ell_1, \ell_2, \cdots, \ell_N, \theta_1, \theta_2, \cdots, \theta_N]$$

and let d be the M-vector difference

$$d = g - f$$

Step 5) Let a measure of how well the 'realized' field matches the specified field be given by the scalar

$$J = \frac{1}{2} d \cdot d$$

Step 6) Input g and x (an initial guess at the configuration) to the program. Compute d and J. If the 'realized' and specified fields do not match up J will be a positive number whose magnitude is indicative of the mismatch. Thus the problem becomes that of perturbing the vector x (iteratively) in such a way as to drive J toward zero (zero indicates a perfect match).

Step 7) To first order, a perturbation to x, denoted by δx, produces a change in J given by $\delta J = -d \cdot f_x \delta x$ where f_x is an M x 3N matrix of partial derivatives

Step 8) If δx is chosen to be

$$\delta x = K f_x^T [f_x f_x^T]^{-1} d$$

where $0<K<1$ is a scalar step size parameter and superscript T denotes matrix transpose

Step 9) Then substituting this δx into the δJ equation would give

$$\delta J = -2KJ$$

indicating that J would be reduced if x were replaced by $x + \delta x$

Step 10) The iterative process then is to try x and if the mismatch (J) is "too big," try

$$x_{NEW} = x_{OLD} + \delta x$$

where δx is given into Step 8.

In summary, the program determines the combined contributions of the elements (f) at each of the specified far field points (g), and computes the residuals (d). The iterative technique then adjusts the in-plane dimensions $\{\ell_i\}$, areas $\{A_i\}$, and tilts $\{\theta_i\}$, so as to drive the residuals toward zero. Since this is an iterative process, the rate and extent of convergence is strongly dependent upon two factors: (a) the etc.) can be ascertained. Effects of antenna errors and wide scan angles are included in this simulation program.

The design optimization is applied to two low-earth-orbit (LEO) space applications: (1) a 23 dB gain, hemispherical coverage antenna supporting five simultaneous beams, and (2) a narrow-beamwidth, corridor coverage antenna with 41 dB gain to five users. Grating lobe degradations are reduced by minimizing the number of elements radiating at a given time and by optimizing the beam switchover characteristics. Resultant patterns with antenna phase and amplitude quantization errors are shown for the main beam and associated sidelobes, as well as the worst case grating lobes.

INITIAL ARRAY OPTIMIZATION PROGRAM

The computer program for determing the initial antenna configuration optimizes the sizing, tilts, and element gains to provide a specified far field gain pattern in two dimensions. Because of reciprocity, the gain for a conformal array may also be considered as a measure of the effective area (A_{eff}) of the antenna in receiving incident microwave radiation. The effective area is equal to or smaller than the actual subtended area because of off-axis scanning losses for each of the antenna elements. Let the effective antenna area be given by:

$$A_{eff} = \eta_{mi}^2 A_i \qquad (1)$$

where A = actual element area (l_{xi} l_i) as shown in Figure 1.

η_{mi} = scanning loss =

$$\left[\frac{1+\cos(\phi_m-\theta_i)}{2}\right]\left\{\frac{\sin\left[\left(\frac{2\pi}{\lambda}\right)l_i \sin(\phi_m-\theta_i)\right]}{\left(\frac{2\pi}{\lambda}\right)l_i \sin(\phi_m-\theta_i)}\right\}$$

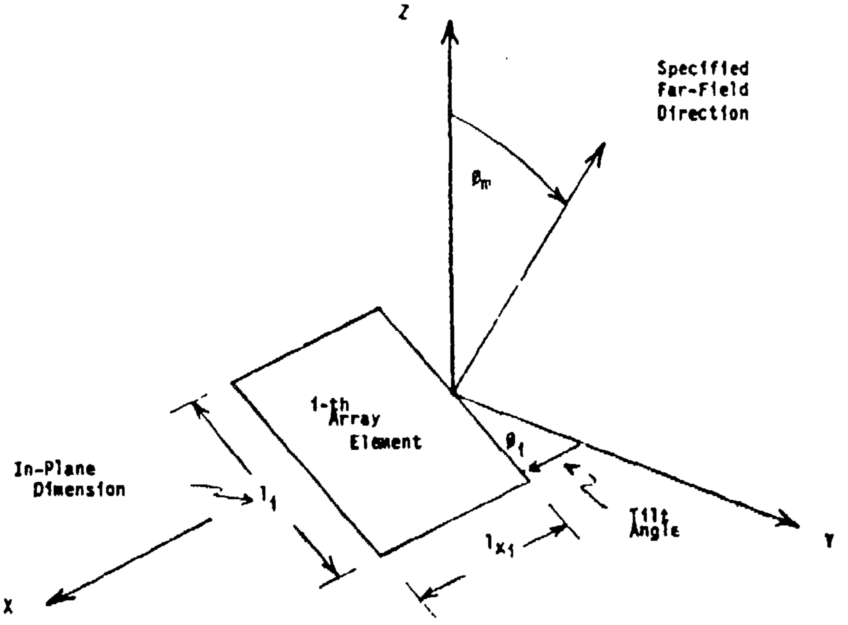

Figure 1. Antenna Coordinate System

Using this gain definition and the antenna configuration as given in Figure 1, an iterative computer program was developed as follows:

Step 1) Consider Figure 1 and note the following definitions.

$\{\phi_m\}$ - field point angles from bore sight
$\{\theta_i\}$ - element tilt angles from bore sight
$\{\ell_i\}$ - in-plane dimensions of elements
$\{A_i\}$ - element area ($l_i l_{xi}$)
$|E_i(m)|^2$ - power from i-th element in the direction of ϕ_m
N - total number of elements
M - total numbers of specified field pts.
$|E_m|^2$ - specified power in direction

Step 2) Assume that

$$|E_i(m)|^2 = \eta_{mi}^2 A_i$$

Step 3) Let f be an M-vector whose elements are the 'realized' power in the directions $\{\phi_m\}$ i.e.,

$$f_m = \sum_{i=1}^{N} |E_i(m)|^2 \qquad m = 1, 2, ---, M$$

and let g be an M-vector whose elements are the specified power in the direction $\{\phi_m\}$ i.e.,

$$g_m = |E_m|^2 \qquad m = 1, 2, ---, M$$

initial estimate of the antenna configuration, and (b) the realizability of the specified far field. The design process thus requires application of engineering judgment. The number of elements (N) can be varied until a configuration is found which provides the best tradeoff between cost and coverage.

This design technique has been applied to two low-earth-orbit antenna systems: (1) a 23 dB gain hemispherical antenna with 0-180° coverage in elevation and ± 20° azimuth 3 dB beamwidth. A cylindrical antenna as shown in Figure 2 with 48 - 2.6 λ x 1.25 λ elements can provide the coverage, and (2) a narrow beamwidth, 41 dB mainbeam gain with off-axis gains as shown in Figure 3. Coverage with large variations in the specifications can be handled by superposition of the high gain beam(s) with a wider low-gain pattern.

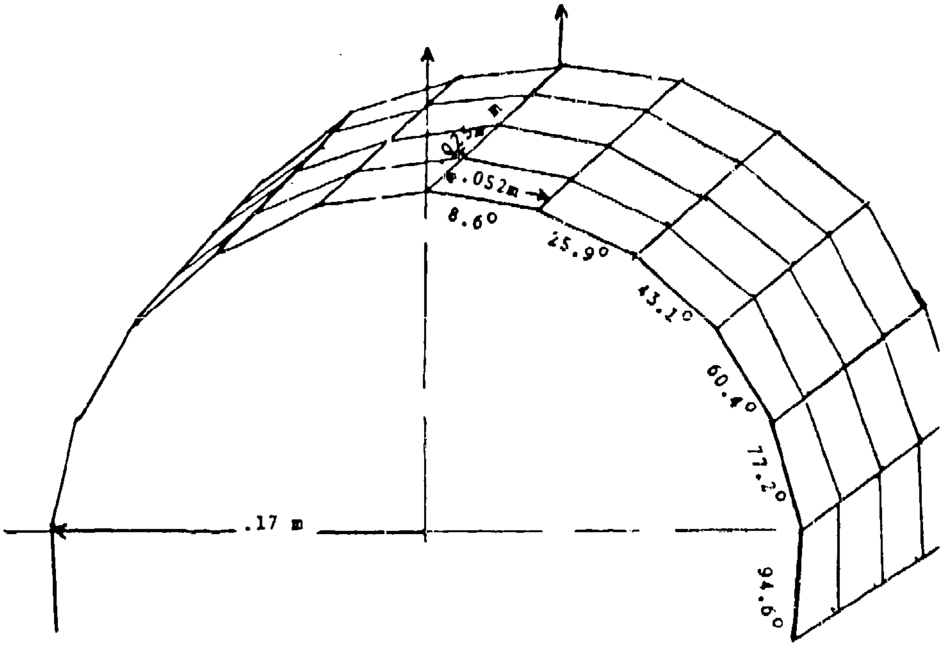

Figure 2. A 23 dB gain hemispherical array with 0-180° elevation and ± 20° azimuth coverages

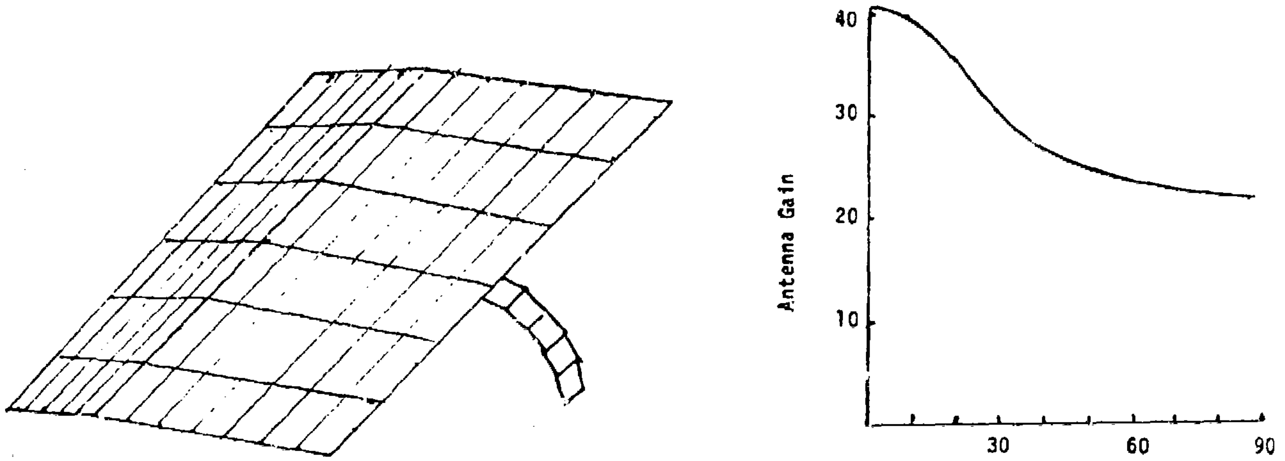

Minimum area conformal array to provide coverage as shown.

Degrees off boresight

Figure 3. High gain (41 dB) array configuration

Once a solution to the simplified in-plane problem is obtained, the results are then used as an input to the more detailed optimization procedure described in the remainder of this report.

COMPUTER ASSISTED DESIGN PROGRAM

A second computer program has been written to calculate and graphically display the radiation pattern of a wide variety of possible conformal array antennas. If the curvature of the array can be approximated by the surface of any ellipsoid, or a section thereof, the program is applicable. By specifying the dimensions of the three major axes of an ellipsoid, a wide variety of surface curvatures are possible including a sphere, cylinder, or plane. Once the surface is defined, the radiating elements can be layed out on it and the location of each phase center can be specified.

The computer program is comprised of four major sections. The first section deals with obtaining the input data that describes the problem. The second section performs the aperture synthesis to obtain the desired radiation pattern. The third section calculates the far field pattern and the last section performs the graphics so that the problem can be visualized.

The first inputs are the dimensions for the three axes of the ellipsoid. Then, truncation parameters are inputted to specify the portion of the ellipsoid's surface on which the array elements are to be laid out. Next, the number of beams is specified along with frequency, element spacing, fill factor, overlap factor, and parameters that control the element pattern factor. Then, the directions of each beam is requested by the computer. Finally, information concerning the sector of space of interest, the type of plot, size, and viewpoint are entered. The computer program now has all of the required input information and is ready to move to the next level of computations.

The second section of the program performs the aperture synthesis. It is determined which elements are to be active and the amplitude and phase requirements of each element. The aperture requirements for one beam at a time are determined. In order to obtain proper element phasing, the coordinates of each element on the ellipsoidal surface must be determined. By complex superposition, the aperture requirements to generate multiple beams is determined.

The program is now ready to determine the far field radiation pattern of the array. Whether or not an element is active is based on the permitted angular difference between the element's normal vector and the beam direction. This permitted angular difference is an input. The contribution of each active element is summed vectorially at some point in space. The phase of each element's contribution is based on its precise location on the ellipsoid, and the amplitude is based on the direction of the element's normal vector and the element pattern factor. These summations are systematically performed over the sector of space of interest and provides the data for the radiation pattern plot.

Various plots are available based on the use of a software graphics package. A great deal can quickly be observed using the 3-D representations shown in the following figures. A kind of "visual optimization" can be performed by making perturbations about the expected solution and taking note of the results. Also, little is known about side lobes and grating lobes when using the approach outlined earlier in this paper to obtain an approximately optimum solution. In most cases, one may desire to observe these features before settling on a final design.

Several examples of radiation pattern plots for conformal arrays are shown in Figures 4 through 6. The left side of the plot shows which elements are active. The right side shows the radiation pattern of the antenna in a three dimensional representation. Field strength, in dB, is plotted against the spherical coordinates theta and phi which are shown on the base plane grid.

Figure 4 shows the pattern of a minimal element cylindrical array, designed to provide 23 dB gain into a specified half plane and + 20° from that half plane. The pattern shown is approximately the same anywhere in the half plane so there is uniformity as theta is varied. However, in moving away from the half plane, increasing phi, note that a grating lobe becomes prominent. This occurs because of the element phase center spacing of more than one wavelength. This tends to happen when attempting to minimize the total number of elements. This is not necessarily a problem depending on the system specification and requirements.

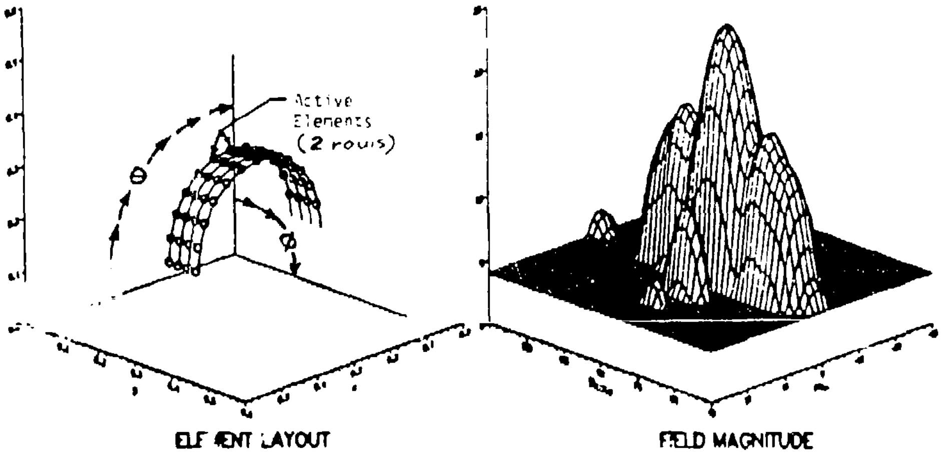

Figure 4a. Cylindrical array - boresight

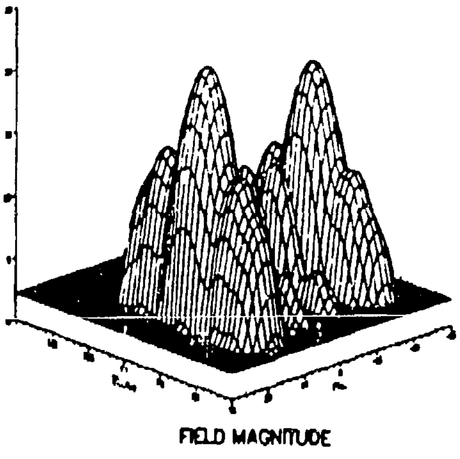

Figure 4b. Cylindrical antenna - steered 20^0

An example of a spherical section array is shown in Figure 5. A much cleaner radiation pattern is observed in this case. It can be seen that side lobes are low and grating lobes do not exist, but many more elements are active that help produce these benefits. When this configuration is steered 20^0 in the phi direction, a grating lobe appears but note that it is of a different shape than the main lobe. In the case of the cylindrical array, the grating lobe has the same characteristics as the main lobe.

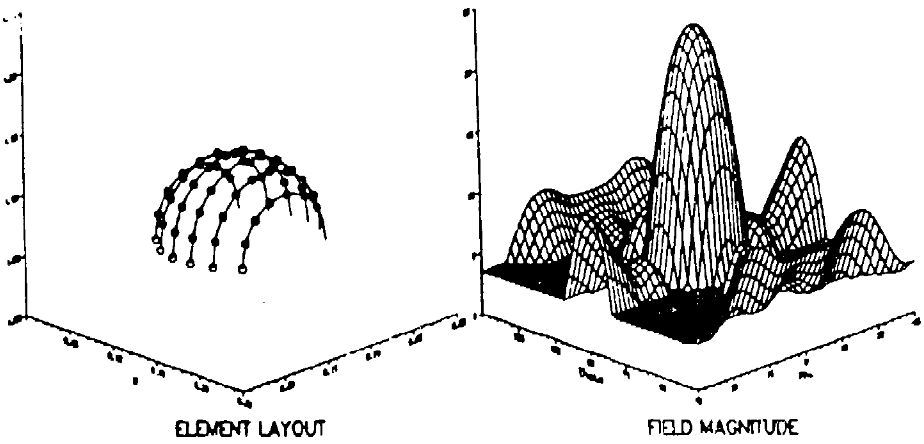

Figure 5a. Spherical array - boresight

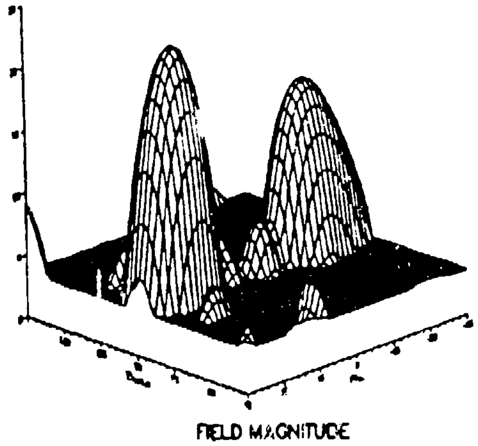

Figure 5b. Spherical array - steered 30°

A high gain minimum field of view planar antenna is shown in Figures 6a and 6b. Note that when the beam is steered only five degrees, a grating lobe appears that looks the same as the main beam.

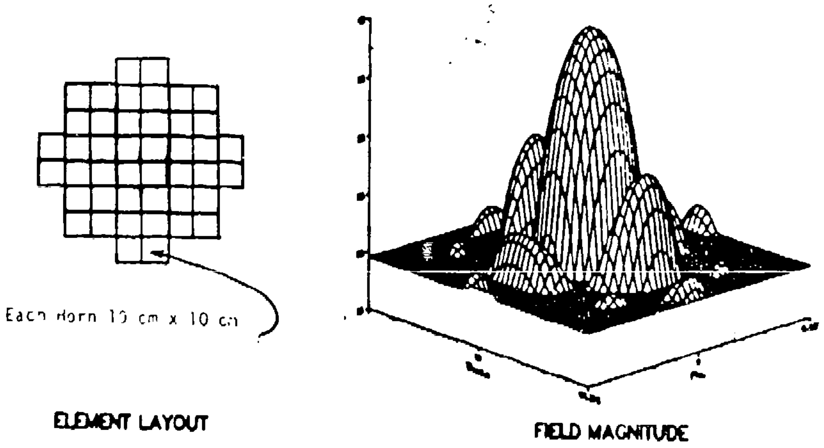

Figure 6a. High gain/limited FOV - boresight

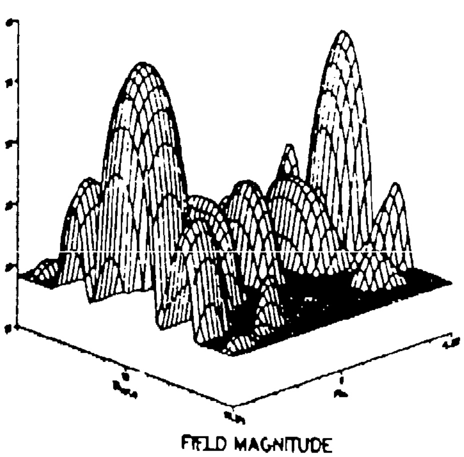

Figure 6b. High gain/limited FOV - steered 5°

Conformal Array Design Curves

For certain specific conformal surfaces, design curves have been derived that are based on active projected aperture considerations. These curves can be used to check on the "reasonableness" of the solutions obtained by the previously mentioned methods. The curves can also be used as the basis for designing certain conformal array antennas if the shape of the conformal surface has already been determined.

If the appropriate conformal surface shape has been determined to be spherical, the curve families shown in the following figures can be used to obtain a desired gain in the range of 20 to 30 dB. Figure 7a can be used to determine the radius of the sphere.

Figure 7A. SPHERICAL ARRAY RELATIONSHIPS

(RADIUS)

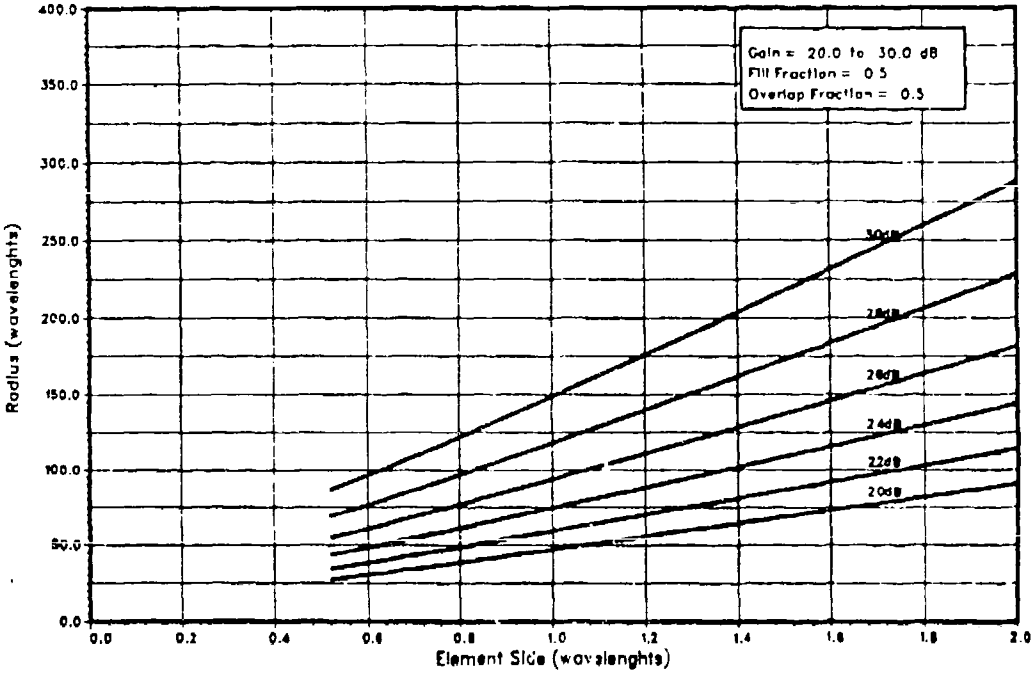

Values are given in wavelengths so that frequency can be eliminated as a variable. The relationships between gain, sphere diameter, and element size, are shown for specified values of fill factor and overlap factor. The "fill factor" is the fraction of the total surface which is "radiating aperture." The "overlap factor" determines which elements of the array are to be active, based on the degree of alignment of the beam direction and the element normal vector. This fraction is in terms of beamwidths. Square elements are assumed, with the element side length as the abscissa. The sphere radius is the ordinate. The family of curves shown in Figure 7b can be used to determine the total number of elements that would be required to cover a hemisphere. It would be assumed that if spherical coverage is required, this would be accomplished with two hemispherical antennas rather than one spherical array antenna. The next family of curves (figure 7c) shows how many elements are active.

Figure 7B. SPHERICAL ARRAY RELATIONSHIPS
(TOTAL NUMBER OF ELEMENTS)

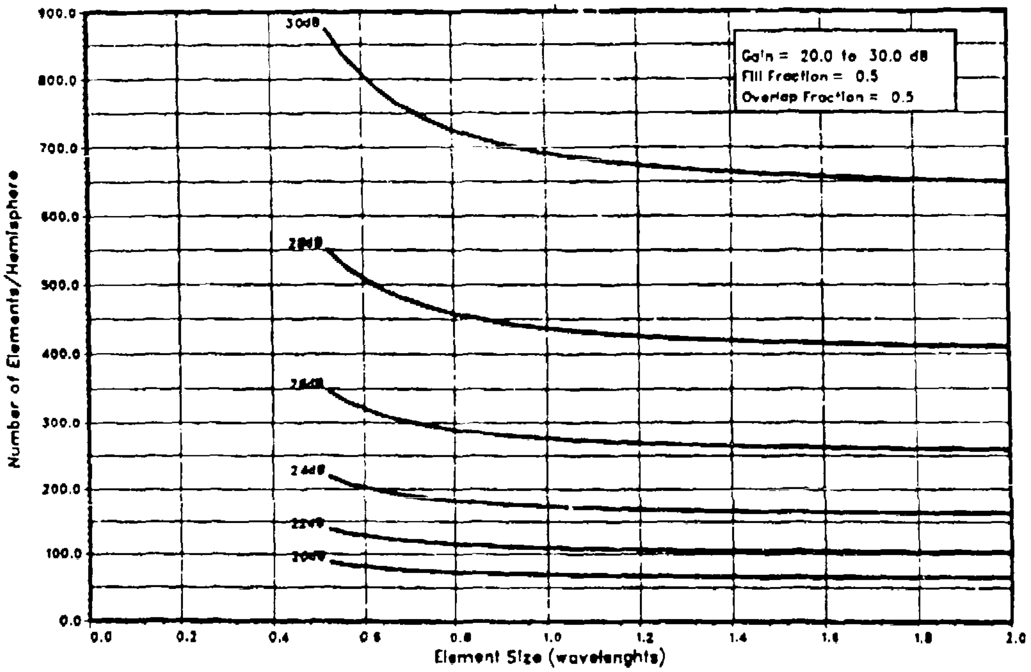

Figure 7C. SPHERICAL ARRAY RELATIONSHIPS

(NUMBER OF ACTIVE ELEMENTS)

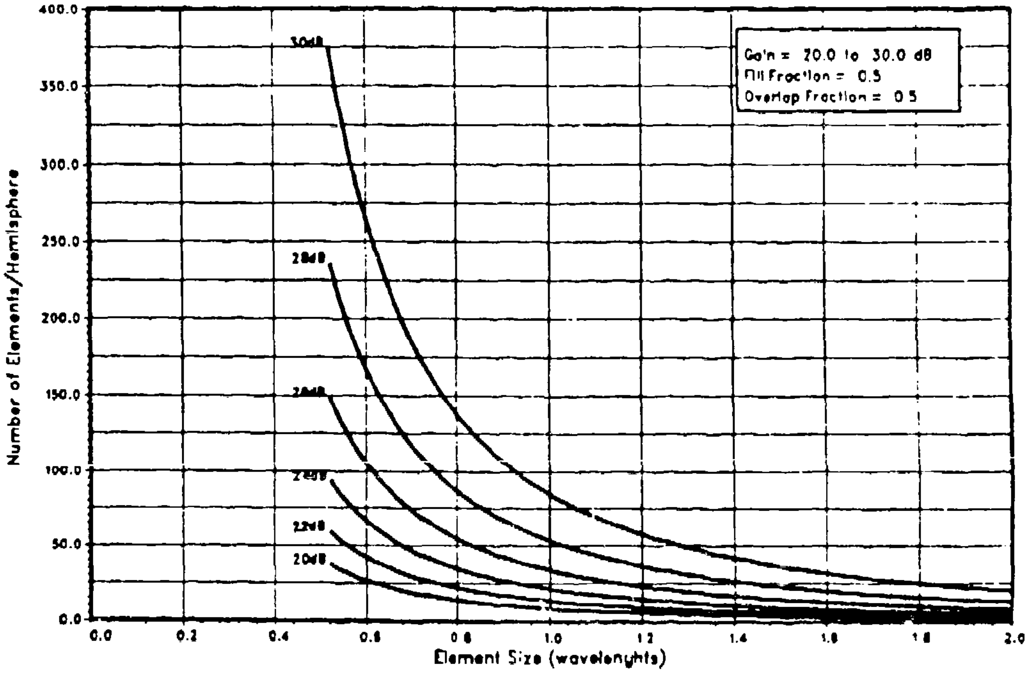

Design curves have also been generated for a cylindrical surface. It can be shown by the procedures in the previous sections that a cylindrical array is appropriate to serve a plane, plus and minus some small angle from the plane. The three families of curves in the following three figures are similar to the spherical array design curves except that an additional factor "cylinder length" must be considered. For the sake of brevity, only the curve set for a cylinder length of four wavelengths is provided. If more gain is required in the plane being served, the length can be increased. If less gain is needed, the cylinder length can be decreased. The radius of the cylinder can be determined from the curves in Figure 8a.

Figure 8A CYLINDRICAL ARRAY RELATIONSHIPS

(RADIUS)

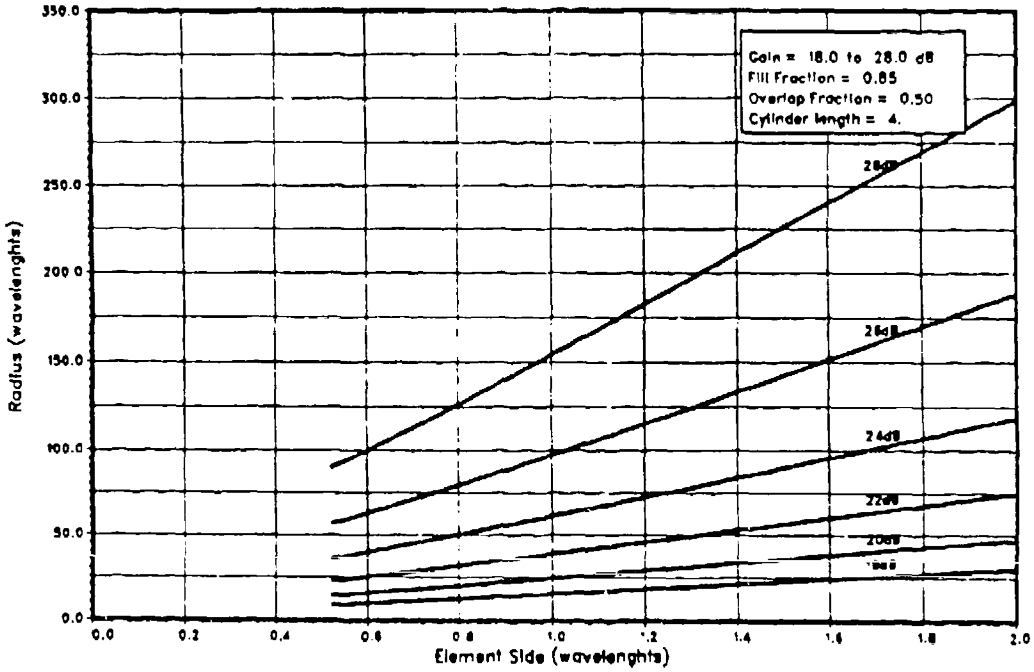

The total number of elements on a half cylinder can be found by referring to the curves of Figure 8b. Keep in mind that cylinder length of four wavelengths is assumed in the number shown on the ordinate. The number of active elements can be found by reference to Figure 8c.

Figure 8B CYLINDRICAL ARRAY RELATIONSHIPS

(RADIUS)

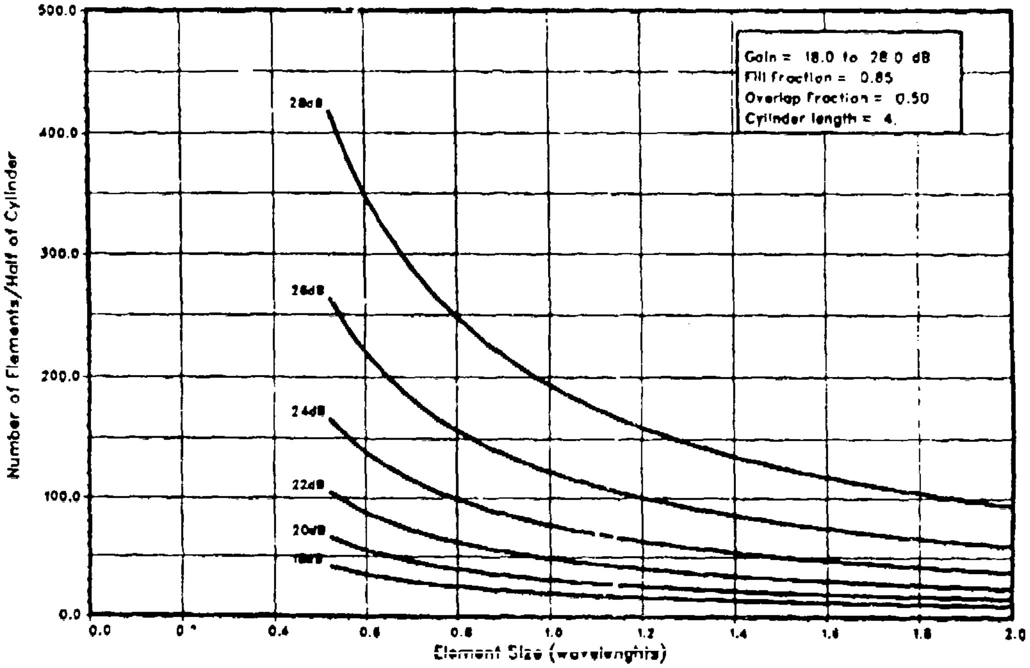

Figure 8C CYLINDRICAL ARRAY RELATIONSHIPS

(TOTAL NUMBER OF ELEMENTS)

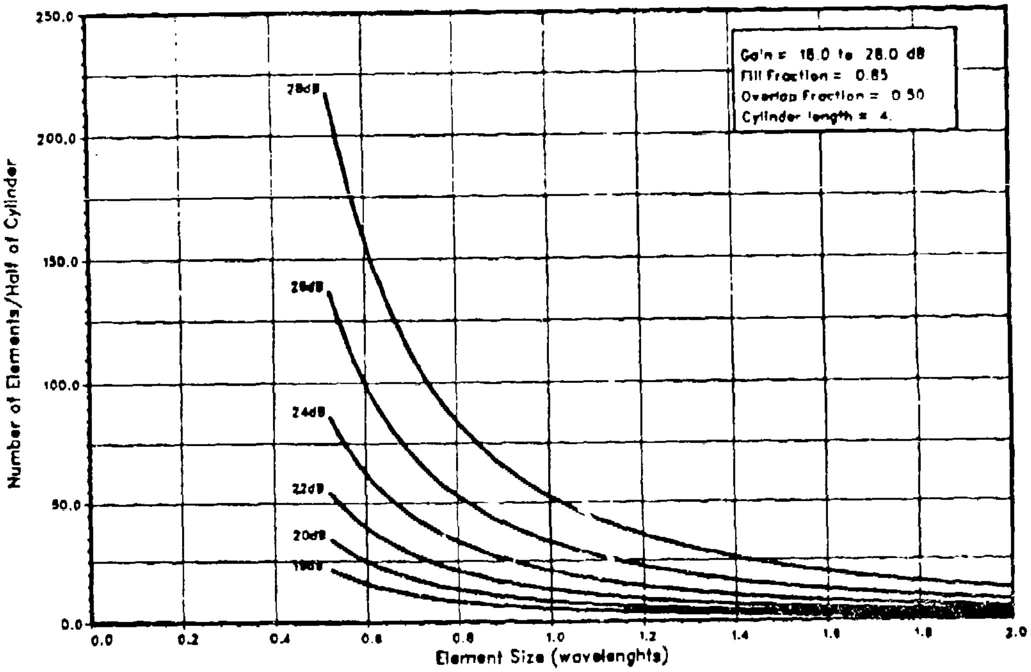

This particular set of curves may not be as useful as for the spherical array because the best element shape is not likely to be square. The element width along the cylinder length will likely be determined by how far out of plane one needs to steer the beam. This will usually lead to rectangularly shaped elements.

Quantization Errors

In addition to minimizing the number of radiating elements, to meet certain gain/coverage requirements, it is also reasonable to minimize the number and resolution of phase shifters. One way to minimize the number of phase shifters is to produce multiple beams by "aperture synthesis" rather than beam forming networks. In this technique only one phase shifter is required per element no matter how many beams are formed. However, amplitude control must also be provided for each element by way of a variable amplifier or variable attenuator. In order to get an idea for the amount of resolution required for the phase shifters and variable amplifiers, several cases were studied. The results of one of these studies is as shown in Figures 9 through 12.

Figure 9 provides a reference plot of four beams formed by an aperture of 15 by 15 elements square. There is no phase or amplitude quantization error in this plot.

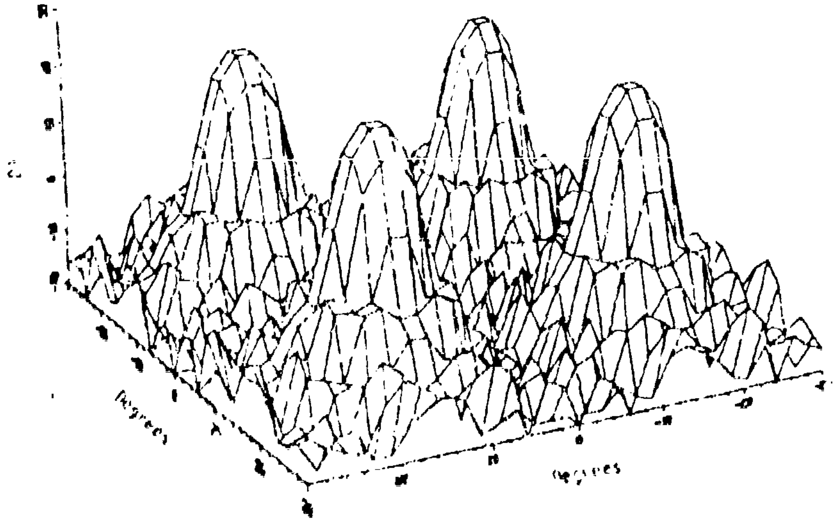

Figure 9. Reference Plot

The next three plots show the effects of quantizing error in phase only. Figure 10a shows the degradation if only one bit of phase control is used (i.e. 0^{0} or 180^{0} phase shift).

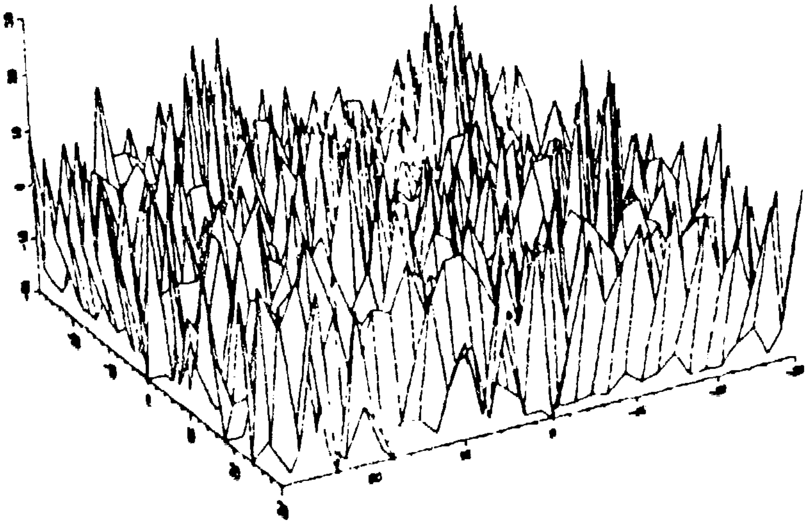

Figure 10a. Phase control - one bit

In the next plot, Figure 10b, two bits of phase control are used. The radiation pattern is markedly improved but still perhaps less than satisfactory. When control is increased to three bits, an additional improvement can be seen in Figure 10c. This process can be continued until the radiation pattern is deemed to be acceptable as shown in Figure 10d.

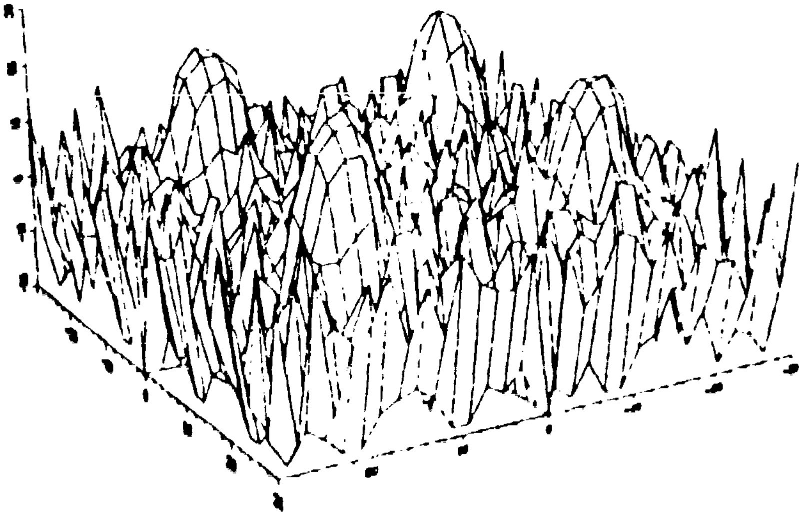

Figure 10b. Phase control - two bits

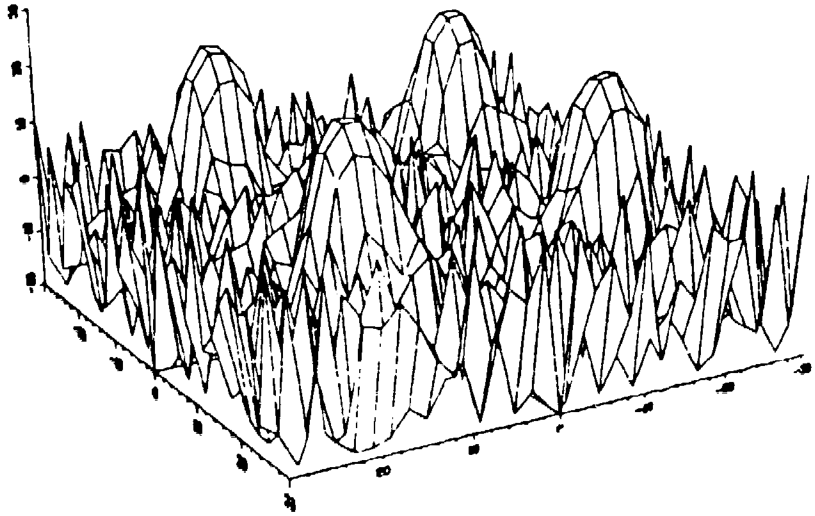

Figure 10c. Phase control - three bits

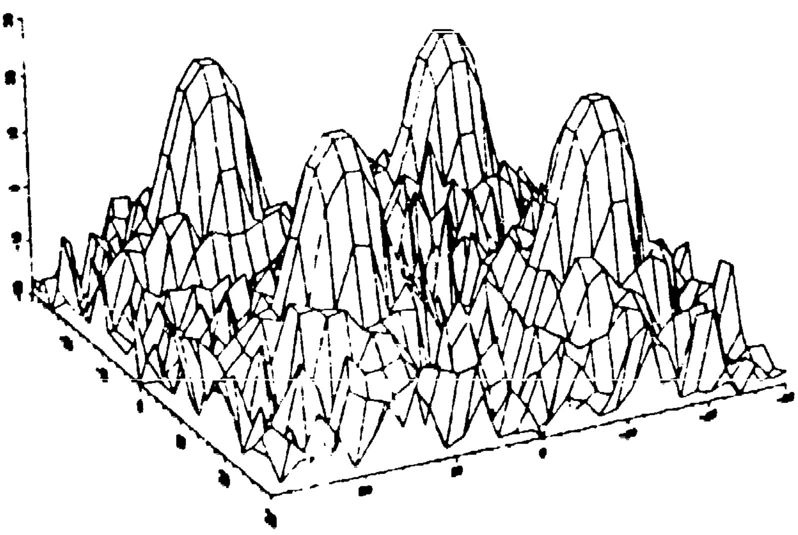

Figure 10c. Phase control - four bits

A similar process was repeated for amplitude resolution control. In this case, amplitude was quantized based on a normalized voltage level between zero and one. For one bit of control, element amplitude was quantized to either zero or one. This is shown in Figure 11a.

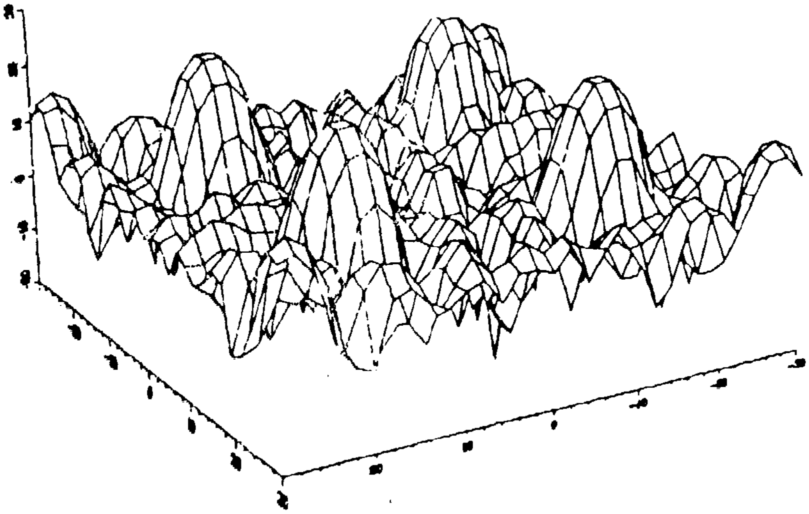

Figure 11a. Amplitude control - one bit

In these cases, phasing is assumed to be perfect. For two bits of amplitude control, element voltage was permitted to be 0, 0.33, 0.67, or 1. As would be expected, the pattern looks much better, as shown in Figure 11b. Finally, three bits of amplitude control were assumed providing eight amplitude levels. Once again the radiation pattern is improved as can be seen in Figure 11c.

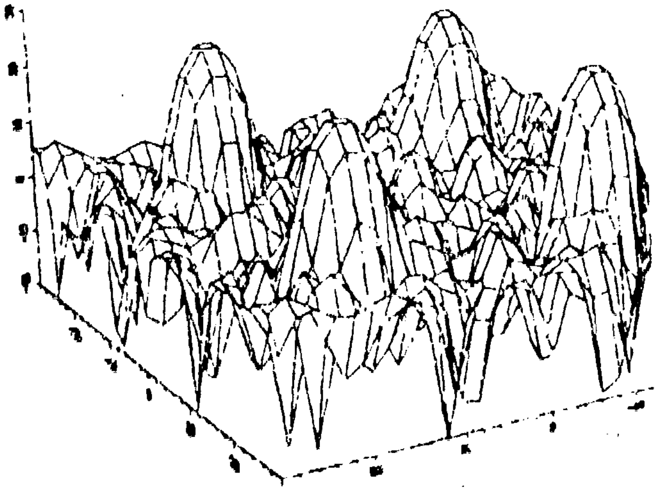

Figure 11b. Amplitude control - two bits

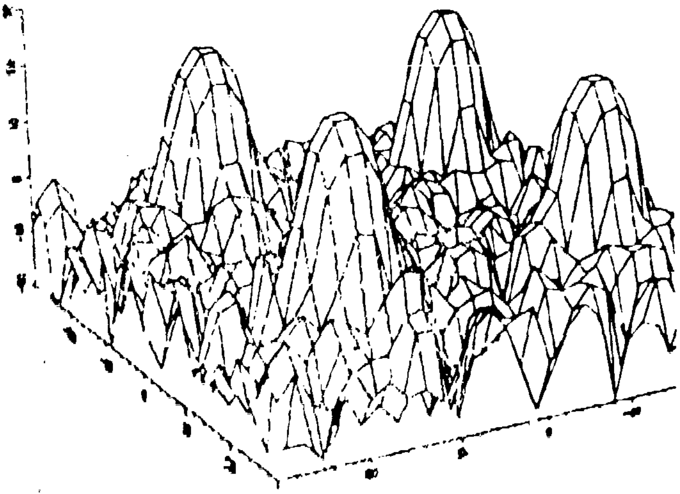

Figure 11c. Amplitude control - three bits

The combined effects of four bit phase control and three bit amplitude control are shown in Figure 12. This should represent a realizeable antenna system for providing four simultaneous beams.

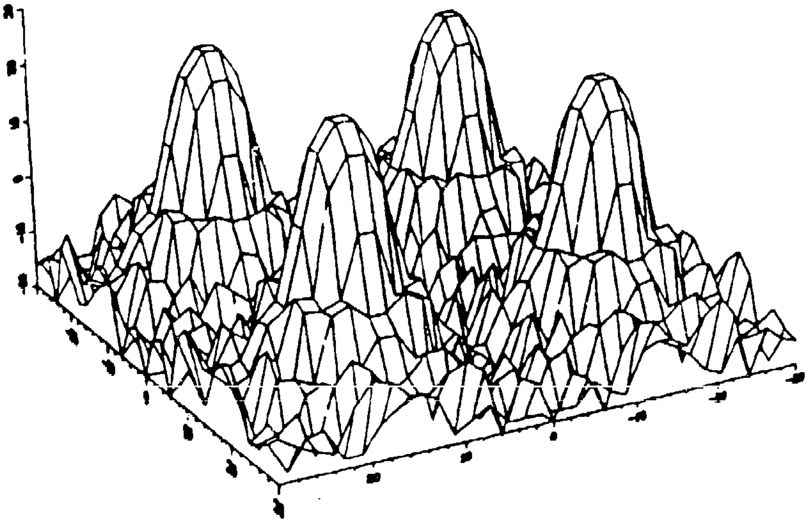

Figure 12. Phase control - four bits
Amplitude control - three bits

SUMMARY

Two antenna configurations were developed using the optimization and design programs. The optimization program provides the initial antenna shaping to achieve a given coverage pattern. The design program calculates the far-field pattern, together with associated grating lobes for the specified antenna shape and placement of elements. Degradations in coverage performance due to various quantization levels in amplitude and phase was also presented. By using these two programs it is possible to minimize the number of radiating elements and limit the resolution of phase shifters and variable amplifiers and associated electronics.

ACTIVE IMPEDANCE EFFECTS IN LOW SIDELOBE AND ULTRA WIDEBAND PHASED ARRAYS

C. E. Grove
Daniel J. Martin
Christopher Pepe
General Electric Company
Aerospace Electronic Systems Department
Utica, NY 13503

I. ABSTRACT

The effect of mutual coupling on active impedance has been viewed in terms of impact on sidelobes and array gain. Results are presented for narrow band (10 percent) and ultra wideband (2+ octave) phased arrays. Theoretical designs incorporating the active impedance were used to fabricate low sidelobe array elements. Analytical data reduction of measured scattering matrix data was used to generate the active impedance for the two arrays.

For the narrowband low sidelobe array designs, a Ku-band and a X-band array design are reported. The Ku-band design was empirical and led to a full linear array whose sidelobe characteristics have been measured and compared to the active impedance analytical predictions. These predictions agree well with measured results. The impact on sidelobe degradation for wide scan and the ability of the phase shifter to compensate for this effect is discussed. The X-band array design was analytically derived using the design procedure which compensates the mutual coupling at a chosen scan angle by adjusting the element self-impedance to minimize the active impedance over a 120° scan sector (reference 1). The analytical technique of pattern predictions which was verified for the Ku-band array was used to predict sidelobes for these active impedances, and the sidelobe degradation with scan is seen. Extending the analysis to simulate a matched design at intermediate scan angles shows the amount of improvement possible by balancing the design to the active impedance mismatch.

For the ultra wideband planar array, the design allowed for grating lobes at broadside at the high frequency end of the band. The scattering matrix has been measured across the band of interest, and the active impedance was computed for the full two-dimensional scanned forward hemisphere. A high mismatch region is predicted at the scan angles corresponding to a slow wave grating lobe emergence; the mismatch improves as the grating lobe moves further into visible space. Increased mismatch is also observed for scanning even when grating lobes are not present, thus corresponding to the leaky wave for the strongly coupled condition. The mismatch effect on the active element pattern is shown to reduce a nearly cosine roll-off by 4.0 dB worst case.

II. NARROWBAND LOW SIDELOBE ARRAY

A. HARDWARE DESIGN

Two similar narrowband phased arrays, both having long linear arrays with phase scanning in azimuth and employing slotted waveguide columns as radiating elements, are considered. Azimuth weighting is set by the array corporate feed, while elevation weighting is fixed by the lengths and offsets of the broadwall longitudinal slots cut in the dielectric waveguide column radiators. Dielectric loading reduces slot spacing and column broadwall width, allowing operation without grating lobes. The array assembly is illustrated in Figure 1.

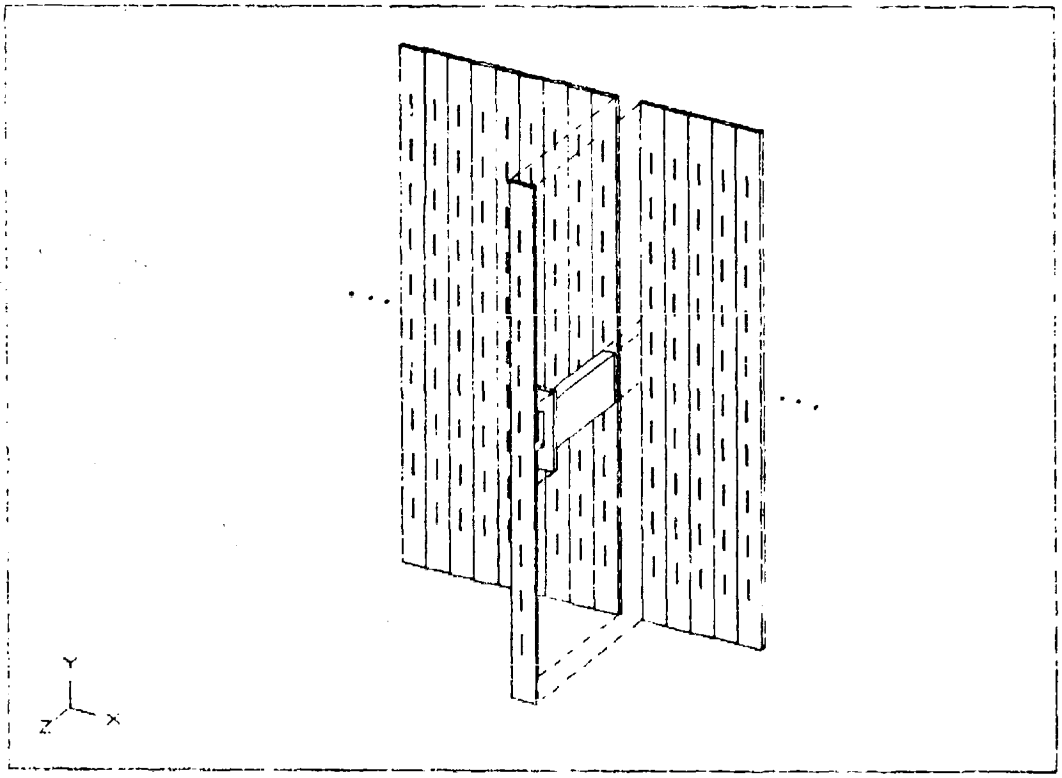

Figure 1. Linear Slotted Array Assembly

A Ku-band array employing nonresonant column radiators was designed and built. Slots were characterized by network analyzer measurements of multislot test columns. Mutual effects between columns were not taken into account in the design.

A similar X-band array was proposed for a different application, and a small test aperture was designed and built. Resonant column radiators were chosen for this design, and the effects of mutuals at zero scan were included by applying the method described by Elliot (1). This iterative technique adjusts slot lengths and offsets until the desired taper and input resistance is met within a certain tolerance. Slots are characterized separately by network analyzer tests and/or method of moments theoretical techniques.

The design program, Slotted Array Synthesis Program (SASP), calculates mutual effects on a linear array of several columns, but adjusts the slots of all columns together and optimizes only the center column. The resulting single unique design is then suitable for a long array of identical elements. In SASP, provisions were allowed for phase shifting the column excitations, permitting an optimum design at some scan off broadside, and therefore improved performance over a wide scan range.

The designed versus realized elevation tapers are plotted in Figure 2, and show a good agreement.

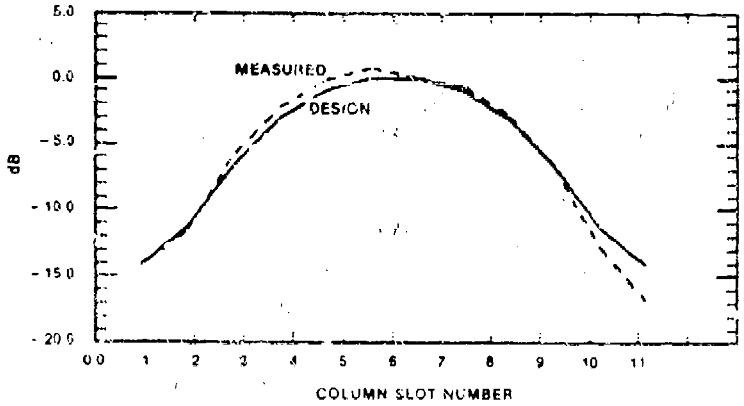

Figure 2. Designed Versus Realized Column Tapers

B. MEASUREMENT OF MUTUALS

Active impedances are measured indirectly by measuring the mutual couplings of an assembled array. Then, the active reflection coefficients ρ_i are determined by

$$\begin{bmatrix} \rho_1 \\ \rho_2 \\ \cdot \\ \cdot \\ \cdot \\ \rho_N \end{bmatrix} = \begin{bmatrix} S_{11} & S_{12} & \cdots & S_{1N} \\ S_{21} & S_{22} & \cdots & S_{2N} \\ & & \cdots & \\ & & & \\ & & & \\ S_{N1} & S_{N2} & \cdots & S_{NN} \end{bmatrix} \begin{bmatrix} w_1 \\ w_2 \\ \cdot \\ \cdot \\ \cdot \\ w_N \end{bmatrix} \qquad (1)$$

where Sij is the aperture scattering parameter (mutual couplings and self-reflection coefficients) and w_i is the vector excitation of the elements. Active impedance is then simply

$$Z_{\text{active } i} = \frac{1 + \rho_i}{1 - \rho_i} \qquad (2)$$

To reduce the amount of data to be taken and processed, the mutuals were only measured on a smaller test array. It was assumed that the long array symmetry conditions still applied, so that the entire S matrix could be built from measurements of the first row only. S_{ii} is represented by the center element, and mutuals are measured as much to the interior of the test array as possible to reduce end element errors in the above assumption. Precautions must be taken in calibration to insure that transmission and reflection phase measurements are referenced at the same plane.

The mutual coupling measurements are plotted in Figure 3. Note that the nonresonant (Ku-band) columns exhibit much lower coupling levels than the resonant (X-band) columns.

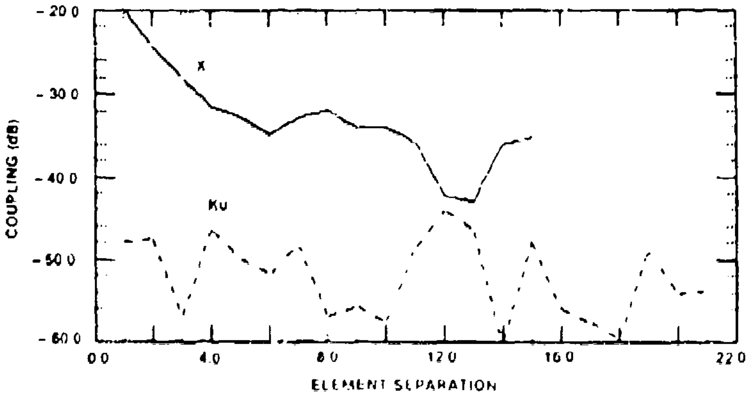

Figure 3. Measured Mutual Couplings

C. ACTIVE IMPEDANCE

Center column active impedances computed for the X-band 16-column test array are plotted in Figure 4 for uniform illumination at three frequencies as a function of scan angle. Since the full size tapered array would be much larger, this plot is representative of the elements interior to the full array. Active impedances for an end element were also plotted for comparison in Figure 5. Error in obtaining the perfect match of the center column at center frequency was mostly attributed to slot characterization error and not to mutual compensation error.

Center column active impedances computed for the Ku-band test array are plotted in Figure 6. They show little variation because of the low mutual couplings. End elements are similar, also due to low mutual coupling. It is concluded that the low mutual coupling results from the nonresonant spacing of the slots on the column.

D. SCAN PERFORMANCE PREDICTIONS

Active impedance variation with scan affects array performance in two ways: gain reduction due to mismatch loss and sidelobe level increase due to added amplitude and phase excitation errors. Excitation errors result from active impedance variation from center to end elements at a given scan, and from element interactions with feed and phase shifter discontinuities. The latter effect dominates for long arrays, and depends on element active VSWR. This interaction was modelled as a random phase angle between the feed discontinuity and the element. The random phase, once set, is then adjusted by twice the beamsteering phase angle, and so models the phase-unbalanced feed with ideal phase shifters as shown in Figure 7.

A computer program was written to calculate active impedance excitation errors, in addition to other errors, and compute patterns. A predicted X-band array pattern without active impedance error modeling is shown in Figure 8a. Addition of the active impedance error modeling then results in the patterns of Figures 8b-d for broadside, 45, and 60 degree scans, respectively. Broadside active impedance errors cause little effect on sidelobes, while scanning raises the sidelobe level due to the increasing active column VSWR and shifting phase between column and feed.

Similar results apply to the Ku-band array, except that little change is seen with scan due to the low mutual coupling level. The only significant sidelobe increase with scan off broadside occurs because phase errors which had been collimated out have changed.

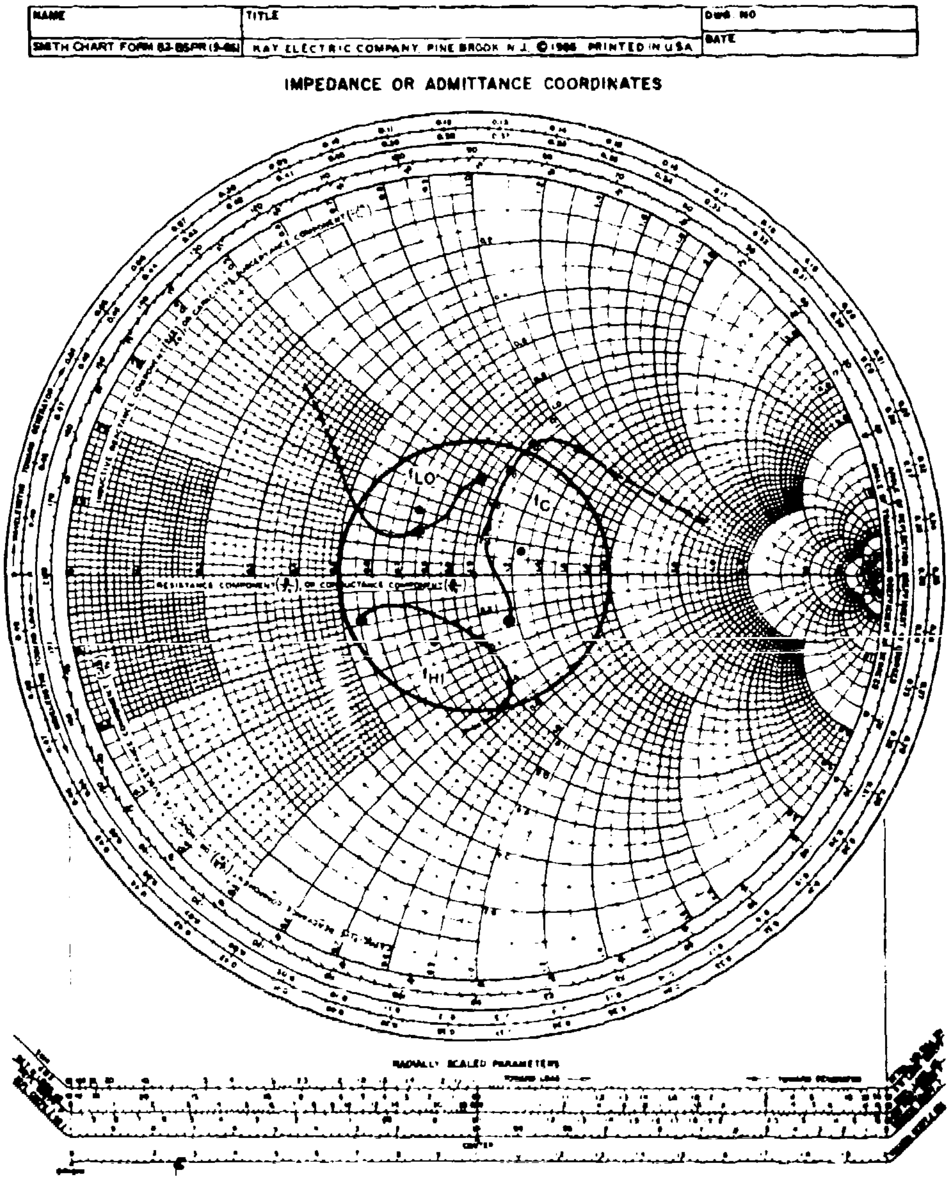

Figure 4. X-Band Center Element Active Impedance

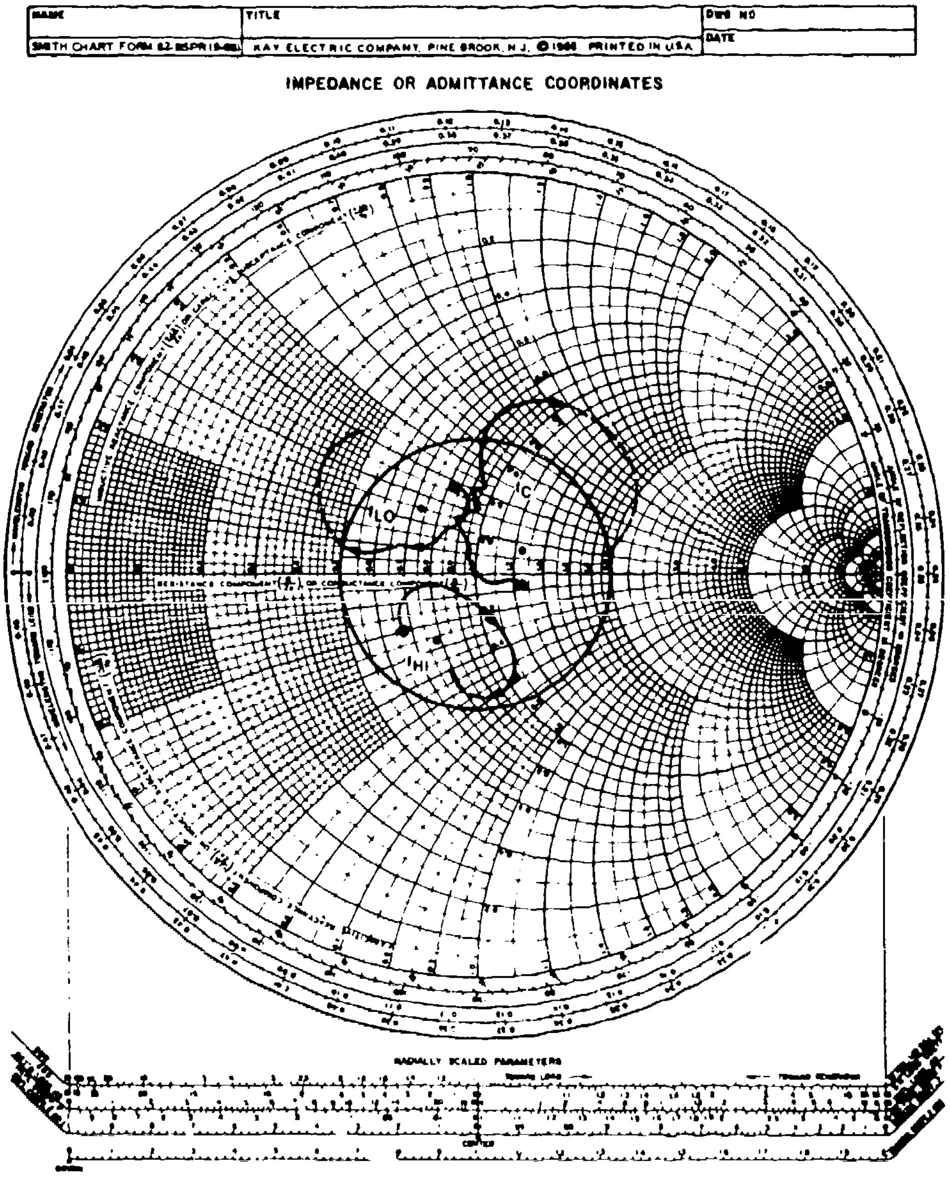

Figure 5. X-Band Edge Element Active Impedance

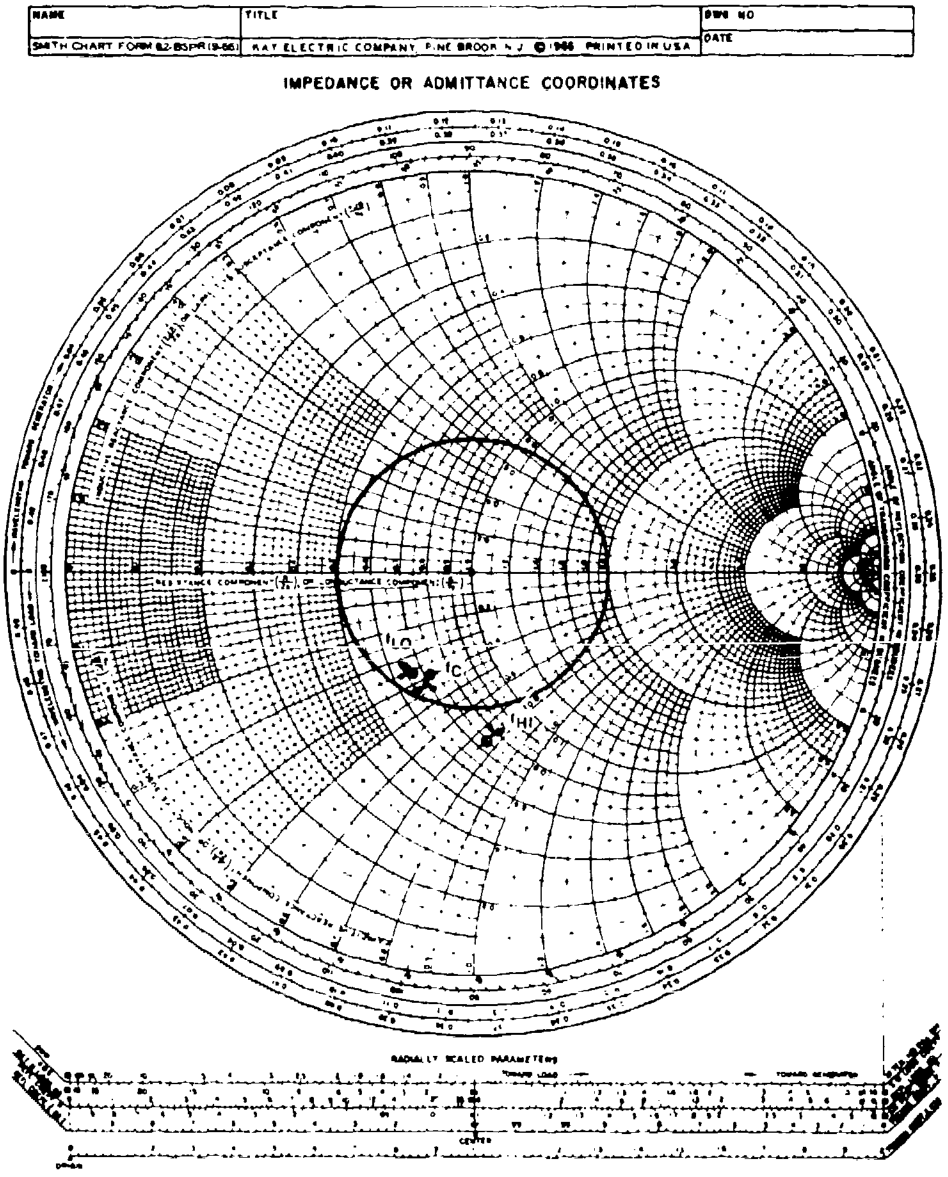

Figure 6. Ku-Band Center Element Active Impedance

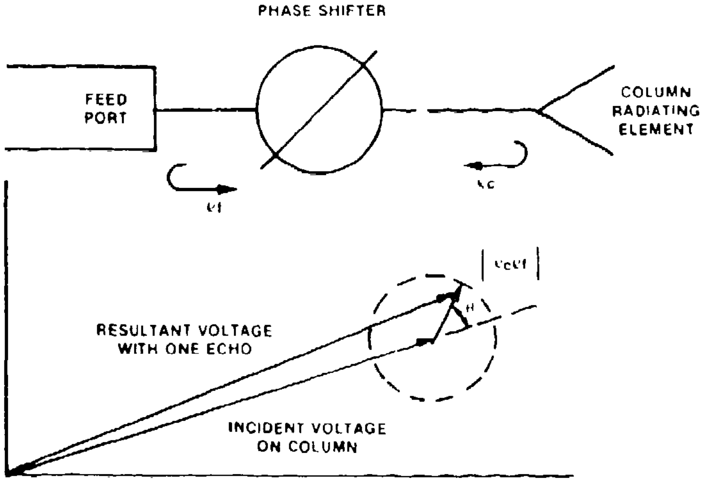

Figure 7. Active Impedance VSWR Interaction Modeling

To study the effects of designing an element with an active match at a scan angle other than broadside, S_{11} is adjusted in Equation 1 to cancel the measured mutuals at the center element at the desired scan. To improve accuracy of this approximate technique, the mutual amplitudes were also adjusted to reflect the change in mismatch loss associated with the change in S_{11}. The interior column VSWR was then calculated at other scan angles, with results presented in Table 1. (This correction was employed in calculating the patterns of Figures 8b-d, for the desired match at broadside.)

To relate the column active VSWR to resulting array excitation errors, and then to array sidelobe levels, use

$$\begin{matrix}\text{RMS phase and}\\ \text{amplitude error}\end{matrix} = \sqrt{\frac{1}{2}\,\overline{\rho_f^{\,2}}\;\overline{\rho_c^{\,2}}},\ \text{volts or radians,} \qquad (3)$$

where ρ_f and ρ_c are the reflection coefficients for the feed and active column. This is easily computed by using Figure 8 and assigning a uniform distribution over 2π radians to the interaction phase angle θ. Equation 3 can then be used to predict the sidelobe level using either the Monte Carlo approach or a statistical percentile distribution estimate.

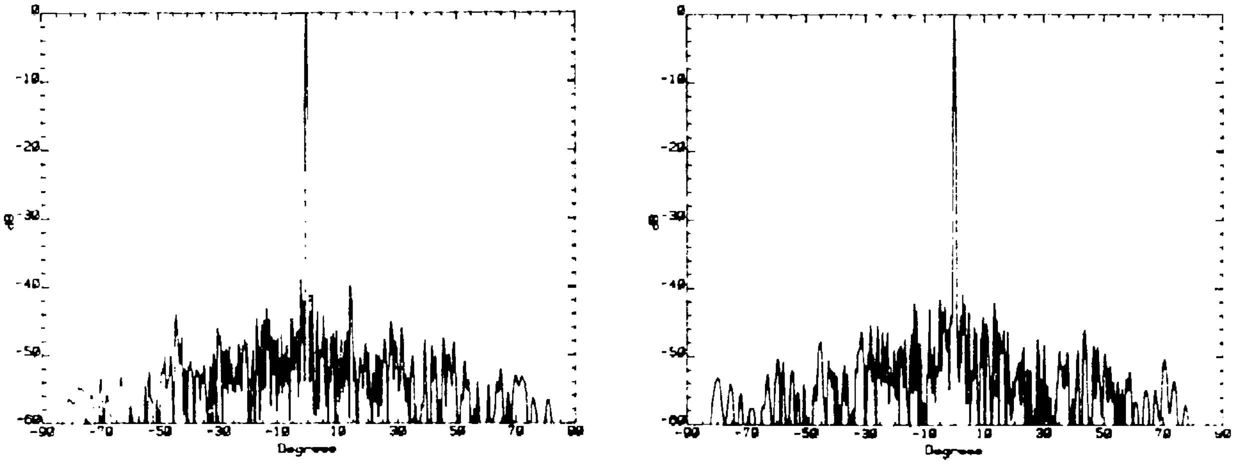

a) Without Active Impedance Error Modeling

b) With Active Impedance Error Modeling at Broadside Scan

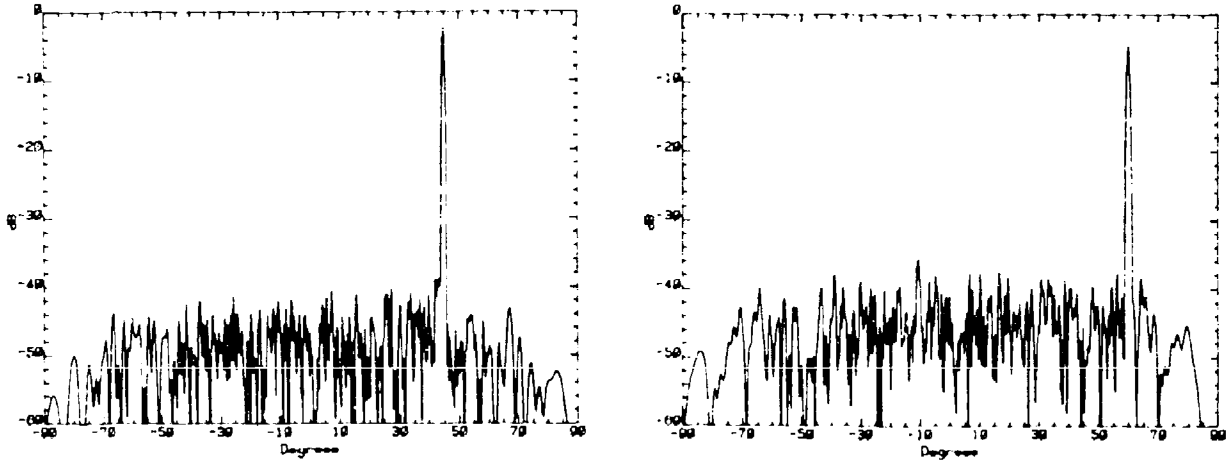

c) With Active Impedance Error Modeling at 45 Degree Scan

d) With Active Impedance Error Modeling at 60 Degree Scan

Figure 8. Predicted X-Band Array Patterns

TABLE 1. ACTIVE VSWR TABLE

Design Match at: \ Scan to	0	15	30	45	52.5	60
0	1	1.14	1.46	1.74	2.49	2.74
15	1.14	1	1.28	1.53	2.19	2.51
30	1.48	1.29	1	1.22	1.72	2.17
45	1.77	1.53	1.22	1	1.40	1.81
52.5	2.43	2.11	1.68	1.38	1	1.49
60	2.61	2.35	2.05	1.74	1.48	1

Scan, θ	ϕ_{rel} at f_o = kd sin θ		with isolated match ($S_{11} = 0$)	
			0° scan	1.50 VSWR
0°	0°	or 0 rad	15	1.33
15°	48.34°	0.844 rad	30	1.18
30°	93.38°	1.630 rad	45	1.20
45°	132.06°	2.305 rad	52.5	1.63
52.5°	148.16°	2.586 rad	60	1.89
60°	161.74°	2.823 rad		

$$K = \frac{2\pi}{\lambda}$$

III. ULTRA WIDEBAND ARRAY

The ultra wideband array was designed to cover approximately 1.5 octaves. The operational requirements and design guidelines for this array allowed for grating lobe existence at broadside starting at mid-band. The effect of the grating lobes is to reduce gain and impact active impedance and thus mismatch. This array allowed for study of the relationship between active impedance and grating lobes.

A. HARDWARE DESCRIPTION

The array consists of 32 elements located in a 4 x 8 array as shown in Figure 9. Each of the 32 elements consists of a slant left and slant right pair which are physically offset. Data presented here is taken on the slant left element of one of these pairs. The elements are TFE glass stripline fed slot line radiators. The array lattice is a 0.75 inch rectangular grid with a 0.375 inch offset between the slant left and slant right elements. The ground plane behind the elements is covered with absorber to attenuate back radiation. The array was designed to operate over the 6-18 GHz band. With the dual linear elements, variable polarization was possible. The array was phase steerable over a 120° cone. The element height above the ground plane is two inches.

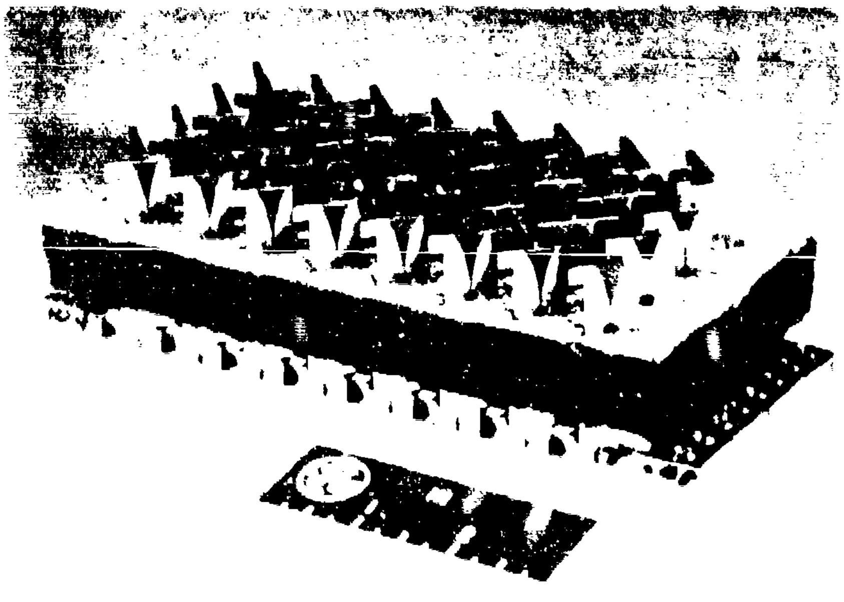

Figure 9. 4 x 8 Array

B. MEASUREMENTS OF COUPLING

Figure 10 shows the array geometry and the designations for coupling measurements. Coupling was measured on an element-to-element basis pair wise with all other elements terminated. This approach represents the free excitation method as opposed to the forced or full excited method. The pair wise data is used to fill a scattering coefficient matrix representing the total 64-element array. The scattering matrix is then multiplied by excitation vectors having phase progressions corresponding to all scan angles in the forward hemisphere. The active reflection coefficient is computed for each case. From this the active impedance is derived. The following equations were applied:

$$D_{mn} = \sum_{p=-\infty}^{\infty} \sum_{q=-\infty}^{\infty} c_{mn,pq}\, a_{pq}$$

$$V_{oo} = a_{oo} + b_{oo}$$

$$I_{oo} = a_{oo} - b_{oo}$$

$$a_{pq} = a_{oo}\, e^{-j[(K\sin\theta\cos\phi)\ pdx]}\, e^{-j[(K\sin\theta\sin\phi)\ q\ dy]}$$

$$\Gamma_a = \frac{b_{oo}}{A_{oo}}$$

$$Z_a = \frac{1 + \Gamma_a}{1 - \Gamma_a}$$

As shown in Figure 10, active impedance was computed for five elements in the array. This data allowed us to represent all conditions of edge effects in predicting total array performance. Since the edge elements were dominated by edge effects and not grating lobe phenomena, this paper will deal only with the most central element.

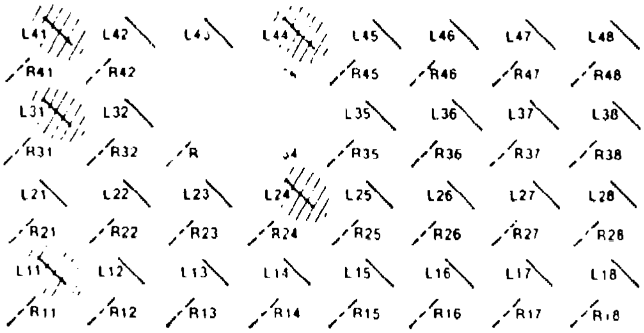

Figure 10. Array Geometry for Coupling Measurement (Rear View)

Active element patterns were also measured for the five elements shown in Figure 10. The same approach, the free excitation method, was used to take the active element patterns. In other words, all elements but the element in question are terminated in 50 ohms. Measurements were made in the E-plane, H-plane, and the diagonal plane. Again, the edge elements were dominated by edge effects in their pattern asymmetry. For the central element, however, the sharpening or narrowing of the element pattern is obvious for the wide spacings used in this array. This element pattern narrowing corresponds to the existence of grating lobes and the loss of gain with scan. For the small array, the element patterns can be combined using superposition to find the total antenna pattern as:

$$\Sigma\Sigma\, g(\theta, \phi)_{m,n} \exp^{-j\,(K_x D_x + K_y D_y)}$$

The measured pattern is given by:

$$g\ (\theta, \phi) = D \cos \theta\ [1 - \left| R\ (\theta, \phi) \right|^2]$$

$$R\ (\theta, \phi) = \Gamma(\theta, \phi)$$

where the mismatch is equal to the active mismatch for elements which are matched to the feedline characteristic impedance. Since this active impedance is a function of scan angles, the effect of mismatch on active element patterns is represented by this equation. The effect of the mismatch not being appropriate for the characteristic impedance of the feedline results in a mismatch loss which can be viewed as a level change in the overall pattern with the pattern shape not being affected. Figure 11 is an active element pattern taken in the H-plane for the central element.

C. RESULTS AND ANALYSIS

Initial coupling amplitude and phase for the central element is shown in Figures 12 and 13 as a function of the spacing between elements and wavelengths. The three primary planes are shown. For the amplitude data, a line of comparison for amplitude decay at one over the distance squared and one over the distance are both shown for reference. This data shows for spacing beyond about one wavelength, the coupling falls off as quickly or faster than one over the distance squared. Thus, for these spacings, the array coupling is less than what would be expected for two isolated elements separated in space. For the H-plane, the data shows coupling stronger than two isolated elements for spacings less than wavelength. This will be shown to have a direct relationship to a high mismatch. The phase data is shown in reference to free space propagation phase delay. For all three planes, the phase delay of the coupling is slower than free space. This slow wave effect will be shown to be related to when the grating lobe emerges in the mismatch. Also, the slow wave effect corresponds to a leaky wave on the

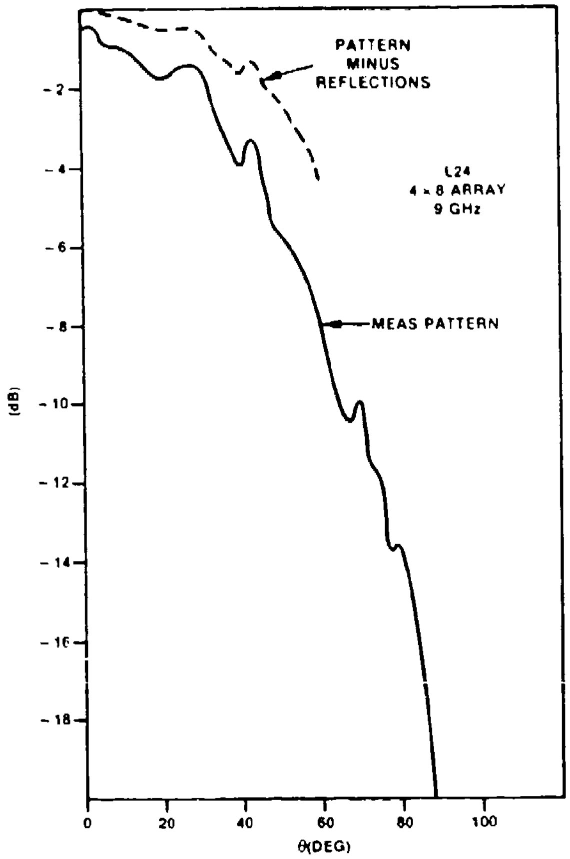

Figure 11.
H-Plane Active Element Pattern

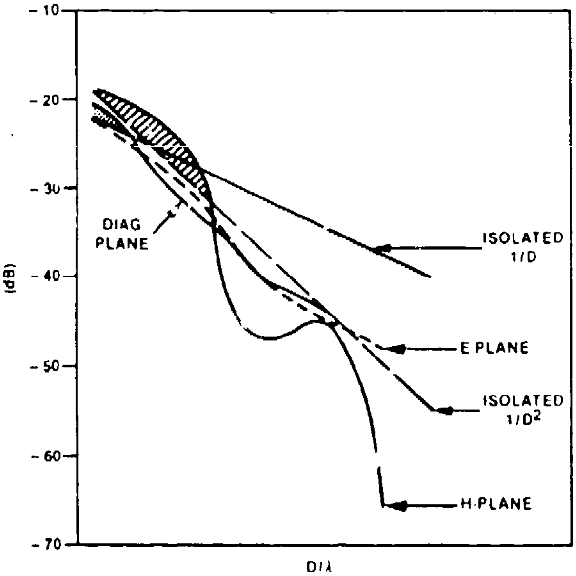

Figure 12. Coupling Amplitude of Center Element 4 x 8 Notch Array

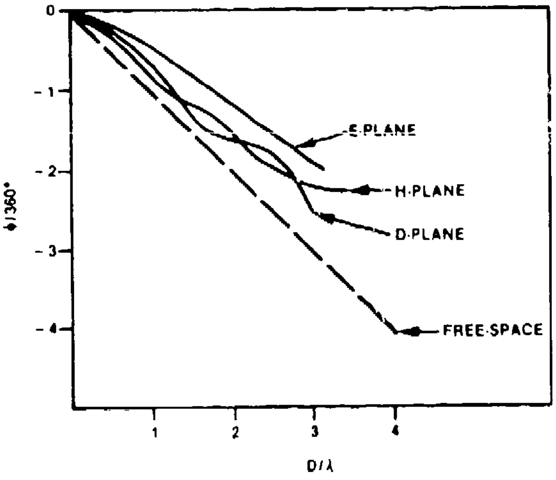

Figure 13. Coupling Phase of Center Element 4 x 8 Notch Array

aperture. This array is small and dominated by edge effects. However, the data shows that the active impedance seen by the center element can be related to leaky wave effects. This type of analysis parallels that developed by Debski and Hanna [reference 2].

From the coupling data, two-dimensional maps of the VSWR versus scan for many frequencies in the band were calculated. Figure 14 shows one of those maps. Reducing the data over all frequencies by searching for the worst case active impedance, the VSWR data in Figure 15 was attained. The individual element self-impedance which can be seen to be fairly well matched is also shown in Figure 15. The active impedance mismatch at boresight degrades this self-impedance from better than two-to-one to better than three-to-one overall frequencies. However, the scan data shows extremely high mismatch occurring between 7 and 10 GHz. This frequency range corresponds to the region of enhanced coupling amplitude shown shaded in Figure 12. The active impedance map of Figure 14 is for 9 GHz and the high mismatch scan region on the diagonal (which is the H-plane for the slant left element) is seen to begin at a scan angle of 40° from broadside. Since the spacing is not appropriate to allow grating lobes even for scanning out to 60° and beyond, this effect is clearly not due to grating lobe emergence. The strong correlation to enhanced coupling and the slow wave effect supports the explanations of Oliner (reference 3). Since it is not grating lobe related, it is not directly affected by the grid, except that the grid, ground-plane, absorber and the element designs influence the ability of the lattice to support a slow wave. Three cuts of the active VSWR versus scan were taken from the map at 9 GHz and are shown in Figure 16. The effect of this high VSWR on the element pattern, commonly referred to as "blindness", was shown in Figure 11. With the mismatch approaching ten-to-one, the blindness effect stays below 4 dB. By taking out the active impedance mismatch at each scan angle in the H-plane, the theoretical matched pattern shown in Figure 11 is derived. This pattern approaches the ideal cosine roll off, and therefore, indicates that the element design is nearly optimum. Improvements in array scan performance must be achieved by changes in the geometry or ground plane in order to alter the enhanced coupling phenomenon.

In Figure 17, a map is shown at 13 GHz where grating lobes appear with scanning. The grating lobe pattern can be easily seen in this map. However, the grating lobe pattern does not directly correspond to the grating lobe emergence predicted for the phase scanning of the array. This is because of the slow wave nature of the coupling. The grating lobes appear sooner for different directions of scan depending on the wave velocity in that plane. The data for the center element in Figure 13 showed variations in wave velocity ranging from 70 to 90 percent of free space. It should be noted that only rarely did the active impedance map show such clear grating-lobe type mismatch areas. The variation of enhanced coupling and grating lobe effects become hard to distinguish in most cases. Also, as can be seen in Figure 17, the grating lobe high mismatch region does not stay mismatched after the grating lobe is fully formed into visible space. Thus, the existence of grating lobes does not necessarily mean a high active mismatch whereas it does, of course, mean a direct loss of gain.

ELEMENT L24
9 0 GHz

MAP UNITS

HORIZONTAL = SIN(THETA)*COS(PHI) = M/30
VERTICAL = SIN(THETA)*SIN(PHI) = - N/18

	REFLECTION COEFFICIENT							
SYMBOL	FROM	TO	SYMBOL	FROM	TO	SYMBOL	FROM	TO
A	0 000	0 025	‡	0 200	0 225	-	0 400	0 450
'	0 025	0 050	5	0 225	0 250	9	0 450	0 500
B	0 050	0 075	·	0 250	0 275	+	0 500	0 625
2	0 075	0 100	6	0 275	0 300	0	0 625	0 750
C	0 100	0 125	=	0 300	0 325	°o	0 750	0 875
3	0 125	0 150	7	0 325	0 350		0 875	1 000
.	0 150	0 175	"	0 350	0 375			
4	0 175	0 200	8	0 375	0 400			

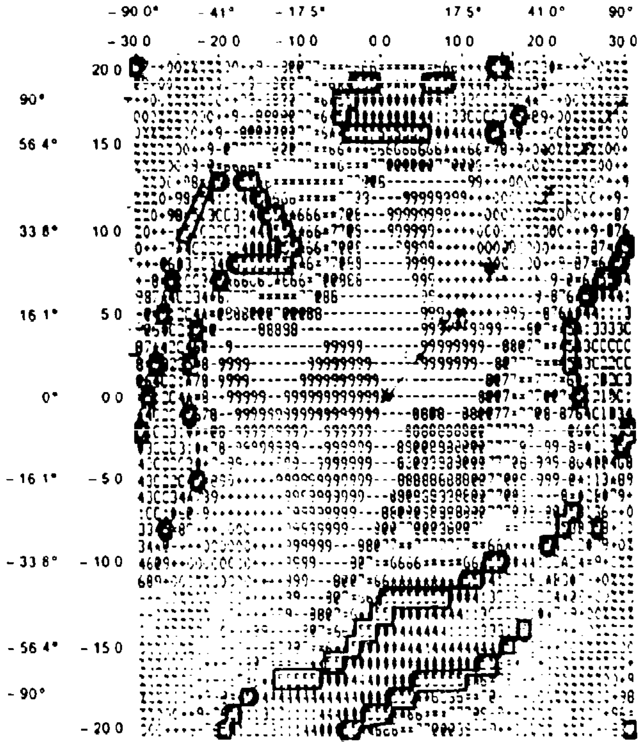

Figure 14. Stripline Notch

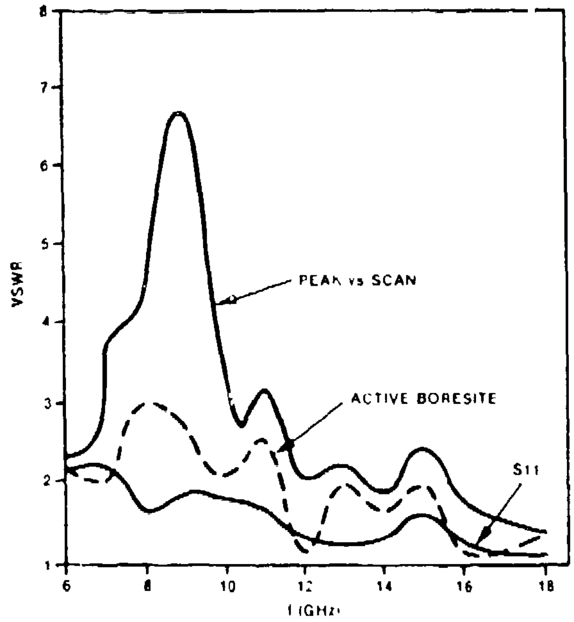

Figure 15. VSWR: Center Element 4 x 8 Notch Array

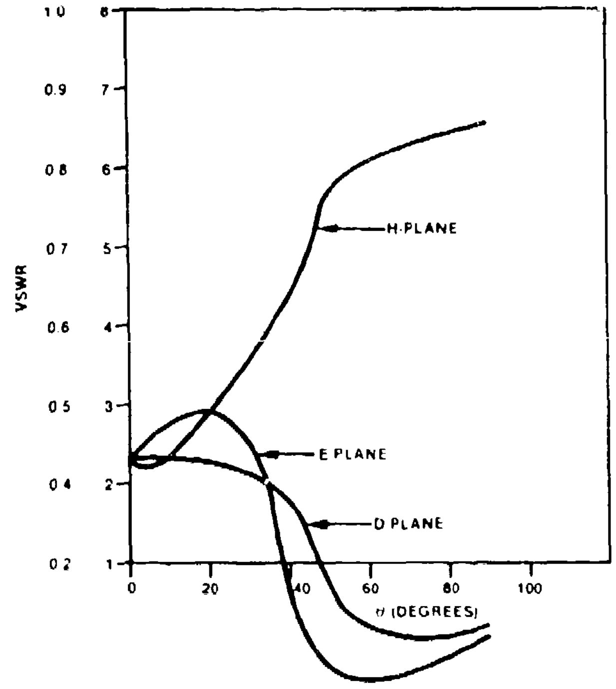

Figure 16. Active VSWR versus Scan H-Plane, Center Element, 4 x 8 Notch Array (9 GHz)

ELEMENT L24
13 GHz

MAP UNITS
HORIZONTAL = SIN(THETA)*COS(PHI) = M/30
VERTICAL = SIN(THETA)*SIN(PHI) = -N/18

REFLECTION COEFFICIENT

SYMBOL	FROM	TO	SYMBOL	FROM	TO	SYMBOL	FROM	TO
A	0 000	0 025	$	0 200	0 225	-	0 400	0 450
1	0 025	0 050	5	0 225	0 250	9	0 450	0 500
B	0 050	0 075	'	0 250	0 275	+	0 500	0 625
2	0 075	0 100	6	0 275	0 300	0	0 625	0 750
C	0 100	0 125	=	0 300	0 325	°o	0 750	0 875
3	0 125	0 150	7	0 325	0 350		0 875	1 000
	0 150	0 175		0 350	0 375			
4	0 175	0 200	8	0 375	0 400			

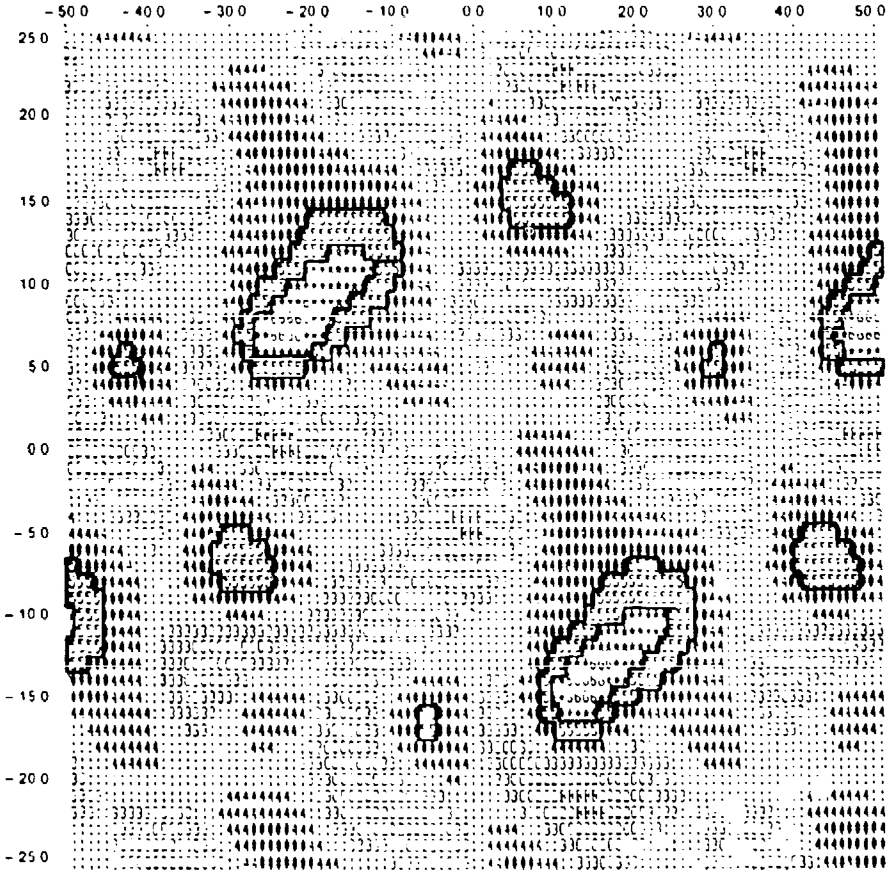

Figure 17. Active Reflection Coefficient

REFERENCES

1. R.S. Elliot, "An Improved Design Procedure for Small Arrays of Shunt Slots," IEEE Transactions on Antennas and Propagation, Vol. AP-31, No. 1, June 1983.

2. Arthur A. Oliner, "Surface-Wave Effects and Blindness in Phased-Array Antennas," Phased Array Antenna, Artech House, 1972, edited by A.A. Oliner and George Knittel, pp. 107-112.

3. T.R. Debski and P.W. Hannan, "Complex Mutual Coupling Measured in a Large Phased Array Antenna," The Microwave Journal, pp. 93-96, June 1965.

CYLINDRICAL LENS ARRAY FOR WIDEBAND ELECTRONIC SCANNING

E. M. Newman, C. M. Ruskowski
Hazeltine Corporation
Greenlawn, N. Y. 11740

Summary

A cylindrical printed-circuit lens-fed phased array can be used to provide wide-angle, wide-instantaneous bandwidth scanning. The fundamental approach has been described by Rotman and Franchi [1, 2, 3]. Hazeltine has designed and built a large printed-circuit lens array to demonstrate the concept. A description of the design, fabrication and test results are presented.

Introduction

A cylindrical-lens phased-array antenna offers the capability for electronically scanning a narrow pencil beam over wide angles in two dimensions, and for handling wide signal bandwidths without using variable time-delay devices.

An investigation of such a lens-array antenna has been conducted by Hazeltine for RADC/EEA. The first part of the program involved the study of the antenna and design of a specific configuration. The second part of the program included the fabrication and test of a lens-array antenna having the following performance objectives:

Scan:	±45° Az. ±25° El.
Total Bandwidth:	5.0 to 5.6 GHz
Instantaneous Bandwidth:	400 MHz
Directive Gain:	38 dB minimum
Aperture Size:	>40 λ Azimuth >30 λ Elevation

The three-dimensional cylindrical lens comprises a stacked set of identical two-dimensional lenses. Each two-dimensional lens consists of two arrays of radiators interconnected by transmission lines. This configuration is shown in figure 1.

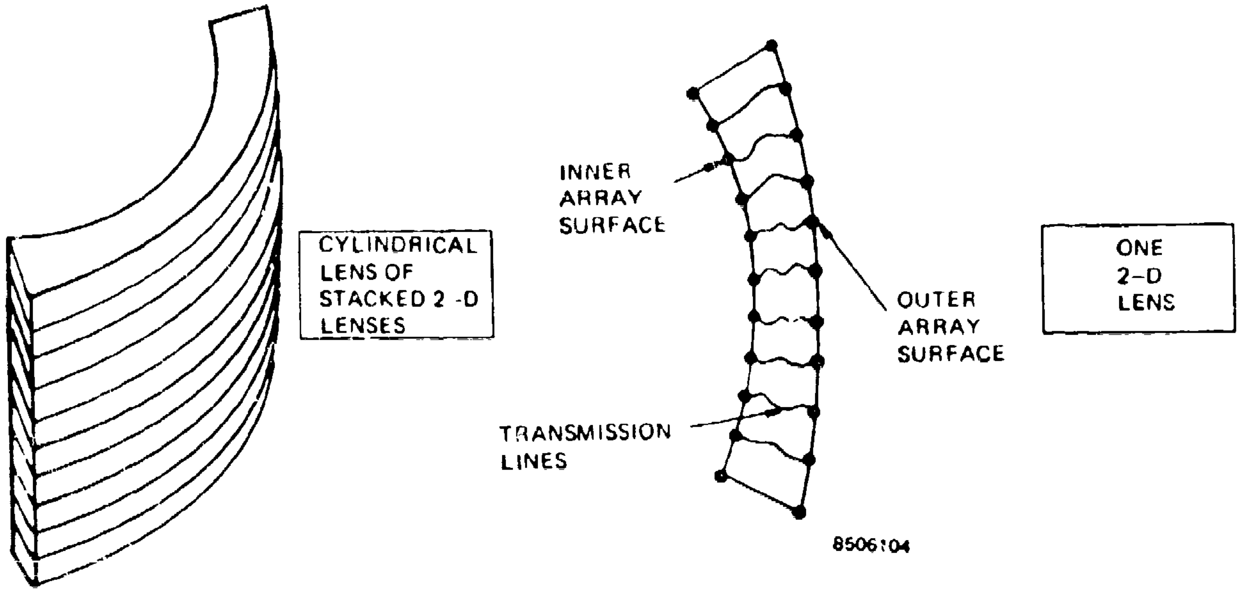

Figure 1. Cylindrical Lens Configuration

There are four degrees of freedom in the design of such a lens: the inner contour, the outer contour, the relative location of the inner and outer array elements, and the lengths of the interconnecting transmission lines. Rotman and Franchi derive a lens design in which the first three of these degrees of freedom are used to provide three points of perfect focusing in the azimuth plane. At azimuth angles between these three directions, the focusing may be imperfect but may still be quite satisfactory.

The fourth degree of freedom, namely the lengths of the interconnecting transmission lines, is used to control the change of azimuth focusing that may occur with the three-dimensional lens when elevation angle is varied. In particular, Rotman and Franchi show that if the lengths of the interconnecting transmission lines are constant throughout the lens, the three points of perfect azimuth focusing are retained independent of elevation angle. Furthermore, at intermediate azimuth angles, the azimuth aberration at any elevation angle is no greater than the azimuth aberration of the two-dimensional lens.

The significance of this result is that a cylindrical lens designed in this way can, when combined with an appropriate line-feed system, provide wide-angle scanning of a narrow pencil beam in both azimuth and elevation. For azimuth scanning, the line feed is displaced in azimuth, while for elevation scanning the line feed aperture is phase steered. This is illustrated in figure 2.

The ability of this constant-line-length cylindrical lens to permit elevation scanning without aberration is analogous to the similar ability of the widely used cylindrical reflector. However, the azimuth-scanning capability of the cylindrical reflector is severely limited by its coma aberration and by the aperture-blocking effect of any centrally-located feed system. The cylindrical lens avoids these limitations.

A phased-array antenna that is electronically scanned can rapidly steer a narrow pencil beam over wide angles. However, if the signal bandwidth (instantaneous bandwidth) is large relative to the array bandwidth, then a phased-array antenna can degrade the signal when the array scans over wide angles. One approach to this problem employs variable time-delay devices in the antenna, but these have some disadvantages. An alternate approach [1, 2, 3] employs the cylindrical-lens antenna as the feeding system for a standard electronically scanned phased array.

Suppose that the scan coverage of an antenna is ± sin θ_h horizontally and ± sin θ_v vertically. This coverage can be divided into M by N equal-size sub-regions, so that each sub-region covers only ±(1/M) sin θ_h by ± (1/N) sin θ_v as indicated in figure 3. If the feeding system for the phased-array antenna can provide a wideband beam that can be electronically switched from the center of one sub-region to another, then the phased array needs to scan over only the relatively small sub-region rather than over the full coverage of the antenna. This will permit a much wider signal bandwidth to be handled without substantial degradation of the signal.

The cylindrical lens antenna has the cability for providing a wideband beam at the center of each sub-region. Each beam in a different azimuth direction requires a line feed that is appropriately displaced in azimuth, as indicated in figure 4. Each beam in a different elevation direction requires a line feed having collimated radiation that is steered by fixed time delays to the appropriate elevation angle, as indicated in figure 4. An electronic switch connects in sequence to each of the M x N line feeds to provide the coarse steering from one sub-region to another. Electronic phase shifters located in the cylindrical lens provide the fine steering over each sub-region.

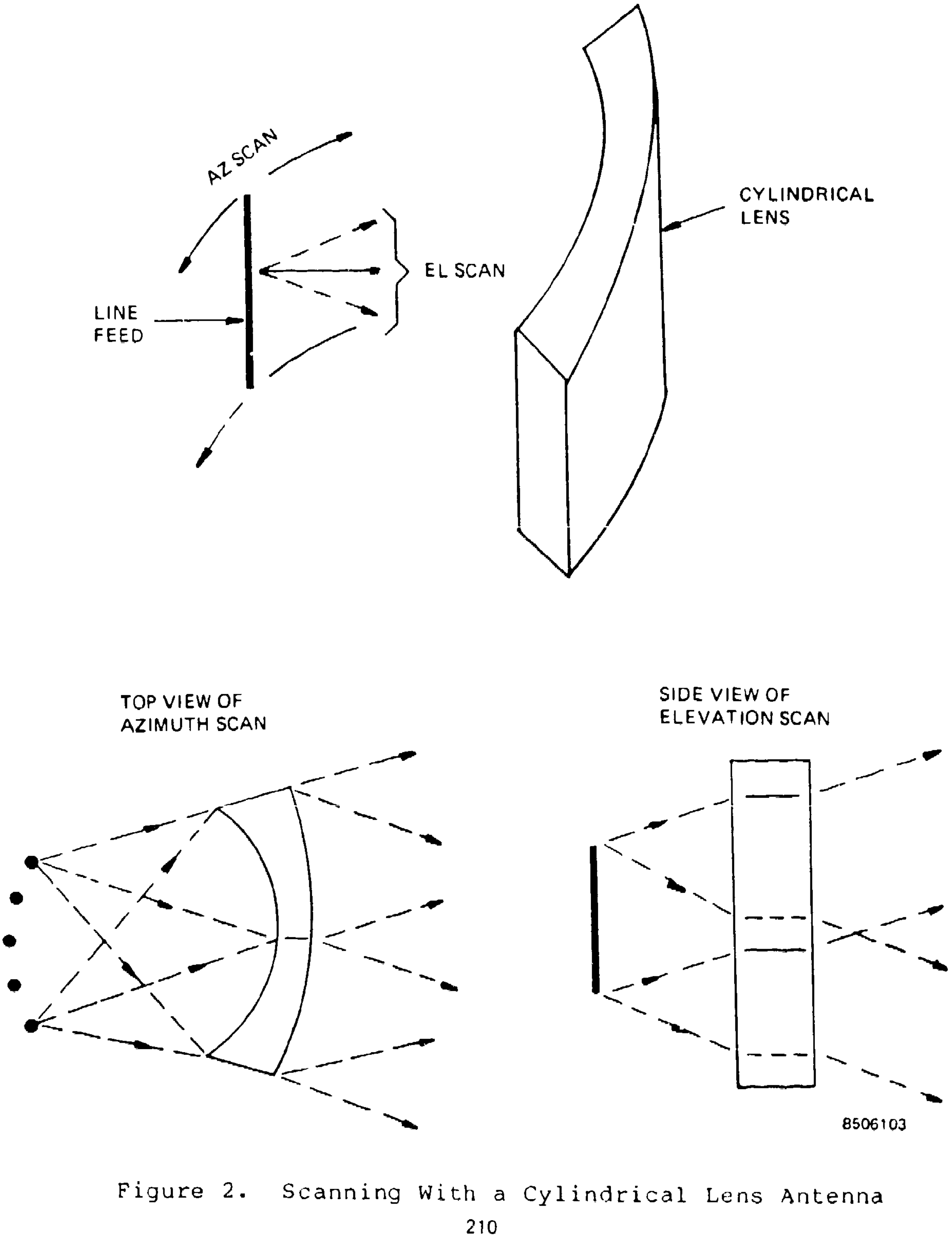

Figure 2. Scanning With a Cylindrical Lens Antenna

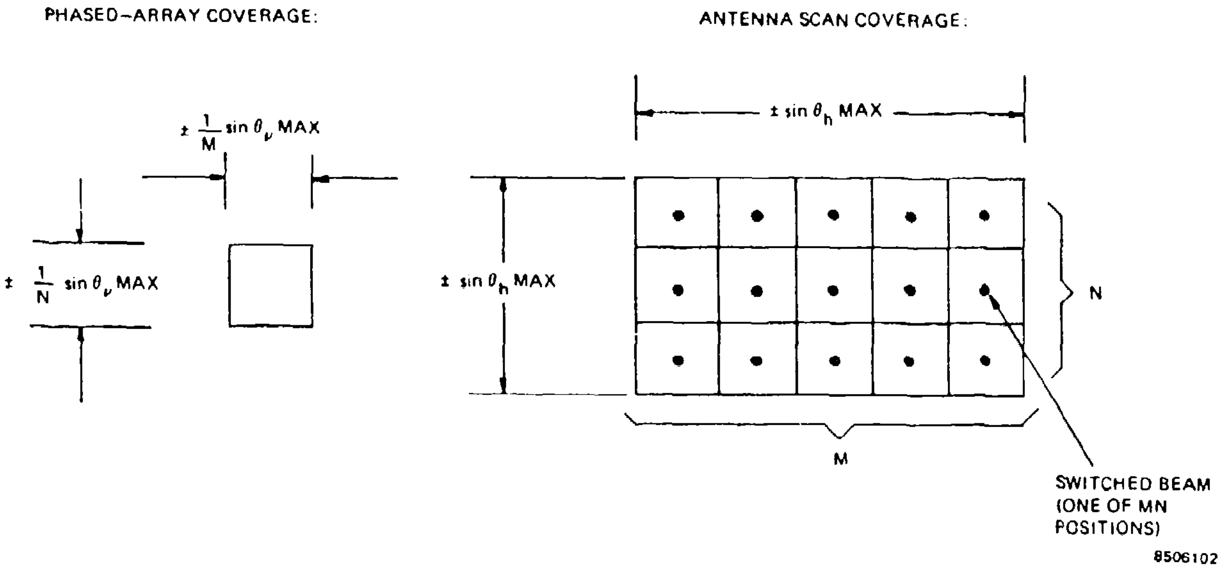

Figure 3. Approach for Wideband Wide-Angle Electronic Scanning

Each coarse beam position provides wide signal bandwidth because the lens antenna with multiple line feeds provides true time-delay steering and focusing. The phased array located in the lens uses simple phase shifters for fine steering the beam, but achieves wide signal bandwidth because of the relatively small size of the scan sub-region compared with the full scan coverage of the antenna.

Lens Configuration Selected for Fabrication

The first phase of the program included a study of several different lens shapes that could be designed using the constrained lens concept. These were termed "dimpled, pointed, hybrid and R-2R". All had a minimum of three azimuth focal points, with the limiting case being the R-2R configuration, which had perfect focusing over the entire azimuth arc.

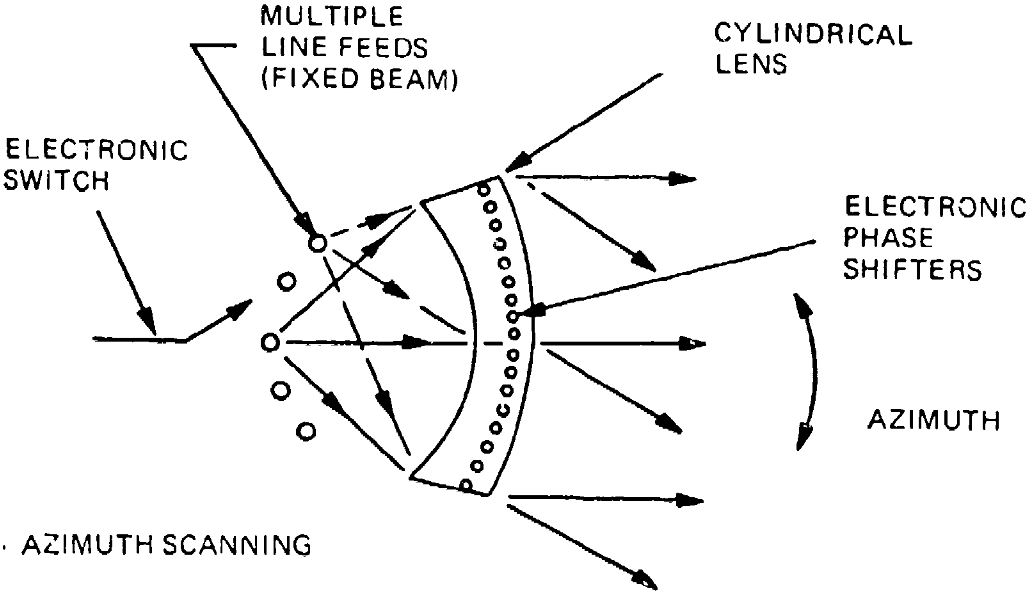

a. AZIMUTH SCANNING

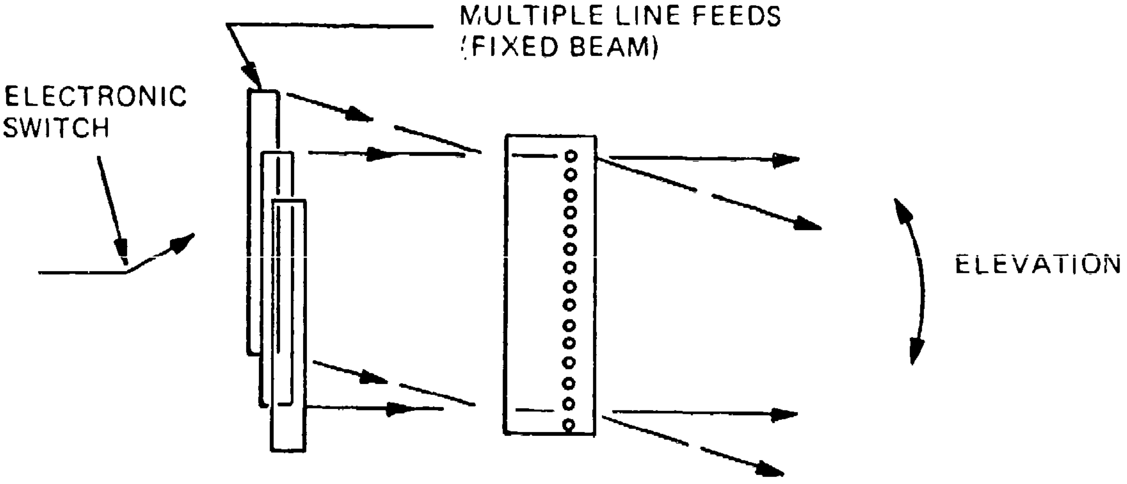

b. ELEVATION SCANNING

8205194

Figure 4. Cylindrical Lens Antenna for Wideband Wide-Angle Electronic Scanning

The R-2R configuration was selected for fabrication based upon:

1. The continuous focused feed arc.
2. The relatively simple geometry.
3. The lack of discontinuities at the center of the lens.
4. The symmetry of the lens.

The antenna configuration selected for fabrication consists of the lens and a single line feed. Figure 5 shows the basic antenna configuration comprising the cylindrical lens and its on-axis feed. An F/D = 0.96 was selected.

The horizontal aperture dimension was chosen as 40 wavelengths at 5.3 GHz, or about 7.4 feet. The vertical length of the line feed is about 35 wavelengths or 6.5 feet, and the lens vertical dimension is 38 wavelengths, or 7 feet.

The lens contains 62 layers of microstrip circuits, each layer containing printed dipoles and interconnecting transmission lines. Element spacing is 0.4 λ in azimuth and 0.6 λ in elevation.

The line feed contains 58 printed circuit elements; each element contains 8 dipoles. Element spacing is 0.6 λ in elevation.

Description of Antenna

The wideband lens-array consists of two principal components; the line feed and the lens. Both are constructed of microstrip transmission lines and components.

Each lens layer contains 106 equal-length microstrip lines that interconnect pairs of radiating elements. Because the width of the lens varies, the lines must be wrapped to fit them into the available space. Figure 6 shows one-half of a lens layer on both top and bottom. The top layer contains the meandered lines (some with stubs which compensate for dispersion in the wrapped-up lines), and the feed and tuning for the printed dipoles. The bottom of the layer contains the ground plane for the microstrip lines as well as the dipoles. All artwork was computer generated.

The layers of the lens were backed by a sheet metal stiffener and spaced by a combination of dielectric and metal standoffs. Figure 7 shows the layers of the lens while figure 8 shows the completed lens prior to the installation of the radome.

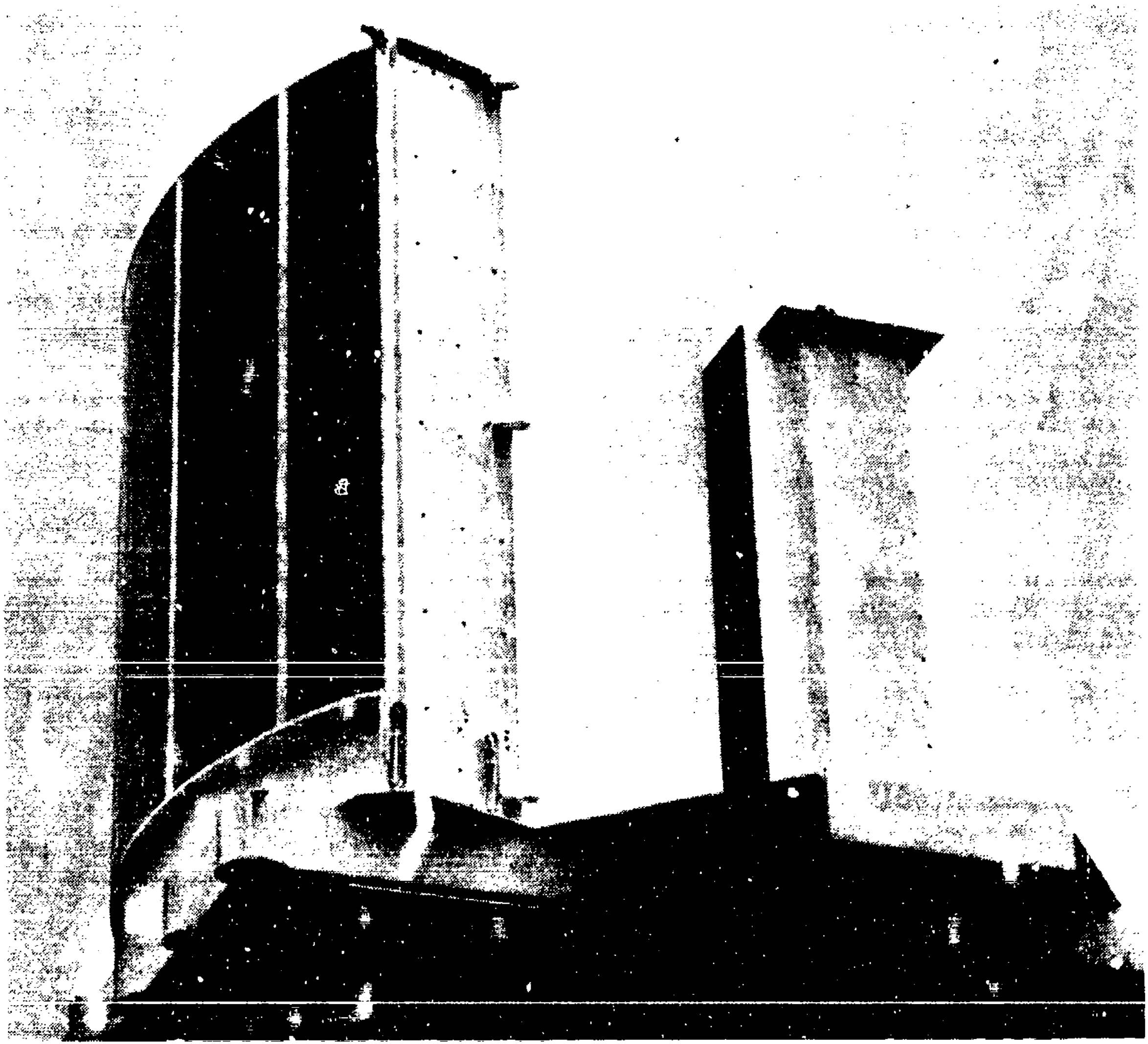

Figure 5. Lens Antenna and Line Feed

The line feed consists of 58 identical microstrip layers. Each layer contains a horizontal row of 8 dipoles excited by a microstrip power divider. The resulting current distribution across the dipole row provides the azimuth feed pattern needed for low antenna azimuth sidelobes.

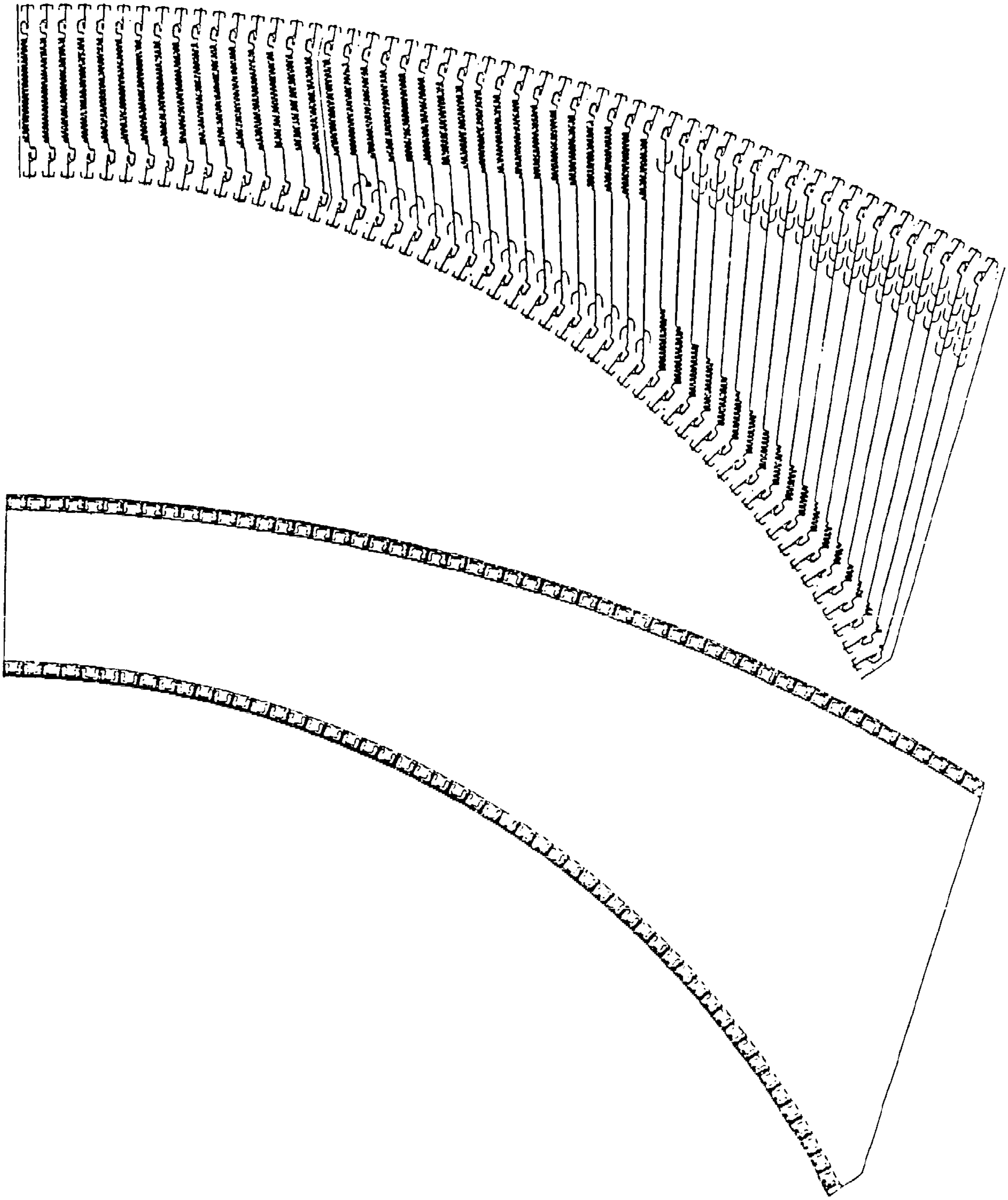

Figure 6. Typical Lens Layer

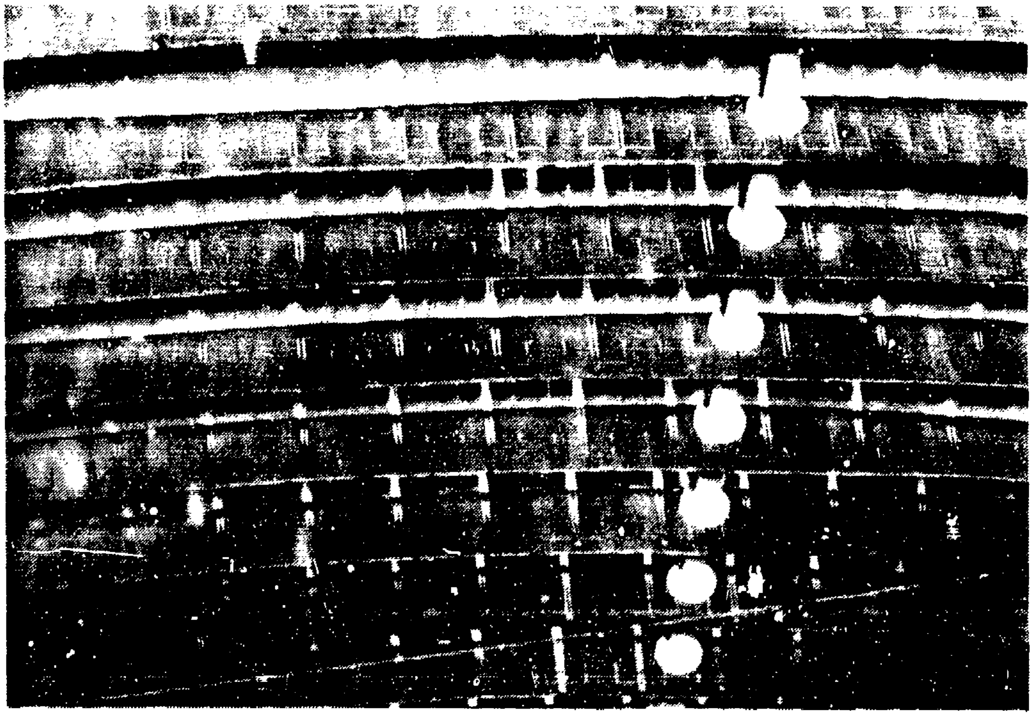

Figure 7. Detailed Lens Layer Construction

The line feed elevation power divider provides the vertical illumination for the line feed layers. Connectors at the network outputs interface it to the corresponding microstrip layers through semi-rigid cable. Each cable was phase-trimmed to provide equal phase lengths from the elevation power divider input to the cable output over the 5.0 to 5.6 GHz band.

The elevation power divider was fabricated on one microstrip board. A sheet-metal backing supports the microstrip and connectors. The fully assembled unit is located mid-way vertically behind the stacked-azimuth layers. The power divider is structurally supported through horizontal stand-offs which attach the power divider to the bent-sheetmetal supports in the column. The assembled layers, interconnecting cables, and elevation power divider are shown in figure 9.

The line-feed radiating element layers and elevation power divider are enclosed in a sheet metal cabinet with a thin radome on the front, to protect the microstrip from weather.

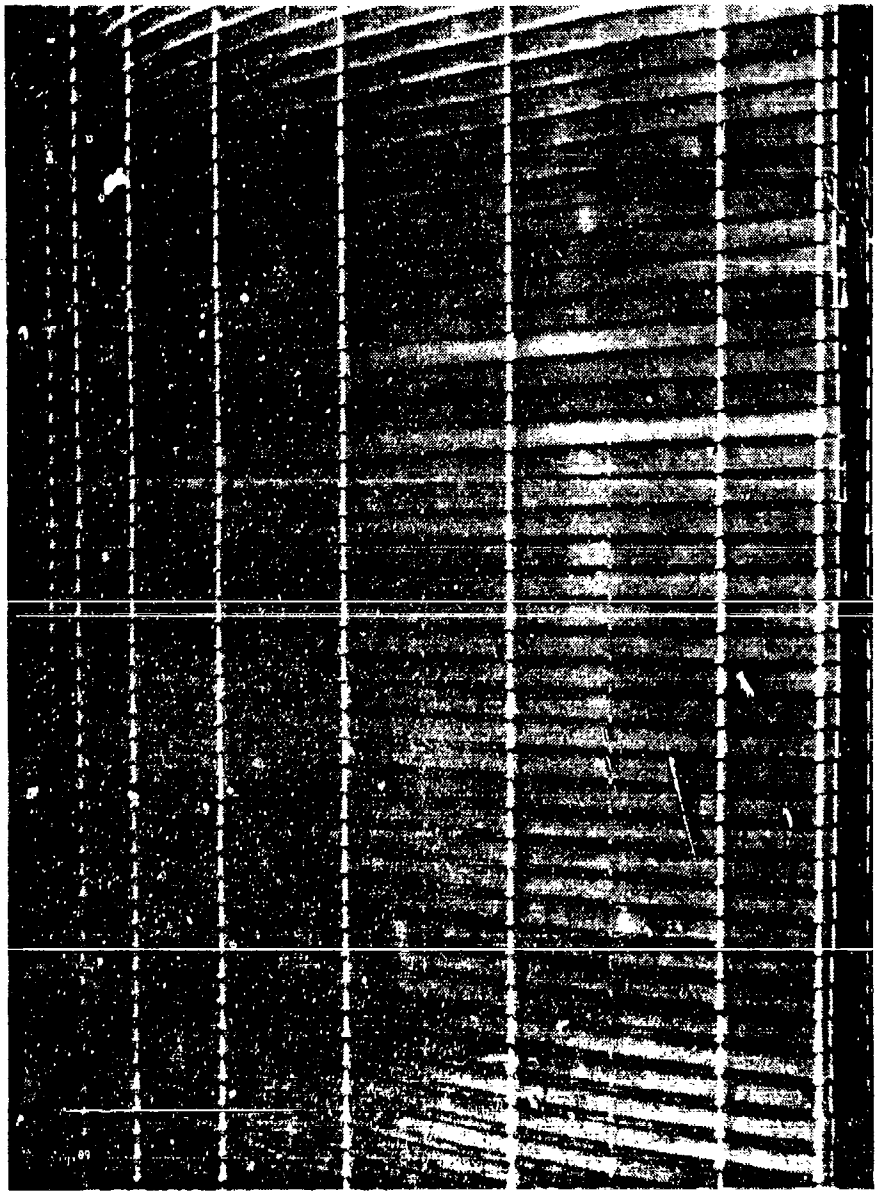

Figure 8. Lens Without Protective Radomes

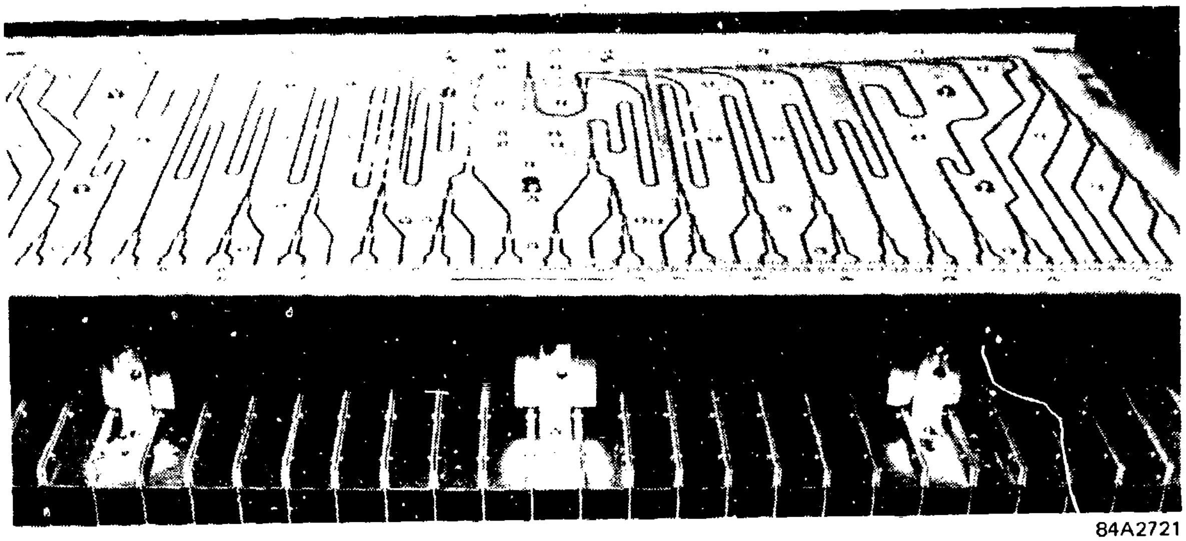

Figure 9. Line-feed Layers and Elevation Power Divider

The line feed assembly is positioned on the antenna support structure via a base assembly which enables adjustment of the feed position.

Figure 5 shows the completed lens and line feed mounted on the support structure.

Test Results

Azimuth patterns were taken for four azimuth scan locations of the line feed, namely, 0°, 15°, 30°, and 45°. Figure 10 shows a representative azimuth pattern measured at 5.3 GHz, 0° azimuth and 0° elevation.

Measurements at wide azimuth scan angles demonstrated the wideband nature of the lens. Figure 11 shows patterns measured at 5.0, 5.3, and 5.6 GHz for an azimuth scan angle of 45°. Note that the beam pointing angle and pattern shape remain nearly constant over the band.

Figure 12 shows measured elevation patterns for both scanned and unscanned conditions. The pattern was scanned by using cable lengths by the line feed and by displacing the feed vertically.

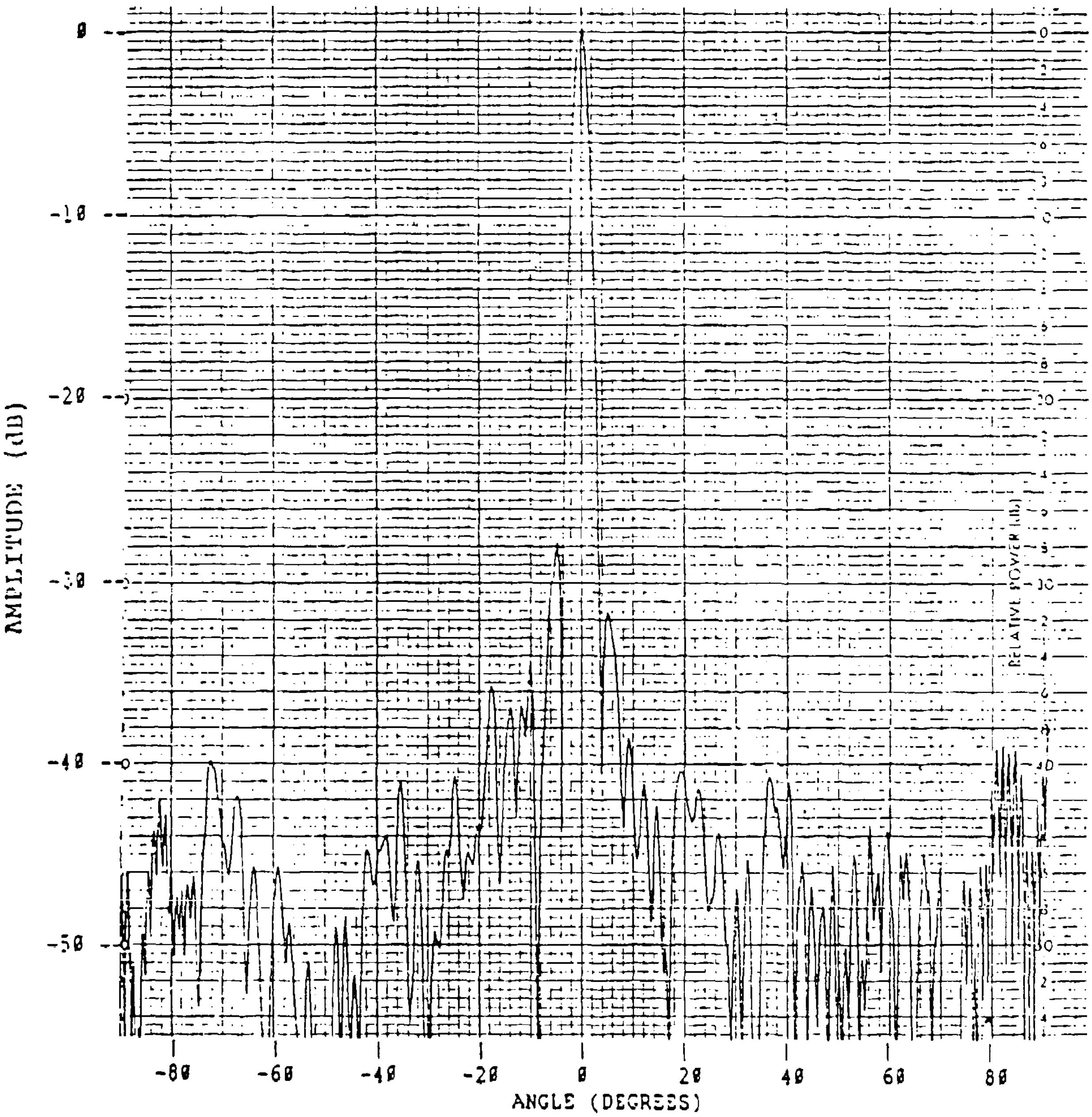

Figure 10. Azimuth Pattern Cut at 5.3 GHz 0 Degree Azimuth Position 0 Degree Elevation

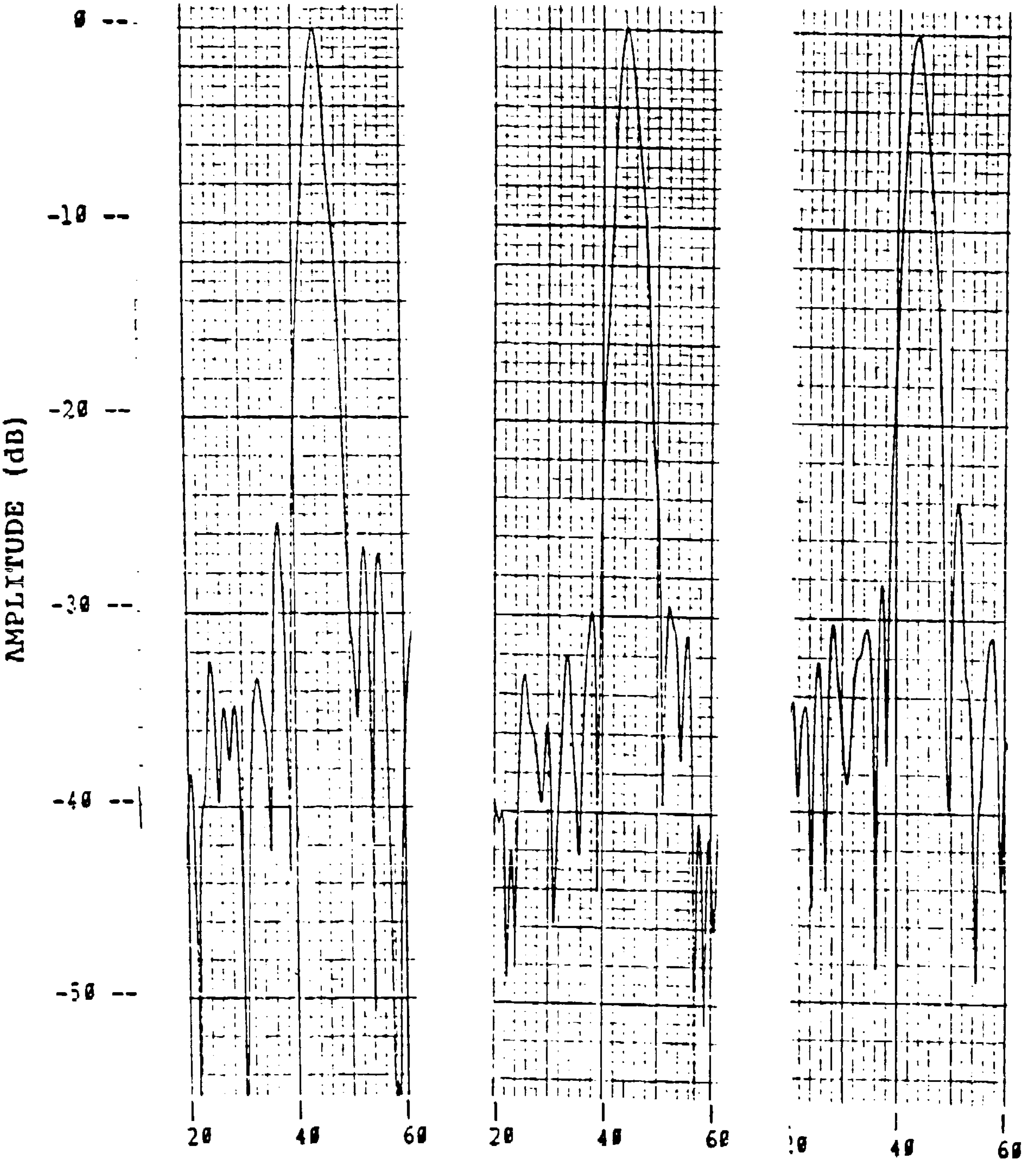

Figure 11. Comparison of Azimuth Patterns versus Frequency at 45° Azimuth Scan

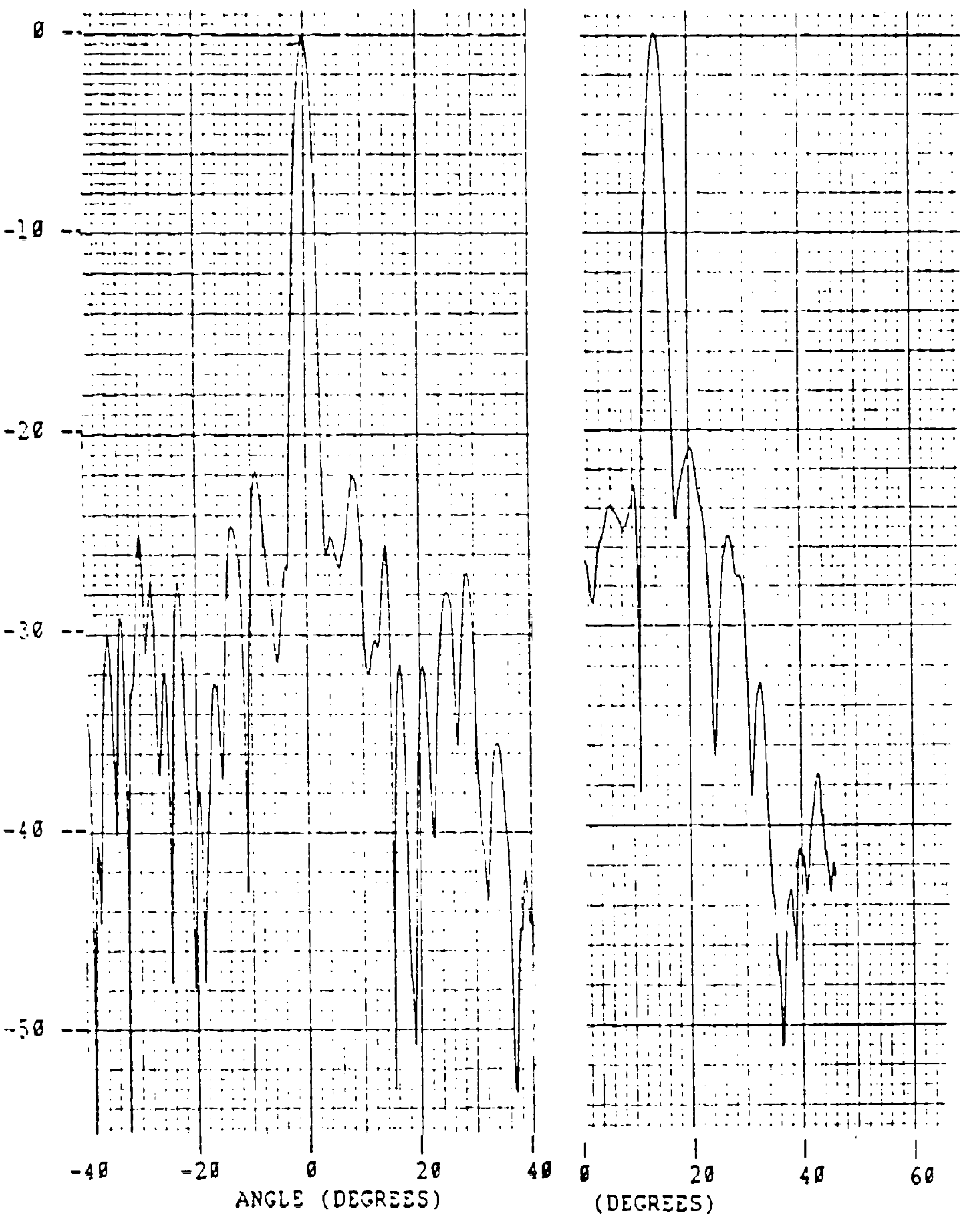

Figure 12. Comparison of Scanned and Unscanned Elevation Patterns at 5.3 GHz.

Summary and Conclusions

The wideband, wide-angle scan capability of the lens is demonstrated by the measured patterns shown. The antenna has been tested to both 45° azimuth scan at 0° elevation, and 30° azimuth simultaneously with 15° elevation beam scanning.

Test results have demonstrated that the lens can be scanned to wide azimuth angles (±45°) over a 5.0 to 5.6 GHz band. The patterns confirm the design of the R-2R lens which provides a circular focal line and allows the patterns to remain perfectly focused for all azimuth angles.

The pattern tests also show that the array can be scanned in elevation by displacing the line feed and scanning the line feed beam. No significant degradation of the elevation patterns was noted with elevation scanning.

The microstrip lens array is a good candidate for wide instantaneous band, wide-angle scanning. Test results demonstrated that the bandwidth is achieved without substantial degradation in gain or pattern performance.

Acknowledgement: This work has been supported by Rome Air Development Center under Contract F19628-80-C-0110. Appreciation is expressed to the project monitor, Dr. Peter R. Franchi, for his helpful comments and support.

References:

1. P. Franchi, N. Kernweis, W. Rotman, "Wideband Microwave Lens Antenna for Tactical Radar Applications", Proceedings of 1980 Antenna Applications Symposium, Allerton Park, Illinois; September 1980.

2. W. Rotman et al, "Cylindrical Microwave Lens Antenna for Wideband Scanning Applications", AD-D008526; February 1981.

3. P. W. Hannan and E. M. Newman, "Study and Design of a Cylindrical Lens-Array for Wideband Electronic Scanning", RADC-TR-83-128, Dec. 1983. AD A138808

ARRAYS OF COAXIALLY-FED MONOPOLE ELEMENTS IN A PARALLEL PLATE WAVEGUIDE

Boris Tomasic
Rome Air Development Center
Electromagnetic Sciences Division
Hanscom AFB, MA 01731

Alexander Hessel
Polytechnic Institute of New York
Microwave Research Institute
Farmingdale, NY 11735

ABSTRACT

Arrays of coaxially-fed monopoles radiating into a parallel plate region are used extensively in various antenna systems. Concave arrays of monopoles backed by a conducting ground surface are employed in space-fed microwave lenses. Convex ring arrays of monopole elements placed coaxially around a conducting cylindrical ground are particularly suitable for applications requiring uniform 360 degree azimuth coverage. Linear arrays of monopoles find various applications in lens antenna systems. In addition, the information derived from the study of these arrays is of considerable help in design of a large variety of conformal arrays.

In this paper the principles of analysis of linear and circular concave and convex arrays of coaxially-fed linear monopole elements within a parallel plate region are described. Expressions for active admittance, coupling coefficients and element patterns are given. For all three array types a unified formulation is obtained. Numerical results are presented for relevant parameter values, judiciously selected to illustrate the various design tradeoffs.

The paper also describes the experimental effort and presents measured data for active impedance, coupling coefficients and element patterns. The measured values show excellent agreement with theoretical results. This agreement strongly supports the validity of the analysis, and furnishes a firm basis for a systematic and accurate array design.

This work was supported by the Rome Air Development Center under project No. 2305J303.

I. INTRODUCTION

Arrays of coaxially-fed monopole elements radiating into a parallel plate region are of interest for various antenna applications. In particular, concave arrays of monopoles backed by a conducting ground surface are employed in space-fed Bootlace, Rotman, R-2R and R-KR microvave lenses, the last two being strictly circular. Convex ring arrays of monopole elements placed coaxially around a conducting cylindrical ground are attractive for radar and communication applications because of their uniform circumferential radiation characteristic and 360 degree azimuth coverage capabilities. Linear arrays of monopoles are used in space-fed beamforming networks as well as in phased arrays. In addition, the information derived from the study of linear arrays is useful in design of conformal arrays. In view of its simplicity, low cost, polarization purity, reasonable bandwith, and power handling capability, the coaxially-fed linear monopole is an attractive choice for an array element in a parallel plate waveguide. Consequently, a detailed knowledge of the radiation and impedance properties of this element in its array environment is essential for a systematic design of high performance arrays.

We present an outline of the analysis of the effects of mutual coupling on active impedance, element patterns, and coupling coefficients in linear, cylindrical concave, and cylindrical convex arrays of coaxially fed monopole elements in parallel plate guide regions. In each case the elements are backed by a conducting ground. The details of derivations will be found in [1] to [7]. For all three array types the analysis takes into account the geometry of the feed system.

For all three array types, unified expressions are given for the active admittance, which contains two types of terms; one which depends on the element geometry only, and the other on array geometry and phasing.

Relations are also presented for coupling coefficients for each array type as well as for element patterns of linear and convex circular arrays. Numerical data illustrate the method of selection of optimal geometry for element match in an array environment, as well as the dependence of important design parameters, such as element pattern phase center, on the element and array geometry.

To validate the theory, experiments were performed. In all cases very good agreement has been found between computer simulation and measurements.

II. FORMULATION

In this section we present the principles of analysis and the resulting expressions for the active admittance, coupling coefficients, and element patterns of a coaxially-fed monopole element in infinite linear, circular concave and, circular convex arrays in a parallel plate guide region.

The analysis takes into account the geometry of the feed system. The probe current is assumed to have only an axial component and no angular variation. This approximation is justified since the probe radius is small compared to the wavelength. Furthermore, the analysis assumes that the field distribution in each aperture is that of the TEM mode of the coaxial feed-line, consistent with the angularly uniform probe current density. The effect on active admittance of neglecting higher modes in the coaxial aperture is very small [1].

A. Array Models

Figs. 1 to 6 show the three array models under consideration. In Figs. 3 and 5 the top plate of the parallel plate waveguide is partially removed to display a section of the array. The infinite linear array and the circular concave and convex ring arrays of coaxially-fed monopoles of length ℓ are located in a parallel plate waveguide of height $h < \lambda/2$, in which only the TEM mode propagates. The uniform inter-element spacing is d. The distance s between the probe elements and the "ground plane" is approximately $\lambda/4$. In circular arrays a ring of radius B contains N equispaced identical monopoles at the distance s from a perfectly conducting circular cylindrical ground surface of radius A. In a concave array $A = B + s$, while in convex array $A = B - s$ where $s \approx \lambda/4$ as shown in Figs. 4 and 6. The probe radius is $a << \lambda$ while the inner and outer radii of the coaxial feed lines are a and b, respectively.

B. Array Excitation, Notation and Coordinates

In the linear array case all elements are initially force-excited with aperture voltages of equal amplitude V_o and a progressive phase factor $\exp(-j\delta p)$ where $\delta = k_{xo}d = kd \sin \hat{\phi}_o$ is the inter-element phase increment and $p = \ldots,-1,0,1,\ldots$ is the element serial number. Similarly, in the circular array case all elements are force-excited with aperture voltages of equal amplitude V_o and a progressive phase according to $\exp(-j2\pi\upsilon p/N)$ where $\upsilon = 0,1,\ldots,N-1$ is the angular wave number and $p=0,1,\ldots,N-1$ is the element serial number. The $p=0$ element denotes the reference element.

We define a local cylindrical coordinate system (ρ,ϕ,z) with the origin at the bottom plate of the parallel plate waveguide centered at the reference ($p=0$) element. In the case of circular ring arrays we define in addition a global cylindrical coordinate system $(\hat{\rho},\hat{\phi},z)$ such that the z-axis coincides with the rotation axis of the ring.

C. Active Admittance Y_a

To evaluate $Y_a(\delta)$, $Y_a(\upsilon)$ use is made of the equivalence principle in that the coaxial TEM aperture electric fields are replaced by suitable magnetic current sources placed on a conducting unperforated bottom wall of the parallel plate guide. By the Floquet Theorem the amplitude V_o of all concentric magnetic currents and all induced probe currents are identical, save for a phase shift factor. The unknown probe current distribution is determined by the requirement that the total axial field component $E_z(\rho,z)$ vanishes on the reference probe surface. Here, $E_z(\rho,z)$ is regarded as a superposition of individual contributions of all unknown, angularly symmetric probe currents and all known (save for the voltage factor V_o) magnetic currents.

The analysis is carried out in parallel for all three array types in a number of steps:

1. A typical contribution E_{zo} is due to combination of a single probe current $J_z(z)$ and a concentric to it magnetic current source $\underline{M}$, where

$$\underline{M}(\rho, z=0) = -\underline{\phi}_o \frac{V_o}{\rho \ \ln \frac{b}{a}} \tag{1a}$$

and

$$\underline{J}(\rho, z) = \underline{z}_o \ J_z(z) \ \delta(\rho - a) \quad , \quad 0 < z < \ell \ . \tag{1b}$$

In (1a) $\underline{\phi}_o$ is the angular unit vector and in (1b) $\delta(\rho - a)$ represents the Dirac impulse function.

As indicated

$$E_{zo}(\rho, z) = E_{zo}(\rho, z; V_o) + E_{zo}(\rho, z; J_z) \tag{2}$$

where the first term is due to $\underline{M}$ and the second to $\underline{J}$. Both field contributions in (2) are represented in terms of radial modes of the parallel plate guide with propagation constant κ_n. They may be written in the form:

$$E_{zo}(\rho, z; V_o) = jK \ V_o(z=0^-) \sum_{n=0}^{\infty} \epsilon_n \ C_n(z) \begin{cases} H_o^{(2)}(\kappa_n \rho) \ \mathcal{J}_n & ; \ \rho > b \\ J_o(\kappa_n \rho) \ H_o^{(2)}(\kappa_n b) - H_o^{(2)}(\kappa_n \rho) \ J_o(\kappa_n a) & ; \ a < \rho < b \\ J_o(\kappa_n \rho) \ \mathcal{H}_n & ; \ \rho < a \end{cases} \tag{3a}$$

with

$$K = \frac{\pi}{2h \ \ln \frac{b}{a}} \tag{3b}$$

$$\epsilon_n = \begin{cases} 1 \ ; \ n = 0 \\ 2 \ ; \ n > 1 \end{cases} \tag{3c}$$

$$C_n(z) = \cos \frac{n\pi}{h} z \tag{3d}$$

$$\kappa_n = \sqrt{k^2 - (\frac{n\pi}{h})^2} \quad , \quad \mathrm{Im}[\kappa_n] < 0 \tag{3e}$$

$$\mathcal{J}_n = J_o(\kappa_n b) - J_o(\kappa_n a) \tag{3f}$$

and

$$\mathcal{H}_n = H_o^{(2)}(\kappa_n b) - H_o^{(2)}(\kappa_n a) \ . \tag{3g}$$

In (3f) and (3g) $J_o(x)$ and $H_o^{(2)}(x)$ denote the Bessel function of the first kind and Hankel function of the second kind, respectively, both of zero order and argument x. Also

$$E_{zo}(\rho,z;J_z) = \frac{C\,\zeta_o}{k} \sum_{n=0}^{\infty} \varepsilon_n \kappa_n^2 C_n(z) I_n \begin{cases} J_o(\kappa_n a)\, H_o^{(2)}(\kappa_n \rho) \ ; \ \rho > a \\ J_o(\kappa_n \rho)\, H_o^{(2)}(\kappa_n a) \ ; \ \rho < a \end{cases} \tag{4a}$$

with

$$C = -\frac{\pi a}{2h} \tag{4b}$$

$$\zeta_o = \frac{1}{\eta_o} = \sqrt{\frac{\mu_o}{\varepsilon_o}} = 376.6 \simeq 120\,\pi \quad [\Omega] \tag{4c}$$

$$I_n = \int_{z=0}^{\ell} J_z(z)\, C_n(z)\, dz \ . \tag{4d}$$

2. The total axial electric field $E_z(\underline{r};\delta)$ for linear array, and $E_z(\underline{r};\upsilon)$ for circular arrays is regarded as a superposition of two contributions, i.e.,

$$E_z(\underline{r};\delta) = E_z^{inc}(\underline{r};\delta) + E_z^{s}(\underline{r};\delta) \qquad \text{(linear)} \tag{5a}$$

$$E_z(\underline{r};\upsilon) = E_z^{inc}(\underline{r};\upsilon) + E_z^{s}(\underline{r};\upsilon) \qquad \text{(circular)} \tag{5b}$$

where the particular solution E_z^{inc} is due to a linear, or a ring array of yet unknown probe currents and the concentric, known magnetic current sources in an infinitely extended parallel plate waveguide in the absence of the conductig ground boundaries. The E_z^{s} is a homogeneous, bounded solution in a unit cell with conducting top and bottom walls and phase-shift side walls, such that

$$E_z(x,y=-s,z;\delta) = 0 \ , \qquad \text{(linear)} \tag{6a}$$

$$E_z(\rho=A,\phi,z;\upsilon) = 0 \ , \qquad \text{(circular).} \tag{6b}$$

3. In this step we determine E_z^s. The form of the homogeneous solution is:

$$E_z^s(\underline{r};\delta) = \sum_{n=0}^{\infty} \sum_{m=-\infty}^{\infty} B_{mn}(\delta)\, C_n(z)\, \frac{e^{-jk_{ymn}y}}{k_{ymn}}\, e^{-jk_{xm}x} \qquad \text{(linear)} \qquad (7a)$$

$$E_z^s(\underline{r};\upsilon) = \sum_{n=0}^{\infty} \sum_{m=-\infty}^{\infty} B_{mn}(\upsilon)\, C_n(z) \begin{cases} J_{\upsilon_m}(\kappa_n\rho) & e^{-j\upsilon_m\phi} \quad \text{(concave)} \\ H_{\upsilon_m}^{(2)}(\kappa_n\rho) & e^{-j\upsilon_m\phi} \quad \text{(convex)} \end{cases} \qquad (7b)$$

where the Floquet wave numbers along the direction of array periodicity are:

$$k_{xm} = k_{xo} + \frac{2\pi}{d} m \quad , \quad k_{xo} = \frac{\delta}{d} \qquad (7c)$$

$$\upsilon_m = \upsilon + \frac{2\pi}{\alpha} m \quad , \quad \alpha = \frac{2\pi}{N} \qquad (7d)$$

with

$$k_{ymn} = \sqrt{\kappa_n^2 - k_{xm}^2}\ . \qquad (7e)$$

The expansion coefficients B_{mn} are determined via (6). To this end we first determine E_z^{inc} at the conducting boundaries as a superposition of individual probe currents and the associated concentric magnetic current contributions centered at $\underline{\rho}_p$ in an infinite parallel plate waveguide. Thus, with reference to Figs 7 and 8, we have

$$E_z^{inc}(\underline{r};\delta) = \sum_{p=-\infty}^{\infty} E_{zp}(\underline{r})\, e^{-j\delta p} \qquad \text{(linear)} \qquad (8a)$$

$$E_z^{inc}(\underline{r};\upsilon) = \sum_{p=0}^{N-1} E_{zp}(\underline{r})\, e^{-j\frac{2\pi}{N}\upsilon p} \qquad \text{(circular)} \qquad (8b)$$

where from (3a) and (4a)

$$E_{zp}(\underline{r}) = \sum_{n=0}^{\infty} f_n(J_z, V_o)\, C_n(z)\, H_o^{(2)}(\kappa_n|\underline{\rho} - \underline{\rho}_p|)\ . \qquad (8c)$$

with

$$f_n(J_z, V_o) = jK\, V_o(z=0^-)\, \varepsilon_n\, \mathcal{I}_n + \frac{C}{k\eta_o} \varepsilon_n\, \kappa_n^2\, I_n\, J_o(\kappa_n a)\ . \qquad (8d)$$

Note that $\underline{r} = \underline{\rho} + \underline{z}_o z$ refers to the field (observation) point.

Using Poisson's sum formula in (8a) and the Addition Theorem for cylindrical functions in (8b) we expand E_z^{inc} in terms of Floquet modes in a unit cell. At a conducting boundary E_z^{inc} takes the form

$$E_z^{inc}(x,y=-s,z;\delta) = -\frac{2}{d}\sum_{n=0}^{\infty}\sum_{m=-\infty}^{\infty} f_n\, C_n(z)\,\frac{e^{jk_{ymn}s}}{k_{ymn}}\, e^{-jk_{xm}x} \qquad \text{(linear)} \qquad (9a)$$

$$E_z^{inc}(\hat{\rho}=A,\hat{\phi},z;\nu) = N\sum_{n=0}^{\infty}\sum_{m=-\infty}^{\infty} f_n\, C_n(z) \begin{cases} J_{\nu_m}(\kappa_n B)\, H_{\nu_m}^{(2)}(\kappa_n A)\, e^{-j\nu_m\phi} & \text{(concave)} \\ J_{\nu_m}(\kappa_n A)\, H_{\nu_m}^{(2)}(\kappa_n B)\, e^{-j\nu_m\phi} & \text{(convex)} \end{cases} . \qquad (9b)$$

Substitution of (9a) and (9b) into (6) yields

$$B_{mn}(\delta) = \frac{2}{d}\, f_n(J_z,V_o)\,\frac{e^{-jk_{ymn}2s}}{k_{ymn}} \qquad \text{(linear)} \qquad (10a)$$

$$B_{mn}(\nu) = -N\, f_n(J_z,V_o)\, H_{\nu_m}^{(2)}(\kappa_n A)\,\frac{J_{\nu_m}(\kappa_n B)}{J_{\nu_m}(\kappa_n A)} \qquad \text{(concave)} \qquad (10b)$$

$$B_{mn}(\nu) = -N\, f_n(J_z,V_o)\, J_{\nu_m}(\kappa_n A)\,\frac{H_{\nu_m}^{(2)}(\kappa_n B)}{H_{\nu_m}^{(2)}(\kappa_n A)} . \qquad \text{(convex)} \qquad (10c)$$

It is interesting to note that by applying Poisson's sum formula to (7a) with $B_{mn}(\delta)$ as given by (10a) one obtains

$$E_z^s(\underline{r};\delta) = \sum_{p=-\infty}^{\infty} H_0^{(2)}(\kappa_n|\underline{\rho} - \underline{\rho}_p + \underline{y}_o 2s|)\, e^{-j(\delta p+\pi)} \qquad (11)$$

which represents an image array contribution to the total axial field. Thus in the case of a linear array the total field can be also found by superposition of the contributions from all real and image array elements.

4. For an observation point $P(\rho,\phi,z)$ on the reference probe $p=0$, the total field E_z is obtained as a superposition of all relevant probe-aperture contributions centered at $\underline{\rho}_p$ and of the appropriate homogeneous solution drived in step 3. Thus,

$$E_z(\underline{r};\delta) = E_{zo}(\rho=a,z) + \sum_{p=-\infty}^{\infty}{}' E_{zp}(|\underline{a} - \underline{\rho}_p|,z)\, e^{-j\delta p} + E_z^s(\underline{r};\delta) \qquad \text{(linear)} \qquad (12a)$$

$$E_z(\underline{r};\nu) = E_{zo}(\rho=a,z) + \sum_{p=1}^{N-1} E_{zp}(|\underline{a} - \underline{\rho}_p|,z)\, e^{-j\frac{2\pi}{N}\nu p} + E_z^s(\underline{r};\nu) \qquad \text{(circular)} \qquad (12b)$$

where, E_{zp} (with $\underline{\rho} = \underline{a}$) for $p > 1$ is given by (8c), and E_z^s by (7).

5. In order to apply the boundary conditions on the reference probe in the unit cell, it is necessary to represent the total tangential field on the probe surface with respect to the reference element $p=0$. To this end we used the Addition Theorem for cylindrical functions to re-expand the fields E_{zp}, $p > 1$ and E_z^s in (12) about an axis centered at the reference element. In view of the rotationally symmetric probe current distribution assumption, only the terms with no angular variation need be considered in this expansion.

6. The unknown probe current density $J_z(z)$ in (8d) is determined in terms of V_0 from the requirement that the total axial electric field $E_z(a,z)=0$. To this end, we expand the probe current density J_z into the series

$$J_z(z) = \sum_{j=1}^{J} c_j \Psi_j(z) \quad , \; 0 < z < \ell \tag{13a}$$

where c_j are the yet undetermined expansion coefficients and

$$\Psi_j(z) = \sin \left[\frac{\pi}{2\ell} (2j-1)(z-\ell) \right] \quad , \; j=1,2,\ldots,J \; . \tag{13b}$$

Imposing the boundary condition

$$E_z(a,z) = 0 \; , \quad 0 < z < \ell \tag{14a}$$

in the Galerkin sense, i.e.,

$$\int_{z=0}^{\ell} E_z(a,z) \Psi_i(z)\, dz = 0 \quad , \quad i=1,2,\ldots,I=J \tag{14b}$$

the following set of linear inhomogeneous equations is obtained for the determination of the unknown probe current expansion coefficients:

$$\sum_{j=1}^{J} A_{ij} c_j' = B_i \quad , \quad i,j=1,2,\ldots,I=J \tag{14c}$$

where

$$A_{ij} = \sum_{n=0}^{\infty} \epsilon_n \left[1 - \left(\frac{n\pi}{kh}\right)^2\right] J_0(\kappa_n a) \left[H_0^{(2)}(\kappa_n a) + J_0(\kappa_n a)\, S_n(\delta,\upsilon)\right] \mathcal{J}_{in}\, \mathcal{J}_{jn} \tag{14d}$$

$$B_i = \sum_{n=0}^{\infty} \epsilon_n J_0(\kappa_n a) \left[\mathcal{H}_n + \mathcal{J}_n\, S_n(\delta,\upsilon)\right] \mathcal{J}_{in} \tag{14e}$$

$$c_i' = -j \frac{Z_0}{V_0(z=0^-)} 2\pi a\, c_i \tag{14f}$$

$$\mathscr{I}_{in} = \begin{cases} -2 \dfrac{\dfrac{(2i-1)\lambda}{2\ell}}{\left[\dfrac{(2i-1)\lambda}{2\ell}\right]^2 - \left(\dfrac{n\lambda}{h}\right)^2} & ; \quad \dfrac{(2i-1)\lambda}{2\ell} \neq \dfrac{n\lambda}{h} \\ -\pi \dfrac{\ell}{\lambda} (-1)^{i-1} & ; \quad \dfrac{(2i-1)\lambda}{2\ell} = \dfrac{n\lambda}{h} \end{cases} \tag{14g}$$

and

$$Z_o = \frac{\zeta_o}{2\pi} \ln \frac{b}{a} = 60 \ln \frac{b}{a} \ . \tag{14h}$$

6. Once the probe current has been found the total magnetic field $H_\phi(\rho, z=0^+)$ in the aperture of the reference element is determined following the procedure indicated in steps 2 to 4.

7. Imposing continuity of $H_\phi(\rho, z=0)$ across the coaxial aperture (in the unit cell) yields the following relation for active admittance, i.e.:

$$Y_a(\delta,\upsilon) = \frac{I_o(z=0^-)}{V_o(z=0^-)} = \frac{2\pi}{V_o(z=0^-)} \int_{\rho=a}^{b} H_\phi(a < \rho < b, z=0^+)\, d\rho$$

$$\approx \frac{1}{4Z_o \dfrac{h}{\lambda} \ln \dfrac{b}{a}} \left\{ \sum_{n=0}^{\infty} \frac{\epsilon_n}{\left[1 - \left(\dfrac{n\pi}{kh}\right)^2\right]} \left[-j \frac{2}{\pi} \ln \frac{b}{a} + \mathscr{I}_n H_o^{(2)}(\kappa_n b) - \mathscr{H}_n J_o(\kappa_n a) \right.\right.$$

$$\left.\left. + \mathscr{I}_n^2 S_n(\delta,\upsilon) \right] - \sum_{n=0}^{\infty} \epsilon_n I_n' J_o(\kappa_n a) \left[\mathscr{H}_n + \mathscr{I}_n S_n(\delta,\upsilon) \right] \right\} \tag{15a}$$

where

$$I_n' = \sum_{i=1}^{I} c_i' \mathscr{I}_{in} \tag{15b}$$

$$S_n(\delta) = 2 \sum_{p=1}^{\infty} H_o^{(2)}(\kappa_n p d) \cos \delta p - H_o^{(2)}(2\kappa_n s) - 2 \sum_{p=1}^{\infty} H_o^{(2)}\left(\kappa_n d \sqrt{p^2 + \left(\frac{2s}{d}\right)^2}\right) \cos \delta p$$

(linear) (15c)

$$S_n(\upsilon) = \sum_{p=1}^{N-1} H_o^{(2)}\left(2\kappa_n B \sin \frac{p\pi}{N}\right) e^{-j\frac{2\pi}{N}\upsilon p} - \begin{cases} N \displaystyle\sum_{m=-\infty}^{\infty} \frac{H_{\upsilon_m}^{(2)}(\kappa_n A)\, J_{\upsilon_m}^2(\kappa_n B)}{J_{\upsilon_m}(\kappa_n A)} & \text{(concave)} \\ N \displaystyle\sum_{m=-\infty}^{\infty} \frac{J_{\upsilon_m}(\kappa_n A)\, H_{\upsilon_m}^{(2)2}(\kappa_n B)}{H_{\upsilon_m}^{(2)}(\kappa_n A)} \ . & \text{(convex)} \end{cases} \tag{15d}$$

All terms in (15a) except S_n depend on the element geometry while as seen from (15c) and (15d), S_n depends only on the array lattice parameters and the phasing δ,υ. The first term in S_n represents the contribution from the real elements except for that of the reference element. The rest of the terms in the expression for S_n correspond to the scattered contribution.

D. Active Reflection Coefficient

For good radiation efficiency it is necessary to match the monopole input active admittance $Y_a(\delta,\upsilon)$ to the TEM coaxial feed-line. The active reflection coefficient at the coaxial aperture plane is

$$\Gamma_a(\delta,\upsilon) = \frac{Y_c - Y_a(\delta,\upsilon)}{Y_c + Y_a(\delta,\upsilon)} \qquad (17)$$

where $Y_a(\delta,\upsilon)$ is given by (15a) and Y_c is the characteristic admittance of the coaxial feed line. As will be shown, for a given inter-element spacing d and parallel plate height h, one can determine the probe length ℓ and the spacing s so that $\Gamma_a = 0$ at a given frequency and particular phasing.

E. Coupling Coefficients

The coupling coefficients S^p are related to the active reflection coefficients by usual relation

$$S^p = \frac{d}{2\pi}\int_{-\pi/d}^{\pi/d} \Gamma_a(k_{xo})\, e^{-jk_{xo}pd}\, dk_{xo} \qquad \text{(linear)} \qquad (18a)$$

$$S^p = \frac{1}{N}\sum_{\upsilon=0}^{N-1} \Gamma_a(\upsilon)\, e^{-j\frac{2\pi}{N}\upsilon p}\,, \quad (p=0,1,\ldots,N-1)\,. \qquad \text{(circular)} \qquad (18b)$$

F. Element Pattern

The far-zone field due to a singly excited element in a match-terminated array environment is

$$E_z^{(e)}(\underline{\rho}) = \frac{d}{2\pi}\int_{-\pi/d}^{\pi/d} E_z(\underline{\rho},k_{xo})\, dk_{xo} \qquad \text{(linear)} \qquad (19a)$$

$$E_z^{(e)}(\underline{\rho}) = \frac{1}{N}\sum_{\upsilon=0}^{N-1} E_z(\underline{\rho};\upsilon) \qquad \text{(circular)} \qquad (19b)$$

where the radius vector $\underline{\rho}$ defines the observation point and the E_z is the total far-field of the active array. In the following two steps we review the derivation of E_z.

1. Relations (5), and (8) apply here as well. Since $h < \lambda/2$, only the $n=0$ term in (7) and (8) contributes to the far field.

2. We re-express E_z^{inc} in (8) in terms of Floquet modes in a unit cell. This is accomplished using once more the Poisson's sum formula for a linear array and the Addition Theorem for a circular convex array. The analytical procedure is described in [1,5,6].

In the linear array case the integral in (19a) is asymptotically evaluated by the stationary phase method. In the circular convex array case however, as $k\rho >> 1$ the first order asymptotic form for $H_{\upsilon_m}^{(2)}(k\rho)$ is employed. In both cases (19) yields the first order asymptotic approximation for the far-field due to a single excited monopole element in an infinite match-terminated array environment, that is,

$$E_z^{(e)}(\underline{\rho}) \simeq \sqrt{\frac{d}{\lambda h}} \sqrt{\frac{\zeta_o}{Z_c}} \frac{e^{-jk\rho}}{\sqrt{\rho}} F(\hat{\phi}) V_{inc} \tag{20a}$$

with

$$F(\hat{\phi}) = \frac{e^{j\frac{\pi}{4}}}{2\pi} \sqrt{\frac{\lambda^2}{dh}} \sqrt{\frac{Z_c}{\zeta_o}} \frac{\zeta_o}{Z_o} [\mathcal{J}_o - I_o' J_o(ka)] \sin(ks \cos\hat{\phi})\, e^{-jks\cos\hat{\phi}} \qquad \text{(linear)} \tag{20b}$$

$$F(\hat{\phi}) = \frac{1}{\pi kB} \sqrt{\frac{Z_c}{\zeta_o}} \sum_{\upsilon=0}^{N-1} \sum_{m=-\infty}^{\infty} T_m(\upsilon)\, e^{-j\upsilon_m(\hat{\phi} - \frac{\pi}{2})} \qquad \text{(convex)} \tag{20c}$$

where for convenience here $\hat{\phi} = \pi/2 - \phi$ and

$$T_m(\upsilon) = j\sqrt{\frac{d}{h}} \frac{N\pi}{2 \ln\frac{b}{a}} [1 + \Gamma_a(\upsilon)] [\mathcal{J}_o - I_o' J_o(ka)] Z_{\upsilon_m} \tag{20d}$$

$$Z_{\upsilon_m} = J_{\upsilon_m}(kB) - \frac{J_{\upsilon_m}(kA) H_{\upsilon_m}^{(2)}(kB)}{H_{\upsilon_m}^{(2)}(kA)} \quad . \tag{20e}$$

In (20d) we used $d \simeq \alpha B$.

The realized element gain pattern

$$G^{(e)}(\hat{\phi}) = \frac{|E_z^{(e)}(\hat{\phi})|^2}{\frac{\zeta_o P_{inc}}{2\pi\rho h}} \tag{21a}$$

defined with respect to the available power $P_{inc} = |V_{inc}|^2/Z_c$, may now be written as

$$G^{(e)}(\hat{\phi}) = 2\pi \frac{d}{\lambda} |F(\hat{\phi})|^2 . \tag{21b}$$

The factor $2\pi d/\lambda$ represents a uniformly illuminated unit cell power gain. This implies that for the linear array $|F(\phi)| \leq 1$.

Denoting the complex field element pattern by

$$\underline{g}^{(e)}(\hat{\phi}) = \sqrt{2\pi \frac{d}{\lambda}} \; F(\hat{\phi}) \tag{22a}$$

(16a) can be expressed in the form

$$E_z^{(e)}(\underline{\rho}) = \frac{1}{\sqrt{2\pi}} \sqrt{\frac{\zeta_o}{Z_c}} \; \frac{V_{inc}}{\sqrt{h}} \; \frac{e^{-jk\rho}}{\sqrt{\rho}} \; g^{(e)}(\hat{\phi}) . \tag{22b}$$

III. NUMERICAL RESULTS AND DISCUSSION

The active admittance Y_a, coupling (scattering) coefficients and element patterns were computed for representative values of array and element parameters to exhibit the significant trends. All of the numerical results refer to monopole elements with a 50 ohm characteristic impedance of the feed-transmission lines. Field amplitude (voltage) element patterns are normalized to the unit cell gain $(2\pi d/\lambda)^{1/2}$. Forty waveguide modes (n_{max}=40) and 10 probe current terms (I=10) were used in Galerkin's procedure.

A. Linear Array

Fig. 9 shows the active impedance at broadside scan vs. probe length (solid curve) for s/λ = 0.15, 0.2, 0.25, 0.3 and vs. probe-ground distance (dashed curve) for ℓ/λ = 0.15, 0.2, 0.25, 0.3. The inter-element spacing is d/λ = 0.4 and the distance between two parallel plates h/λ = 0.369. The coaxial-feed line with dimensions a/λ =0.11, b/λ =0.034 and is loaded with teflon (ϵ_r=2). The Smith chart is normalized to 50 ohms. It is seen that impedance curves exhibit a resonance approximately for ℓ/λ = 0.23, s/λ = 0.16. For $\ell/\lambda < 0.23$ the active admittance is capacitive, for $\ell/\lambda > 0.23$, inductive. It is observed that the active impedance is more sensitive to changes ℓ/λ than of s/λ. It was found that for a given value of d/λ and h/λ, one can determine ℓ/λ, s/λ such that the active reflection coefficient Γ_a = 0.

For design purposes Fig. 10 displays a sample contour plot of the magnitude of reflection coefficient vs. probe length (ℓ/λ) and vs. probe to ground distance s/λ. It is seen that for ℓ/λ = 0.233, s/λ = 0.1627, the active reflection coefficient $\Gamma_a(\hat{\phi}_o = 0^o)$ = 0.

For the geometries of Figs. 9 and 10, Fig. 11 shows active impedance at broadside vs. frequency. It is seen that the frequency bandwith corresponding to a VSWR of 2:1 is approximately 40%.

Fig. 12 exhibits the active impedance variation vs. scan for the same geometry and for the three frequencies: $f = 0.9f_c$, f_c, $1.1f_c$.

Fig. 13 exhibits the dependence of the element pattern amplitude on inter-element spacing. In each case the array and element geometry are appropriate to a broadside match. It is observed that while for $d/\lambda = 0.4$ the pattern is smooth, for $d/\lambda = 0.6$ the element pattern exhibits a substantial drop-off near $\phi = 42^o$. This drop-off is caused by an end fire grating lobe condition (EGL) which occurs at

$$\phi_{EGL} = \sin^{-1} \left(\frac{\lambda}{d} - 1 \right) . \tag{23}$$

For the same geometry, Fig. 14 exhibits the element pattern phase dependence on element spacing d/λ. One observes that the phase varies only by a few degrees up to the EGL drop-off. Thus, the EGL position essentially determines the limit of usefulness of the element, both in amplitude and phase. Since the phase reference point is at the probe location we conclude that the phase center location is near the probe element.

For the same geometry of Fig. 9, Fig. 15 shows the amplitude of the coupling coefficients for two element spacings. As expected, coupling coefficients decay monotonically vs. element number. Also as will be seen in the next figure, for elements distant from the excited monopole the coupling is primarily due to the parallel plate guide TEM mode, the amplitude of which decays as $1/\sqrt{r}$. For this reason the coupling coefficients vs. element number p decay faster for $d/\lambda = 0.6$ than for $d/\lambda = 0.4$ as can be seen from Fig. 14. Also it is interesting to note that $S^o = -9.2$ dB for $d/\lambda = 0.4$ and $S^o = -13.2$ dB for $d/\lambda = 0.6$ which, since both arrays are matched at broadside, confirms the fact that coupling from neighboring elements to the reference p=0 element is stronger for smaller element spacing.

Fig 16. exhibits the phase of the coupling coefficients for two element spacings. For convenience we define S^P as

$$S^P = |S^P| \, e^{-j\phi_p} \tag{24a}$$

where

$$\phi_p = kdp + \Delta\phi_p \, , \quad k = \frac{2\pi}{\lambda} \, . \tag{24b}$$

The second term in (24b) is plotted in Fig. 16 while the first term (kdp) represents the phase delay from the reference element (p=0) to element p of TEM mode in the parallel plate waveguide. Thus, for elements close to the excited one the coupling is due to the TEM mode, plus contributions of higher non-propagating parallel plate waveguide modes. For elements further removed, the coupling is primarily due to the TEM mode.

It is found that the active admittance and element patterns are relatively insensitive to parallel plate height and probe radius in the range $0.3 \leq h/\lambda \leq 0.4$ and $0.01 \leq a/\lambda \leq 0.04$ ($b=2.3a$ so that $Z_c=50$ ohms) and is therefore not shown.

B. Concave Circular Arrays

A numerical evaluation of coupling coefficients was carried out using (19b). In all cases the height of the lens cavity $h/\lambda = 0.369$, and the inner (probe) and outer radii of coaxial feed-line are $a/\lambda = 0.011$, $b/\lambda = 0.034$. The characteristic impedance of the feed-line is $Z_c = 50\ \Omega$.

Fig. 17 shows the magnitude of the coupling coefficients $|SP|$ (solid circles) for element spacing $d/\lambda = 0.4$, probe length $\ell/\lambda = 0.233$ and probe to ground distance s/λ 0.1627. The array and element geometry correspond to the reference array matched at broadside scan. The latter is defined as an infinite linear array with the element and array geometry identical to that in the concave array. Open circles in Fig. 17 represent $|SP|$ of the reference array. It is seen that the initial decay of coupling coefficients in a concave array follows that of the corresponding linear reference array. Gradually, however, the decay rate of $|SP|$ decreases and the curve $|SP|$ vs. p passes through a dip with a subsequent rise accompanied by a ripple. Such behavior was also found in the case of aperture elements [8] and was explained in terms of Periodic Structure Rays; the dip region constitutes a transition between a quasi-linear behavior, near the excited element, and the ray region past the dip. In the ray zone, as discussed in [8], the direct ray contribution establishes the average level of the $|SP|$ curve, while the ripple is due to the interference between the direct ray and the multiply reflected rays (primarily a singly reflected ray).

In Fig. 18 the amplitude of coupling coefficients is presented for two element spacings $d/\lambda = 0.4$ and $d/\lambda = 0.6$. For $d/\lambda = 0.4$ element and array geometry is that of Fig. 17 while for $d/\lambda = 0.6$ the probe length is $\ell/\lambda = 0.25$, and the probe to ground distance $s/\lambda = 0.245$ (this geometry corresponds to a reference array matched for broadside scan). Fig. 18 also shows the effect of spacing $d/\lambda > \lambda/2$. A pronounced oscillatory behavior is found near the excited element, and a drop-off per wavelength sharper than that for $d/\lambda < \lambda/2$ is seen. A higher average coupling level is also observed in the diametrically opposite region around $p \approx N/2$. The latter is caused by the increased broadside realized element gain $2\pi d/\lambda$ for $d/\lambda = 0.6$ as compared to that for $d/\lambda = 0.4$. The oscillations are due to "grating lobe rays" (see [8]) which are multiply reflected in the lens cavity. Such grating lobe contributions, and consequently element spacings greater than $\lambda/2$, are undesirable for low side lobe lens designs, since they can give rise to significant distortion of illuminations. Furthermore since the elements are not matched for grating lobe angles, cavity resonances can be excited.

Fig. 19 shows the comparison of $|SP|$ for two different lens radii in the ratio 2:1. It is seen that both the dip level and the coupling level in the region of the receiving elements is lower for larger values of kA.

C. Convex Circular Array

Based on the analysis of section II element patterns and coupling coefficients were computed. In order to maximize the broadside element gain, a matching network appropriate to in-phase excitation of all monopoles was employed throughout. As already mentioned the element field patterns were normalized to the unit cell gain $(2\pi d/\lambda)^{1/2}$ and ten probe current terms were used in Galerkin's procedure. Several numerical results for element patterns and coupling coefficients are presented for the following element geometry: $a/\lambda = 0.011$, $b/\lambda = 0.034$, $\ell/\lambda = 0.25$, $h/\lambda = 0.369$ and $s/\lambda = 0.25$.

Fig. 20 illustrates the dependence of the element field pattern on the inter-element spacing d/λ. Comparison with the equivalent infinite linear array is also given (for $d/\lambda = 0.6$). It is observed that all patterns exhibit a substantial drop-off near ϕ_{EGL} = arc $\sin(\lambda/d - 1)$. In the linear array case this drop-off is caused by an and-fire grating lobe condition and in the cylindrical array by its quasi-linear counterpart as discussed in [9] for the case of a cylindrical array of axial strip-dipoles. The curves of Fig. 20 also exhibit a ripple in the broadside region, whose amplitude diminishes with closer element spacings and becomes negligible for $d/\lambda = 0.5$. The ripple is due to the interference of the direct element radiation (with equivalent linear array element pattern) with the grating lobes of quasi-linear subarrays excited by creeping wave phase gradient as discussed in [9].

Fig. 21 illustrates the element pattern dependence on the array radius. It is seen that in the shadow region the pattern falls off exponentially, which indicates that it is primarily due to a single creeping wave with an angular attenuation constant proportional to $(k A)^{1/3}$. The ripple in the 180° region, similarly to that found in the case of conducting cylinder, is a result of the interference of two creeping waves traveling in opposite directions around the cylinder.

Coupling coefficients for the circular and its infinite linear reference array are presented in Figs. 22 and 23. As expected, in the circular array the coupling coefficients initially follow that of linear array. For elements far from the excited one (p=0), the coupling coefficients decrease exponentially which again indicates that the main contribution is primarily due to a single creeping wave.

IV. EXPERIMENTS

In this section we describe the experimental efforts and present measured data for active impedance, coupling coefficients and element patterns supporting the validity of the theoretical analysis.

A. Linear Array

To validate the numerical results for active admittance a one and two-half element waveguide simulator was constructed[4]. It simulates the active impedance of the infinite linear array at center frequency $f_c = 5$ GHz ($\lambda_c = 2.360"$). The separation between the two parallel plates is $h = 0.369\ \lambda_c$ (0.872") and the inter-element spacing d = 0.4 λ_c (0.936"). The inner and outer radii of the teflon-filled coaxial feed-lines are a = 0.01 λ_c (0.025") and b = 0.034 λ_c (0.081"), respectively. The array was matched at broadside scan, at center frequency f_c. For this case ℓ =0.234 λ_c (0.550") and s = 0.163 λ_c (0.384").

For the array and element specified above, a one and two-half element waveguide simulator was built to measure the active impedance. The single mode simulator is shown in Fig. 24. The simulator waveguide dimensions are 1.872 x 0.872 which correspond to standard C-band rectangular waveguide. The waveguide was terminated in a matched load with a VSWR < 1.02 over the frequency band 4 to 6 GHz. The array elements were Omni Spectra's Flange Mount Jack Receptacle. The device simulates scan conditions from 52° off-broadside at 4 GHz through 40° off-broadside at f_c = 5 GHz to 32° off-broadside at 6 GHz.

Fig. 25 shows the theoretical and the measured active impedance vs. frequency. The Smith Chart normalization is 50 ohms. Excellent agreement may be observed across the operating band. The two results for the reflection coefficient differ less than 1% in magnitude and less than 3 degrees in phase.

To measure the coupling coefficients, for the same element and array geometry, a 30-element linear array of coaxially-fed monopoles in an (4 x 6) feet parallel plate waveguide was built. To simulate an infinite parallel plate region a 5-inch pyramid of absorbing material was placed along the edges of the parallel plates. This enabled us to measure coupling coefficients to a -35 dB level without evidence of significant internal reflections. Coupling coefficients were measured with the HP-8410 Automatic Network Analyzer for seven consecutive neighboring elements.

Figs. 26 and 27 present a comparison between the measured and computed values of coupling coefficients in amplitude and phase, respectively. The difference between the two results is less than 0.3 dB in amplitude and less than 3 degrees in phase.

To measure the far-field element patterns, a linear array of eleven monopole in a parallel plate region was constructed. The axis of rotation was at the probe location of the center element. This (receiving) element was connected to a 20/20 Scientific Atlanta Antenna Analyzer; other array elements were match-terminated with 50 ohm coaxial loads. The element patterns were measured on a 2000 foot antenna range.

Figs. 28 and 29 show the behavior of the amplitude and phase of the element pattern for the following geometry: h/λ = 0.3, d/λ = 0.72, ℓ/λ = 0.22, a/λ = 0.019, b/λ = 0.062. The amplitude pattern is normalized to the unit cell gain $\sqrt{2\pi d/\lambda}$. It is seen that the amplitude and the phase curves are approximately constant up to $\hat{\phi}$ = 25° off broadside. The amplitude pattern exhibits a substential drop-off near $\hat{\phi}$ = 25° while the phase pattern begins to increase linearly with the observation angle. Since the phase is referenced to the center element, Fig. 29 also indicates that in the region 0° < $\hat{\phi}$ < 25° the "phase center" coincides with the element location. The ripple in both curves is caused by edge effects.

The dashed curves in Figs. 28 and 29 represent computed element patterns of the monopole element in an infinite array environment. Good agreement between measured and theoretical results is observed.

B. Concave Circular Array

To verify the results for coupling coefficients and to ascertain the effects of curvature in a concave array environment four concave arrays were built. Comparison between theoretical and experimental values for coupling coefficients will be given during the presentation.

C. Circular Convex Array

To validate the theoretical results for coupling coefficients and element patterns a circular convex ring array of coaxially-fed monopoles in a parallel plate waveguide was constructed. The array contains 64 elements between two circular parallel plates with an E-plane (radial) flare as shown in Figs. 30 and 31. The flare is to simulate an infinite parallel plate region. The center frequency is f_c = 7.5 GHz. To observe the creeping wave grating lobe ripple effect in the element pattern, an inter-element spacing d = 0.6 λ_c (0.945") was chosen. The parallel plate height was h = 0.369 λ_c (0.581"). The probe length and probe to cylindrical ground distance were selected so that the infinite linear reference array would be matched at broadside scan, i.e.: ℓ = 0.248 λ_c (0.390"), s = 0.242 λ_c (0.380"). The array elements were 50 ohm Omni Spectra's Jack Receptacles with a = 0.016 λ_c (0.025"), b = 0.051 λ_c (0.081") and with teflon dielectric.

Coupling coefficients were measured down to -55 dB in amplitude which corresponds approximately to the seventh element from the excited reference element (p=0). Beyond this low amplitude level, reflection from the E-plane flare influenced the measured results.

Figs. 32 and 33 present a comparison between the measured (open circles) and theoretical (solid circles) coupling coefficient values in amplitude and phase, respectively. The difference between the two results is less than 1.0 dB in amplitude and less than 5 degree in phase.

The element pattern was measured on the far-field range. The axis of rotation was at the location of the receiving element which was connected to a 20/20 Scientific Atlanta Antenna Analyzer while other elements were terminated in 50 ohm coaxial loads.

Figs. 34 to 36 show a comparison between measured (solid curve) and the calculated (dashed curve) element pattern amplitude and phase, respectively. Excellent agreement between measured and theoretical results may be observed.

V. CONCLUSIONS

An analysis of infinite, linear, circular concave and circular convex arrays of coaxially fed monopole elements in a parallel plate waveguide region is presented in a unified form in terms of element factor and structure factor.

The close agreement of the experimental and theoretical results for active impedance, coupling coefficients, and element patterns strongly supports the validity of the analysis, and furnishes a firm basis for the matched element design method that was developed.

The knowledge of the element patterns in the array environment and of the phase center location which has been shown to be near the element (for element spacing not exceeding say 0.6 λ) serves to improve the design accuracy of Rotman and other feed-through lenses, as well as of linear and conformal arrays.

REFERENCES

1. B. Tomasic and A. Hessel: "Linear Phased Array of Coaxially-fed Monopole Elements in a Parallel Plate Waveguide" RADC Report to be published in 1985.

2. A. Hessel and B. Tomasic: "Mutual Coupling in Bootlace Lenses", International URSI Symposium Digest, Munich, W. Germany, 1980.

3. B. Tomasic and A. Hessel: "Linear Phased Array of Coaxially-fed Monopole Elements in a Parallel Plate Guide", IEEE/AP-S Symposium Digest, p. 144, Albuqerque, New Mexico, May 1982.

4. B. Tomasic and A. Hessel: "Linear Phased Array of Coaxially-fed Monopole Elements in a Parallel Plate Waveguide - Experiment", IEEE/AP-S Symposium Digest, p. 23, Vancouver, Canada, June 1985.

5. B. Tomasic: "Circular Array of Coaxially-fed Monopole Elements in a Parallel Plate Waveguide - Theory", ISAP Symposium Digest, Kyoto, Japan, August 1985.

6. B. Tomasic: " Circular Array of Coaxially-fed Monopole Elements in a Parallel PLate Waveguide - Theory", ISAE Symposium Digest, Beijing, Peoples Republic of China, August 1985.

7. B. Tomasic: "Circular Array of Coaxially-fed Monopole Elements in a Parallel Plate Waveguide - Experiment", 1985 Symposium on Antenna Applications Proceedings, Monticello, Illinois, September 1985.

8. B. Tomasic and A. Hessel: "Ray Analysis of Mutual Coupling in Arrays on Concave Surfaces", Ballistic Missile Defense Advanced Technology Center, Report POLY-MRI-1440-84, October 1984.

9. J.C. Herper, A. Hessel, and B. Tomasic: "Element Pattern of an Axial Dipole in a Cylindrical Phased Array, Part I: Theory", IEEE Transaction on Antennas and Propagation, p.259, Vol. AP-33, March 1985.

Acknowledgement: The authors thank Mr. James P. Kenney for performing the experimental work and Dr. Hans Steyskal for the use of his cylindrical convex array for experimental purposes.

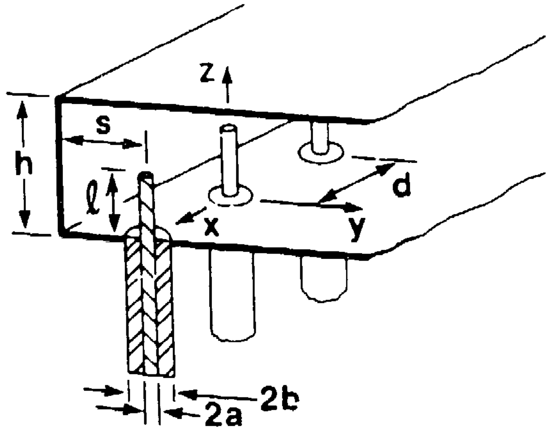

Fig. 1 Linear array of coaxial monopole elements in a semi-infinite parallel plate waveguide

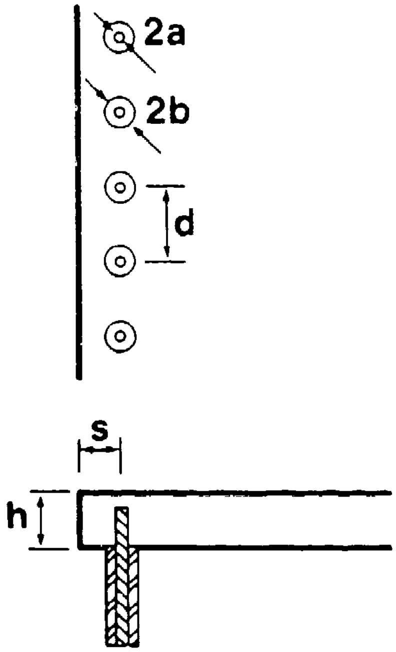

Fig. 2 Top and side view of the linear array model

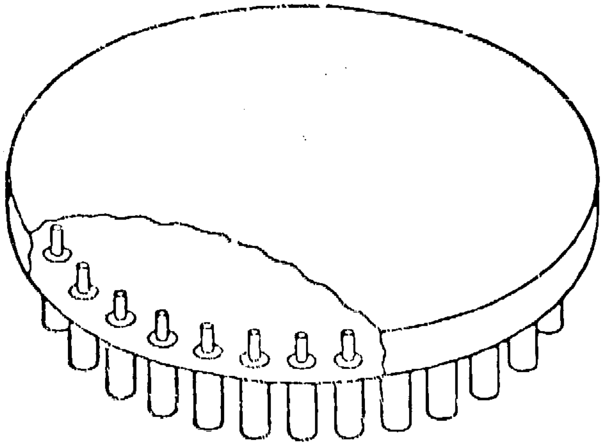

Fig. 3 Circular concave array of monopole elements in a parallel plate waveguide

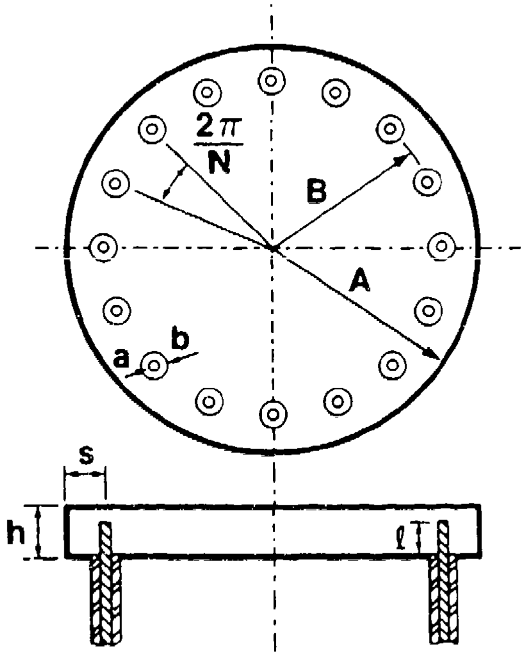

Fig. 4 Top and side view of the circular concave array model

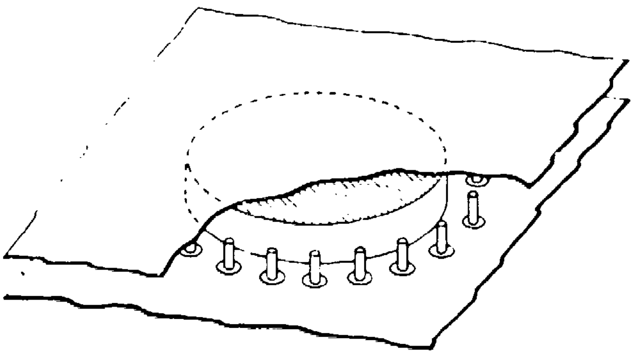

Fig. 5 Circular convex array of coaxial monopole elements in an infinite parallel plate waveguide

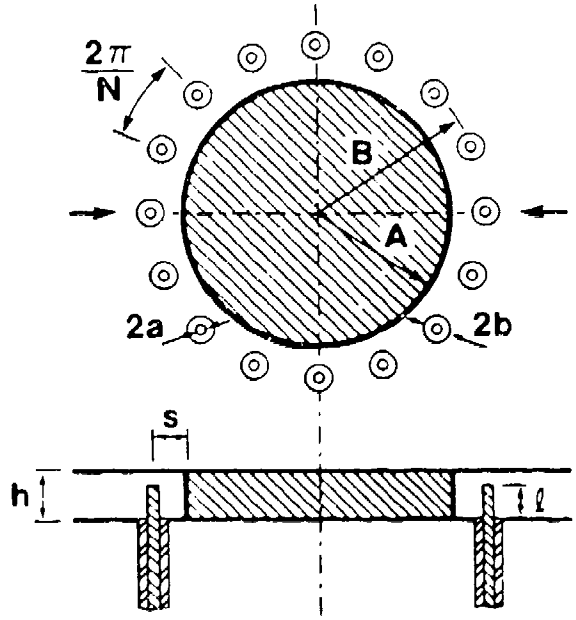

Fig. 6 Top and side view of the circular convex array model

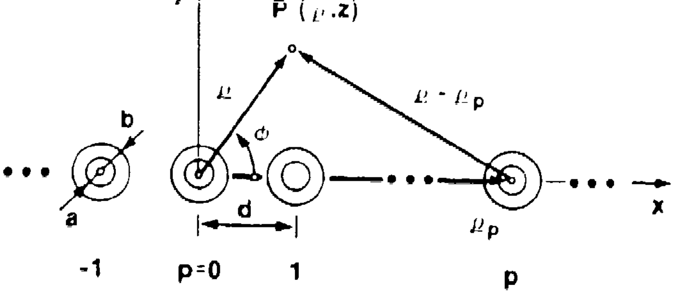

Fig. 7 Linear array geometry for evaluation of $E_z(\underline{r};\delta)$

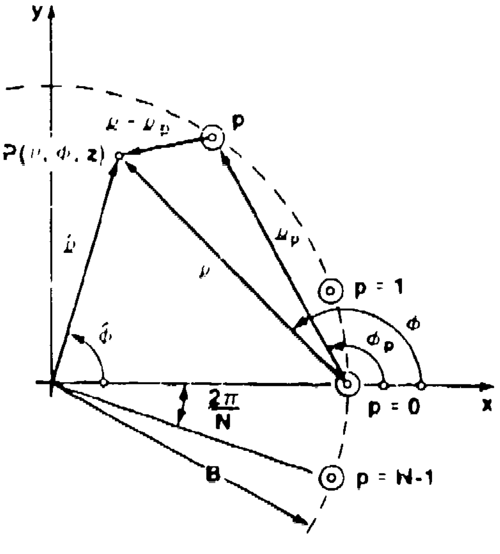

Fig. 8 Circular array geometry for evaluation of $E_z(\underline{r};\upsilon)$

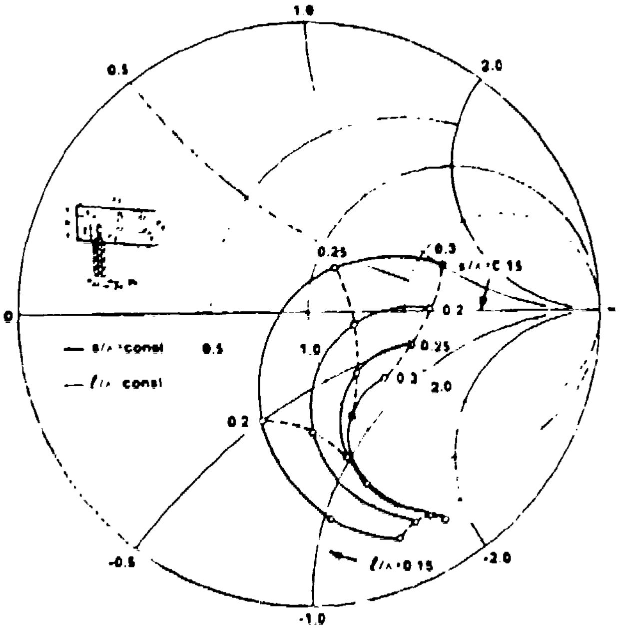

Fig. 9 Linear array active impedance vs. probe-ground distance and vs. probe length ($d/\lambda=0.4$, $\phi_o=0^\circ$)

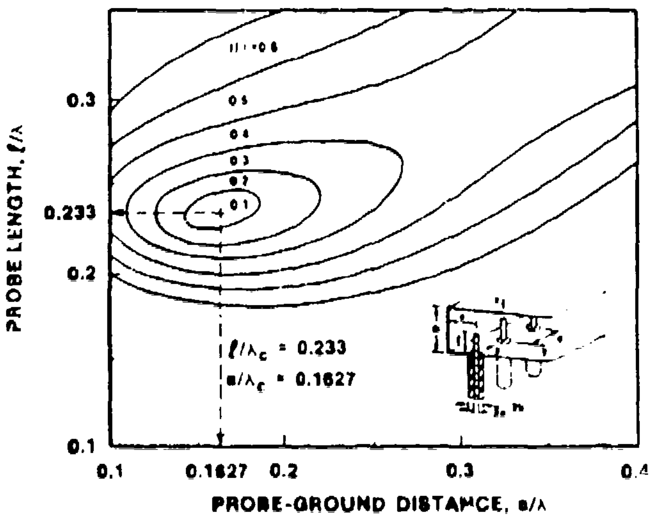

Fig. 10 Linear array active reflection coefficient vs. probe-ground distance and vs. probe length ($d/\lambda=0.4$, $\phi_o=0^\circ$)

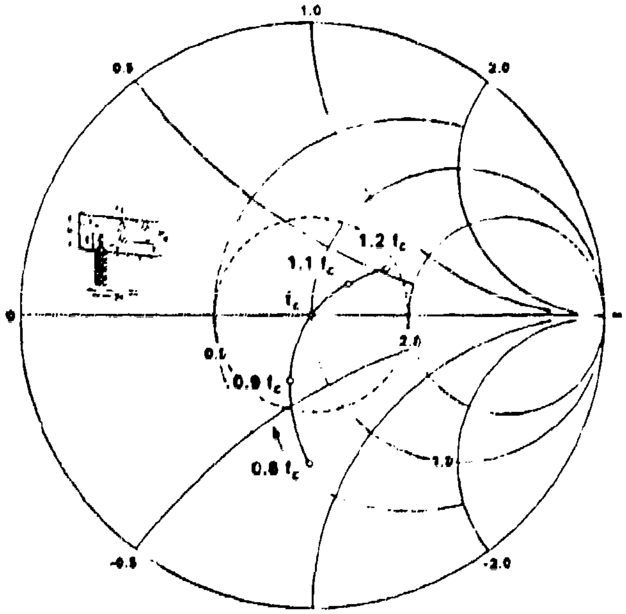

Fig. 11 Linear array active impedance vs. frequency ($h/\lambda_c=0.369$, $d/\lambda_c=0.4$, $\ell/\lambda_c=0.233$, $s/\lambda_c=0.1627$, $a/\lambda_c=0.011$, $b/\lambda_c=0.034$, $\phi_o=0^\circ$)

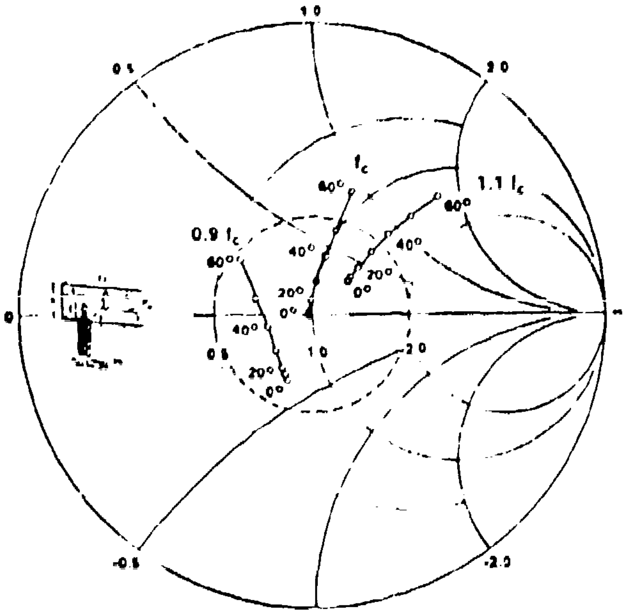

Fig. 12 Linear array active impedance vs. scan ($d/\lambda=0.4$, $\phi_o=0^\circ$)

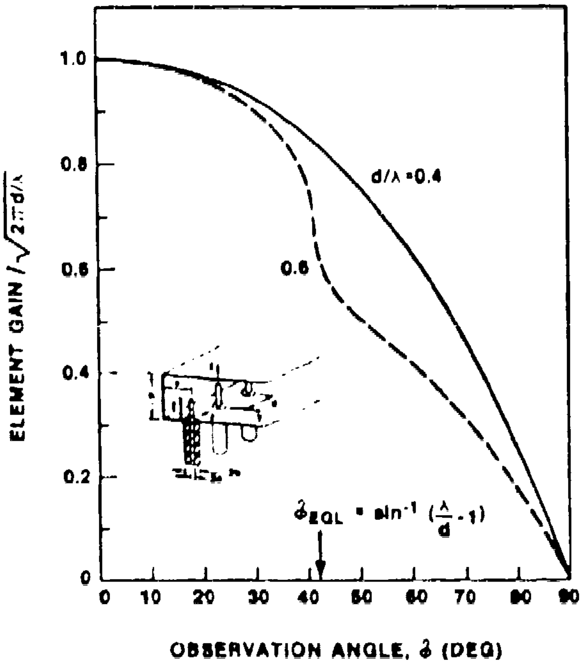

Fig. 13 Linear array element pattern amplitude. Parameter: $d/\lambda=0.4$, 0.6
($d/\lambda=0.4$; $\ell/\lambda=0.233$, $s/\lambda=0.1627$)
($d/\lambda=0.6$; $\ell/\lambda=0.25$, $s/\lambda=0.245$)

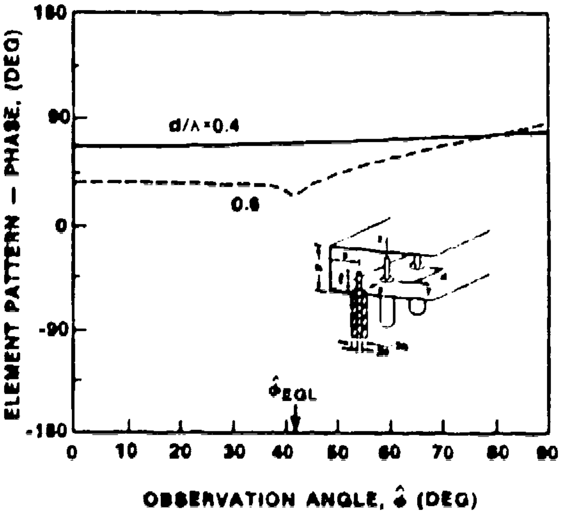

Fig. 14 Linear array element pattern phase. Parameter: $d/\lambda=0.4$, 0.6
($d/\lambda=0.4$; $\ell/\lambda=0.233$, $s/\lambda=0.1627$)
($d/\lambda=0.6$; $\ell/\lambda=0.25$, $s/\lambda=0.245$)

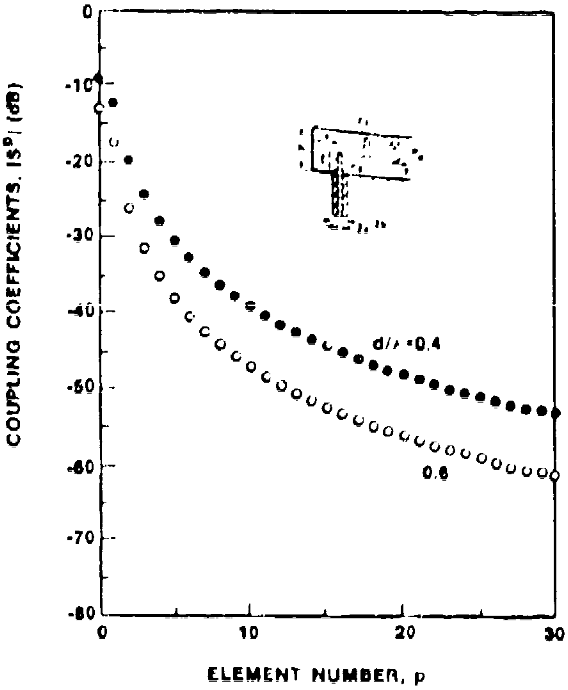

Fig. 15 Linear array coupling coefficient amplitude.
Parameter: $d/\lambda=0.4$, 0.6
($d/\lambda=0.4$; $\ell=0.233$, $s/\lambda=0.1627$)
($d/\lambda=0.6$; $\ell=0.25$, $s/\lambda=0.245$)

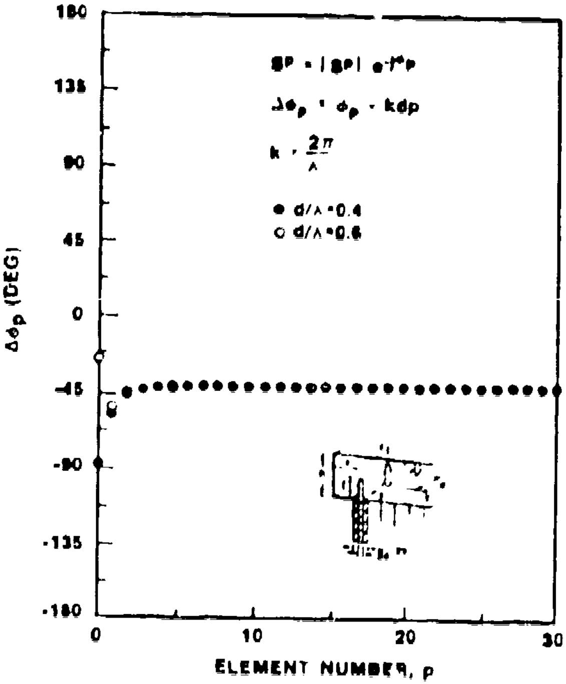

Fig. 16 Linear array coupling coefficients phase.
Parameter: $d/\lambda=0.4$, 0.6
($d/\lambda=0.4$; $\ell=0.233$, $s/\lambda=0.1627$)
($d/\lambda=0.6$; $\ell=0.25$, $s/\lambda=0.245$)

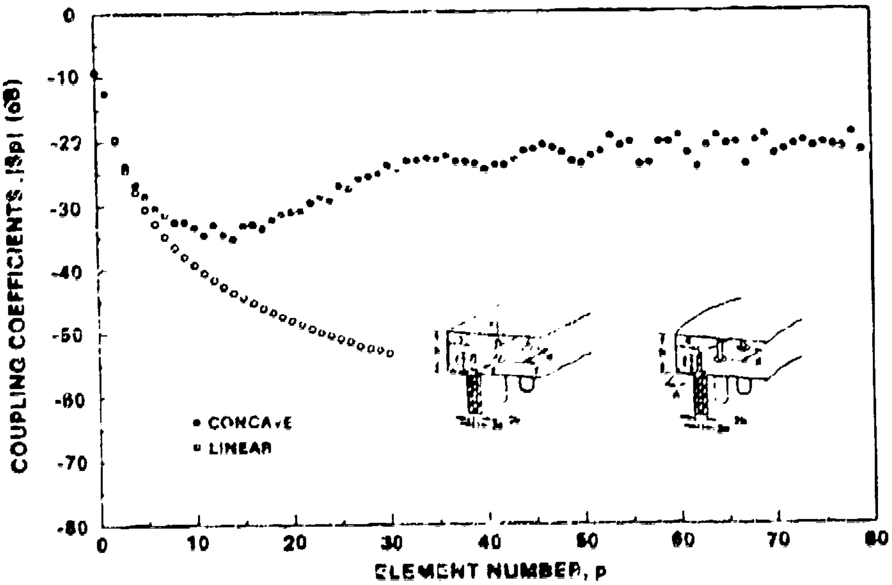

Fig. 17 Amplitude of coupling coefficients for circular concave and the linear reference array (d/λ=0.4, ℓ/λ=0.233, s/λ=0.1627, kA=64, N=159)

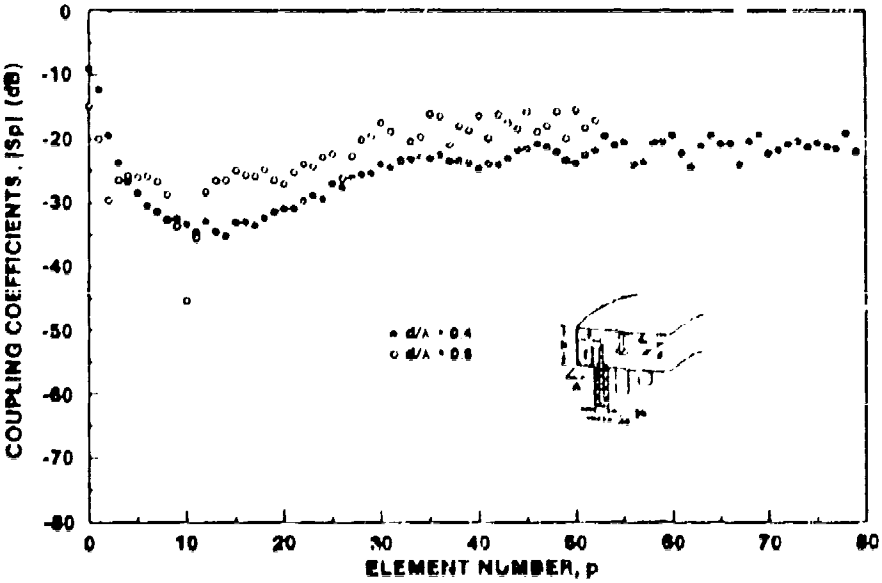

Fig. 18 Amplitude of coupling coefficients for circular concave arrays. Parameter: d/λ=0.4, 0.6, kA=64,(d/λ=0.4; ℓ=0.233, s/λ=0.1627, N=159), (d/λ=0.6; ℓ/λ=0.25, s/λ=0.245, N=105)

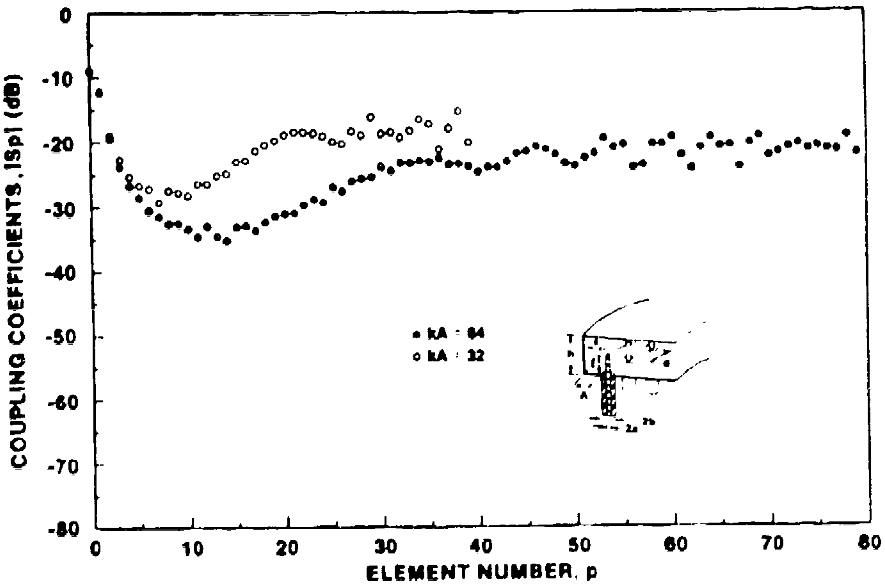

Fig. 19 Amplitude of coupling coefficients for circular concave arrays. Parameter: kA=32, 64 (d/λ=0.4; ℓ/λ=0.233, s/λ=0.1627)

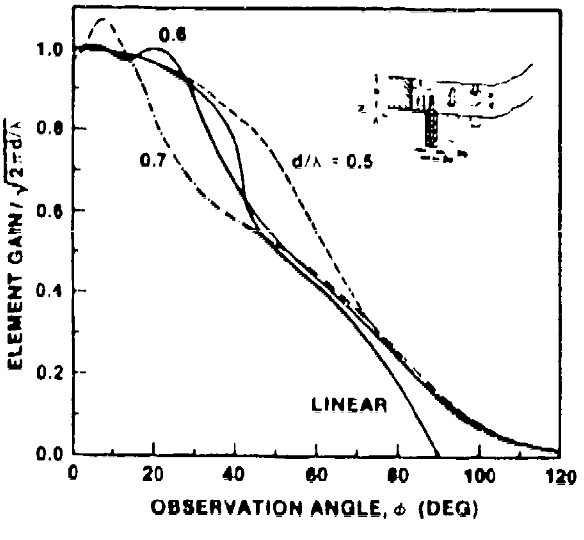

Fig. 20 Circular convex array element pattern amplitude. Parameter: d/λ=0.5, 0.6, 0.7 (kA=60)

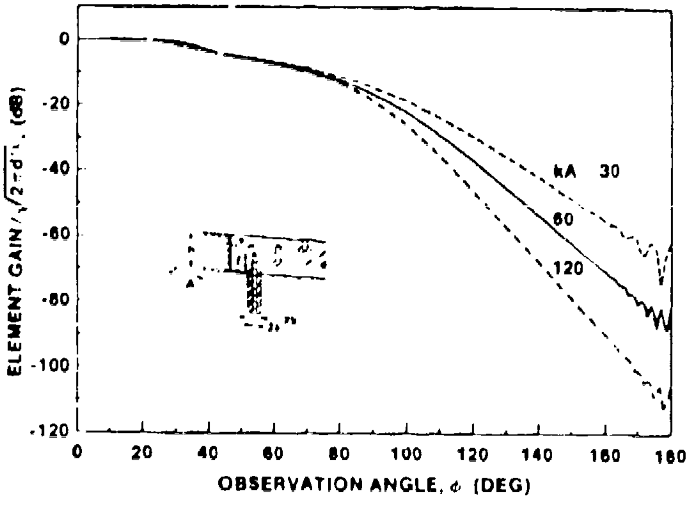

Fig. 21 Circular convex array element pattern amplitude. Parameter: kA=30, 60, 120 (d/λ=0.6)

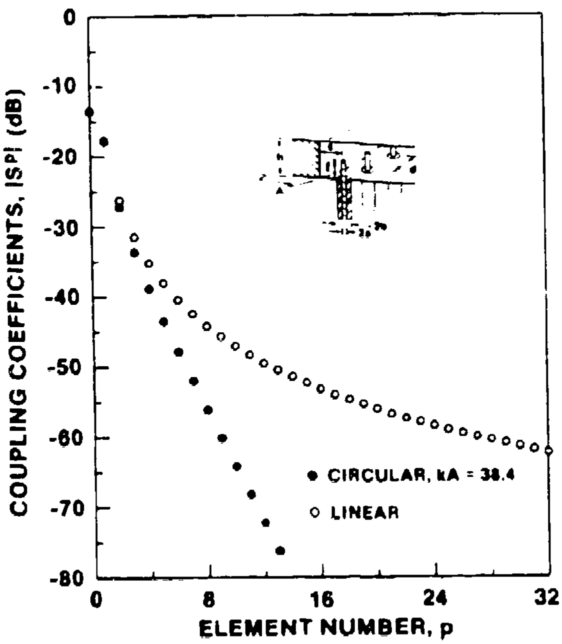

Fig. 22 Coupling coefficient amplitude for circular convex and the reference linear array ($d/\lambda=0.6$, $\ell/\lambda=0.25$, $s/\lambda=0.245$, $kA=38.4$)

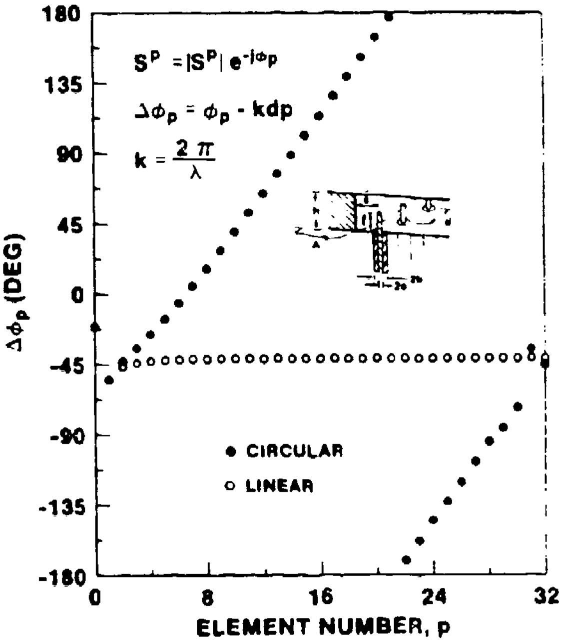

Fig. 23 Coupling coefficient phase for circular convex and the reference linear array ($d/\lambda=0.6$, $\ell/\lambda=0.25$, $s/\lambda=0.245$, $kA=38.4$)

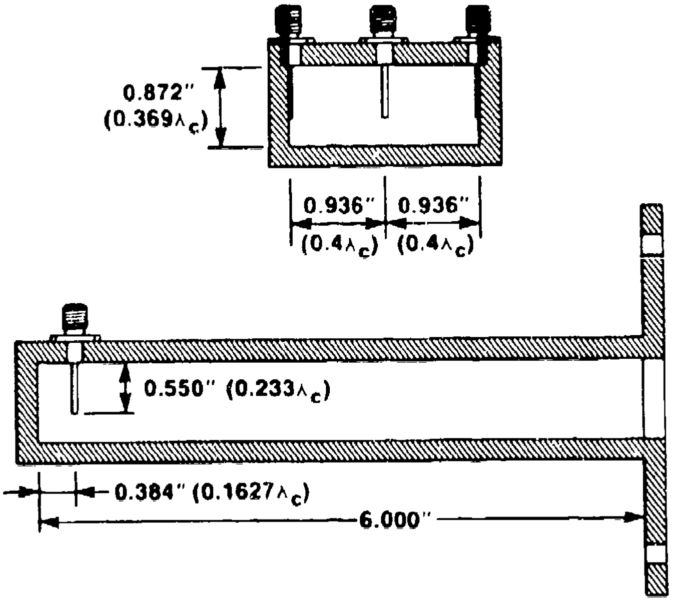

Fig. 24 A one and two-half element waveguide simulator ($f_c=5$ GHz)

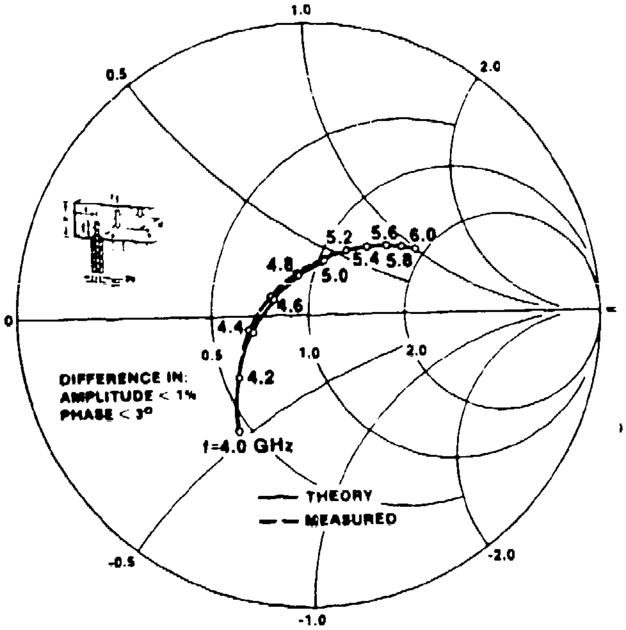

Fig. 25 Active impedance vs. frequency - theory and simulator measurements

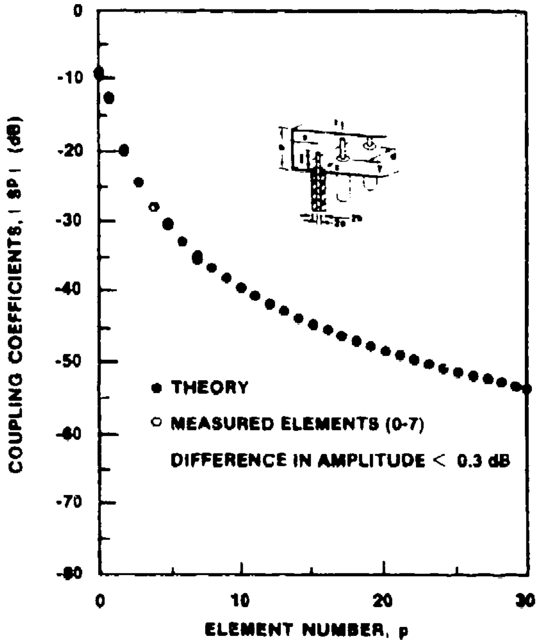

Fig. 26 Theoretical and experimental amplitude of coupling coefficients for linear array (d/λ=0.4, ℓ/λ=0.233, s/λ=0.1267)

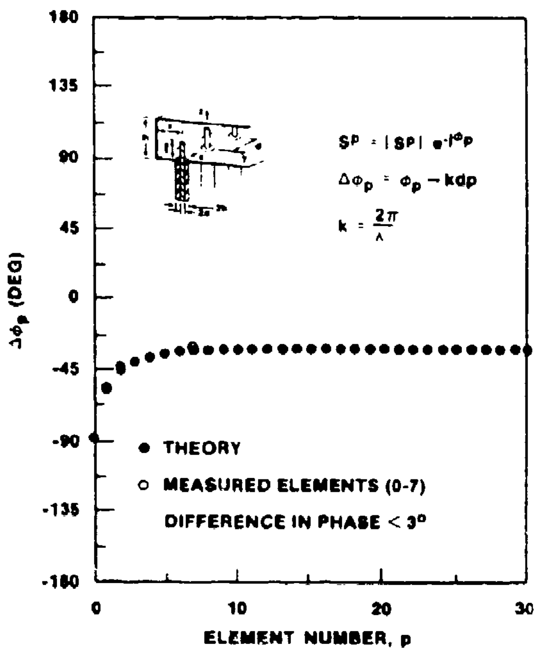

Fig. 27 Theoretical and experimental phase of coupling coefficients for linear array (d/λ=0.4, ℓ/λ=0.233, s/λ=0.1267)

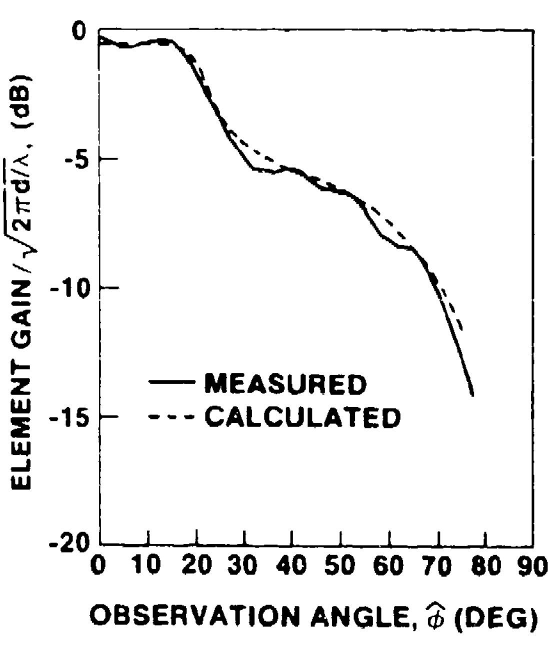

Fig. 28 Theoretical and experimental element pattern amplitude for linear array (d/λ=0.72, ℓ=0.22, s/λ=0.25)

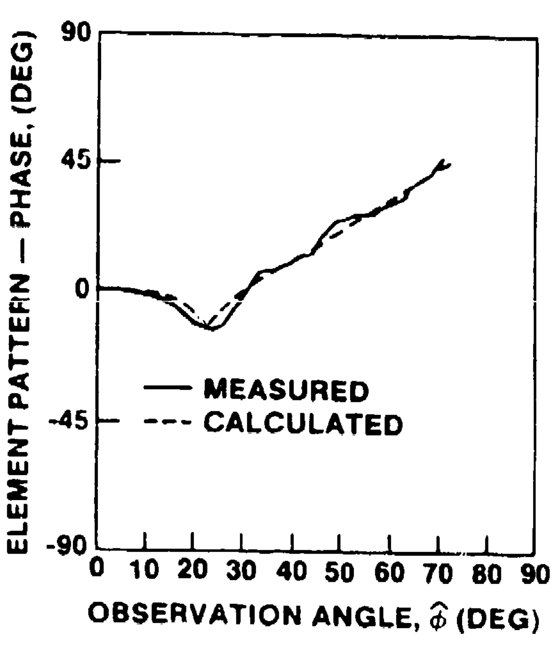

Fig. 29 Theoretical and experimental element pattarn phase for linear array (d/λ=0.72, ℓ=0.22, s/λ=0.25)

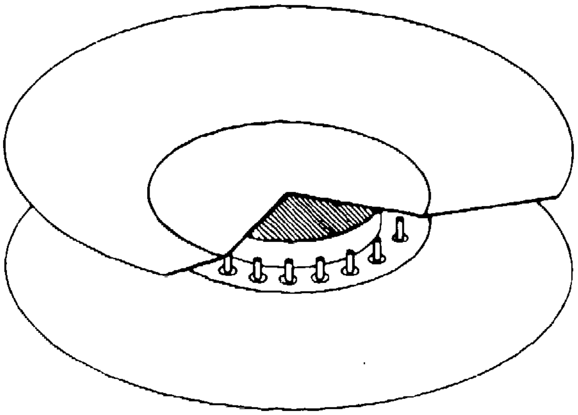

Fig. 30 A 64-element circular convex array of coaxial monopoles in a parallel plate waveguide

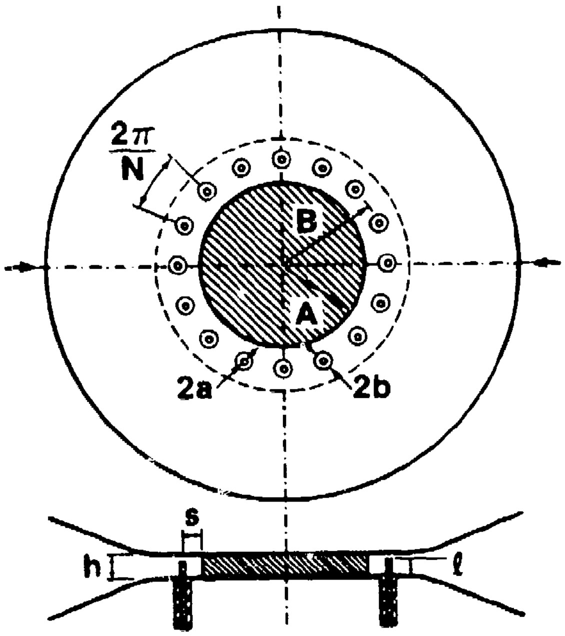

Fig. 31 Top and side view of circular convex array

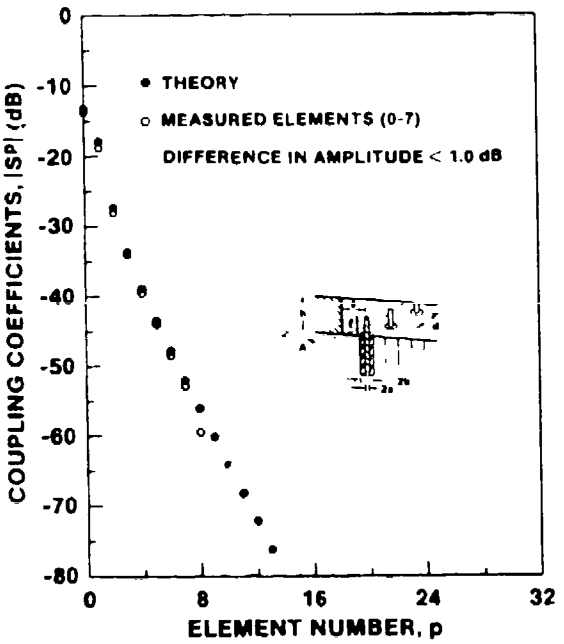

Fig. 32 Theoretical and experimental amplitude of coupling coefficients for circular convex array (d/λ=0.6, ℓ/λ=0.25, s/λ=0.245, kA=38.4)

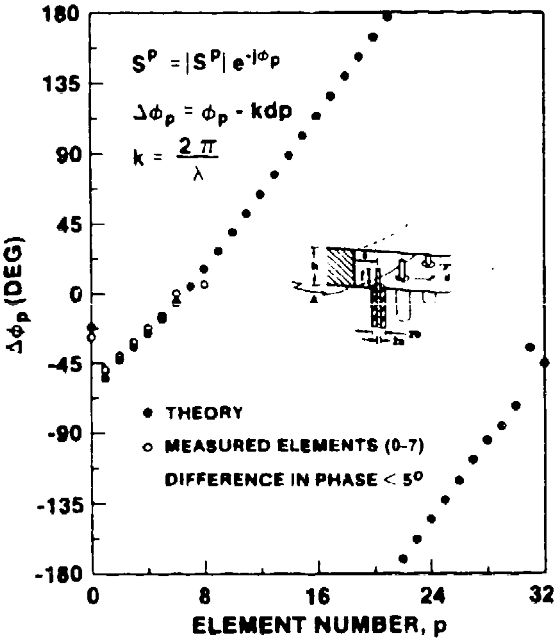

Fig. 33 Theoretical and experimental phase of coupling coefficients for circular convex array (d/λ=0.6, ℓ/λ=0.25, s/λ=0.245, kA=38.4)

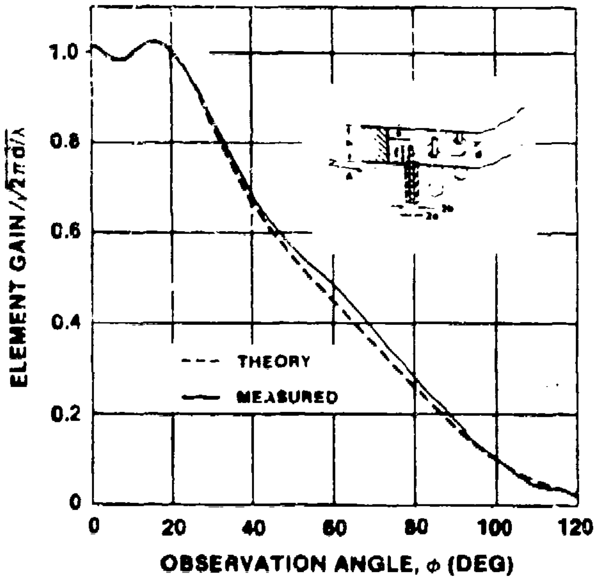

Fig. 34 Theoretical and experimental element pattern amplitude (linear scale) ($d/\lambda=0.6$, $\ell/\lambda=0.25$, $s/\lambda=0.245$, $kA=38.4$, $N=64$, $f=7.5$ GHz)

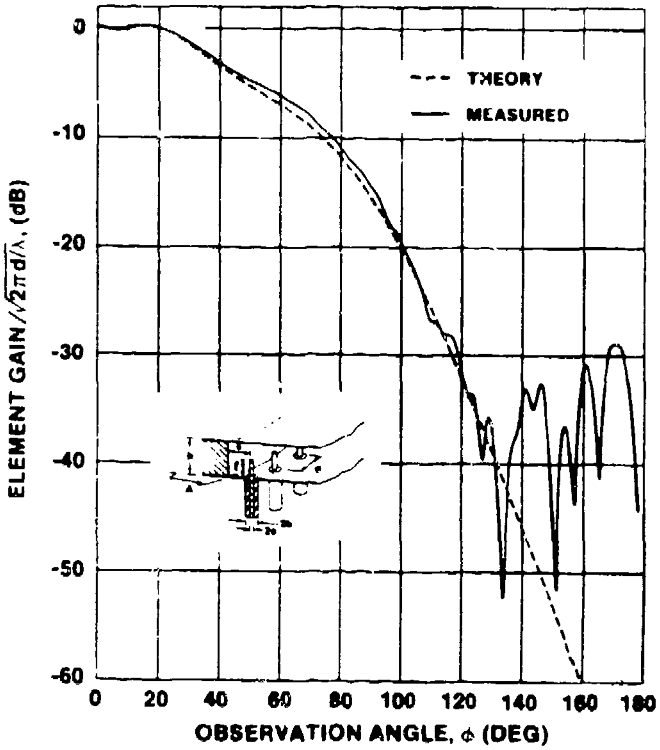

Fig. 35 Theoretical and experimental element pattern amplitude (log scale) ($d/\lambda=0.6$, $\ell/\lambda=0.25$, $s/\lambda=0.245$, $kA=38.4$, $N=64$, $f=7.5$ GHz)

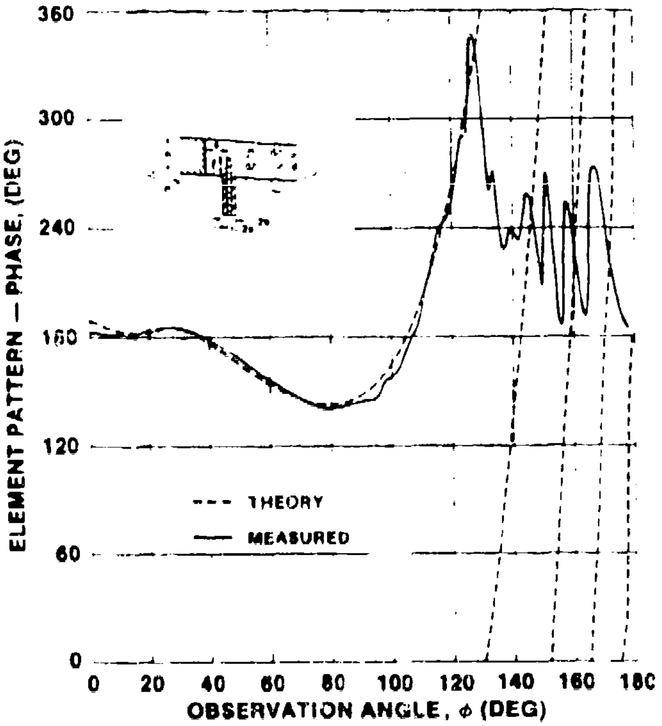

Fig. 36 Theoretical and experimental element pattern phase ($d/\lambda=0.6$, $\ell/\lambda=0.25$, $s/\lambda=0.245$, $kA=38.4$, $N=64$, $f=7.5$ GHz)

NEW TIME DELAY TECHNOLOGIES FOR PHASED ARRAY SYSTEMS

by

L.R. Adkins, H.L. Glass, K.K Jin, and F.S. Stearns
Rockwell International - Science Center

Y.T. Ataiiyn, R.L. Carter, and J.M. Owens
The University of Texas at Arlington

D.D. Stancil
North Carolina State University

ABSTRACT

Variable time delays are necessary in phased array systems to prevent phase squinting and pulse stretching. Methods for providing these time delays include (1) an assortment of fixed cables, (2) charge coupled devices (CCDs), (3) ferrite loaded cables, (4) surface acoustic wave (SAW) devices, and (5) magnetostatic wave (MSW) devices. Fixed cables are bulky, limiting the number which can be employed per system. CCDs, ferrite loaded cables and SAW devices are applicable primarily at frequencies below 1 GHz and provide relatively small delay differentials. MSW wave technology is capable of operating at frequencies up to 20 GHz and providing differential time delays on the order of tens of nanoseconds. An MSW device has recently been demonstrated with a bandwidth of 250 MHz centered at 3 GHz. This device has a phase error across the band of less than 10° and is capable of providing nearly 50 nanoseconds differential delay. Thus, MSW technology appears to be the most promising technique for the next generation of phased array systems.

INTRODUCTION

The need for enhanced performance and miniaturization in phased array system components has fueled the exploration of new techniques for providing time delays. Ideally a time delay component should be small, rapidly tunable over a delay range of a few tens of nanoseconds, have excellent phase linearity characteristics, and be inexpensive. It is the purpose of this paper to review techniques presently available for providing time delays and to discuss alternate approaches which are being evaluated for the next generation of phased array systems. Emphasis will be placed on recent advances in the state-of-the-art for one particular approach, the magnetostatic wave (MSW) delay line.

True time delays perform two principal functions in phased array systems: 1) they eliminate "phase squinting" in broad band beams and 2) they allow the undistorted transmission and reception of narrow pulses. Consider the first problem. In a phased array antenna the beam is steered by adjusting the phase of the electromagnetic signals transmitted or received at each of a large number of radiating elements so that the radiated waves add coherently only in a specified direction. If frequency independent phase shifters such as diodes are used to provide the needed phase shift, then for a given steering angle the signal will be strictly coherent only at one frequency. Consider an array of radiators with spacing d as shown in Figure (1a). If the steering angle is and D is the path difference between adjacent radiators, then the relation between θ , d, and D is given by $d*Sin(\theta)= D$. Thus, the required phase at each radiator for wavelength lambda will be $2*\Pi*D/lambda$. Clearly, a frequency independent phase shifter can satisfy this requirement only at one frequency. Other frequency components will sum coherently in slightly different directions, and the net system result will be high sidelobes outside a relatively narrow passband. In effect a broad band imaging system has been "squinted" into a narrower band one.

The second problem, the pulse distortion of a narrow pulse, is independent of bandwidth and will arise whenever the steering angle is large. This is illustrated in Figure (1b). Let T_A represent the time required for an electromagnetic signal to travel across an antenna array. If the beam is steered an angle θ away from the array normal, then the leading edge of a transmitted pulse from the near side of the array will arrive at a target $T_A*Sin(\theta)$ earlier than the leading edge of the pulse transmitted from the far side of the array. In effect the pulse width will be stretched by an amount $T_A*Sin(\theta)$. Since T_A is usually on the order of a few tens of nanoseconds, the effect is important only for narrow pulses. However, narrow pulses are mandatory when high resolution imaging of a target is required, and thus the problem is highly significant.

TIME DELAY TECHNIQUES

Fixed Delay Elements

In most present day systems time delays are provided by an assortment of fixed transmission lines, either stripline or cable. An excellent elementary review of this approach has been given by Brookner[1] in a recent Scientific American article. For large angle sweeping a 3-bit phase shifter consisting of three unequal length striplines is provided at each radiating element. These lines have paths equivalent to 1/2, 1/4, and 1/8 wavelength and can be combined to give phase differences of 0° to 360° in steps of 45°. The three striplines together are less than one wavelength long, so that the total phase shift is never more than 360°. Thus, although broad band operation is realized, high resolution, narrow pulses a few tens of wavelengths wide cannot be reconstructed unambiguously using these elements alone.

For narrow pulse work, the array is commonly divided into subarrays, and each of these units is provided with a 3-bit phase shifter comprised of long cables. For a system such as the COBRA DANE radar, delays as long as 64 wavelengths can be obtained for each subarray. Although this technique is believed to be adequate for most current applications, there is necessarily some distortion of the pulse due to the finite delay across each subarray. However, it is clearly impractical to provide each element of the array with long delay lines, since something like 100 miles of cable would be required for a radar like COBRA DANE. Even using the subarray approach about one mile of cable is necessary. It would clearly be desirable to replace these long lengths of cables with compact modules, and therefore considerable effort has been expended in recent years in exploring novel methods of varying delays electronically.

Charge Coupled Devices

In principle a charge coupled device (CCD) is capable of providing electronically variable time delays. A CCD is a signal sampling device; charge injected into a semiconductor by an input signal is transferred along an array of predefined cells by means of a series of multiple phase electrodes. For N cells the signal is delayed by an amount $T_d=N/f_c$ where f_c is the clock frequency or the rate at which the shift registers transfer the charge down the cells. Thus, for a given N cells, the delay can be changed by changing the value of f_c. However, sampling theory states that for a waveform to be completely reconstructed, its frequency can be no more than one half the sampling rate or $f_c/2$. The electron mobility of silicon limits the clock rate to 500 MHz, and the maximum clock rate reported using GaAs is 1 GHz. Thus variable time delays using CCDs are restricted to low frequency applications.

Ferrite Loaded Helical Transmission Line

An electronically tunable delay line using a coaxial cable and a ferrite rod has been reported by Clark[2]. For this arrangement the center conductor of the coax cable is removed and replaced by a helix which has been wrapped around a ferrite core. A schematic is shown in Figure (2a). When a magnetic field is applied to this structure the permeability of the ferrite rod will change, thus changing the impedance seen by the signal. The time delay per unit length for a transmission line with inductance L and capacitance C is given by $t_d=(LC)^{.5}$. Therefore, a change in impedance will produce a change in delay. However, this technique is useful only at frequencies below about 150 MHz, since it depends on the difference between the initial (unmagnetized) permeability and the permeability at saturation. At low frequencies this can be substantial as shown in Figure (2b). Here the dispersive and dissipative components of the permeability (u' and u", respectively) are plotted as a function of frequency. Near the gyromagnetic resonance frequency, the difference between saturated and unsaturated mu is minor. At frequencies up to 150 MHz the maximum differential delay reported is 4 nanoseconds with an applied field differential of 160 oe. The advantage of this approach is that it has high power-handling capability (at least 50 watts) and is therefore attractive for HF and VHF applications.

Surface Acoustic Waves

The velocity of a surface acoustic wave (SAW) propagating on a piezoelectric crystal is changed by applying a voltage across the acoustic path. Joshi[3] first reported the technique of applying a voltage across the thickness of a lithium niobate ($LiNbO_3$) crystal to change the SAW velocity, as shown in Figure (3). This required a thin metal electrode in the acoustic path which necessarily introduced some dispersion and additional loss. Working at a center frequency of 74 MHz, he was able to obtain a fractional velocity change of 82 X 10^{-12} for one volt/meter applied field.

For a 20 mil thick substrate a fractional delay differential of 9×10^{-4} was obtained with a bias of 5 kv. For a one centimeter path length this works out to about 2 nanoseconds delay change. Budreau et al[4] working at 1 GHz have also investigated this method, along with an alternate technique in which an in-plane bias is applied to the crystal via two metal electrodes on opposite side of the propagating path. Although the efficiency of this latter scheme is much less in terms of volts/meter, the freedom to make the spacing between the electrodes arbitrarily close allows the attainment of a differential delay similar to that obtained with the normal field approach in terms of absolute volts applied. The advantage of the scheme is that both the dispersion and the insertion loss are not degraded, since the acoustic wave does not propagate through a metal electrode. When working with the field normal to the crystal plane, Budreau et. al. thinned some of their substrates to 160 um to reduce the absolute voltage required for a given field strength. Their best result was a fractional delay change of $.9 \times 10^{-6}$ per applied volt. Thus, using a 5 kv normal field bias and the thinner substrates a delay differential of approximately 14 nanoseconds could be obtained on a crystal with a one centimeter path length.

An alternate method of varying the SAW velocity has been reported by Ganguly et al[5]. Their approach was to deposit a thin nickel film on a $LiNbO_3$ crystal between the SAW transducers. Application of a magnetic bias field across this layered structure could then change the SAW velocity via the magnetoelastic interaction. The operating frequency of this device was 210 MHz, and a maximum delay change of less than one nanosecond was obtained with an applied bias field of several Koe.

As with CCDs and the ferrite loaded helix, a SAW delay line is most effective at frequencies in the VHF band or below. The 1 GHz region investigated by Budreau et al is close to the upper limit of SAW technology due to the difficulty of transducer fabrication (electrodes less than 1 um wide are needed at 1 GHz for first harmonic operation) and elastic wave propagation losses. Also, the delay differentials obtainable are relatively short. On the other hand, the magnetostatic wave (MSW) technology discussed in the following section has the potential of operating at frequencies as high as 20 GHz with differential delays on the order of tens of nanoseconds.

Magnetostatic Delay Line

Considerable progress has been made recently toward the realization of an MSW variable time delay device which can operate in the microwave frequency range and provide electronically tunable delays of a few tens of nanoseconds. This device has been developed under the sponsorship of RADC through a joint effort of Rockwell International, The University of Texas at Arlington, and North Carolina State University.

The propagating medium for magnetostatic wave (MSW) devices consists of a epitaxial ferrite film (usually yttrium iron garnet or YIG) on a garnet substrate. This structure is usually prepared in the form of a bar with input and output transducers at each end. This device is placed between the poles of a magnet, and an rf signal is fed into one transducer. An illustration of a standard MSW delay line is shown in Figure (4)[6]. At a specific combination of signal frequency and magnetic field strength, magnetic spin waves will be launched from the input transducer down the bar. And these waves are reconverted into electromagnetic energy at the output transducer. Since the velocity of magnetostatic waves in the YIG is some three orders of magnitude smaller than electromagnetic waves in free space, a substantial delay is realized with a delay path of about one centimeter. Magnetostatic waves are somewhat analogous to surface acoustic waves, but they have two advantages for phased array systems applications: 1) they operate from 1 GHz to 20 GHz and 2) their frequency of operation can be electronically tuned by changing the value of the magnetic bias field.

MSW delay lines are inherently dispersive; i.e., the group velocity does not in general equal the phase velocity. The specific dispersive characteristics of a MSW delay line are dependent on a number of variables, but one useful feature is that the slope of the dispersion can be either positive or negative, depending on the orientation of the magnetic bias field. This aspect has been exploited in the design of a variable delay line which operates at a center frequency of 3 GHz and exhibits a delay differential of approximately 40 nanoseconds.

A schematic of the approach is shown in Figure (5). Two MSW delay lines having dispersive characteristics with slopes of opposite signs are cascaded together. If the dispersions are linear and the slopes are equal in absolute magnitude then the net dispersion will be zero across the passband. If one delay line is provided with a constant bias while the bias on the other is varied, the net delay will change but remain flat as a function of frequency over the passband. We will refer to a device of this type as a MSW cascaded delay line (CDL). A laboratory version of the approach was first reported by Sethares and Owens[7] and an improved laboratory version was reported by the present authors in 1983[8] This device has now been packaged and is shown in Figure (6).

The negatively sloped dispersion is provided by a backward volume wave (MSBVW) delay line while a surface wave (MSSW) delay line gives the positive slope characteristic. The MSBVW mode is obtained when the bias field is parallel to the direction of propagation, while a field applied in the plane of the film, but perpendicular to the direction of propagation, produces the MSSW mode. One problem inherent in MSW dispersion is that it is in general non-linear. Thus, some method for linearizing these characteristics must be employed. For the MSBVW delay line the dispersion was linearized by adjusting the spacing between the film and the ground plane. For the MSSW delay line a variable ground plane was provided. These techniques are described in more detail by Chang et al[9] and in reference [8].

The packaging deserves some comment. It is important that the fields seen by the delay lines be uniform to prevent additional unwanted dispersion. Such uniformity is readily achieved with large laboratory magnets, but small packaged components are another matter. Our approach was to place the biasing magnets at opposite ends of the packages and focus their fields along the central axis by means of a series of smaller magnets with opposing fields suitably spaced along the remaining sides, top, and bottom. As the fields required were relatively small (600 oe), ferrite magnets were used throughout. In the photograph the magnets are the dark colored rectangles, while the light rectangles are aluminum spacers. The uniformity of the biasing fields was excellent using this technique. The variable field was provided by means of coils in the MSBVW package, although for this initial package less emphasis was placed on the design of the coils to vary the field than on the permanent magnets to provide the basic magnetic environment. The outer shell of the package was stainless steel.

The dispersive characteristics of the packaged MSSW and MSBVW delay lines are shown in Figure (7), and the net dispersion from the complete CDL is given in Figure (8). The figure shows a delay differential of approximately 23 nanoseconds across the band. The maximum delay change which has been demonstrated with this configuration is 47 nanoseconds. The critical characteristics of this device can be summarized as follows:

obtained with the MSW CDL, while a maximum variation of 4 nanoseconds has been reported for the helix and about 10 nanoseconds for the SAW delay line. In the SAW case a voltage on the order of kilovolts was required to realize the reported change.

The main drawbacks to the MSW device are sensitivity to temperature change, moderate insertion loss, and low power handling capability. The power handling capability is intrinsic to the magnetostatic interaction process, but the insertion loss characteristic and temperature stability can be expected to improve with further research. Thus, the results reported here indicate that MSW devices will be capable of meeting many of the time delay requirements of future generation phased array systems.

Table I

Technique	Frequency	Maximum Reported Differential Delay	Delay Change Method
CCD	< 500 MHz		Clock Rate
Helix	< 300 MHz	4 nanoseconds	160 oe H_{bias}
SAW	< 1 GHz	14 nanoseconds	5 kv Potential
MSW	1 GHz-20 GHz	47 nanoseconds	120 oe H_{bias}

ACKNOWLEDGEMENT

This work was supported by the US Air Force Systems Command (Electronic Systems Division) under contract No. F19628-82-C-0098.

REFERENCES

1. Eli Brookner, "Phased Array Radars", Scientific American, 252, pp. 94-102(1985).

2. Donald E. Clark, "HF Low-Loss Nanosecond Variable Delay Line", IEEE SOUTHEASTCON 1981 CONFERENCE PROCEEDINGS, CH1650, pp.135-139(1981).

3. S.G. Joshi,"Electronically Variable Time Delay in a $LiNbO_3$ SAW Delay Line", Proceedings of the IEEE, 70, pp. 95-96(1982).

4. Alan J. Budreau, Gary J. Scalzi, Paul H. Carr, and Henry L. Bertoni, "Electrostatically Variable SAW Delay Lines - Theory and Experiment", IEEE Trans. Sonics and Ultrasonics, SU-31, pp. 646-641(1984).

5. A.K. Ganguly, K.L. Davis, D.C. Webb, and C. Vittoria, "Magnetic Control of Surface Elastic Waves in a Novel Layered Structure", Magnetism and Materials-1976, Joint MMM-INTERMAG Conference, June 15-18, 1976, pp. 259-261(1976).

6. Martin R. Stiglitz and James C. Sethares, "Magnetostatic Waves Take Over Where SAWs Leave Off", Microwave Journal, 25, pp. 18-38 (February 1982).

7. J.C. Sethares, J.M. Owens, and C.V. Smith, "An Electronically Variable Magnetostatic Wave Time Delay Device",Electronics Letters, 16, p. 825(1980).

8. L.R. Adkins, H.L. Glass, F.S. Stearns, K.W. Chang, R.L. Carter, and J.M. Owens, "Electronically Variable Time Delays Using Cascaded Magnetostatic Delay Lines", Journal of Applied Physics, 55, pp. 2518-2520(1984).

9. K.W. Chang, J.M. Owens, and R.L. Carter, "Linearly Dispersive Time-Delay Control of Magnetostatic Surface Wave by Variable Ground-Plane Spacing", 19, pp. 546-547(1983).

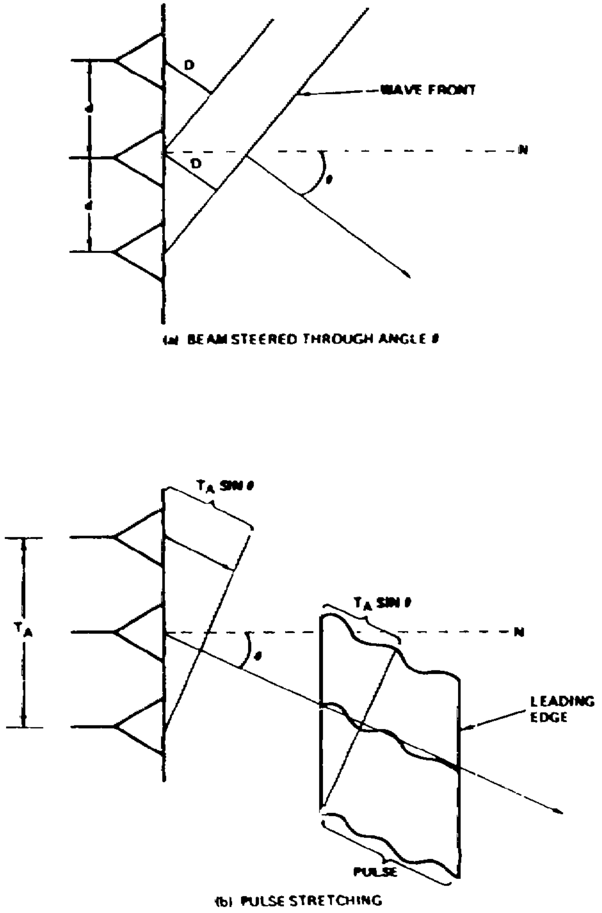

Figure 1. Phased Array Antennas

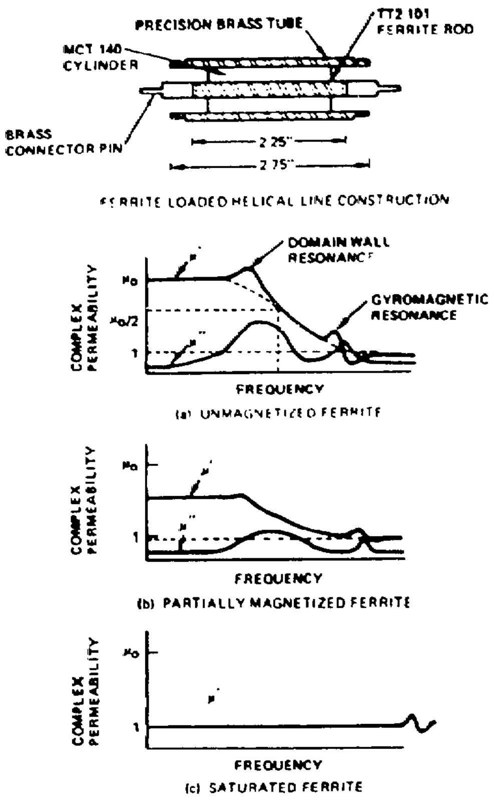

Figure 2. Predicted Behavior of Ferrite Material (after Clark, 1981)

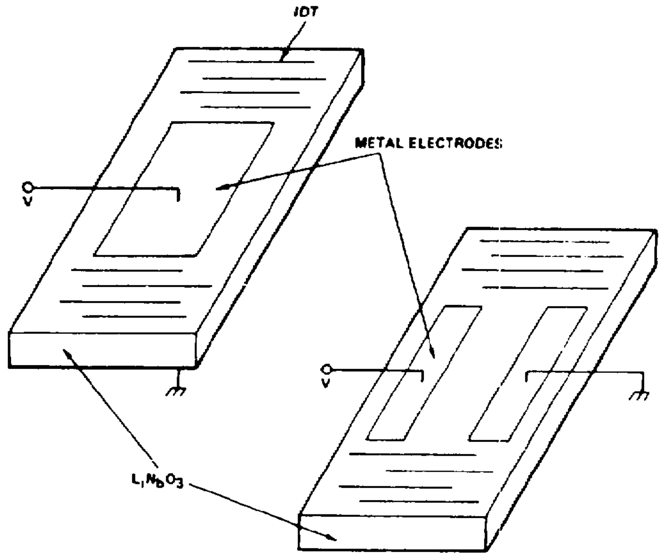

Figure 3. Electronically Variable Time Delays Using Saw Delay Lines

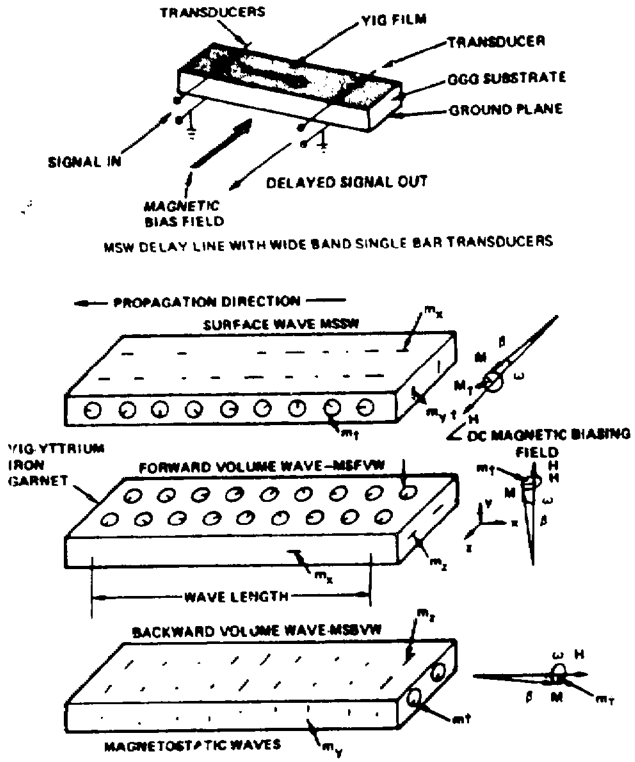

Figure 4. Diagrams Depicting Excitation of MSSW, MSFVW and MSBVW (after Stiglitz and Sethares, 1982)

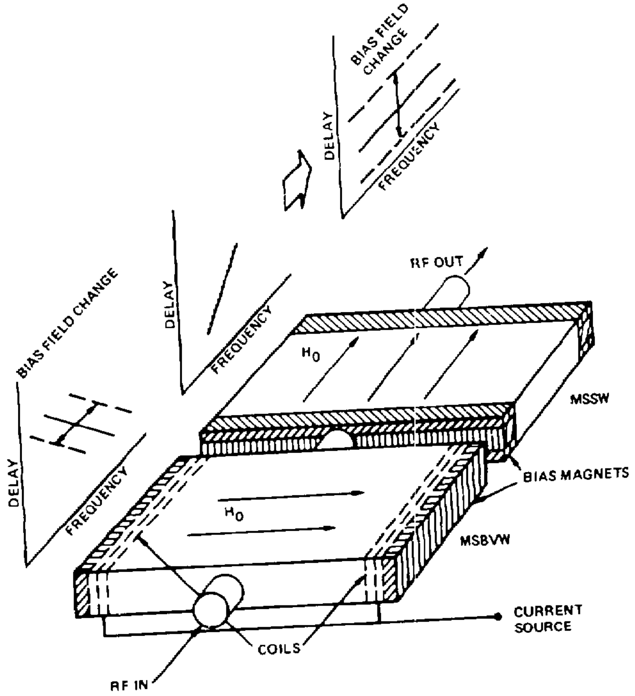

Figure 5. Electronically Tunable Time Delay Using a Magnetostatic Wave Cascaded Delay Line (CDL)

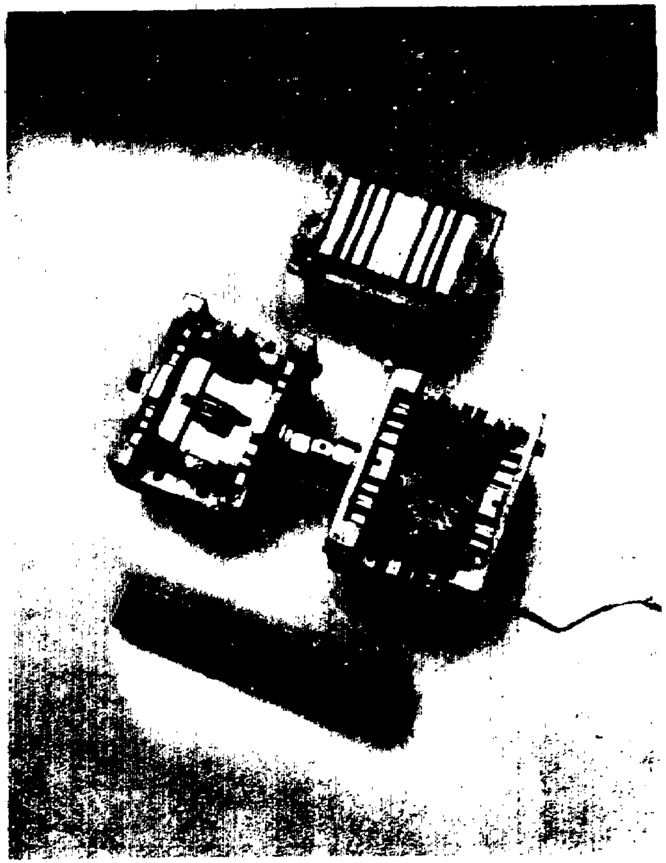

Figure 6. Packaged MSW CDL

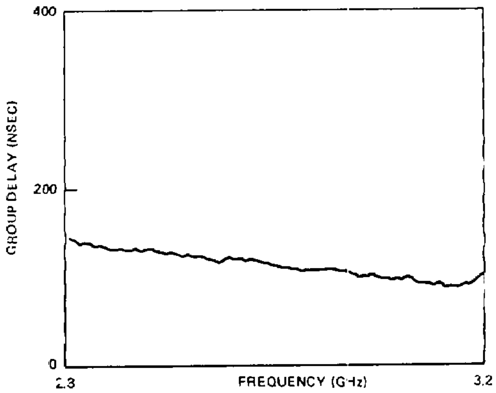

(a) MSBVW

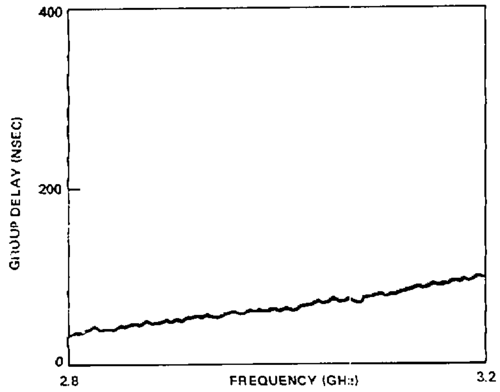

(b) MSSW

Figure 7. Linear Dispersions with MSBVW and MSSW Delay Lines

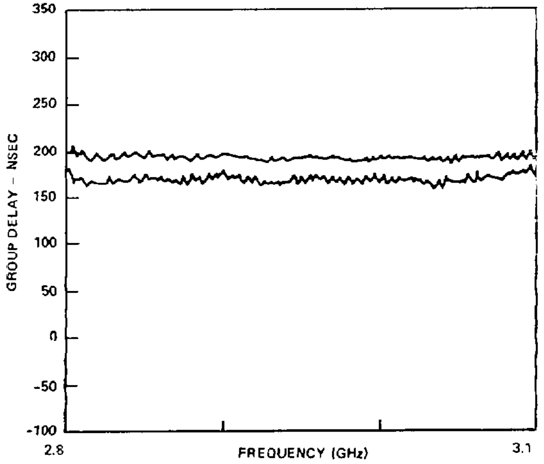

Figure 8. CDL Net Dispersion for Two Values of Coil Current

SCAN COMPENSATED ACTIVE ELEMENT PATTERNS

by

R. C. Hansen

Consulting Engineer
Tarzana, CA 91356
818-345-0770

SUMMARY

The active performance of a planar array of slot-monopole elements is investigated. An improved mutual coupling algorithm is devised that combines slot-monopole and monopole-monopole couplings into a single Romberg integration. In spite of the close monopole-to-monopole coupling in an array, these elements provide scan compensation. Active conductance vs polar angle is nearly independent of scan plane. Active susceptance while not independent exhibits much less variation than do plain slots. Active element patterns are nearly independent of scan plane thru grating lobe incidence. Matching at an optimum polar angle yields a .6 db improvement over the grating lobe free range. Adjustment of monopole length and offset promises to allow larger optimum matching improvement.

PURPOSE

It is well known that mutual coupling changes the performance of array antennas with scan angles (Oliner & Malech, 1966; Hansen, 1983). It is also known through work of Wheeler and others that an ideal element power pattern of a conical cos θ would provide scan independent performance for half-wave spacing; for larger spacings the ideal element pattern is more complex (Wasylkiwskyj & Kahn, 1977). Although the ideal element pattern can be closely approximated by exciting a suitable set of higher modes in a waveguide radiator, simple elements with scan compensation have mostly eluded antenna designers. A salient exception is the slot with astride monopoles, developed by Clavin (1954, 1974). This type of element is relatively easy to construct although the monopole pins do protrude from the the slot ground screen. Slot-monopoles as isolated elements give nearly equal E- and H-plane patterns but it is not clear how they would behave when used as elements in a closely spaced array. This concern arises because the monopoles are then oriented parallel for maximum coupling and are closely spaced. The purpose of this paper is to investigate the performance of slot-monopole elements in rectangular arrays utilizing a square lattice. The active element pattern will be used as an indicator of array performance.

MUTUAL ADMITTANCE BETWEEN SLOT-MONOPOLES

The active element pattern of an element near the center of a large array is obtained from the active input admittance of that element. This in turn is obtained from knowledge of the mutual admittances between elements in the array and thus it is necessary to develop an algorithm for calculating mutual admittance between slot-monopoles. The algorithm contains three types of couplings: slot-to-slot, monopole-to-monopole, and slot-to-monopole (Elliott, 1980); see Fig. 1:

$$Y_{12} = \frac{2}{\eta^2}\left\{ Z_{s1,s2} + \left(\frac{\alpha \sin kh_m}{\sin k\ell_s/2}\right)^2 [\, 2z_{m1,m3} - Z_{m1,m4} - Z_{m2,m3} \,] \right.$$

$$\left. - \frac{4\,\alpha \sin kh_m}{\sin k\ell_s/2} [\, CP_{s1,m3} - CP_{s1,m4} \,] \right\}$$

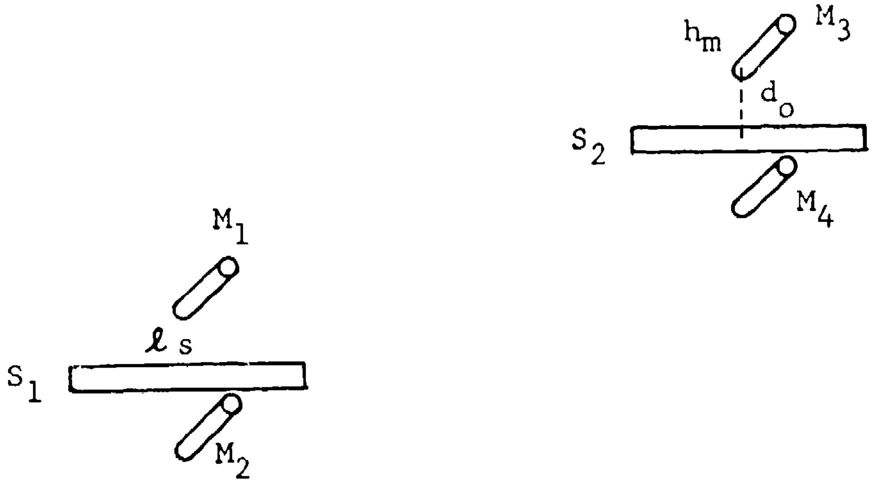

Fig. 1

Slot-Monopole Mutual Coupling Geometry

where $\eta=120\pi$ and:

$$\alpha = \frac{1 - \cos k\ell_s/2}{2 \sin kd_o\ (1 - \cos kh_m)}$$

The Z_{ss} and Z_{mm} are mutual impedances between like elements, while CP is a voltage coupling from slot-to-monopole or vice versa. The trig factors account for the slot and monopole lengths being different from half-wavelength and quarter-wavelength respectively. The slot-to-monopole coupling was developed by Papierz, Sanzgiri, and Laxpati (1977). They integrate the exact near field, in cylindrical coordinates, of the slot over the monopole, under the assumption of sinusoidal field distribution. Elliott does a similar calculation but chooses to integrate over the slot, which involves two exponential terms and integration over the entire slot length. Integration over the monopole involves three exponential terms but integration is only required over one monopole due to symmetry. This approach is believed to be faster and is used in this paper. Integration over the monopole allows the three monopole-monopole mutual impedances to be calculated in the same numerical integration, thus providing a further increase in speed. To perform the integration, complex Romberg integration of order 3 is used. This integration subroutine has a fixed order and does not calculate error coefficients; thus it is much faster and more efficient than Rombergs commonly found in subroutine libraries. Accuracy tests determined that an order of 3 gives rapid results and an accuracy of .1% except for very small couplings. Asymptotic approximations for large separations have generally been unsatisfactory: when used for the spherical waves in the numerical integration there is little saving; when used for the Sine and Cosine Integrals many terms are required due to the slow convergence of the asymptotic series For large separations a more satisfactory solution is to use Romberg of order 2. The slot-slot mutual impedance utilizes a Carter zero order subroutine published by Hansen & Brunner (1979). All results given by Elliott have been validated using the slot-monopole mutual admittance subroutine.

ARRAY CALCULATIONS

Large arrays are of primary interest and a unit cell type calculation (Oliner and Malech, 1966) could probably be developed for slot-monople elements. In place of this the large array approximation (Lincoln Labs, 1965) is used. In this approximation all elements of a large finite array are assumed to have the same mutual coupling environment; edge effects are thus neglected. However when the array is large the effect of edges upon center elements becomes negligible, and thus the large array approximation compares very closely with unit cell calculations. The array is rectangular with the elements reposing on a rectangular lattice. For convenience the number of elements along x and along y is assumed to be odd. Since all elements enjoy the same mutual impedance environment, Floquet's theorem applies and all element fields are identical except for the progressive Floquet phase which is a function of scan angles. Thus no matrix inversion is needed for this problem, but the effects of a finite array are included due to the summation of mutual impedances over the actual elements. The active impedance of any element, which is conveniently taken as the center element, is given by:

$$Z_{act} = 4 \sum_{1}^{N} \sum_{1}^{M} Z_{nm} \cos\,(nkd_x u + mkd_y v) + Z_{oo}$$

$$+ 2 \sum_{1}^{N} Z_{on} \cos\,(nkd_x u) \quad + 2 \sum_{1}^{M} Z_{om} \cos\,(mkd_y v)$$

where Z_{nm} is the mutual impedance or admittance between the center element and the nmth element. As usual u and v are:

$$u = \sin\theta \cos\varphi \,, \quad v = \sin\theta \sin\varphi$$

A standard spherical coordinate system is used, with the slot parallel to the x-axis, and the z-axis normal to the array. The lattice spacings are d_x and d_y, while N and M are each half the number of elements on the x and y principal axes not counting the center element. Thus it can be seen that this large array formula sums up the mutual effects of all the elements. As the array becomes larger the mutuals added represent smaller contributions so that for a large array the finite array results approach those for an element in an infinite array, calculated for example by the unit cell method.

The active element pattern is computed from the active admittance $Y_a(\theta)$ using the conjugate reflection coefficient suitable for admittance matching:

$$\Gamma(\theta) = \frac{Y_a^*(\theta) - Y_m}{Y_a(\theta) + Y_m}$$

When the active element pattern is normalized to unity at broadside with an admittance match (θ =0), the result is (Hansen,1983):

$$G_{act}(\theta) = \frac{R_a(0)\, g_{iso}(\theta)}{R_a(\theta)} \left[1 - |\Gamma(\theta)|^2 \right]$$

Here $g_{iso}(\theta)$ is the isolated element gain pattern.

Results of the calculations are shown in Figs. 2 and 3, using N and M sufficiently large that an infinite array is approximated. Slot lengths are chosen to make the active admittance at θ =0 real. Fig. 2 shows active element pattern for a square lattice of .6λ for E-,H-, and diagonal planes, while Fig. 3 is for spacing of .7λ . Even though the monopoles are closely coupled the active element pattern values vs scan plane are within a db from broadside to the grating lobe incidence angle. In contrast Fig. 4 gives active element pattern for an infinite waveguide slot array (Oliner and Malech, 1966); approaching grating lobe incidence in the E- plane a rapid drop occurs. Shorter slots with monopoles with lattice spacing closer to λ/2 also offer improved performance but such slots are shorter than resonant length and require external slot matching.

Matching of the active element admittance at a polar angle greater then zero has long been used for arrays that scan in only one plane; for conventional elements the susceptance slopes are of opposite signs in the E- and H- planes so matching off broadside is of small value for two-dimensional scanning. With slot-monopoles the conductance vs θ curves for different scan planes are close; the susceptance curves although not exhibiting the marked opposite behavior of plain slots do not track sufficiently well to allow near optimium matching for all φ.

Taking the array of Fig 2 as an example the grating lobe appears at 41.8 deg; for one scan plane matching at this angle produces the flattest active element pattern over the useful range of θ. But in some other scan planes there is no improvement. An optimum match for both E- and H- planes occurs at θ =32 deg with results shown in Fig 5, where the close tracking of the curves is evident. At θ =0 the gain, relative to broadside match, broadside gain, is -.23 db, while at the grating lobe angle the

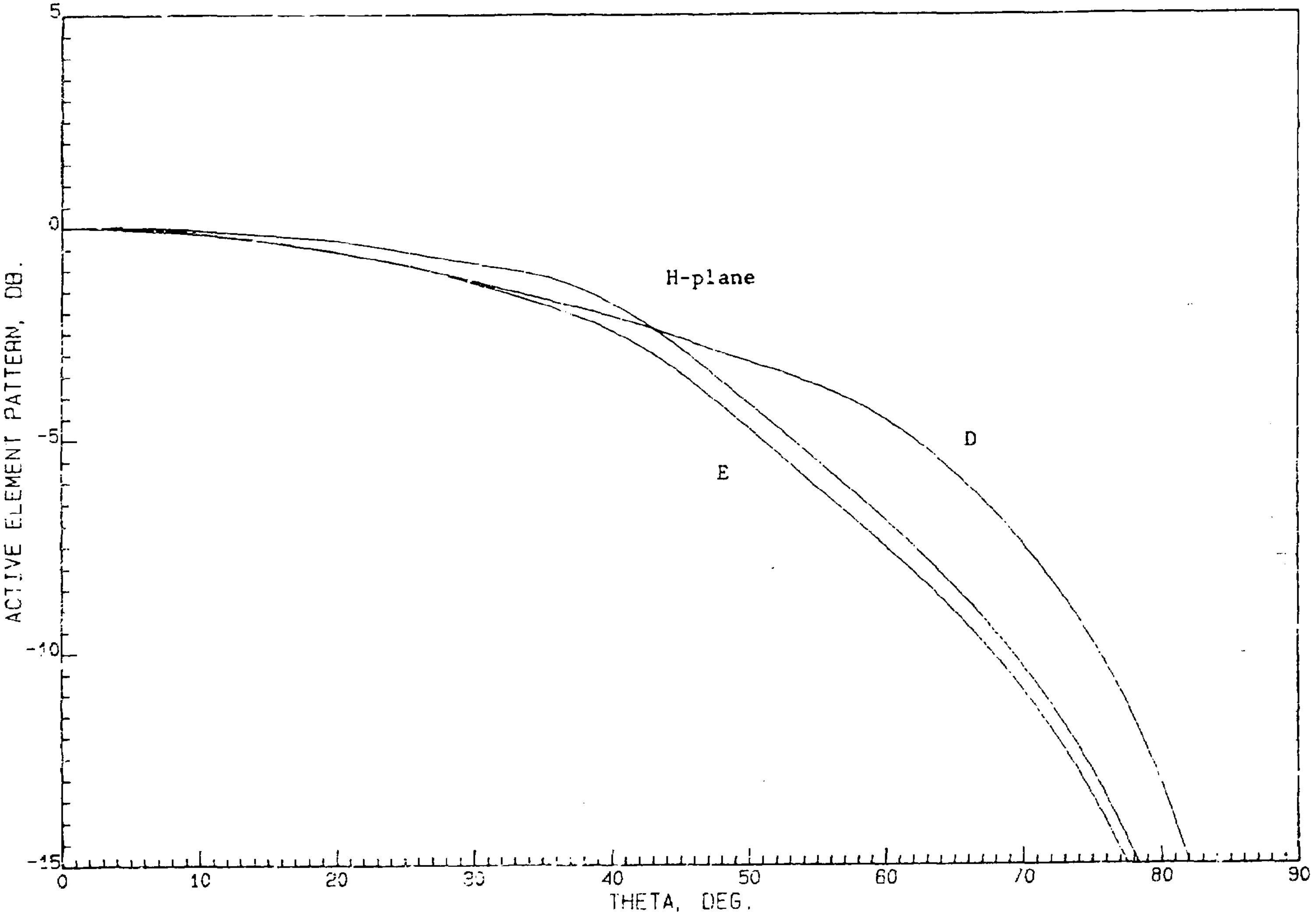

SLOT-MONOPOLE LARGE ARRAY APPROX., L=.564 WV, DX=DY=.6 WV

Fig. 2

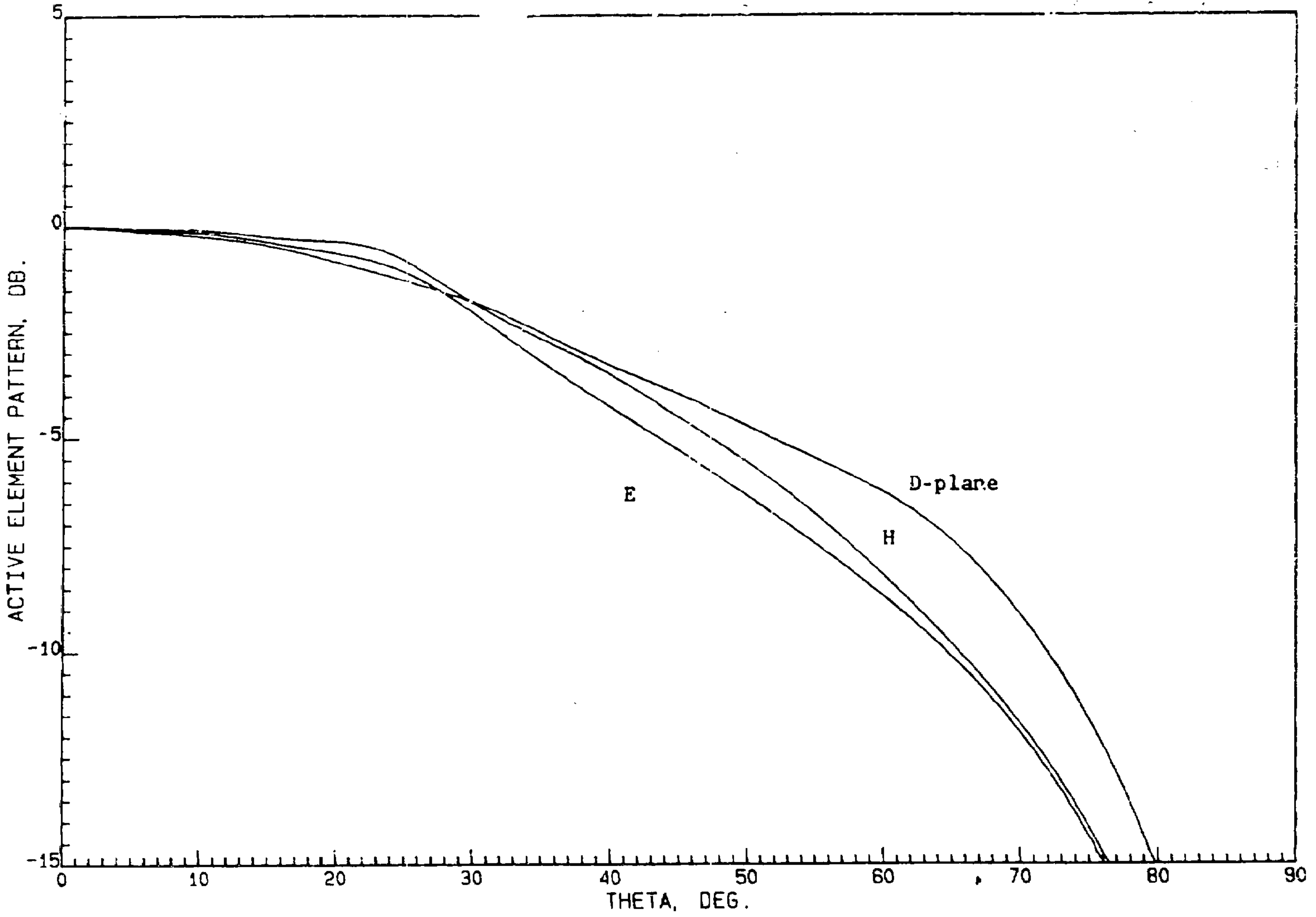

SLOT-MONOPOLE LARGE ARRAY APPROX., L=.576 WV, DX=DY=.7 WV

Fig. 3

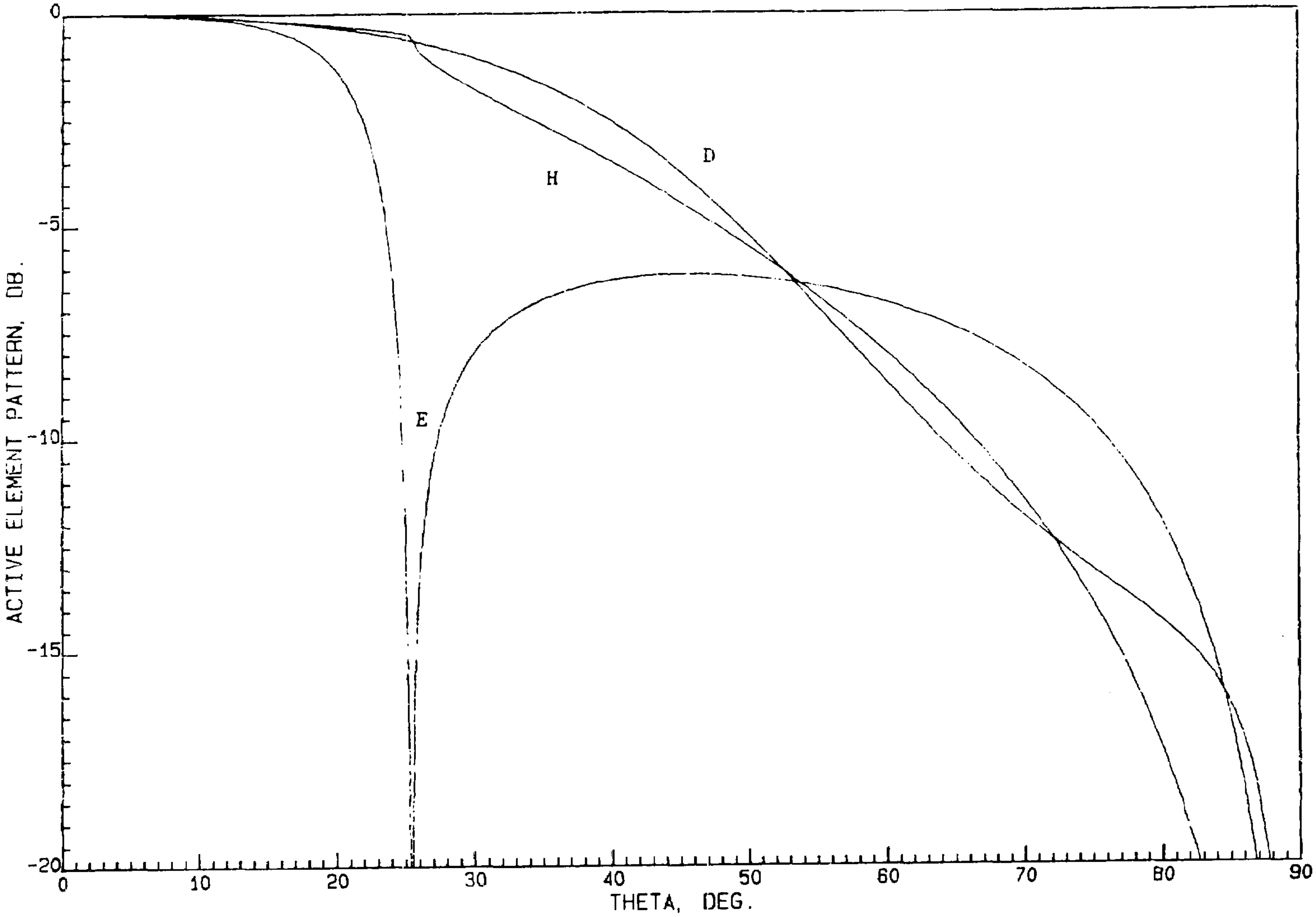

SLOT ARRAY, WR-90 AT 9375 MHZ, L=.547 WV, DX=DY=.7 WV

Fig. 4

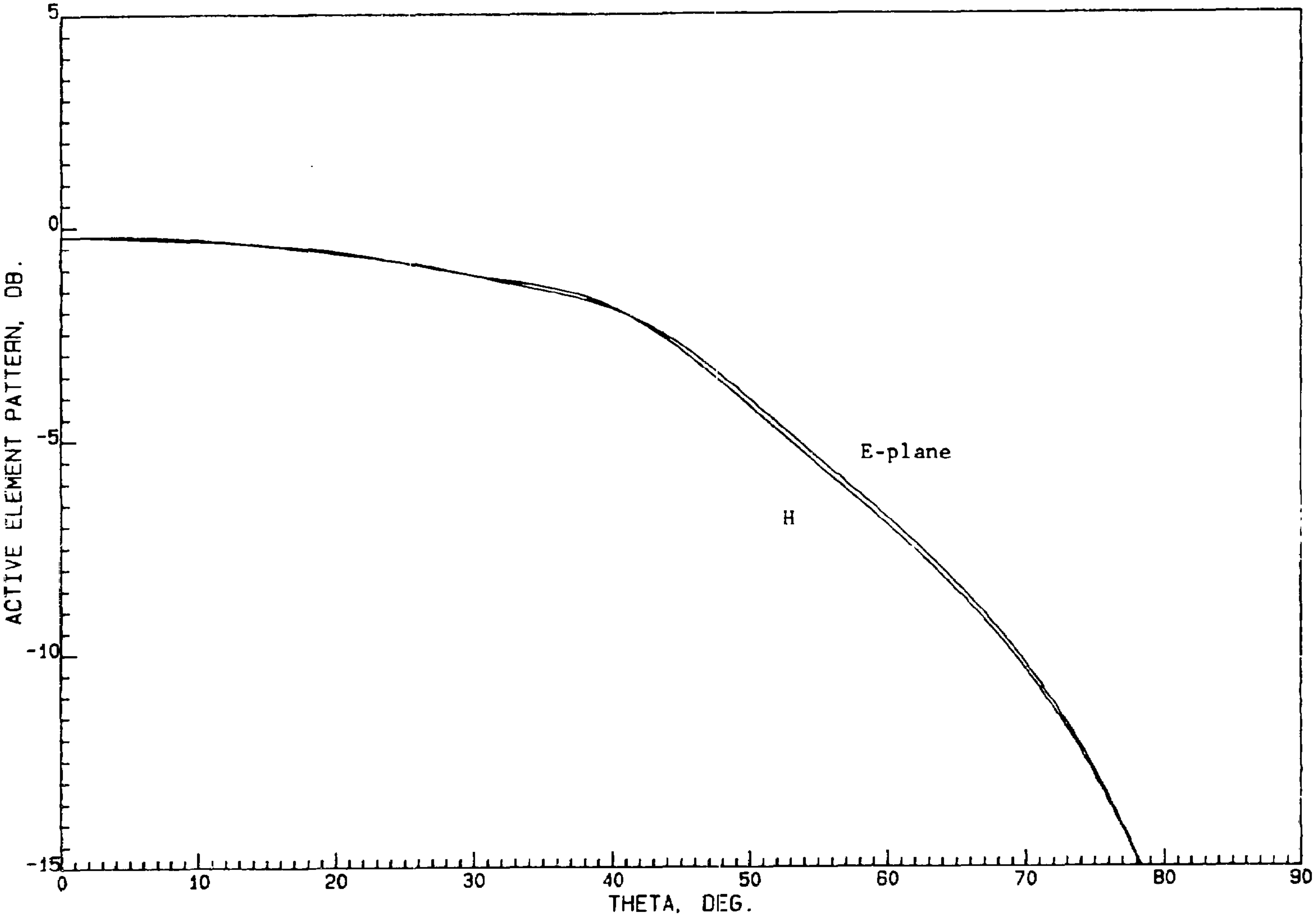

SLOT-MONOPOLE ARRAY, L=.564 WV, DX=DY=.6 WV, OPT. ANGLE MATCH

Fig. 5

result is -2.16 db, representing an improvement over the broadside match case of .6 db.

The monopole length and offset were set to match the E-and H-plane patterns for an isolated slot-monople; probably a re-adjustment for active element pattern match would increase the optimum matching improvement.

In conclusion, the slot monopole, a simple scan compensated element, offers excellent scan performance in all planes of scan. And gain may be optimized over a scan range by properly selecting the matching angles.

REFERENCES

A. Clavin, "A New Antenna Feed Having Equal E- and H-plane Patterns", Trans. IEEE, Vol. AP-2, July 1954, pp. 113-119

A. Clavin, D. A. Heubner & F. J. Kilburg, "Improved Element for Use in Array Antennas", Trans. IEEE, Vol. AP-22, July 1974, pp. 521-526

R. S. Elliott, "On the Mutual Admittance Between Clavin Elements", Trans. IEEE, Vol. AP-28, Nov. 1980, pp. 846-870

R. C. Hansen, "Planar Arrays", Chap. 10 in "Handbook of Antenna Design, Vol. 2", A. W. Rudge et al eds., IEE/Peregrinus, 1983

R. C. Hansen & G. Brunner, "Dipole Mutual Impedance for Design of Slot Arrays", Microwave Journal, Vol. 22, Dec. 1979, pp. 54-56

Lincoln Labs., "Phased Array Radar Studies", TR 381, 31 Mar 1965, Lincoln Labs., MIT.

A. A. Oliner & R. G. Malech, "Mutual Coupling in Infinite Scanning Arrays", Chap. 3 in "Microwave Scanning Antennas, Vol. 2", R. C. Hansen, ed., Academic Press, 1966

A. Papierz, S. M. Sanzgiri & S. R. Laxpati, "Analysis of Antenna Structure with Equal E- and H-plane Patterns", Proc. IEE, Vol. 124, Jan. 1977, pp. 25-30

W. Wasylkiwskyj & W. K. Kahn, "Element Pattern Bounds in Uniform Phased Arrays", Trans. IEEE, Vol. AP-25, Sept. 1977, pp. 597-604

FERRITE MATERIALS FOR MILLIMETER WAVE PHASE SHIFTERS

G. P. Rodrigue
School of Electrical Engineering
Georgia Institute of Technology

ABSTRACT

The development of high performance, low cost ferrite phase shifters poses problems to both materials and structure engineers. Upper limits on saturation magnetization seem inescapable and indicate a decreasing figure of merit for millimeter phasers with increasing frequency. Hexagonal ferrites of either uniaxial or planar form offer some promise of improved performance, but these materials are not commercially available.

Waveguide designs scaled to millimeter frequencies appear to be quite expensive and not amenable to mass production techniques. Other open waveguide structures have possible cost advantages, but apparently at a reduction in performance levels.

Introduction

"Microwave" ferrite applications have spanned the frequency range from UHF and below to 100 GHz and above. Ferrite materials have served a variety of important functions in phased array systems; their non-reciprocal properties have been applied to isolators, circulators, and phase shifters. Both reciprocal and non-reciprocal phase shifters have been employed as beam steering elements in phased array radars. Ferrite phase shifters have primarily been used from S or C-band up through K_A band. At lower frequencies, reciprocal diode phasers have something of a competitive edge. At frequencies above about 30 GHz no very satisfactory solution exists today. Diode phasers suffer from high loss, and ferrites seem hampered by intrinsic limitations in maximum achievable magnetization.

The millimeter wave range of frequencies place unusual demands on the ferrite component designer. Ferrite devices generally operate in either a fixed bias field condition or as a remanent state device. For most fixed field devices, higher operating frequencies demand increasingly large magnetic fields; the required field increases about linearly with increasing frequency. For remanent state devices, optimum performance is realized for

$$\frac{\gamma 4\pi M_s}{\omega} \approx 0.7 \tag{1}$$

where:

γ = 2.8 MHz/gauss
$4\pi M_s$ = saturation magnetization (in gauss)
ω = operating frequency (Hz)

This equation indicates that a saturation magnetization of approximately 2500 gauss is optimum for X-band phasers, 7500 gauss for 30 GHz phasers, 15,000 gauss for 60 GHz phasers, and 22,500 gauss for 90 GHz phasers. Room temperature values of saturation magnetization for commercially available ferrites are limited to less than 5500 gauss. There seems little hope that significantly larger values of saturation magnetization will be achieved.

Saturation magnetization also plays an important role in circulator design, where the achievable bandwidth also varies directly with the ratio, $\gamma 4\pi M_s/\text{freq}$. Thus as the operating frequency increases the fractional bandwidth of ferrite circulators decreases. Of course, in any device the specific rf design, the particular modes utilized, etc., will also affect performance. But the inherent desirability of higher magnetizations at millimeter wave frequencies seems inescapable.

The term "ferrite" includes ceramic materials of the spinel, garnet, or hexagonal crystal structures that contain iron and other magnetic ions in oxide form. These three crystal structures are all ferrimagnetic (having anti-parallel alignment of neighboring magnetic moments), and this ferrimagnetism places an upper limit on the realizable values of saturation magnetization.

Basic Ferrite Performance and Limitations

The performance of all ferrite devices is based on their permeability tensor. This tensor written in the undamped approximation is given by:

$$\mu = \mu_0 \begin{bmatrix} & +j\kappa & 0 \\ -j\kappa & \mu & 0 \\ 0 & 0 & \mu_z \end{bmatrix} \qquad (2)$$

where:

$$\mu = 1 + \frac{\omega_m \omega_0}{\omega_0^2 - \omega^2} \quad ; \quad \kappa = \frac{\omega_m \omega}{\omega_0^2 - \omega^2} \qquad \mu_z = 1.0$$

$$\omega_m = \gamma 4\pi M_s \quad ; \quad \omega_0 = \gamma H_{DC} \quad .$$

For materials operated in the remanent state or in a saturated state but with zero bias field applied $\omega_0 \doteq 0$. For remanent state devices then $\mu = 1$, $\kappa = \frac{-\omega_{mr}}{\omega}$ where $\omega_{mr} = \gamma 4\pi M(\text{remanent})$. The non-reciprocal action of ferrite devices is based on differences between plus and minus states of magnetization and therefore, on the relative magnitude of the term κ. At remanence this term is, in fact, the ratio $\gamma 4\pi M_R/\text{freq}$. For reciprocal devices the effective electrical length of the ferrite is determined by its effective permeability, given by

$$\mu_{eff} = \frac{\mu^2 - \kappa^2}{\mu} \quad . \tag{3}$$

For remanent devices:

$$\mu_{eff} \doteq 1 - \kappa^2 = 1 - \left(\frac{\gamma 4\pi M_R}{\omega}\right)^2 \quad .$$

The effective permeability again varies with $\frac{\omega_m}{\omega}$.

Figure 1 is a plot of μ and κ as a function of normallized bias field ($\sigma = \frac{\omega_o}{\omega}$) and for two different values of normallized magnetization, $m = \frac{\omega_m}{\omega}$. Non-reciprocal phase shift requires κ values significantly different from 0.0 and μ_{eff} values significantly different from 1.0.

Large values of κ can be reallized by increasing $\gamma 4\pi M_s$/freq. or by increasing the applied field. The normal operating point for remanent phase shifters is point A, zero bias field. This is also the operating point for most broad-band circulators. Points B and C indicate field values at which $\mu = \kappa$ and $\mu_{eff} = 0$. From these points to the resonant region ($\sigma = 1.0$) μ_{eff} becomes negative, and the electromagnetic waves are excluded from the ferrite. Near $\sigma = 1.0$, resonance loss prohibits phaser operation. Clearly, as one increases the d.c. field κ increases and μ decreases from 1.0. Many high power circulators and phase shifters operate biased above resonance. ($\sigma > 1.0$) Thus, two approaches are available for increasing the non-reciprocal activity of a ferrite ($\frac{\kappa}{\mu}$) or the controllable electrical length of a ferrite (μ_{eff}): a.) increasing the saturation magnetization, or b.) increasing the applied bias. These two approaches to the realization of suitable material characteristics for millimeter wave devices will be discussed below.

High Saturation Magnetization. For millimeter wave devices the desirability of having available materials with high saturation magnetization is obvious. However, in magnetic insulators, all ferrimagnetic materials, maximum values of room temperature saturation magnetization are about 5500 gauss for a variety of microwave ferrites. This limit seems fundamental for presently known crystal structures for reasons outlined below.

All ferrites are magnetic oxides. Superexchange is responsible for supporting the spontaneous magnetization, and this coupling results in anti-parallel (or nearly so) alignment of the moments of nearest magnetic neighbors. As a result the magnetic ions of each unit cell of the spinel structure can be assigned to eight

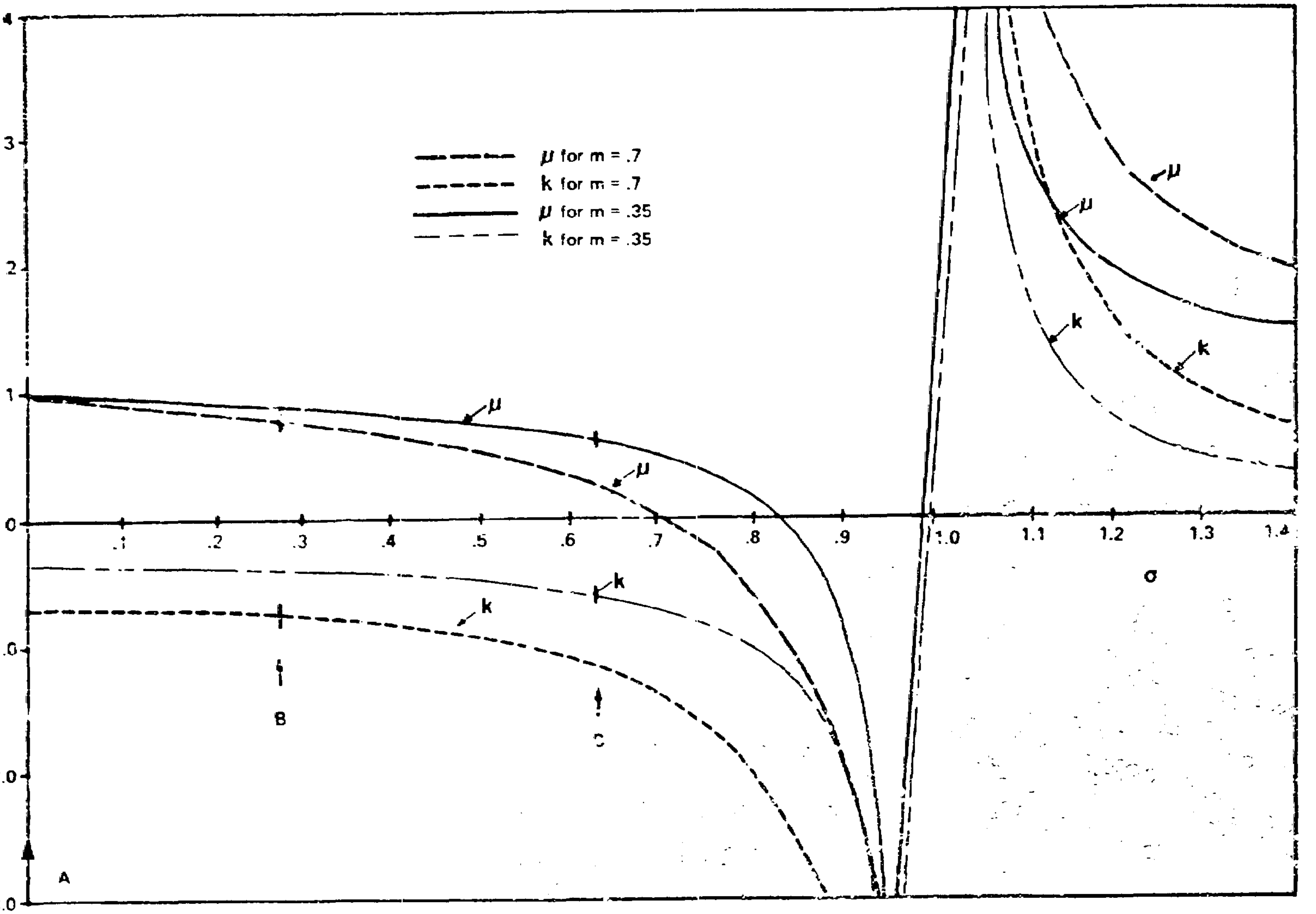

Figure 1. μ and k as a function of normalized biasfield, $\sigma = \gamma H_0/\omega$.

A sites and sixteen B sites, those in the garnet structure to sixteen a sites, twenty-four c sites, and twenty-four d sites. The total saturation magnetization, M_T, is the result of the anti-parallel alignment of magnetic moments on these various sites.

$$\text{In spinels: } M_T = 16\ M_B - 8\ M_A$$
$$\text{In garnets: } M_T = 24M_d - 16M_a \quad 24M_c$$

The spinel structure clearly has a less compensated magnetization and an inherently larger achievable saturation magnetization.

To maximize the saturation magnetization one might first imagine using the most highly magnetic ions available, Fe^{+3}, Mn^{+2} (unbalanced spin of 5/2) in the spinels. This yields a zero degree Kelvin saturation magnetization of 7,000 gauss for Mn^{+2} and a room temperature value of 5000 gauss. (Its Curie temperature is 600° K.)

By replacing magnetic ions on A sites by non-magnetic ions (e.g. Zn^{+2}) the A-sublattice magnetization can be reduced, with a consequent increase in M_T. Unfortunately this also lowers the exchange field (as originally described by Neel[1]) that supports the spontaneous magnetization. The Curie temperature is thus decreased, and with increasing substitution the room temperature saturation magnetization will ultimately decrease. This was studied many years ago in the NiZn and MnZn series. Data shown in Figure 2 illustrate those trends for MnZn ferrite.

The partial substitution of Zn provides the largest currently available values of room temperature saturation magnetization, about 5500 gauss in both the LiZn and NiZn ferrites.

Although garnet materials can contain the physically larger and more magnetic rare earths (e.g. Gd^{+3} with a spin unbalance of 7/2), the more complex sublattice structures and the higher degree of compensation makes them apparently incapable of large saturation magnetization values.

The structure of the hexagonal ferrites is composed of blocks that are spinel "S" layers interleaved with unique, barium containing, "R" layers, or more complex "T" layers. The barium ferrite structure is shown in Figure 3. (The S, R, and T terminology is that of Smit and Wijn[2].) The largest net magnetization occurs in the spinel "S" blocks; R and T layers act to dilute the saturation magnetization. Thus hexagonal ferrites have saturation magnetization values at best equal to

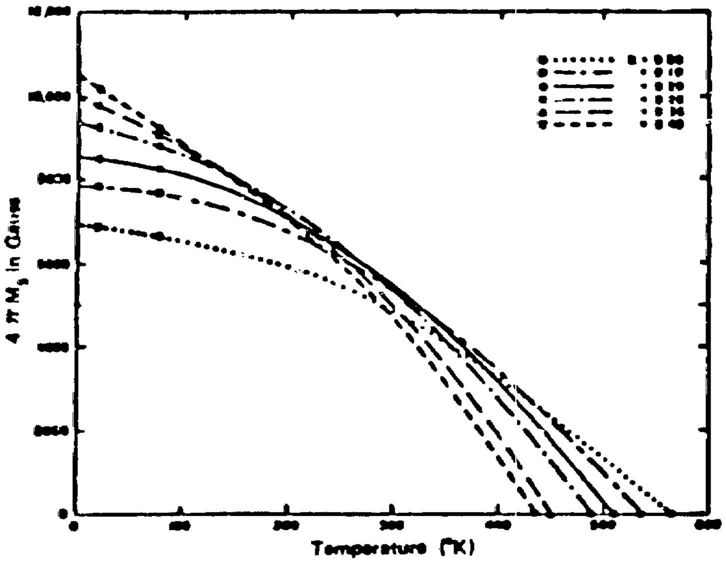

Figure 2. Saturation Magnetization of Polycrystalline $Mn_{1-x}Zn_xO_4$ as a Function of Temperature for $0 \leq x \leq 0.40$ (From Handbook of Microwave Ferrite Materials, W. H. Von Aulock, Academic Press.)

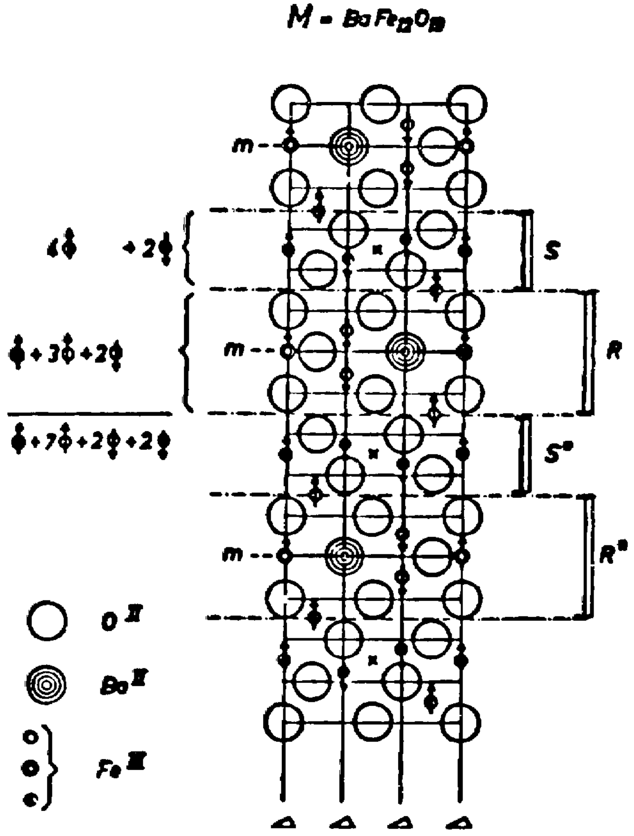

Figure 3. Unit Cell Structure of the Barium Ferrite (BaM) Cross-section of the Magnetoplumbite Structure M, with the C Axis Vertical. The Arrows Indicate the Spin Orientations. (From Ferrites, J. Smit and H.P.J. Wijn: John Wiley.)

those of the spinels.

At present, there is no apparent solution to the quest for higher saturation magnetization. Existing ferrimagnetic crystal structures seem to offer possibilities for only marginal improvements. The bottom line seems to be that there is little hope of greatly increasing the range of saturation magnetization available in ferrite materials.

Increased D.C. Field Values. The use of an externally applied dc field to increase, or control, the values of μ and κ, as indicated by equation 2 and Figure 1 has long been a feature of many microwave ferrite devices. Resonance isolators traditionally employ a dc field approximately given by $\frac{\omega}{\gamma}$; above resonance circulators and phase shifters also employ large dc fields in their operation. The requirement of having an externally applied field is in many cases unattractive in system performance because of excessive power requirements. Moreover, at millimeter wave frequencies the field specified by $\frac{\omega}{\gamma}$ (30,000 oe for 90 GHz) may exceed realizable flux densities. In anisotropic ferrite materials an internal field, the anisotropy field, can be used to replace an externally applied field. There is indeed no "free lunch", and the price of this internal field is grain alignment in the ceramic.

The traditional spinel and garnet materials are fabricated in ceramic, unoriented form and are entirely isotropic in their performance. They may also be prepared in single crystal form, in which case the individual crystals have a small degree of anisotropy. This anisotropy is manifest in the fabrication of YIG filters where some degree of crystal orientation is employed. But today, aside from the YIG filter area, virtually all ferrite devices employ polycrystalline materials.

The hexagonal class of ferrites is commonly prepared in oriented grain form. The hexagonal crystal structure has a high degree of both physical and magnetic anisotropy. The individual crystallites form in platelet geometries and can be oriented in the pressing stage so that the c-axis (short axis of platelets) of individual crystallites are all aligned parallel, thus defining a unique orientation in the ceramic.

Hexagonal ferrites appear in two basic forms, uniaxial and planar. In a uniaxial ferrite the anisotropy energy produces a torque that aligns the magnetization along the c-axis of the unit cell of each crystallite. This produces a unique direction in the ceramic along which the "anisotropy field" acts much as would an externally applied field. This field has been used for decades in designing millimeter wave resonance isolators[3] and more recently for hexagonal millimeter wave filters.[4] The magnitude of the internal field can be controlled by ionic substitution of, for example, strontium and aluminum in the barium ferrite material ($BaFe_{12}O_{19}$). Uniaxial hexagonal materials appear ill-suited for use in digital phase shifters since the remanent magnetization must be varied to control the phase shift. The large uniaxial anisotropy field favors a fixed magnetization, as in permanent magnets. While flux reversal through domain wall motion is possible in multi-domain particles and in single crystals, domain wall motion is slow and coercive fields large, 50 to 75 oe for large crystals of uniaxial compounds. For millimeter wave devices in which the volume of the material is quite small, it may be the case that the total switching energy of a toroid is at a tolerable level even though the coercive field is in the range of 50 to 70 oe.

Planar ferrites have an anisotropy energy that is minimized when the magnetization of each unit cell lies in the plane perpendicular to the c-axis. Within that "easy" plane, little or no orientational dependence is shown, and the magnetization can be easily switched in this plane. It seems reasonable to take advantage of the natural phenomena of easy orientation in the plane in applications where switching of the magnetization is needed. One concern in using oriented planar materials in remanent devices is that in plane anisotropy may be so small as to make remanence ratios quite small.

The elements of the permeability tensor for grain oriented hexagonal ferrites with no applied field are given as:[5]

$$\text{Uniaxial:} \quad \mu = 1 + \frac{\omega_m \omega_A}{\omega_A^2 - \omega^2} \quad ; \quad \kappa = \frac{\omega_m \omega}{\omega_A^2 - \omega^2} \tag{4}$$

$$\text{Planar:} \quad \mu_{xx} \doteq 1 + \frac{\omega_m \omega_A}{\omega^2} \quad ; \quad \mu_{yy} \doteq 1 \quad ; \quad \kappa \doteq \frac{-\omega_m}{\omega}$$

It can be seen that the anisotropy field of uniaxial materials enters these equations just as does an externally applied field. For planar materials the effect is more subtle. For the vertical slab geometry shown in Figure 4 an external permeability tensor can be used to relate B and H fields in the ferrite loaded waveguide in a perturbation approach. Then the permeability elements for the

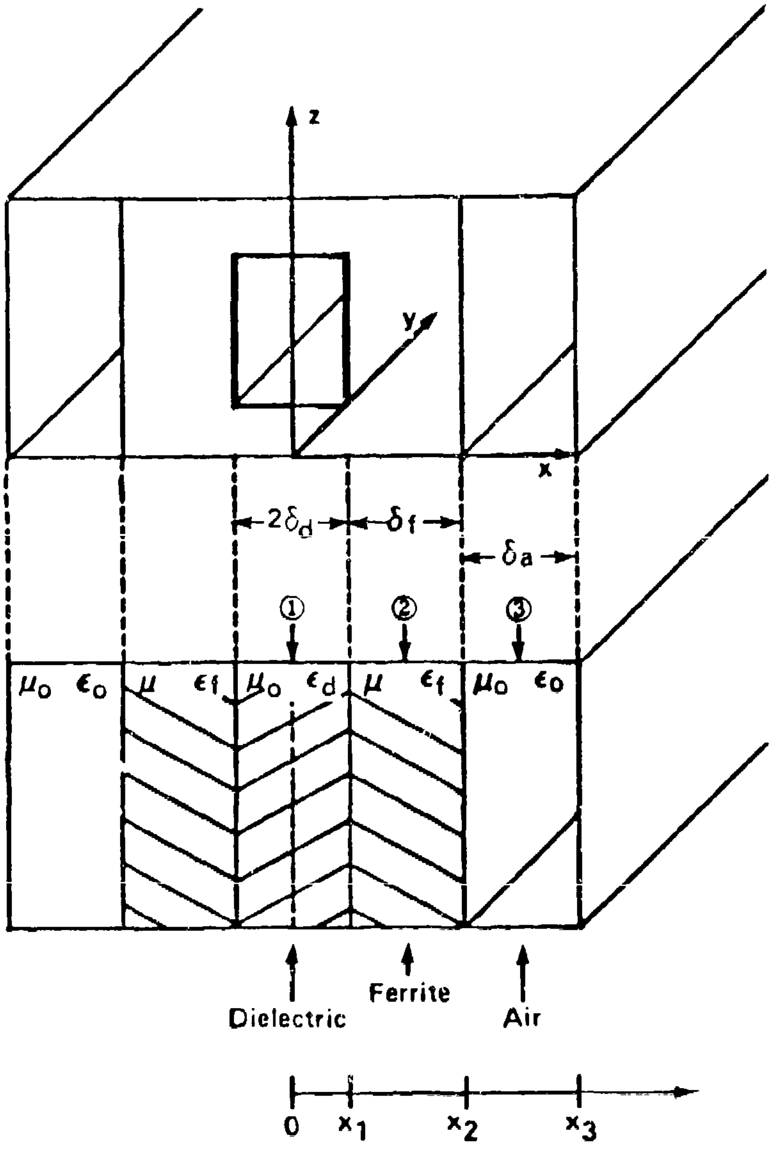

Figure 4. Rectangular Waveguide Loaded with Ferrite and Dielectric.

planar case become:

$$\mu_{xx} = 1 + \frac{\omega_m \omega_x}{\omega_x \omega_y - \omega^2} \quad ; \quad \mu_{yy} = 1 + \frac{\omega_m \omega_y}{\omega_x \omega_y - \omega^2} \qquad (5)$$

where:

$$\omega_x = \gamma[H_A + (N_y - N_z)\, 4\pi M_s]$$

$$\omega_y = \gamma[(N_x - N_z)\, 4\pi M_s] \ .$$

The effective permeability is then:

$$\mu_{eff} = \frac{\mu_{xx}\,\mu_{yy} - \kappa^2}{\mu_{yy}} \qquad (6)$$

Control of phase shift is dependent on achieving control of μ_{eff}. Note that as $\frac{\omega_m}{\omega}$ decreases, so also does κ, while μ_{xx}, μ_{yy}, and μ_{eff} approach 1.0. The decrease in κ (or $\frac{\omega_m}{\omega}$) with increasing operating frequency is a fundamental problem at millimeter waves.

Non-reciprocal action in a waveguide structure is proportional to $\frac{\kappa}{\mu}$, which in the present case would be represented by $\frac{\kappa}{\mu_{xx}}$.

In order to compare the relative merits of different materials in phase shifter applications, one can use the external susceptibilities developed above. In the remanent state the externally applied d.c. field is approximately zero ($H_o \doteq 0$). For a thin walled toroid the appropriate demagnetizing factors vary with toroid dimensions, but reasonable estimates might be $N_x = .8$, $N_y = .2$, $N_z = 0$.

These values are used in Equations 5 and 6 to compute the effective permeability as a function of planar anisotropy field H_A. Figure 5 shows the results of this calculation for a saturation magnetization of 2.8×10^5 A/m ($4\pi M_s = 3500$ g.) with operating frequency as the parameter. Points on the ordinate correspond to results for an isotropic ferrite (where $H_A = 0$).

These results show that the anisotropy torque affects μ_{eff} as does an increase in $4\pi M_s$. At 30 GHz an anisotropy field of 8×10^5 A/m (10 Koe.) and a saturation magnetization of 2.8×10^5 A/m ($4\pi M_s = 3500$ g.) yield a μ_{eff} comparable to that hypothetically obtained from an isotropic ferrite with a saturation magnetization of 6.5×10^5 A/m ($4\pi M_s = 8000$ g.). Values of saturation magnetization greater than 4.4×10^5 A/m ($4\pi M_s = 5500$) are not obtainable in microwave ferrites at

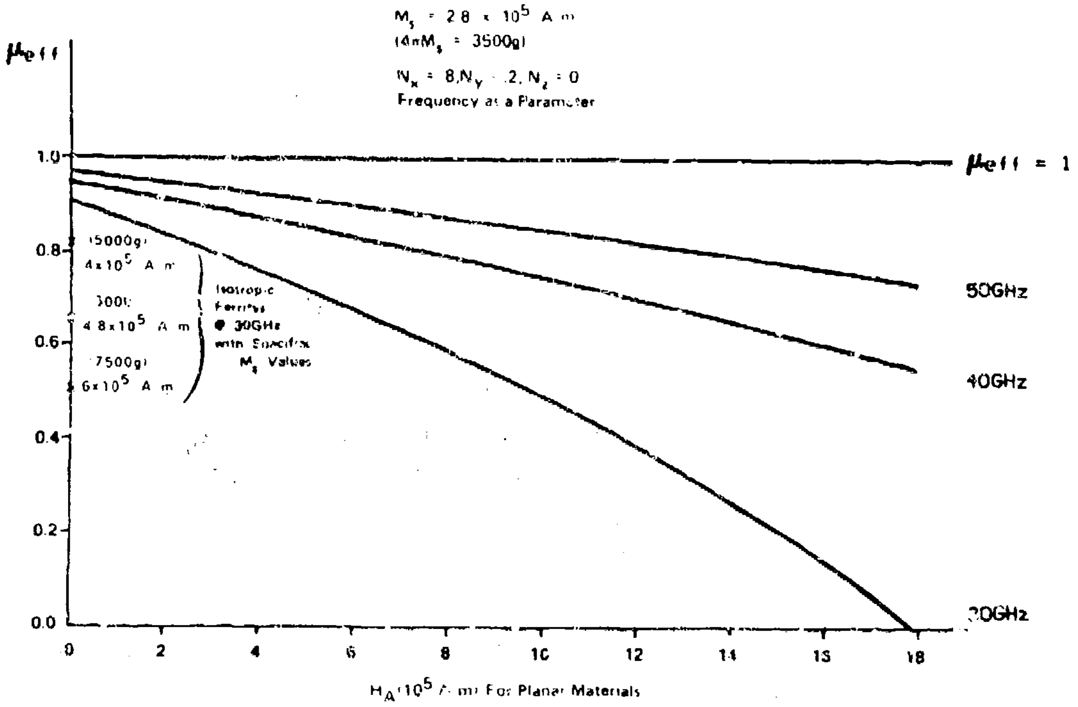

Figure 5. Effective Permeability as a Function of Planar Anisotropy Field.

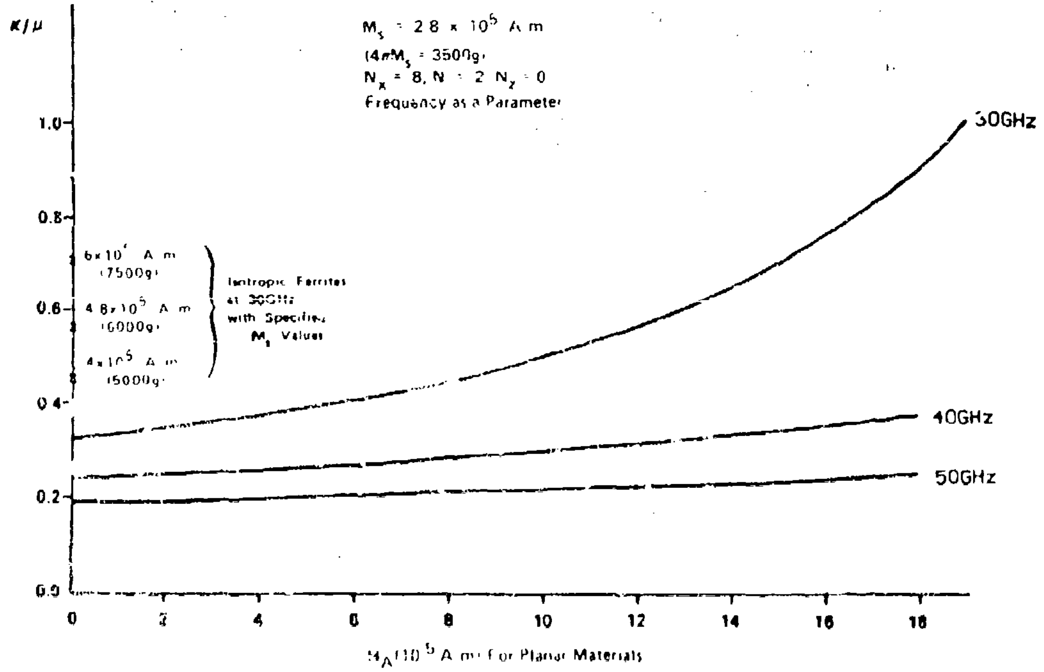

Figure 6. κ/μ as a Function of Planar Anisotropy Field.

room temperature.

Figure 6 shows computed curves for κ/μ as a function of planar anisotropy field. This ratio is the key to non-reciprocal action. The effect of planar anisotropy energy on κ/μ is also like that obtained by increasing saturation magnetization. A planar anisotropy of 8×10^5 A/m (10 Koe.) in a material with saturation magnetization of 2.8×10^5 A/m (3500 g.) causes κ/μ to increase by 54% at a frequency of 30 GHz over that of an isotropic ferrite.

The transverse operator method has also been used to study the effects of planar anisotropy on the propagation constants of a rectangular waveguide loaded with ferrite.[6] Again the lossless case was studied as an approximation to off-resonance operation. The geometry of Figure 4 was used to model a single rectangular toroid in a waveguide. Results of sample calculations are tabulated in Table I. The planar anisotropy field almost triples the computed differential phase shift. These results again indicate that the planar anisotropy increases differential phase shift as an increase in magnetization does. It should be noted that this material is still far removed from ferromagnetic resonance and its attendant losses.

Patton[7] has shown that low field loss and zero permeability (propagation cut-off) both occur for:

Uniaxial: $\omega_A = \omega - \omega_m$

Planar: $A = \dfrac{\omega^2 - \omega_m^2}{\omega_m^2}$

These values set upper limits on allowable anisotropy fields.

Available Materials

Spinels

At this time the materials most widely used for millimeter wave devices, are the lithium zinc ferrites of the spinel crystal structure with saturation magnetizations of approximately 5,000 gauss. Nickel zinc materials having approximately the same saturation magnetization, are also available and occasionally used. However, the nickel zinc materials have a higher coercive force and a somewhat higher inherent magnetic loss than do the lithium zinc compounds.

Table 1. Computed Differential Phase Shift for Various Frequencies and Material Properties

Freq. (GHz)	$4\pi M$ (gauss)	H_{AN} (oe.)	$\Delta\phi$ (deg/cm-GHz)
35	3,500	12,000	11.14
		0	4.67
	5,500	0	7.6
50	3,500	12,000	6.22
		0	3.23
	5,500	0	5.17

$\delta_a = 0.13\ \lambda_o$; $\delta_d = 0.04\ \lambda_o$; $\delta_f = 0.08\ \lambda_o$; $\varepsilon_f = \varepsilon_d = 16$.

Table 2. Hexagonal Ferrites

Material	Anisotropy	H_A (oe)	$4\pi M_s$ (gauss)	ε_r	Tc (°C)
SrM	Uniaxial	19,900	4,500	23	480
$SrAl_{\delta}M$ δ = 0 to 1.3	Uniaxial	19,900 to 45,000	4,500 to 1,000	23 to 125.	480 to 320
Ba M	Uniaxial	17,000	4,800	18	450
NiCo W δ = 0 to 0.4	Uniaxial	12,400 to 4,000	3,600 to 3,000	15 to 12.6	530
CoZn W	Planar	2,200	4,530	18	450
CuZnY	Planar	11,000	2,300	20	230
Zn_2 Y	Planar	14,000	2,200	14	250
Co_2 Y	Planar	28,000	2,300	-	340

In addition to higher $4\pi M_s$ levels other material characteristics could bear improvement. The microstructure of lithium zinc ferrites currently presents something of a problem. BiO fluxing agent, added to promote sintering at lower temperatures, tends to collect unevenly at grain boundaries and to produce explosive grain growth. This grain growth may produce rather large macropores of such a size as to be comparable to the final wall dimensions of a toroid intended for millimeter wave devices. The surfaces of lithium zinc ferrites are also frequently subject to considerable pitting in the machining process, also as a result of non-uniformities in grain growth and grain boundary characteristics. This pitting is a serious limitation when designing devices to a millimeter wave scale.

At millimeter wave frequencies the ferrite ceramic microstructure is of increased importance because of the much smaller tolerances allowable at the higher frequencies. In many instances, economical device fabrication schemes involve the metallization of the ferrite surface to form a waveguide enclosure or conducting plane. Because conducting loss is increased when the conductivity of the metal is decreased, or when the surface roughness becomes comparable to a skin depth, it is all the more important at millimeter wave frequencies to have a carefully controlled microstructure.

The microstructure of nickel zinc ferrites is considerably superior at this time to that of lithium zinc ferrites, but the higher coercive force and higher intrinsic magnetic loss arising from the presence of nickel ions seems to be an inherent difficulty. Thus of the candidate spinel compositions, the lithium zinc ferrite seems the outstanding choice albeit, considerable work needs to be done in improving its microstructure for ultimate millimeter wave applications.

Hexagonal Ferrites

Uniaxial - The barium or strontium M-compounds with partial substitution of Al to control $4\pi M_s$, and hence anisotropy field, offers a good selection of material properties (see Table 2). Unfortunately the small volume market makes this material unattractive to most traditional ferrite suppliers, and their availability is quite limited.

Planar - No planar hexagonal materials are currently available. These materials were subject to some study in the 1960's, but are not commercially prepared today. Table 2 lists some planar materials with typical characteristics as determined from earlier studies.

Single Crystals

Single crystals of all types of ferrites offer the possibility of greatly improved microstructure, and the small size requirements of millimeter wave devices seems compatible with the developing technology of single crystal growth. Both flux grown and liquid phase epitaxy grown single crystals of ferrites and garnets can be prepared. Hexagonal materials have also been grown from a flux in both uniaxial and planar forms. Single crystal materials seem most readily applied in those cases where a relatively small volume of ferrite is needed as in resonant isolator applications, where the material is biased to ferromagnetic resonance and is in a highly active state, thus requiring little volume interaction in order to control the flow of millimeter wave signals. Another logical choice for single crystal applications is in circulators, where the material acts as a resonator itself and thus has high concentrations of rf fields in the ferrite medium. Phase shifter applications involve rather weak and extended interactions of the rf fields with the magnetic material. The material is biased normally well below resonance where μ is not greatly different from 1.0, and where κ is small. As a result, the amount of control that can be realized is relatively weak. In order to achieve 360° of phase shift, a total insertion phase of something over 2,000 degrees must be accommodated. This means that the total volume of ferrite necessary to achieve the desired function (differential phase shift of 360 degrees) is relatively large.

Structures

Phase shift is achieved by controlling the permeability, and hence electrical length, of the ferrite loaded propagation structure. When reasonably high ratios of ω_m/ω can be realized, 360° of controllable phase shift can be obtained in a device whose overall electrical length is about 1,500°. At millimeter wave frequencies where ω_m/ω values are reduced, the insertion phase (overall electrical length) will be considerably increased. Since dielectric, magnetic and most importantly ohmic loss increases with electrical length, the figure of merit (differential phase shift per unit loss) can be expected to decrease at millimeter waves.

Best figures of merit have historically been achieved in waveguide phasers. This is in large measure due to the low ohmic loss of such devices. Waveguide phase shifters have been constructed for non-reciprocal performance in single or dual toroid versions generally with a dielectric rib down the center of the waveguide (see Figure 6). Reciprocal ferrite phase shifters are usually based on the dual mode principle and involve a round or rectangular rod of ferrite metallized to form a ferrite filled waveguide; the magnetic path is closed external to the waveguide structure. Both of these basic reciprocal and non-reciprocal phaser designs involve mechanical tolerances that become difficult and expensive to realize at the higher frequencies. While millimeter wave reciprocal and non-reciprocal phasers have been constructed up to 90 GHz, the prospect of any mass production of such items is quite poor. A number of alternate waveguiding structures have been explored for millimeter wave devices, these include microstrip, slot line, fin line, and dielectric waveguides. Because of its inherent compatibility with integrated circuit techniques, microstrip line has had something of a popular edge.

Both microstrip line and slot line seem to suffer from a potential difficulty with ohmic loss. In each of these cases the concentration of magnetic fields in the vicinity of a small conductor with rather sharply defined edges leads to an expectation of increased ohmic loss.

Dielectric waveguide and its close relative, image guide, seem to have advantages in terms of ohmic loss and may offer some promise for millimeter wave phasers. Such open structures do, however, suffer from radiation problems at discontinuities and bends.

As a result of these considerations one would deduce that waveguide phasers probably represent an optimum performance although at a cost of fabrication that appears to be excessive. The challenge of millimeter phasers remains for both ferrite materials designer and for microwave structure engineer: development of low cost, high performance phasers.

References

1. L. Neel, Ann. de Phys. 3, pp. 137-198 (1948).
2. J. Smit and H. P. J. Wijn, Ferrites, John Wiley and Sons, New York, NY 1959, p. 177ff.
3. D. R. Taft, G. R. Harrison, and L. R. Hodges, Jr., "Millimeter Resonance Isolators Utilizing Hexagonal Ferrites", IRE Trans. MTT-11, Sept. 1963, pp. 346-350.
4. Dean Nicholson, "A High Performance Hexagonal Ferrite Tunable Bandpass Filter for the 40-60 GHz Region", 1985 IEEE MTT-S International Microwave Symposium Digest, p. 229.
5. I. Bady, "Ferrites with Planar Anisotropy at Microwave Frequencies", T-MTT, Vol. 9, No. 1, January 1961, pp. 52-62.
6. Stephen B. Thompson and G. P. Rodrigue, "The Application of Planar Anisotropy to Millimeter Wave Ferrite Phase Shifters", IEEE Trans. MTT, November 1985.
7. C. E. Patton, "Hexagonal Ferrite Materials for Phase Shifter Application at Millimeter Wave Frequencies", private communication.

RAPID IN-FLIGHT PHASE ALIGNMENT OF AN ELECTRONICALLY PHASE-SCANNED ANTENNA ARRAY

Harold Shnitkin

Norden Systems, Inc., Norwalk, CT. 06856

ABSTRACT

Low sidelobe performance of a phased array antenna requires tight phase tolerances at the antenna aperture. To maintain these tight tolerances throughout the life of an electronically phased array requires periodic retesting and phase correcting of the array elements to compensate for phase errors arising from aging, deformation and component replacement. To accomplish such phase correcting without returning the antenna to an antenna test site or calibration laboratory, a self-test/phase-correcting method which can be performed rapidly while the antenna is mounted on a moving vehicle has been invented.

This "in-flight" phase alignment technique exercises the electronic phasers of the antenna array, while injecting RF into the antenna through a special "BITE" coupler system. The alignment procedure calls for phase and amplitude measurements at the antenna terminals which, after subsequent computations, generate the required phase and amplitude corrections for all array elements. After these are applied to the antenna via a beam steering computer, a low sidelobe radiation pattern will result. A detailed description of the alignment technique is presented, followed by test results obtained with an electronically phased array antenna.

BACKGROUND

When a phased array antenna is first assembled it usually exhibits considerable phase and amplitude errors due to component, manufacturing and assembly tolerances resulting in a low gain and high sidelobe performance. It is customary to measure the radiated phase and amplitude of every element of the array, determine its deviation from the design value and proceed to correct for these errors by making either mechanical or electrical adjustments. These measurements are laborious, require access to the antenna radiating surface, and must be performed with laboratory type of precision to yield a low sidelobe antenna radiation pattern. Thus a technique to perform these measurements more quickly, without field probing the aperture and without restrictions upon the surrounding environment would save considerable expense in aligning a phased array for low sidelobes and monitoring its alignment status as well as performing phase corrections periodically while mounted to a moving vehicle. Thus aperture phase may be readily compensated for the effects of aging, distortion and component replacement without returning the antenna to a repair depot. In addition, the success of the antenna performance mission can be guaranteed just prior to the mission time or, if necessary, altered or aborted.

It should be stated at the outset that the precision of an aperture phase-probe, namely about 1.5 degrees RMS, is not quite obtainable with the automated electronic technique; the latter can be counted on to achieve 3 degrees RMS aperture phase precision. A portion of the additional error is due to less precise measuring accuracy, the remainder to the exclusion of the mutual coupling effect between the array elements.

To assure that an antenna possesses very low sidelobes usually demands first a coarse phase alignment, followed by a second, more accurate phase alignment. By performing the first alignment using the automated electronic method and the second alignment using the precision aperture phase-probe method about half the original phase alignment time can be saved.

PREVIOUS WORK

A phase/amplitude aperture measuring technique of an electronically phased array not requiring access to the antenna radiating surface was described by Dan Davis in the February 1978 issue of the Microwave Journal. Mr. Davis' method required that the antenna be installed on a precision rotating positioner while receiving a far-field radiated signal. Antenna phase and amplitude values received at the antenna input port are accurately measured for N prescribed angular positions of the rotating antenna positioner, where N represents the number of radiating elements in the antenna array. Subsequent computations by means of a relatively simple algorithm generates the radiated phase and amplitude values of every element of the antenna array. Addition of the negated values of the measured degrees of phase and dB's of amplitude deviation to each element excitation voltage results in a optimum maximum gain and minimum sidelobe antenna.

The automated/electronic "in-flight" aperture alignment technique departs from Mr. Davis' approach by eliminating both the requirement for a rotating positioner as well as for a far-field radiated signal, but retaining his phase and amplitude measurement at the antenna input port as well as his algorithm. The "in-flight" technique is intended for one-dimensional electronically phased arrays and substitutes electronic scanning for the rotating positioner and a signal-inject coupler system for the radiating signal source. Thus it is faster and can be performed while the antenna is in motion without an external cooperative transmission.

DESCRIPTION OF TECHNIQUE

A travelling wave array feed is added to the one-dimensional electronically scanned antenna with minimal perturbation. As shown in figure 1 a transmission line, possessing a matched termination, traverses along the backside of the radiating aperture. Equally spaced identical couplers of about -50 dB coupling values are installed between the terminated transmission line and each antenna radiating element. Thus the transmission line with the equally spaced couplers excites the radiating elements with approximately equal amplitude and a linear phase taper. The former is assured by the low coupling value, since even for a thousand element array the excitation level varies only a few tenths of a dB between the first and the last element. The latter is due to the equal spacing and resulting uniform phase increments. A convenient implementation might be a waveguide transmission line with a series of small coupling holes. This arrangement would cause a signal injected into the travelling wave feed to simulate a far-field signal from an angular direction θ, measured from the aperture normal, where sin θ = (free space wavelength)/(guide wave length). For practical cases θ is about 45 degrees.

The purpose of the travelling wave feed, also known as a BITE coupler system, is to simulate far-field signal reception without either an antenna range or a near-field probe in front of the aperture. It is further possible to vary the angle-of-arrival of the simulated far-field transmission by means of the electronic phasers. For each angle-of-arrival a particular set of uniformly incremented phaser settings can be computed.

The actual alignment sequence starts with the computation of a preferred set of angle-of-arrivals so that a simplified algorithm may be used later for the computation of element voltages. From this set of angles a set of phaser setting for all radiating elements and all angles will be computed. The test procedure calls for stepping all phasers through these computed phase settings to simulate N sequential angles-of-arrival at the aperture for an array of N radiator elements. (see Fig. 2) In essence, the phasers provide electronic scan through N scan angles, of the BITE coupler injected signal. During this electronic scan mode an RF receiver measures phase and amplitude of reception for each scan position and passes this information to the Element Voltage Computer via A/D converters and a computer interface unit. There the algorithm to compute element voltages and phases is applied and the results stored in the element voltage correction memory. Amplitude values are compared to the designed aperture illumination voltages with resulting dB error fed to the printer. Phase values are compared to a constant zero value and the resulting errors fed to the printer as well as to the beam steering computer. The latter causes these values of computed element phase to be subtracted from the commanded phase value to each phaser. This subtraction intends to compensate the measured phase error by means of modified phaser settings.

The entire cycle of electronic scan, phase/amplitude measurement, element voltage compensation and phase error compensation in the beam steering computer is repeated several times to asymptotically arrive at a compensated uniformly phased aperture. Depending upon computer speed the entire process requires only a few seconds.

At the end of this process the quality of the alignment may be displayed via the printer. For example, all element phase and amplitude errors or the measured electronic radiation patterns may be outputted. A simpler output would give mean and average sidelobe level as well as the location and error values for only those elements exceeding a predetermined threshold. Thus the antenna pattern quality may be quickly assessed and any faulty elements quickly identified.

It should be noted that prior to this alignment procedure a check on the functioning of each phaser must be performed since this procedure depends upon their proper functioning. Should any faulty phasers be found, the various algorithms must be modified to exclude them.

One technique to accomplish faulty phaser locations is to exercise one phaser at a time by incrementing its phase command uniformly from 0° to 360° while injecting a test signal into the BITE coupler system and observing the received voltage vector. This technique works best if those phasers not being diagnosed are set to random phase commands. This causes the modulation of the receiver voltage to be discernible, resulting in a uniformly rotating modulation vector for a properly operating electronic phaser.

THEORY OF OPERATION

For a linear array of N elements a set of N complex algebraic equations can be written, each representing the far-field radiated voltage in terms of the individual element's voltage excitation. This set of equations can be solved for element voltage excitations in terms of the far-field radiated voltages by matrix inversion. The first set of equations is obtained from measured received voltages at the antenna input port when illuminated by a constant magnitude wavefront emanating from a direction θ_m, measured from the array normal, where m is stepped from 1 to N.

For simplicity the following rigorous analysis assumes the antenna to be in the transmitting mode. For an array of even number of elements, N, spaced S distance apart, the far-field transmitted voltage in direction θ_m is

$$E\ (\theta_m) = \sum_{k=1}^{N} V_k \cdot \exp[j(N/2+0.5-K)(2\pi S/\lambda)\sin\theta_m] \qquad (1)$$

where both, $E(\theta_m)$ or V_k, the element excitation voltage, are complex quantities. In order to simplify the solution of V_k, the values of θ_m are chosen as

$$\sin\theta_m = (\lambda/2ns)(N + 1 - 2\ m) \text{ , where m is stepped from 1 to N.} \qquad (2)$$

resulting in N beamwidth increments between $\theta_m = -90°$ and $\theta_m = +90°$.

Substituting equation (2) into equation (1), yields

$$E(\theta_m) = \sum_{k=1}^{N} V_k \cdot \exp[j(N/2 + 0.5-k)(2\pi/N)(N/2 + 0.5 - m)] \qquad (3)$$

where m is stepped from 1 to N.

For a set of N equations the exponent term becomes a matrix which is symmetrical about both diagonals. Because of this symmetry between the indices K and m, the inverted matrix is the complex conjugate of the matrix of equation (3) multiplied by a constant. Since only relative values of V_k are of interest, this constant has been omitted, yielding:

$$V_k = \sum_{m=1}^{N} E(\theta_m) \cdot \exp[-j(N/2 + 0.5 - k)(2\pi/N)(N/2 + 0.5 - m)] \qquad (4)$$

The similarity of equation (3) and (4) is analogous to a discrete Fourier Transform, which if performed twice yields the original values of the variable. This appears appropriate since a far-field radiation pattern is the Fourier Transform of the aperture distribution.

To simulate a uniform wavefront arriving at an angle θ_m, by means of the BITE coupler system, the K^{th} array phaser must be commanded to

$$\phi_k = (2\pi k)(S/\lambda)(\sin\theta_m - \lambda/\lambda_g) \qquad (5)$$

where S is the element spacing and λ_g the wavelength in the BITE coupler waveguide.

These values of ϕ_k are compensated for the travelling wave feed phase taper by the subtraction of the λ/λ_g term.

Thus by commanding the phasers to ϕ_k for all values of K from 1 to N, as per equation (5), measuring E (θ_m) at the antenna receiver port for all values of m from 1 to N, and substituting the measured E (θ_m) values into equation (4), all element voltage excitations can be computed.

TEST RESULTS

The in-flight phase alignment technique was verified on a particular 36 horn linear array antenna. Array element spacing was 0.507 wavelengths, and λ/λ_g in the BITE coupler system was 0.734. An HP-9825 computer with specially designed address/command interface circuitry was used to command a set of 36 ferrite phase shifters. An HP-8409C network analyzer system, which contains the above mentioned HP9825 computer, was used to perform the antenna receiver port measurements of $E(\theta_m)$, compute the element voltages, V_K, compute, store, and apply element phase corrections, and print the results. The system configuration of figure 1 as well as the computation flow chart of figure 2 were followed.

The resulting phase alignment performance is demonstrated by the computer print-out shown in figures 3 after just one alignment sequence, and in figure [illegible] five iterative alignment sequences.

Both [illegible]es give the electronic scan angle, θ_m, in degrees in column 1 and measured received voltages at the antenna input port in columns 2 and 3 for array element number, K, in column 4. Column 5 shows the calibration phase correction stored from the last alignment sequence, while columns 6 and 7 give the computed element power, both as relative dB value and as deviation from designed illumination. Finally column 8 lists the computed element voltage phases. Columns 1 and 2 also demonstrate antenna pattern quality, such as main beam shape and sidelobe level just prior to the last alignment sequence, while columns 7 and 8 are a measure of amplitude and phase accuracy of the aperture after the last alignment sequence.

Specifically, figure 3 indicates a poorly formed antenna beam, beam squint and high sidelobes before alignment, that is with zero calibration phase; in addition figure 3 shows several dB of computed element voltage error and random computed aperture phase values.

After five iterative alignment sequences a well aligned aperture is demonstrated in figure 4. Here the beam is well formed and points in the direction of $\theta_m = 0°$; also low sidelobes are evident (col. 2). With the phase calibration values of column 5, aperture amplitude error is mostly under one dB, while average phase error is under one degree. The exceptions to these accuracy values are found near the edges of the array where signal levels are lower and measuring accuracies are degraded by noise; however, here the effect of aperture error upon radiation pattern is minimum. A second reason for the greater errors at the array edge is the presence of mutual coupling at the actual aperture, which is unfortunately omitted when energizing the antenna via the BITE coupler. Mutual coupling effects, one should recall, are similar throughout the array except at its edges where radiating elements possess neighbors on only one side.

CONCLUSIONS

A technique permitting phase alignment of an electronically scanning array has been demonstrated without resorting to near-field probing or radiation from a test transmitter in the far-field. This technique is therefore applicable to in-flight testing. It was further demonstrated that the alignment accuracy achievable leads to a low sidelobe radiation pattern.

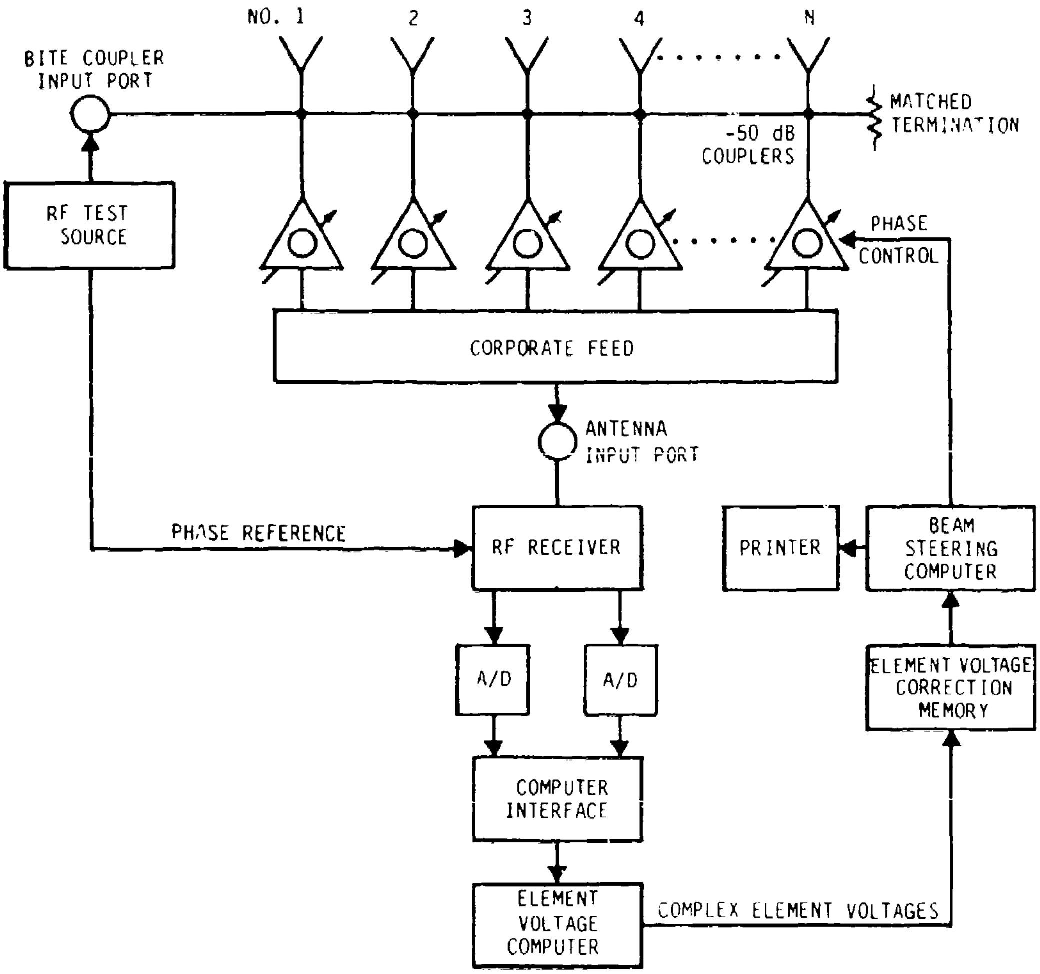

Figure 1. Block Diagram of Automated/Electronic Antenna Alignment System

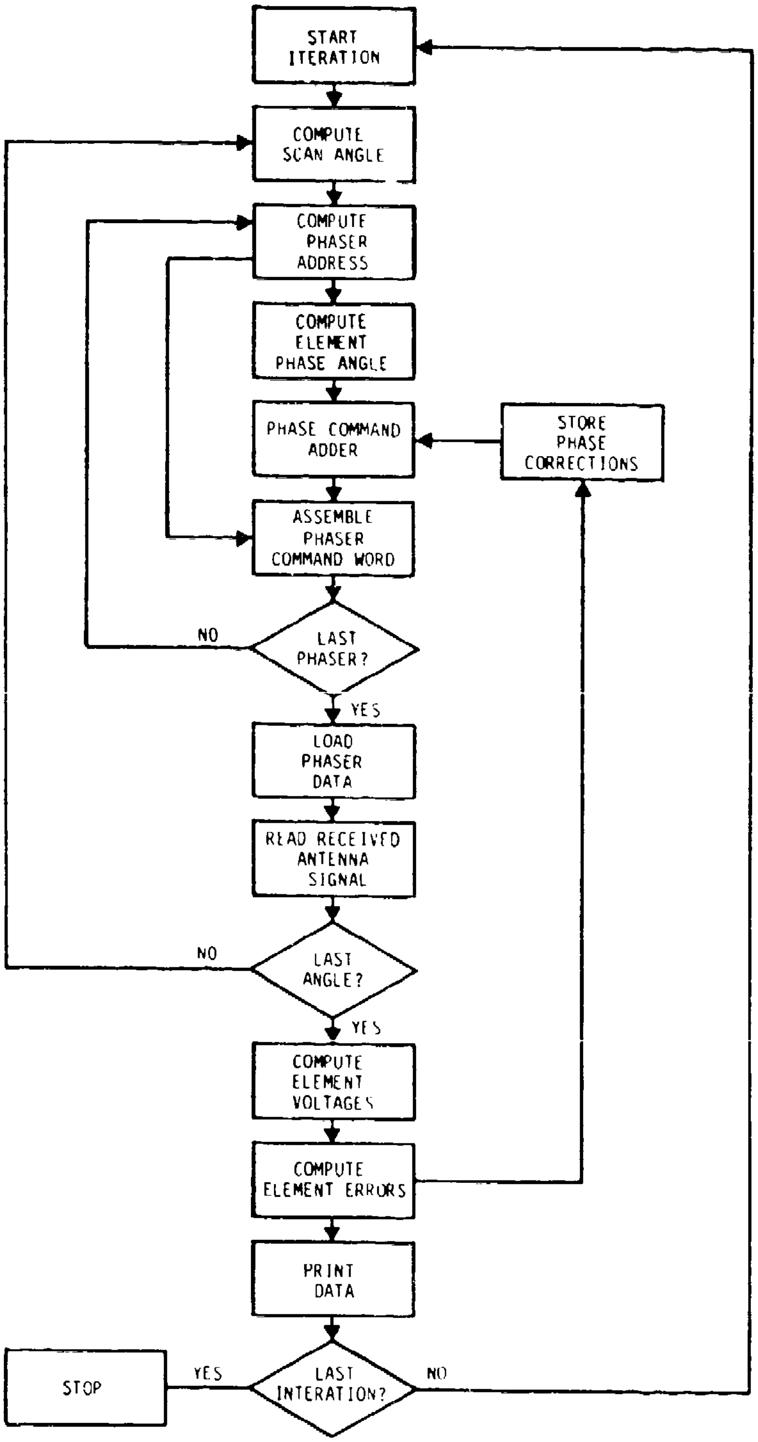

Figure 2. Computation Flow Chart for In-Flight Phase Alignment

BITE AUTO-ALIGNMENT

CYCLE #1

MEASURED PATTERN				CALCULATED APERTURE DISTRIBUTION			
SCAN ANGLE	POWER (dB)	PHASE (deg)	ELEMENT	CAL PHASE	POWER (dB)	ERROR (dB)	PHASE (deg)
-75.54	-9.6	-141.8	1	0	-20.27	+2.69	-13.0
-65.92	-12.6	-115.8	2	0	-22.81	-0.89	-150.8
-59.06	-2.1	-14.2	3	0	-23.42	-3.94	-188.4
-53.35	-0.3	-48.3	4	0	-20.78	-4.02	-234.1
-48.33	-1.5	-103.7	5	0	-11.42	+2.67	-294.3
-43.76	-6.9	-157.6	6	0	-11.01	+0.77	-264.2
-39.52	-10.5	147.7	7	0	-10.06	-0.32	-56.4
-35.52	-7.0	140.0	8	0	-7.07	+0.91	-336.2
-31.71	-13.3	-175.0	9	0	-6.38	-0.05	-119.4
-28.06	-7.4	-91.6	10	0	-4.15	+0.93	-321.7
-24.52	-7.5	-56.2	11	0	-3.92	-0.01	-130.8
-21.08	-9.6	47.0	12	0	-1.65	+1.25	-62.4
-17.72	-9.7	79.5	13	0	-2.05	0.00	-210.3
-14.42	-3.0	104.5	14	0	0.74	2.10	-209.5
-11.17	-2.8	148.9	15	0	-0.44	+0.37	6.8
-7.95	-4.2	-154.4	16	0	-0.60	-0.19	-273.9
-4.76	-6.9	-145.1	17	0	-0.82	-0.69	-50.1
-1.59	-3.1	-174.6	18	0	0.00	0.00	0.0
1.59	-6.2	170.4	19	0	-1.42	-1.42	-346.6
4.76	-7.6	-171.0	20	0	0.27	-0.14	-50.6
7.95	-2.5	175.0	21	0	-0.99	-0.58	-292.4
11.17	-1.2	128.5	22	0	0.07	0.88	-1.9
14.42	-4.1	78.5	23	0	-1.71	-0.35	-239.8
17.72	-12.5	21.5	24	0	-1.63	+0.42	-260.2
21.08	-19.6	-10.8	25	0	-2.64	+0.26	-88.0
24.52	-9.7	-97.8	26	0	-3.74	+0.17	-158.7
28.06	-13.7	-111.1	27	0	-4.76	+0.32	-21.0
31.71	-10.6	136.1	28	0	-5.45	+0.98	-118.5
35.52	-5.4	150.8	29	0	-7.24	+0.74	-6.0
39.52	-9.5	-163.8	30	0	-7.87	+1.87	-53.2
43.76	-2.4	-134.5	31	0	-11.97	-0.19	-263.3
48.33	-0.8	-90.7	32	0	-12.28	+1.81	4.4
53.35	0.0	-47.6	33	0	-16.85	-0.09	-282.4
59.06	-8.9	-15.2	34	0	-25.36	-5.88	-151.6
65.92	-9.8	-144.5	35	0	-18.50	+3.42	-72.0
75.54	-10.0	-111.3	36	0	-21.53	+1.43	-55.4

Figure 3. Computer Results of 36 Element Array Phase Alignment - One Sequence

BITE AUTO-ALIGNMENT

CYCLE #5

MEASURED PATTERN				CALCULATED APERTURE DISTRIBUTION			
ELECTRONIC SCAN ANGLE	POWER (dB)	PHASE (deg)	ELEMENT	CAL PHASE	POWER (dB)	ERROR (dB)	PHASE (deg)
-75.54	-30.8	69.6	1	71	-24.70	-1.74	8.3
-65.92	-35.3	90.2	2	153	-19.93	1.99	-2.1
-59.06	-40.1	86.2	3	184	-19.91	-0.45	2.8
-53.35	-41.7	-42.2	4	236	-16.04	0.72	0.8
-48.33	-31.8	-10.7	5	314	-13.71	1.38	-0.6
-43.76	-44.1	-16.3	6	270	-10.43	1.35	0.5
-39.52	-37.1	-18.7	7	68	-7.95	1.79	-0.9
-35.52	-39.1	71.9	8	353	-7.55	0.43	0.1
-31.71	-31.1	45.9	9	121	-5.62	0.81	0.0
-28.06	-41.6	80.4	10	327	-4.25	0.83	-0.5
-24.52	-37.6	1.3	11	136	-3.32	0.59	-0.4
-21.08	-38.9	-173.3	12	67	-1.51	1.39	-0.2
-17.72	-36.3	-37.8	13	214	-0.93	1.02	-0.0
-14.42	-32.1	-31.7	14	217	0.74	2.10	-0.4
-11.17	-29.8	-8.6	15	358	-0.29	0.52	0.3
-7.95	-30.5	3.5	16	279	0.02	0.43	0.3
-4.76	-17.1	156.7	17	64	0.24	0.37	0.2
-1.59	-0.0	165.3	18	0	0.00	0.00	0.0
1.59	0.0	167.2	19	354	-1.34	-1.34	-0.6
4.76	-16.9	175.4	20	57	0.53	0.66	-0.1
7.95	-30.2	-32.0	21	299	-0.33	+0.08	0.1
11.17	-29.7	-17.6	22	11	0.08	+0.73	0.2
14.42	-32.1	10.4	23	250	-1.16	+0.20	0.0
17.72	-33.7	16.7	24	264	-1.63	+0.42	0.5
21.08	-40.1	156.0	25	94	-2.05	+0.85	-0.5
24.52	-37.[illegible]	-23.0	26	164	-3.50	+0.41	-0.1
28.06	-41.3	-87.4	27	24	-5.36	-0.28	0.1
31.71	-31.8	-75.0	28	124	-5.75	+0.68	-0.1
35.52	-39.1	-94.2	29	4	-7.32	+0.66	0.7
39.52	-35.9	-8.5	30	62	-8.93	+0.81	0.9
43.76	-38.3	-18.7	31	268	-11.73	+0.05	0.4
48.33	-32.3	-14.1	32	342	-13.36	+0.73	-1.3
53.35	-40.2	3.2	33	279	-16.83	-0.07	-1.0
59.06	-47.0	-141.2	34	77	-20.20	-0.81	-1.9
65.92	-36.5	-120.3	35	55	-21.13	+0.79	3.7
75.54	-31.2	-97.3	36	11	-22.37	+0.59	2.3

Figure 4 Computer Results of 36 Element Array Phase Alignment - Five Successive Sequences

DISPLACED PHASE CENTER ANTENNA NEAR FIELD MEASUREMENTS FOR SPACE BASED RADAR APPLICATIONS*

A.J. Fenn, F.G. Willwerth, H.M. Aumann
Massachusetts Institute of Technology/Lincoln Laboratory
P.O. Box 73, Lexington, MA 02173

ABSTRACT

The displaced phase center antenna (DPCA) concept is commonly suggested for use in large space deployable phased array radar systems, for purposes of cancelling ground clutter. In the case of a planar array, the ability to perform DPCA is limited, largely, by the amplitude and phase errors produced in the transmit/receive array modules as well as in the array beamformer. A measure of the amount of clutter cancellation which can be achieved by a DPCA array, is referred to as the beam decorrelation or the displaced phase center radiation pattern similarity. To characterize such antennas requires precision measurements of the far-field radiation patterns generated by two or more independent aperture illuminations having physically separated phase centers. Due to long range requirements and mechanical considerations, direct far-field measurements may not be practical for large fragile space-deployable DPCA systems and so an alternative measurement approach is addressed.

An investigation of the use of planar near field measurements to characterize the performance of displaced phase center antennas is made. The details and description of a subscale DPCA corporate-fed phased array and near field scanner are discussed. DPCA results are quantified experimentally under a number of test conditions; scan angle, frequency, phase center displacement, and simulated module outages. It is shown that the test array beam decorrelation computed from measured near field data is in good agreement with far field measurements and theoretical predictions.

---

* This work has been sponsored by the Department of the Air Force.
The views expressed are those of the author and do not reflect the official policy or position of the U.S. Government.

1. INTRODUCTION

Space based radar (SBR) systems must naturally cope with detecting and tracking targets against the strong background clutter of the earth. With a conventional pulse doppler system, the doppler spectrum of the clutter is controlled by utilizing apertures with narrow-beam radiation patterns. In contrast, smaller phased array apertures can be realized by considering the DPCA concept. With "simultaneous beam" DPCA, clutter is cancelled rather than avoided by employing two independent receive phase centers to effectively form two co-located monostatic radars[1]. This concept is depicted in Fig. 1, where a moving target and a moving SBR DPCA platform are shown. Here, the full aperture is used for two successive pulse transmissions and on receive two overlapping portions of the aperture are used. The phase-center displacement between the receive apertures is adjusted to compensate for the platform velocity. Thus, for two pulses separated in time by one PRI (pulse repetition interval) the first reception occurs at the forward phase center and the second reception is made at the trailing phase center. During a PRI the clutter is assumed to be stationary; however, during this interval the target moves. Due to this motion, the target has a relative phase shift. There is no such phase shift from the clutter during this time. The result is that when the signals received by the two phase centers are subtracted, the clutter is significantly cancelled leaving a signal return which depends on the amount of target phase shift in the PRI. Optimizing the target return is accomplished by varying the PRI, which requires variable phase center separations. The amount of clutter cancellation achieved is limited by how well the two phase center radiation patterns are matched in amplitude and phase, primarily over the main beam.

To compute the clutter cancellation or decorrelation of two DPCA radiation patterns it is necessary to form the pattern correlation matrix

$$M = \begin{bmatrix} M_{11} & M_{12} \\ M_{21} & M_{22} \end{bmatrix} \qquad (1)$$

where

$$M_{11} = \iint \left| E_o(\theta, \phi) \right|^2 \left| E_1(\theta, \phi) \right|^2 A(\theta, \phi)\, d\theta\, d\phi \qquad (2)$$

$$M_{22} = \iint \left| E_o(\theta, \phi) \right|^2 \left| E_2(\theta, \phi) \right|^2 A(\theta, \phi)\, d\theta\, d\phi \qquad (3)$$

$$M_{12} = \iint \left| E_o(\theta, \phi) \right|^2 E_1(\theta, \phi)\, E_2^*(\theta, \phi)\, A(\theta, \phi)\, d\theta\, d\phi \qquad (4)$$

$$M_{21} = \iint \left| E_o(\theta, \phi) \right|^2 E_2(\theta, \phi)\, E_1^*(\theta, \phi)\, A(\theta, \phi)\, d\theta\, d\phi \qquad (5)$$

where (θ, ϕ) are standard sperical coordinates,

$E_O(\theta, \phi)$ is the electric field pattern of the transmitting antenna,

$E_1(\theta, \phi)$ and $E_2{}^*(\theta, \phi)$ are the electric field patterns of the two receiving antennas (* denotes conjugate),

$A(\theta, \phi)$ is a weighting function that depends on the radar waveform, the clutter model, and the geometry of the problem.

The integrals in Eqs. 2-5 are obtained by numerical integration. In this paper, we assume $A(\theta, \phi) \equiv 1$ so that the decorrelation is dependent on the antenna pattern match only. The clutter cancellation measure or beam decorrelation is given in terms of the correlation matrix elements by

$$C = 1 - \frac{\left| M_{12} \right|^2}{M_{11} M_{22}} \qquad (6)$$

The radiation patterns of a DPCA array can be measured directly on a conventional far-field antenna range. Such measurements were performed on the Multiple Antenna Surveillance Radar (MASR)[2,3]. These measurements required a precision linear positioner for establishing a common center of rotation and identical multipath for the different phase centers. For small durable arrays it is straightforward to provide one dimensional movement, but for relatively large and delicate space deployable antennas this may be difficult and impractical due to both mechanical and range length considerations. An alternate approach is to use near field antenna measurements to predict the far-field radiation pattern. This concept is illustrated in Fig. 2 for two phase centers displaced by the distance p. Array translation is avoided by shifting two independent near field probe scan planes by the same distance p. Near field measurements are rapidly becoming a conventional means for evaluating antenna performance; however, the technique does not appear to have been applied to multiple phase center arrays. This paper shows experimentally that near field DPCA measurements are practical. The paper is organized as follows: The details of a subscale SBR phased array are described in Section 2. A description of the near field scanner is given in Section 3. In Section 4, measured DPCA results are shown.

2. SUBSCALE SBR TEST ARRAY DESCRIPTION

The pertinent geometry for an SBR in low altitude orbit is shown in Fig. 3. For a downward pointed SBR platform, the maximum and minimum scan angles are approximately 60 degrees and 30 degrees, respectively. A 30-degree cone has been excluded from the scan sector, primarily due to clutter considerations at high grazing angles. In this case the phased array radiating elements are not required to have maximum gain at broadside (contrary to conventional designs), but rather a pattern minimum or null is desirable. For uniform coverage between the 30 and 60 degree cones, the choice of an omnidirectional array radiating element becomes apparent. A number of such elements have been designed [4,5,6] and tested - the simplest being a vertically polarized monopole as shown in Fig. 4.

The subscale SBR test array was chosen to have 96 radiating elements arranged in 8 rows and 12 columns with a hexagonal lattice. Two rows of passively terminated elements are used to avoid edge effects as depicted in Fig. 5. A front view of the assembled array is shown in Fig. 6. The DPCA architecture is implemented by two independent beam forming networks as shown in Fig. 7. Fig. 8 shows one of the test array modules (receive only) which consists of two channels, each containing 6-bit digital phase shifters and 7-step (0-10 dB) digital attenuators. The phasers provide beam agility while the attenuators provide the function of phase center movement. To meet a goal of 40 dB beam decorrelation, maximum rms errors of 3.0 degrees and 0.5 dB at the element level were required.

3. NEAR FIELD SCANNING SYSTEM

A vertically-oriented 5 ft. by 10 ft. planar scanner was constructed for measuring the near field of the above test array. The primary purpose of the experiment was a proof of concept for DPCA near field measurements. Since clutter cancellation depends primarly on the main beams being matched, no attempt was made to accurately predict wide-angle sidelobes. Most of the near-field scans were truncated at a level 15 to 20 dB down from the peak amplitude of the near field. Even at wide scan angles, the main beam is accurately predicted for this amount of truncation so DPCA beam similarity measurements are possible.

A block diagram of the near field scanning system is shown in Fig. 9. The probe x,y position is measured accurately with a pair of Bausch & Lomb ACU-RITE linear interferometer scales. The system is controlled with a desk-top computer.

A photograph of the test array positioned in front of the near field scanner, is shown in Fig. 10. The near field probe is a dual-polarized circular waveguide which is surrounded with absorber.

4. RESULTS

Prior to array pattern measurements the test array was calibrated by positioning the near field probe in front of each monopole element, and stepping through all phase and amplitude states of the modules. After calibration, the module rms amplitude and phase errors were less than 0.5 dB and 2.7 degrees, respectively. These errors meet the requirements for 40 dB clutter cancellation in a 96-element array.

To compute DPCA performance, two receive patterns and one transmit pattern are required. For transmit and receive patterns, a two-dimensional cosine taper with -10 dB edge illumination was used.

As a large number of array test conditions were of interest, it was desired to reduce the number of near field data samples. Since the array illumination used here is separable, a single centerline cut produces nearly the same principal plane far-field pattern as would be computed from a two-dimensional set of near field data. Centerline cuts have been demonstrated by Newell and Crawford as being useful in obtaining approximate far-field patterns[7]. All of the data which follow are derived from centerline near-field measurements at a distance 1.5 wavelengths from the test array. The sample spacing used was 0.2 wavelengths which was selected primarily to reduce errors which may occur due to multipath. The conventional near field to far field transformation with probe compensation discussed by Joy and Paris is used[8,9].

A typical radiation pattern for the main beam electronically steered to -40 degrees is shown in Fig. 11. The measured and theoretical data are in good agreement over the main beam and the first few sidelobes. Next, a two-way amplitude pattern cut for two phase centers displaced by 5.0 inches (1 column of the array) is shown in Fig. 12. The two main beams (denoted A and B) appear to be well matched and this can be quantified by computing the beam correlation matrix from which the beam decorrelation (or clutter cancellation) can be calculated. The two beams A and B are considered the two receive patterns, and a separate pattern denoted the transmit pattern is measured using the full aperture. The decorrelation as a function of pattern threshold is shown in Fig. 13. It is seen that the decorrelation is relatively converged once the sidelobe level is reached. In other words, main beam match is the primary factor in achieving the desired goal of pattern decorrelation. The beam decorrelation as a function of frequency is shown in Fig. 14. The 40 dB cancellation goal is met over nearly a 15-percent bandwidth. The degradation at 1.2 GHz is attributed to excessive phase errors in the module. Next, the DPCA cancellation as a function of scan angle is shown in Fig. 15. The design goal is met over much of the 30-60 degree scan sector. The decorrelation degrades rapidly as the beam is steered toward the null of the monopole pattern. The beam decorrelation for zero and five-inch phase center separations is shown in Table 1. This table also indicates very good agreement in decorrelation when comparing the results of far-field measurements and computer simulations. Finally, the DPCA cancellation as a function of module failures is shown in Fig. 16 for uncompensated and compensated conditions. Here, uncompensated means that a failure in one phase center does not affect the other phase center. Compensated refers to a situation where a module fails in one phase center and, to maintain good match between the phase centers, the corresponding element in the second phase center is purposely turned off. The result is that the compensated array has a slow degradation, as opposed to the uncompensated array which degrades rapidly with increase in module failures. Compensation is clearly an effective means for achieving good pattern match.

5. CONCLUSIONS

A subscale SBR phased array designed for two-channel "simultaneous-beam" DPCA operation has been tested using conventional planar near field measurements. The 96-element corporate-fed phased array used simple monopole radiating elements to achieve wide-angle scan coverage. DPCA beam decorrelation has been measured under a number of test conditions; scan angle, frequency, phase center displacement, and simulated module failures. The measurements indicate that 40 dB beam decorrelation is achieved for scan angles 30° to 60° from broadside, 15-percent bandwidth, and module failures with compensation up to 10%. The measured results are in good agreement with far field measurements and theoretical predictions.

REFERENCES

1. E.J. Kelly and G.N. Tsandoulas, "A Displaced Phase Center Antenna Concept for Space Based Radar Applications," IEEE Eascon, Sept. 1983, pp. 141-148.

2. M.L. Stone and W.J. Ince, "Air-to-Ground MTI Radar Using a Displaced Phase Center Phased Array," IEEE International Radar Conference, April 1980, pp. 225-230.

3. G.N. Tsandoulas, "Unidimensionally Scanned Phased Arrays," IEEE Transactions on Antennas and Propagation, Vol. AP-28, No. 1, January 1980, pp. 86-99.

4. J.C. Herper and A. Hessel, "Performance of λ/4 Monopole in a Phased Array," IEEE Antennas and Propag. Society, 1975 Symposium Digest, pp. 301-304.

5. A.J. Fenn and F.G. Willwerth, "Mutual Coupling in Monopole Phased Array Antennas," IEEE Antennas & Propag. Society, 1984 Symposium Digest, pp. 875-878.

6. A.J. Fenn, "Arrays of Horizontally Polarized Loop-Fed Slotted Cylinder Antennas," IEEE Trans. Antennas and Propag., Vol. AP-33, No. 4, April 1985, pp. 375-382.

7. A.C. Newell and M.L. Crawford, "Planar Near-Field Measurements on High Performance Array Antennas," Electromagnetics Division, Institute for Basic Standards, National Bureau of Standards, NBSIR 74-380, July 1974.

8. D.T. Paris, W.M. Leach, and E.B. Joy, "Basic Theory of Probe-Compensated Near-Field Measurements," IEEE Trans. Antennas and Propag., Vol. AP-26, No. 3, May 1978, pp. 373-379.

9. E.B. Joy, W.M. Leach, G.P. Rodrigue and D.T. Paris, "Applications of Probe-Compensated Near-Field Measurements," IEEE Trans. Antennas and Propag., Vol. AP-26, No. 3, May 1978, pp. 379-389.

Table 1
MEASURED BEAM DECORRELATION FOR VARIOUS PHASE CENTER SEPARATIONS
(BASED ON 1-D PATTERN CUT)

p (inches)	Decorrelation (dB)		
	Measured Near Field	Measured Far Field	Theory
0	-45.0	-44.8	-44.2
5.0	-46.0	-44.0	-44.9

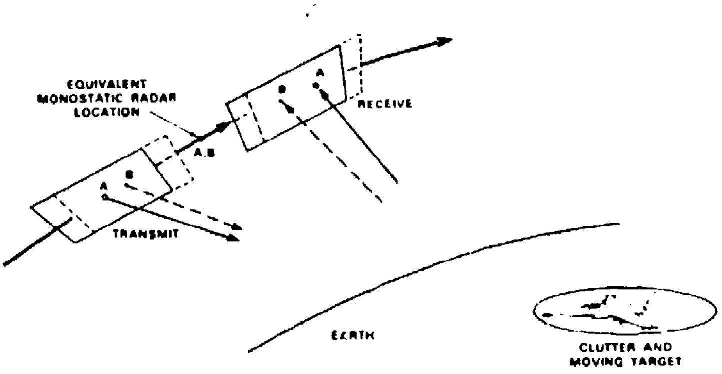

Fig. 1 "Simultaneous beam" DPCA applied to SBR target detection.

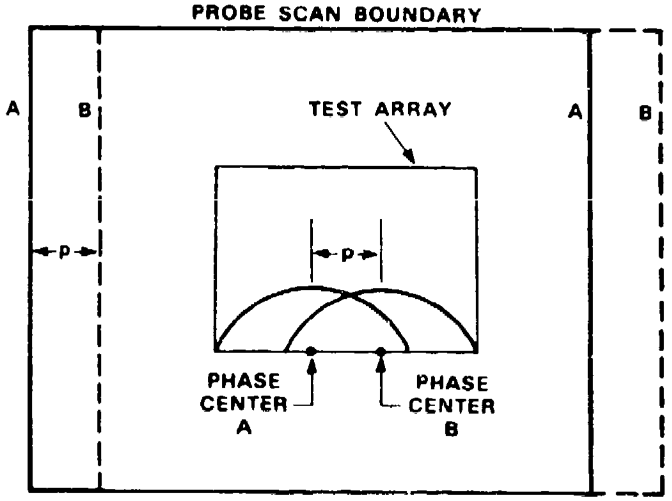

Fig. 2 DPCA near field measurement concept.

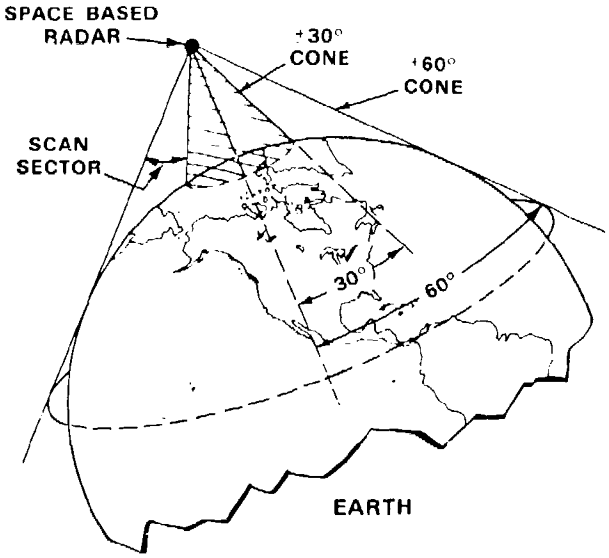

Fig. 3 SBR antenna coverage.

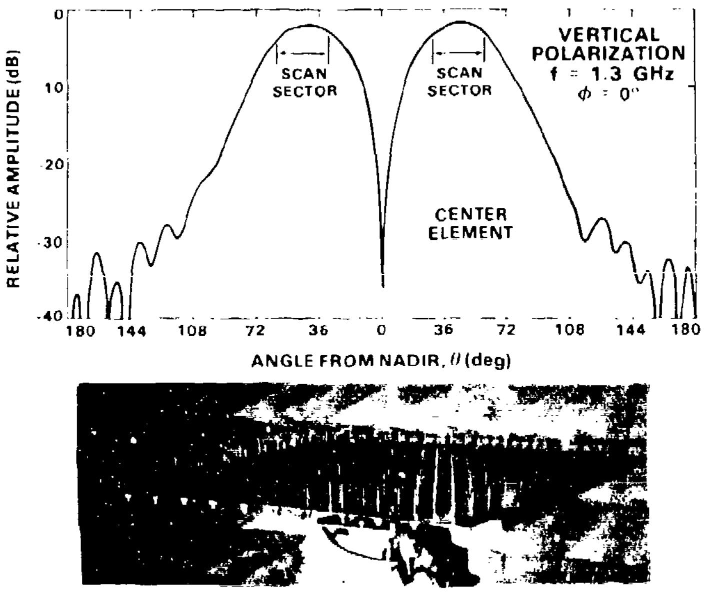

Fig. 4 Cylindrical monopole antenna element pattern, measured in a 121-element array (shown), suitable for coverage of the scan sector of Fig. 3.

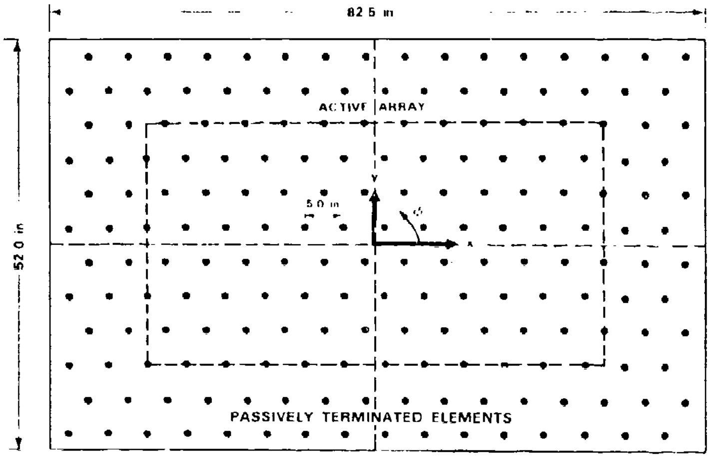

Fig. 5 96-element test array layout.

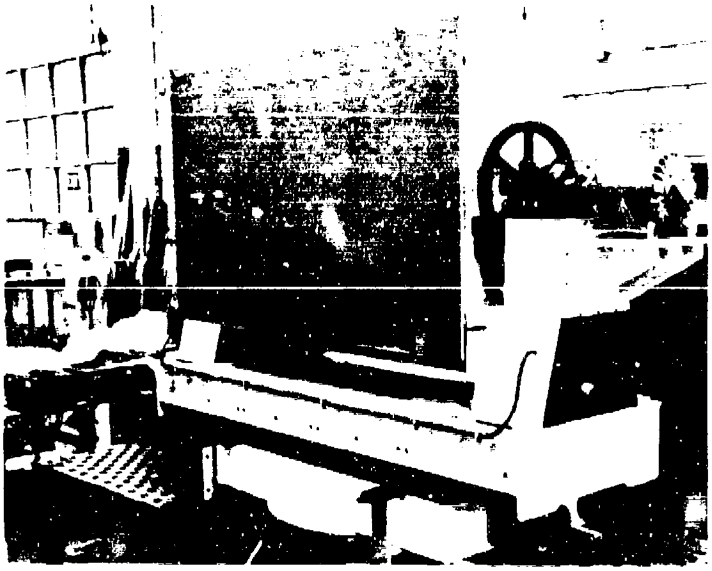

Fig. 6 96-element monopole phased array photograph.

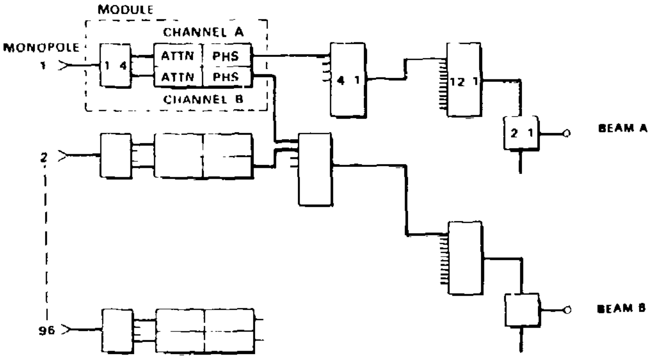

Fig. 7 Test Array DPCA implementation.

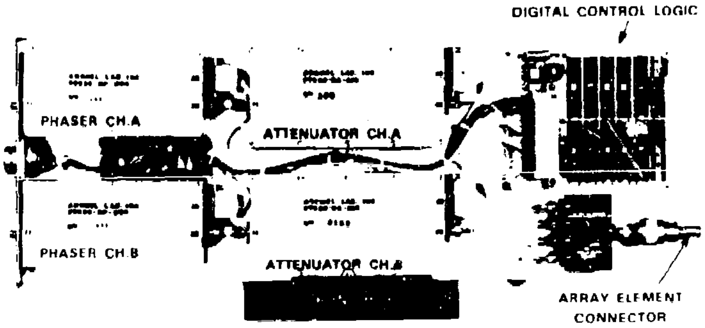

Fig. 8 Test array module photograph.

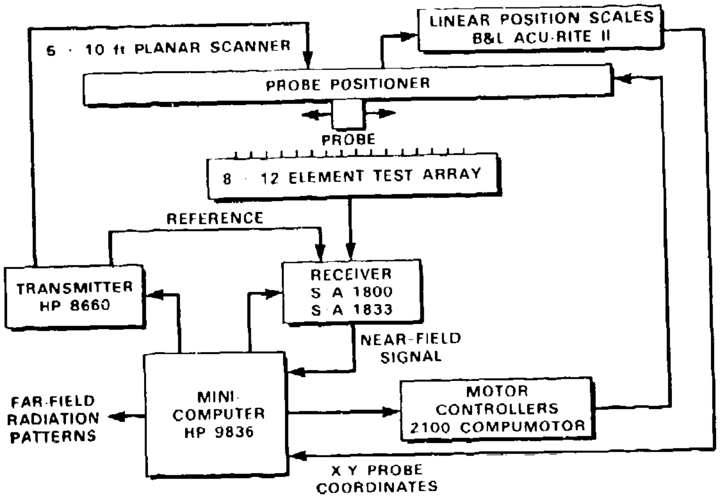

Fig. 9 Near-field scanner system block diagram.

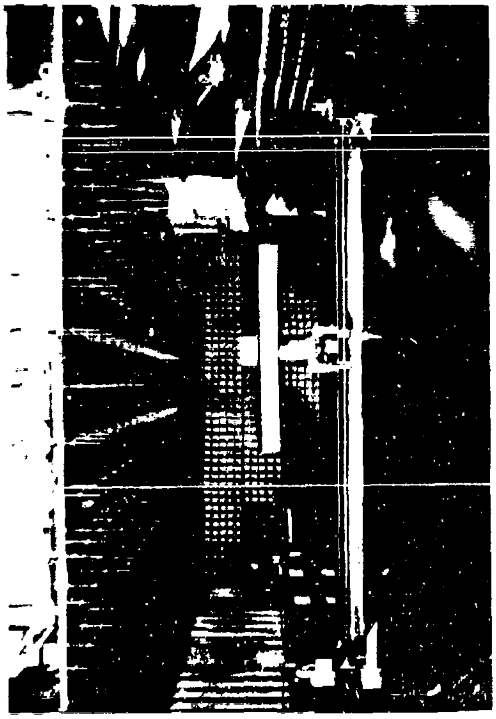

Fig. 10 Photograph of monopole array in near field facility.

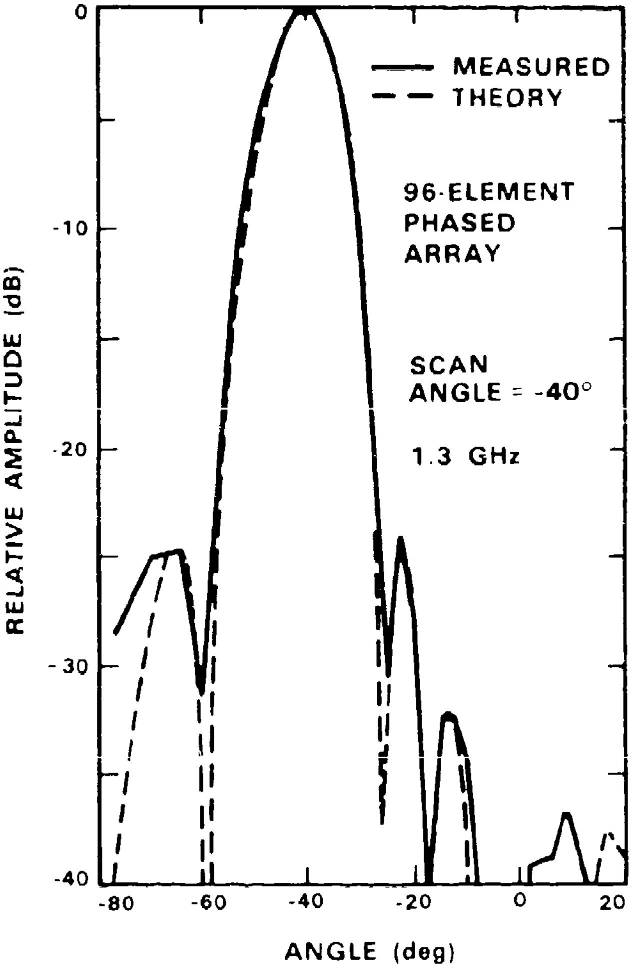

Fig. 11 Far-field pattern computed from near field measurements.

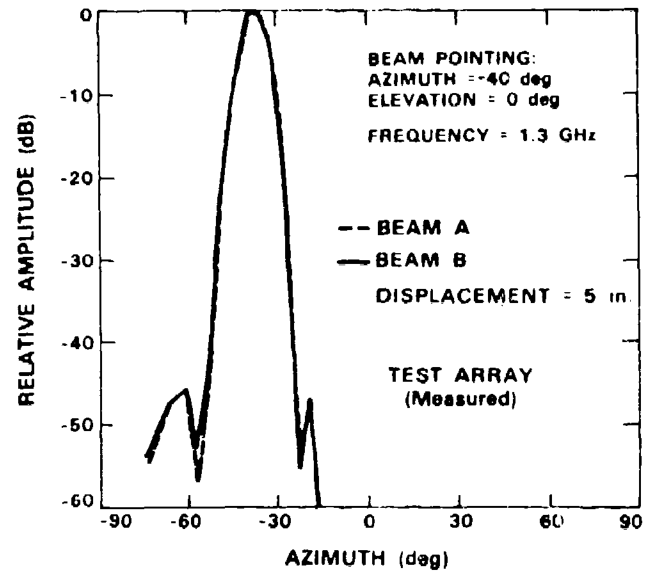

Fig. 12 Measured two-way azimuth cut amplitude pattern.

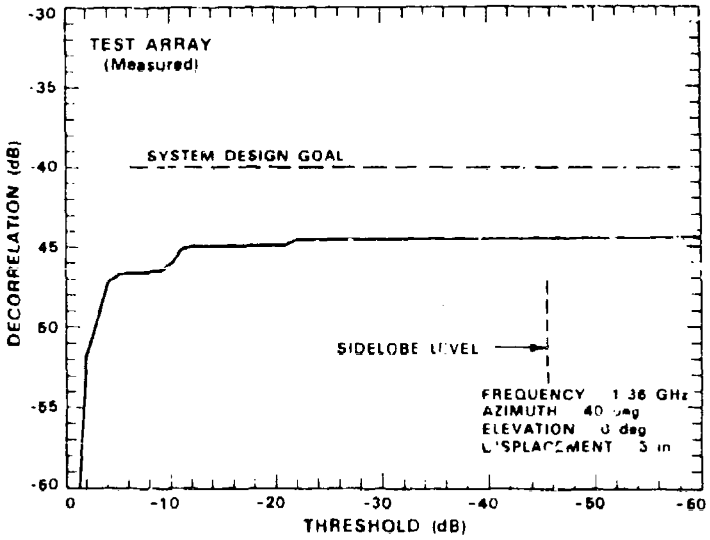

Fig. 13 Beam decorrelation as a function of pattern threshold.

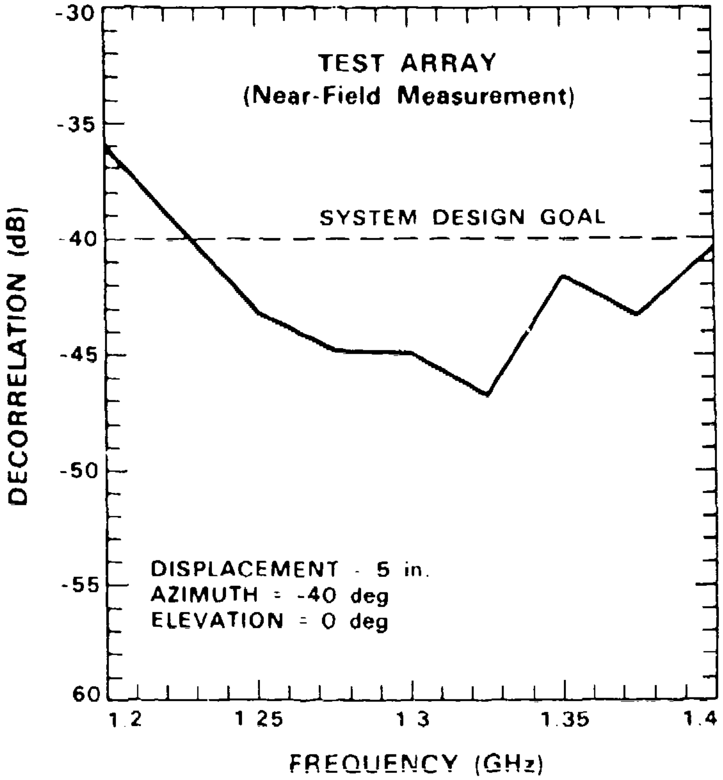

Fig. 14 Beam decorrelation as a function of frequency.

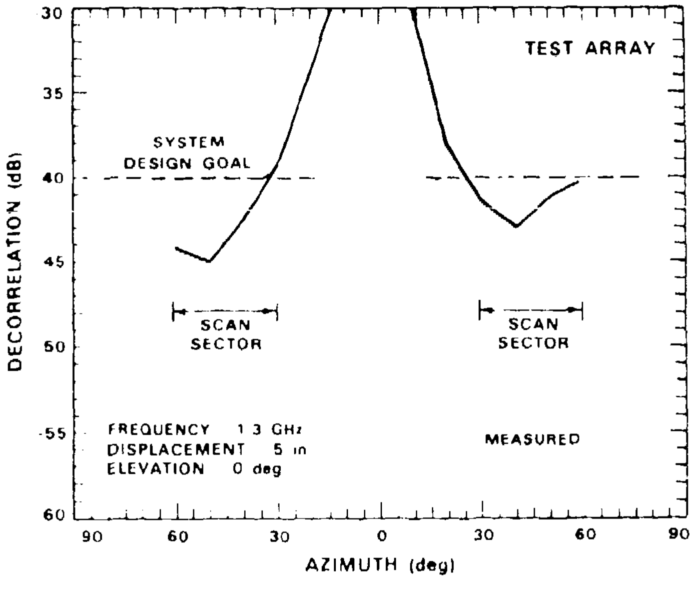

Fig. 15 Beam decorrelation as a function of azimuth scan angle at center frequency 1.3 GHz.

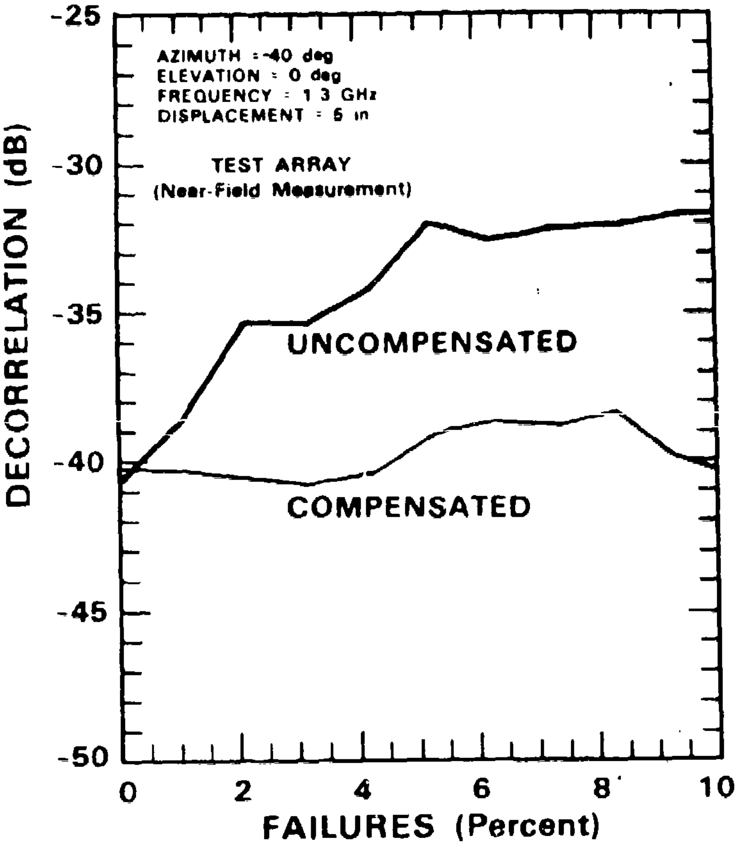

Fig. 16 Beam decorrelation as a function of module failures.

☆ U.S. GOVERNMENT PRINTING OFFICE 1985--502-384--20,130

MISSION
of
Rome Air Development Center

RADC plans and executes research, development, test and selected acquisition programs in support of Command, Control, Communications and Intelligence (C^3I) activities. Technical and engineering support within areas of competence is provided to ESD Program Offices (POs) and other ESD elements to perform effective acquisition of C^3I systems. The areas of technical competence include communications, command and control, battle management, information processing, surveillance sensors, intelligence data collection and handling, solid state sciences, electromagnetics, and propagation, and electronic, maintainability, and compatibility.

Printed by
United States Air Force
Hanscom AFB, Mass. 01731